MAGNETIC ELECTRON LENSES BASED ON THE UNIFORMLY MAGNETIZED ELLIPSOID

A Thesis submitted for the degree of

DOCTOR OF PHILOSOPHY

in

The University of Aston in Birmingham

by

ADIL ABDULLAH ALSHWAIKH

DEPARTMENT OF PHYSICS

March 1979

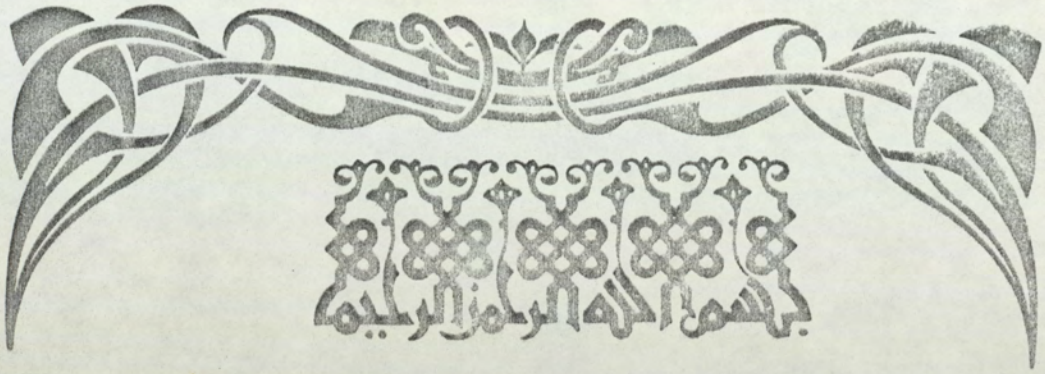

DEDICATED TO

ALHASAN IBN ALHAYTHAM (ELHASIN) (965-1028)

The man from my home town of Basrah, who was the original pioneer in optics studies. His firm foundations and theories form a solid basis for contemporary achievements in electron optics.

MAGNETIC ELECTRON LENSES BASED ON THE UNIFORMLY MAGNETIZED ELLIPSOID

Adil Abdullah Laili Alshwaikh

This thesis is concerned with mathematical models of magnetic pole-piece lenses. It extends the well-known square-top field model, which gives a good representation of double polepiece lenses to the calculation of spiral distortion and chromatic change in magnification and rotation.

The main aim of the project however is to propose and evaluate the uniformly magnetised ellipsoid as a possible basis for an understanding of the electron-optical properties of magnetic single pole-piece lenses. The special case of a magnetized hemisphere is shown to be of special importance since it provides a realistic model for such lenses and is adapted to mathematical analysis. For convenience, this model will be called the spherical model.

On the basis of this model, the coefficients of spherical aberration , Chromatic aberration and image distortion of single pole-piece lenses in various modes of operation have been calculated. The results so obtained enable one to select conditions of operation for minimum lens defects.

The results of this theoretical investigation give a valuable insight into the behaviour of practical single pole piece lenses, whose focal properties could not previously be accounted for in detail.

The analysis of the spherical model has also been extended to the calculation of the pre-field characteristics and the aberration coeff-icients of chromatic change in magnification and rotation. The results are compared with the known characteristics of conventional lenses.

Two modes of operation of single-pole lenses are considered in some detail. One is the possibility of using such a lens as a single-field condenser objective lens. The other relates to the possibility of com-bining two single-pole lenses in a projector system that is free from spiral distortion.

Finally, the ideas and results obtained from the theoretical analysis are compared with presently available experimental data on single-pole lenses.

Key Words

Aberration correction, electron microscopy, electron optics, lens aberration, lens computations, magnetic lens, magnetic lens model, snorkel lenses, spherical aberration, spherical field model, spiral distortion, square top field model.

CONTENTS

Page

LIST OF FIGURES

LIST OF SYMBOLS

Note: The symbol shown in square brackets is the computer equivalent (indentifier) for the symbol shown.

$A(z)$ [AX(k)] Distance function [A(z) = B(z)/NI] in computation of electron optical properties

$A(\sigma)$ Self demagnetizing factor

a Sphere radius and ellipsoid axis

$B(z)$ Axial flux density

B_m Maximum flux density

b Ellipsoid axis

c Ellipsoid axis

C_c Chromatic aberration coefficient

C_d Radial distortion coefficient

C_r Chromatic change of rotation coefficient

C_s Spherical aberration coefficient

C_{sp} Spiral distortion coefficient

C_m Chromatic change of magnification coefficient

D_{rad} Radial distortion coefficient ($D_{rad} = C_d/R^2$)

D_{sp} Spiral distortion coefficient ($D_{sp} = C_{sp}/R^2$)

$\overline{D}_{sp}$ Contribution to the spiral distortion coefficient of an intermediate individual element of the field distribution

DT_{sp} Spiral distortion coefficient of rotation-free system

d Half-width of any single-pole field distribution or half of the width of any symmetric field

d_f Half-width factor [$d_f = Bod/\mu_0 NI$]

e_m Electon charge (1.60219×10^{-19}C)/Mass of electron (9.1×10^{-28}gram)

e Eccentricity

F_p Projector focal length of a double lens

f = Focal length (e.g. f_p, f_{obj} and f_t)

f_{pre} [FPRE] Focal length of pre-field

g Particular solution to the paraxial ray equation

h Particular solution to the paraxial ray equation

I Intensity of magnetization

J Bessel function

K Excitation parameter ($K^2 = eB^2/8mV$)

k Excitation parameter ($k^2 = d^2eB^2/8mV$)

L Projection distance

L_1, ℓ [L] Separation distance between two field distributions in a correcting system for spiral distortion

L_2, [L2] Distance between the second lens in the correcting system and the screen

M Magnification parameter ($M = f_{po}/f_p$)

M_1 The magnification of the first lens at the second lens

M_F Final magnification of correcting system at the screen

m Ratio of finite conjugates in the square topped field

m_f Degree of flux concentration used by Kanaya et al (1976)

N Factor of demagnetization named by Professor H. du Bois

NI Lens excitation (ampere-turns)

P [P1] Excitation parameter ($NI/V_r^{\frac{1}{2}}$)

Pℓ Principal plane

Q_{rad} [QR] Radial distortion parameter of magnetic electron lens ($Q_{rad} = f_p D_{rad}^{\frac{1}{2}}$)

Q_{sp} [QS] Spiral distortion parameter of magnetic electron lens ($Q_{sp} = D_{sp}^{\frac{1}{2}} f_p$)

q Ratio between two asymmetrical field half-widths ($q = d_1/d_2$)

R Radius of pole-piece

r Height of the beam from the axis

r' The slope of the ray r

S Gap width of a lens

U Distance function ($U = kd/2Z$)

u Distance of the source from the lens

V_r Accelerating voltage

V Volume

v_r Relativistically corrected accelerating voltage [$V_r = v_o(1 + 0.978 \times 10^{-6} v$].

v Distance of the image of the source from the lens

X Particular solution to the paraxial ray equation

x Distance along the axis of the lens with respect to d

Y Particular solution to the paraxial ray equation

Y_o Neumann's Bessel function of the second kind of zero order

y Height of the beam from the axis with respect to d

Z Distance along the axis of the lens

Z_f Focal point

Z_i Position of image plane

Z_n The value at which $J_n(U) = 0$

Z_o Position of object

Z_p The intersection point of the asymptote to the ray leaving the field with the axis

$Z_{p\ell}$ Position of principal plane

Γ Gamma function

δ Special constant $\delta = x/a = y/b = z/c$

η Special function related to m_f

θ Angle of rotation of the image caused by the magnetic field of the lens

κ Magnetic susceptibility

λ Special function defined as $\frac{x^2}{a^2+\lambda} + \frac{y^2}{b^2+\lambda} + \frac{z^2}{c^2+\lambda} = \delta^2$

μ Permeability (Permeability in vacuum $\mu_0 = 4 \times 10^{-7}$ H/m)

ν Integer number

ξ Paraxial ray parameter for the exponential field distribution

$[\xi = \frac{k}{\ell n 2} \cdot \exp(-\ell n 2 . z/d)]$

ρ Radial height of Gaussian ray in the image

$\Delta\rho$ Distortion in the image

σ Special function defined as $\frac{x^2}{a^2+\sigma} + \frac{y^2}{b^2+\sigma} + \frac{z^2}{c^2+\sigma} = 1$

ϕ The angle defined geometrically as $\phi = \tan^{-1}(z/d)$

χ Ray solution to the paraxial ray equation with the condition at the object plane

χ $\chi_o = 0$ and $\chi_o' = 1$ Particular solution to the paraxial ray equation

ψ Special function related to $z/\eta d$ as; $d\psi/d(z/\eta d) = (1-\psi^2)m_f$

Ω Original uniform magnetic field

Ω_{in} Magnetic potential inside the solid

Ω_{out} Magnetic potential outside the solid

ω Paraxial ray parameter for the Bell-shaped field ($\omega^2 = 1+K^2$)

ACKNOWLEDGEMENT

I should like to express my thanks and appreciation to my supervisor, Professor T. Mulvey, for suggesting the project of research, and for penetrating comments and stimulating discussion at all stages throughout the work.

I am also grateful to Dr. F. Z. Marai for making available programs for the investigation of the electron-optical properties and aberrations of magnetic lenses and for useful discussions at the beginning of this work.

I would like to thank Mr. H. Elkamali, for providing some experimental data relating to magnetic lenses. In addition, I would like to acknowledge the help of the Rutherford Laboratory in computing the flux density distribution in a conical pole piece.

My thanks are also due to Mr. A. Ridha for his assistance with the experimental part of my work.

Finally, I wish to express my gratitude to my brothers for their support and encouragement.

1. INTRODUCTION

Several electron optical features and elements are common to all types of electron microscopes such as the transmission (TEM), scanning (SEM) and Scanning Transmission electron microscope (STEM). They are similarly shared by many other related instruments, including the electron-probe microanalyser and the electron diffraction camera. An important element in all these electron optical instruments is the magnetic electron lens.

The iron-free solenoid is an interesting example of a magnetic lens. It may consist of either a wire or tape wound round a non-magnetic core and has an appreciably lower spherical aberration (Basset and Mulvey, 1969) than that of conventional lenses. A noteworthy investigation has been carried out by Marai (1977) on a wide range of these lenses.

1.1 The Magnetic Pole-piece Lens

Magnetic lenses in which the magnetic field is created by energizing coils and iron pole-pieces can be divided into two categories, double pole-piece lenses and single pole-piece lenses.

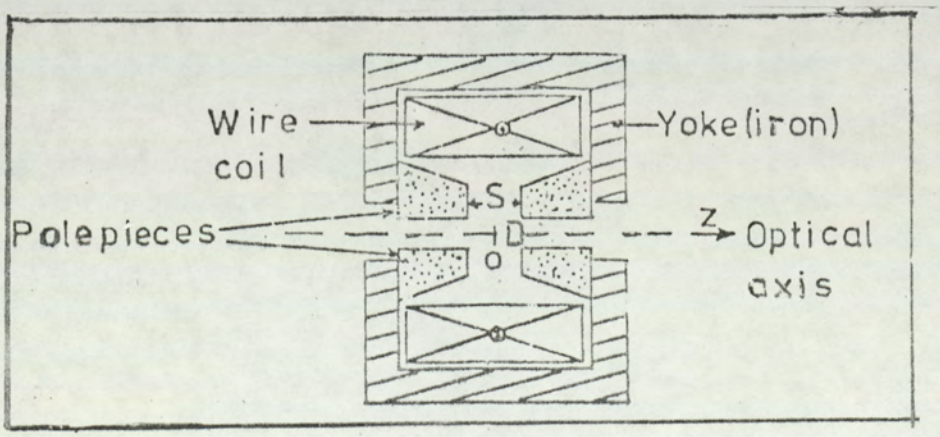

Fig. 1.1 Schematic cross-section of a symmetrical double-pole magnetic lens.

1.1.1 Double pole-piece magnetic lens

The most commonly used magnetic electron lenses are double pole lenses (fig.1.1); they consist essentially of a coil of wire wound on a core of ferromagnetic material of high magnetic permeability. The iron core of the lens is bored to a diameter D along the axis of the coil to allow the electron beam to pass through a gap of width S which is formed between two iron pole-pieces. The axial magnetic field in the gap S is therefore non-uniform and this gives rise to the refractive action of the lens, the properties of which can be expressed in terms of the ratio S/D of gap width to inner diameter.

Many authors have published useful studies covering these lenses. Amongst these may be mentioned the papers by Liebmann and Grad (1951), Durandeau and Fert (1957), (Fert and Durandeau, 1967) and later still a comprehensive review by Mulvey and Wallington (1969). If the diameters, are unequal, then the axial field distribution of the double pole lens will become asymmetrical. Some of the important properties of assymetrical double-pole lenses were discussed by Liebmann (1951, 1955A, 1955B), Yanaka and Watanabe (1966).

1.1.2 Single pole-piece lenses

If we divide a double pole piece lens in two, midway between the pole-pieces, we will then be left with two single pole-piece lenses; each lens now has one polepiece called the snout.Fig.(1.2) shows single pole lenses (snorkel) used for SEM and for STEM and TEM (Mulvey, 1974). Several papers have now been published giving account of the development of this lens, such as those of Mulvey and Newman (1973A), Mulvey (1974) and Mulvey and Marai (1974).

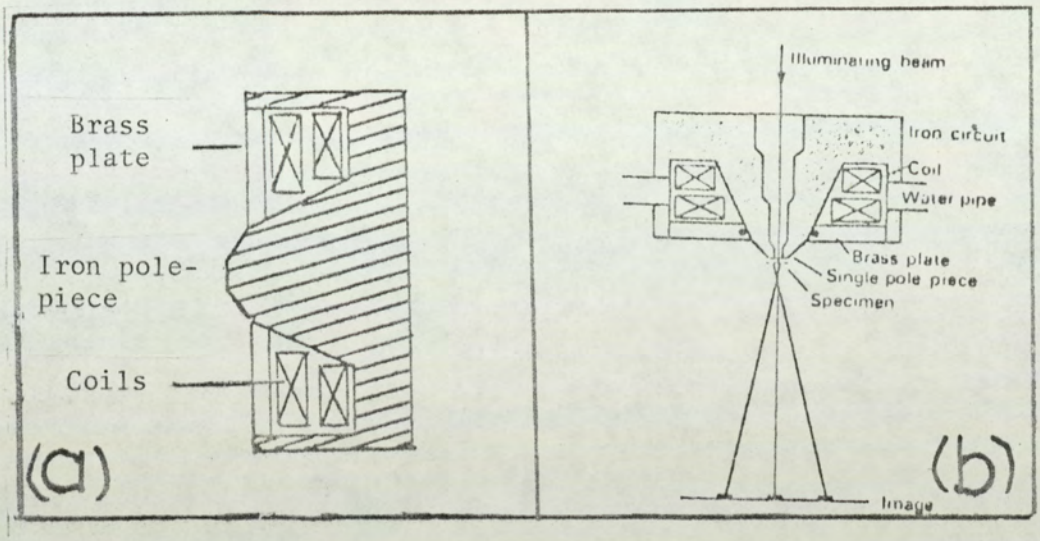

Fig. 1.2 The single pole lens. (a) Single pole-piece lens for SEM; (b) Singe pole piece lens for STEM and TEM.

Such a lens may be used as an objective lens in TEM and STEM (Mulvey, 1974) or otherwise as a projector and objective lens (Mulvey and Newman, 1973B), (Juma and Mulvey, 1975). Some experimental single pole lenses have been developed in this department by Mulvey and his colleagues. These miniature lenses are often simply called a mini-lens. Some basic experiments on these lenses have been done by Mulvey and Newman (1972, 1973A and 1973B), Juma and Mulvey (1955), Lambrakis et al (1977) and Elkamali and Mulvey (1977).

For cooling the winding of this type of lens, water is directly applied to them, and this has been proved as being very effective. Further research is now taking place in this department to improve appreciably the efficiency of the cooling method.

1.1.3 The axial magnetic field distribution

The magnetic field of a lens can be produced in a number of diff-

erent ways. One way is to employ current-carrying coils without a magnetic circuit. In this way it is possible to concentrate the magnetic flux within a limited region and to obtain a higher field with a given coil. The axial value of this field, which is produced from an iron-free coil, can be easily calculated by the Biot-Savart law.

This magnetic field, brought about by the coil can also be associated with a high permeability magnetic circuit; this becomes saturated when the magnetic induction reaches a value of around 2.2 Tesla. Basically, there are four different methods for calculating the axial magnetic field distribution. The first is the relaxation method (Liebmann and Grad, 1951) which applies to scalar potentials and is used also to find the field inside the magnet), then there is the differential finite element method (Munro 1972); alternatively one may choose the integral finite element method (Trowbridge et al, 1972), or proceed experimentally by the Hall-probe gaussmeter method. The last two methods were used to measure the axial field distribution of some experimental single pole lenses mentioned in various parts of this thesis. The last method, however, is not usually capable of measuring the field distribution inside the snout itself because a standard gaussmeter probe cannot usually be inserted in the bore of the lens.

If high permeability material are uniformly magnetized a magnetic field will be produced outside the solid. The field outside solids may be calculated mathematically, many magnetic problems of this type were in fact solved back in the nineteenth century. One such problem solved in this way is that of the uniformly magnetized iron sphere (Kelvin, 1872). These sources of fields can also be determined, in special

cases, by the use of an electrostatic analogy as illustrated in the work on the uniformly magnetized ellipsoid. Finally, the few lenses which have permanent magnets can have their field distribution calculated by one of the well-known analytical equations descibed by Grivet (1972).

1.2 Mathematical models for magnetic lenses

Magnetic field models are analytical expressions that represent the axial field distribution B(z) of magnetic lenses. Such models make the electron-optical properties of the field distribution easy to study and interpret.

Each model gives a design basis for a lens, especially when the model is capable of being realised physically.

In various aspects of electron-optics research, different mathematical models were proposed to represent the axial field distribution B(z). Some of these will now be summarized because reference will be made to them at different parts of this thesis.

Many field models deal exclusively with double-pole lenses. Examples are the Glaser Bell-shaped field (Glaser, 1941B), that of Grivet-Lenz (Grivet, 1952 and Lenz, 1950), the "three-halves field" (Kanaya,1955) and the square-top field (Durandeau and Fert, 1957). While the exponential field (Marai and Mulvey, 1974) and the spherical field (Alshwaikh and Mulvey, 1977) deal with single pole lenses.

A large selection of papers has appeared containing the first type of model, plus the analytical expression for its aberration. A few of

the names which come to mind in connection with these are those of Scherzer (1937), Kanaya (1955), Kamminga (1968), Hawkes (1972) and Grivet (1972). It was Kanaya and his colleagues (1976) who developed the mathematical expression that generalizes the above models.

The main purposes of this thesis are (a) to extend the theoretical study of double pole piece lenses by using their mathematical models. This study includes some important aberrations such as spiral distortion. (b) to investigate some theoretical pole piece lenses, since it is difficult to apply the double pole piece lens model to single pole piece lenses; (c) to find realistic models and thus an optimum design pole piece lens, where a correlation exist with its actual pole piece structure; (d) to study in detail one of the more realistic model named uniformly magnetized sphere (Alshwaikh and Mulvey, 1977) and to investigate its applications. In addition, the above model is used in this thesis to find the optical characteristics and aberrations of single pole piece lenses.

1.2.1 Models for double pole piece lenses

A summary is given here of the properties of two specific mathematical models for double pole piece lenses. These two models are useful for checking numerical calculations. In addition it is possible to extend the range of previous calculations to include certain aberrations such as spiral distortion, chromatic change in magnification and chromatic change in rotation.

Such programs can then prove fruitful in the study of focal properties and various aberrations for new types of lenses.

Constant axial field (square top field)

The homogeneous field $B(z) = B_o$ of field width S between abscissa $z = \pm S/2$, as shown in fig.1.3 is most useful as a first approximation because any field distribution can be divided into successive intervals and each interval treated as a separate square-top field (fig.1.4).

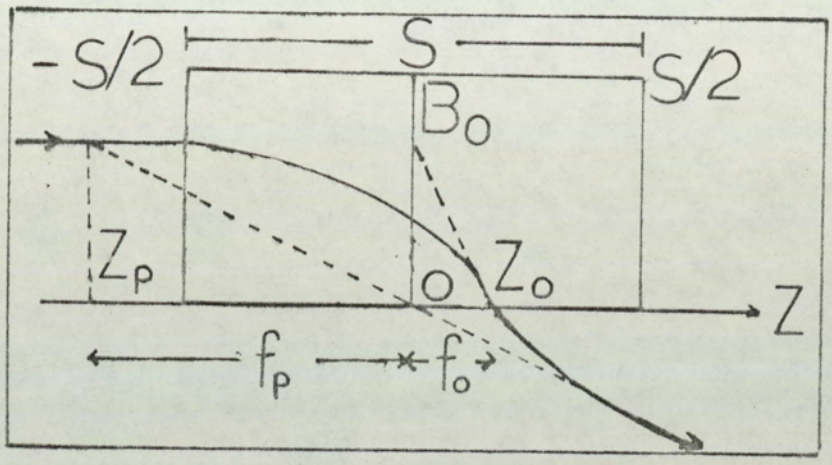

Fig. 1.3 The square top field model and the definition of the main focal parameters

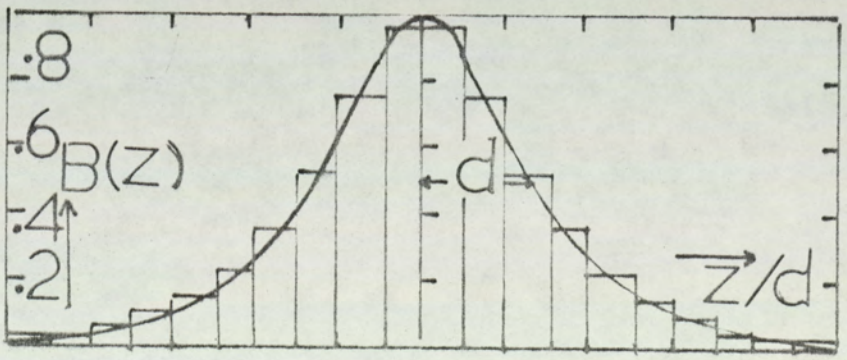

Fig. 1.4 A magnetic field distribution divided into successive square top fields

The corresponding paraxial ray equation may be written:

$$d^2r/dz^2 + K^2r = 0 \qquad \ldots (1.1)$$

where

$$K = (e/8mV_r)^{1/2} B(z)$$

and (e/m) is the ratio of charge to mass of the electron. V_r is relativistically corrected accelerating voltage and r is the height of the trajectory through the field. For an incident ray of initial slope r_o' and distance r_o from the axis, the trajectory at any point at a distance z from the origin takes the form

$$r = r_o\cos[K(S/2+z)] + (r_o'/K)\sin[K(S/2+z)] \qquad \ldots (1.2)$$

The slope r' of the ray is given by

$$r' = r_o'\cos[K(S/2+z)] - Kr_o\sin[K(S/2+z)] \qquad \ldots (1.3)$$

The objective focal distance z_o, (see fig.1.3) is given by

$$z_o = [\pi/2K - S/2] \qquad \ldots (1.4)$$

The projector focal length (f_p) obeys the relation

$$S/f_p = (KS)\sin(KS) \qquad \ldots (1.5)$$

Equation (1.5) applies also for f_{obj} up to an excitation KS = $\pi/2$, and the objective focal length when z_o is inside the lens (i.e. KS > $\pi/2$)

$$f_{obj}/S = 1/KS \qquad \ldots (1.6)$$

The general characteristics of this field are shown in fig. 1.5

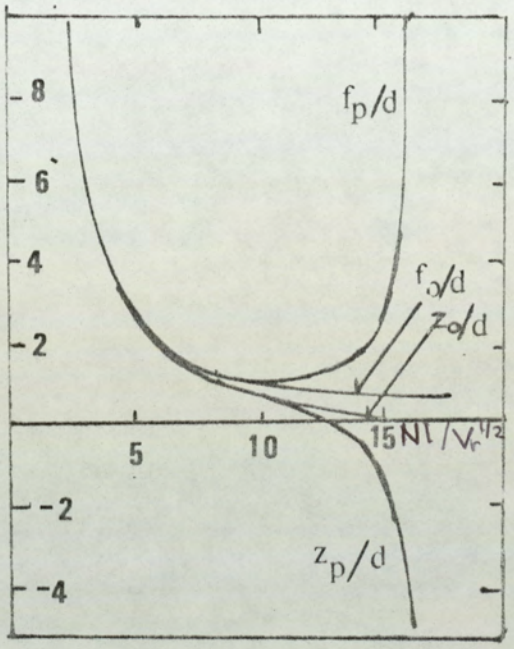

Fig. 1.5 The focal properties of the square top field model

The Bell-shaped field

This field is described by the function

$$B(z) = B_o / [1+(z/d)^2]^n \qquad \ldots (1.7)$$

where d = half of the half-width and the maximum field (B_o) occurs at the lens centre (fig.1.6) and n is an integer

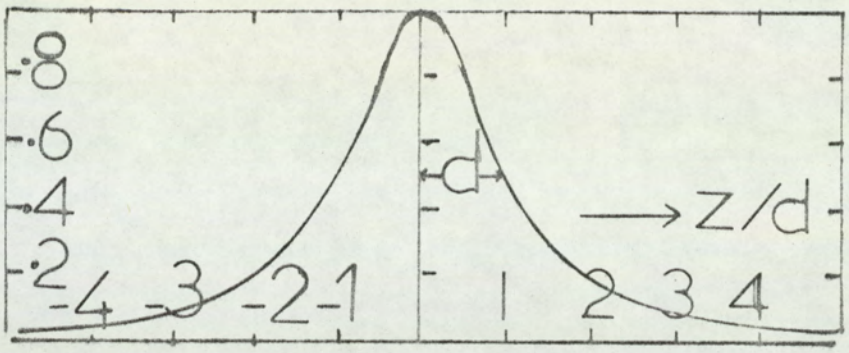

Fig. 1.6 The Glaser Bell-shaped model and the definition of 'half-width' (d)

This investigation is concerned with the case n = 1.

Putting $k = eB_o^2 d^2/8mV_r$, $\omega = (1+k^2)^{\frac{1}{2}}$, $\phi = \tan^{-1}(z/d)$

The general solution of equation (1.1) for this field is

$$r/d = \sin\omega\phi/\omega\sin\phi \qquad \ldots (1.8)$$

The slope r' at $z = -\infty$ is given by

$$r' = -\sin\omega\pi/\omega \qquad \ldots (1.9)$$

The projector focal length has the value

$$f_p/d = \omega\operatorname{cosec}\omega\pi \qquad \ldots (1.10)$$

General form of double-pole lens fields

There are many models which deal with double pole lenses but each of them is restricted to a particular type of field. So the generalization of previous models is highly desirable. Kanaya et al (1976) have made an attempt to present a complete solution of magnetic lens models. The magnetic field distribution of half width (d) are described in the

general form

$$B(z\eta/d) = B_o(1-\psi^2)^{(2m_f-1)/2)} \qquad \ldots (1.11)$$

where the function ψ is related to the coordinate z/d as

$$\frac{d(z/d)}{d\psi} = \frac{-(1-\psi^2)^{m_f}}{\eta} \qquad \ldots (1.12)$$

The parameter (m_f) takes on the special values 0.5, for the constant field, 1 for the Lenz-Grivet field, 1.1 for the three-halves field and 1.5 for the Bell-shaped field. It should be noted that η is related to m_f through a special function shown later in fig. 4.1.

The paraxial ray equation of the above general form is given by

$$(1-\psi^2)(d^2y/d\psi^2) - 2m_f\psi(dy/d\psi) + K^2y = 0 \qquad \ldots (1.13)$$

where $$K = (e/8mV_r)^{\frac{1}{2}} \cdot (\eta d) \cdot B_o$$

Equation (1.13) can be solved in terms of the hypergeometric function F,

$$y = AF[\alpha,\beta,\gamma,(\psi+1/2)] + B(\frac{\psi+1}{2})^{1-\gamma} F[\alpha+1-\gamma,\beta+1-\gamma,2-\gamma,(\psi+1)/2] \qquad \ldots (1.14)$$

where A and B are constants with

$$\alpha+\beta+1 = 2m_f, \quad \gamma = m_f, \quad \alpha\beta = -K^2$$

Kanaya and his colleagues, derived exact analytical expressions for all the important optical properties as a function of the parameter m_f. It is therefore possible to select designs of minimum aberration.

1.2.2 Models for single pole lens

A difficult task arises if an attempt is made to apply the above models to single pole lenses.

Mulvey and Newman (1973) found that it is not possible to apply the above field distributions to a single pole lens. It is necessary therefore to look for models from which the properties of single-pole lenses can be deduced.

The exponential field

The axial field distribution of the exponential field takes the form

$$B(z) = B_o \exp . (-z\ell n2/d) \qquad \ldots (1.15)$$

where B_o is the maximum field and (d) is the total width of the axial field distribution from the maximum field to the axial point where the field drops to half the maximum.

Glaser (1952) derived the paraxial ray equation for this field as follows:

$$(d^2y/d\xi^2) + 1/\xi(dy/d\xi) + Y = 0 \qquad \ldots (1.16)$$

where $Y = r/d$ and $\xi = (K/\ell n2)\exp.(-z\ell n2/d)$.

The curve representing the model (fig.1.7) consists of two parts, a steep part coinciding with the vertical axis and an exponentially decaying part. For the sake of convenience the vertical part will be called the steep edge while the other part will be called the sloping edge.

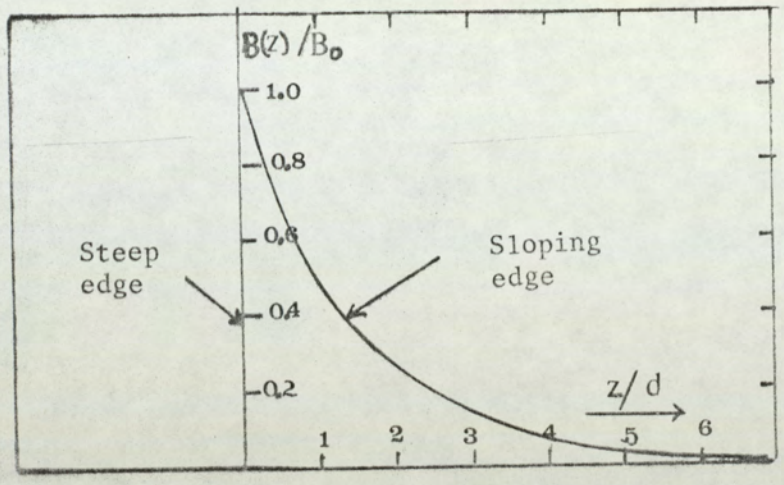

Fig. 1.7 The exponential field model showing the two edges

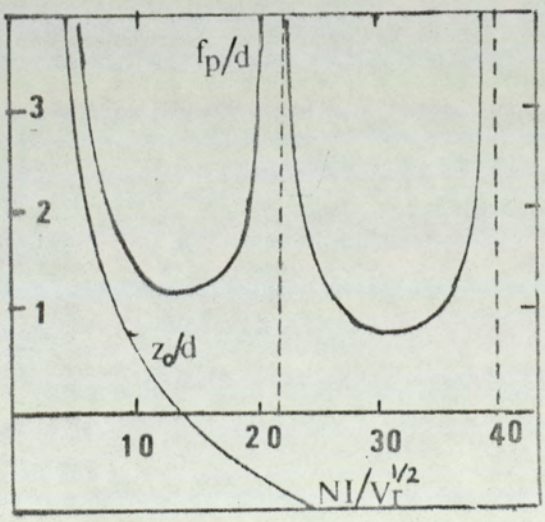

Fig.1.8 The focal properties $f_{p/d}$ and $z_{o/d}$ as a function of the excitation parameter $NI/V_r^{\frac{1}{2}}$

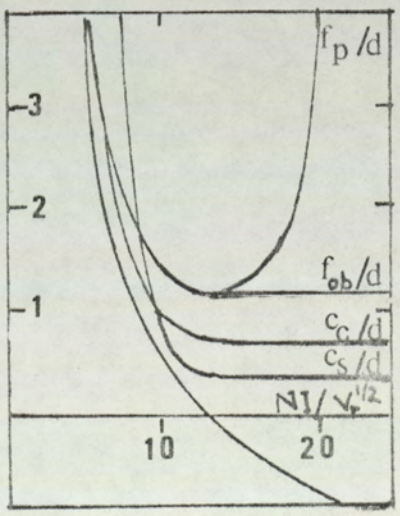

Fig. 1.9 The focal properties and aberration coefficients of the exponential field model

A particular solution when the ray is incident on the sloping part of the field starting at $z = \infty$ with initial height $r = 1$ and $r' = 0$ (fig.1.7), the solution of equation (1.16) takes the form

$$r/d = J_o(\xi) = J_o(K/\ell n2.\exp.(-z\ell n2/d) \quad \ldots (1.25)$$

An extensive investigation of this case was carried out by Marai (1977). His results are as follows:

$$z_{F/d} = 1.44\ell n(NI/V_r^{\frac{1}{2}}) - 3.69 \quad \ldots (1.26)$$

where z_F is always positive (i.e. $NI/V_r^{\frac{1}{2}} > 13$).

The focal lengths takes the form:

$$f_{obj/d} = fp/d = 7.77NI/V_r^{\frac{1}{2}}.J_1(0.1857\ NI/V_r^{\frac{1}{2}}) \quad \ldots (1.27)$$

Notice that this equation for f_{obj} only applies in the region $0 < NI/V_r^{\frac{1}{2}} < 13$. For $NI/V_r^{\frac{1}{2}} > 13$, the objective focal length is constant and given by

$$f_{obj/d} = 1/\ell n2.\xi_1.J_1(\xi_1) = 1.156 \quad \ldots (1.28)$$

Fig.1.8 shows the parameters z_F/d and f_p/d as a function of excitation parameters $NI/V_r^{\frac{1}{2}}$ for two zones. The general optical properties of this field according to these analytical expressions with some aberration parameters, such as chromatic (C_c) and spherical aberration (C_s) coefficients are shown in fig.1.9.

The general solution for this field is discussed in detail in chapter 3. The results obtained with the ray incident on the sloping

edge agree with those obtained by Marai (1977). The special case of the ray incident on the steep edge is also treated.

The exponential field (Marai, 1977) has proved satisfactory when applied to certain single-pole lenses, but the model has several imperfections. One of these is that objective focal length, chromatic aberration coefficient and spherical aberration coefficient are constant in the region $NI/NI_o > 1.0$, (fig. 1.9) while they increase slowley for real field distributions.

It may well also share some of the disadvantages of certain double pole fields namely that it may not satisfy Laplace's equation. This means that it is not readily possible to correlate the axial field distribution with the physical structure of the magnetic circuit.

It may therefore be more profitable to start with a known magnetic structure whose magnetic field can be calculated analytically. It therefore seems useful to investigate the fields due to different geometrical shapes of soft iron placed in a uniform magnetic field.

1.2.3 Fields due to a uniformly magnetized solid

It is difficult to correlate the exponential field model with an actual pole piece structure of single pole piece lenses (see fig.1.2), and so find an optimum design. For this reason, it seemed desirable to have a method whereby the effect of pole shape of the lenses can be readily investigated. Consider, for example, the magnetic potential (Ω) at an external point P due to a uniformly magnetized solid, fig.1.10.

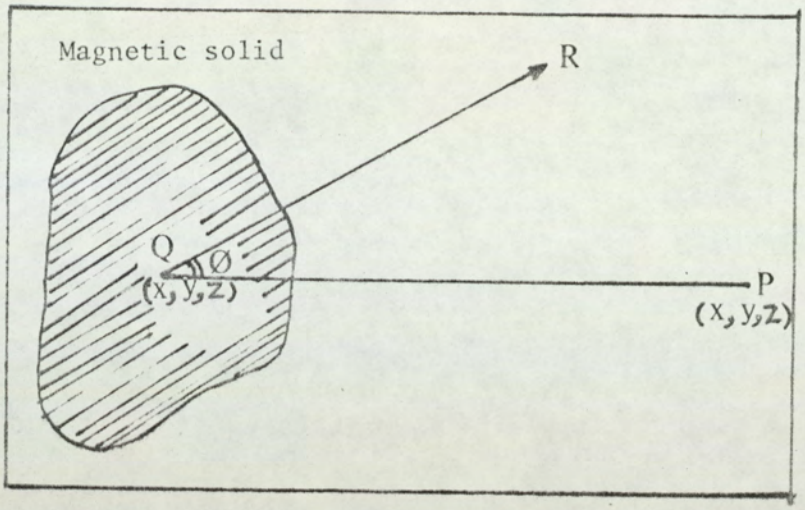

Fig.1.10 Uniformly magnetized solid. $\overline{QR}$ is proportional to the intensity I of magnetization. QP is the optical axis.

The following method (Ramsey, 1937) can be used.

We may regard the magnet as composed of a large number of elementary magnets of moment IdV, where I and dV are the intensity of magnetization and volume element respectively. Let x_1, y_1, z_1 be the coordinates of a point Q at such an element. Let P be an external point (x,y,z) and let QP = r make an angle θ with direction of I. Take the axis of x in the direction of I. Then the potential at P due to the elementary magnet is $IdV \cos\theta/r^2$ or $IdV \frac{\partial}{\partial x}(1/r)$. Hence the potential at P due to the whole solid is given by

$$\Omega = I \frac{\partial}{\partial x_1} (\frac{1}{r}) dV \qquad \ldots (1.29)$$

Integrating through the volume, putting

$$r^2 = (x-x_1)^2 + (y-y_1)^2 + (z-z_1)^2 \qquad \ldots (1.30)$$

so that $$\frac{\partial}{\partial x_1}(\frac{1}{r}) = - \frac{\partial}{\partial x} \cdot \frac{1}{r}$$

Therefore

$$\Omega = -\int I \frac{\partial}{\partial x}\left(\frac{1}{r}\right) dV$$

or

$$\Omega = -\frac{\partial}{\partial x}\int \frac{I dV}{r}$$

But $\int IdV/r$ represents the potential at P fig.1.10. due to uniform distribution of matter of density I, so that the potential of the magnet can be found by applying the operator $-\partial/\partial x$ to the potential of this uniform distribution of matter.

Magnetic field due to a magnetized ellipsoid

It is a long and complicated procedure to determine the field inside and outside a ferromagnetic ellipsoid placed on a uniform magnetic field, (fig.1.11).

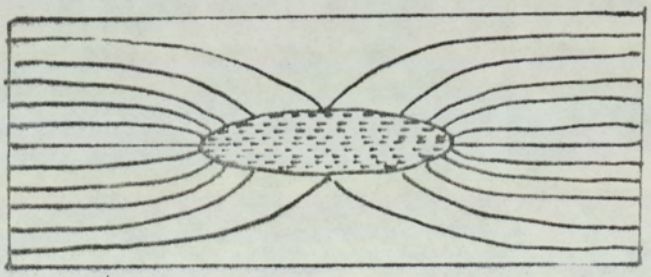

Fig.1.11 Short ellipsoid of infinitely permeable material in a uniform field

For our purpose it is sufficient to state the main formulas only.

Assuming an ellipsoid with variable axis x,y,z inside the ellipsoid had semi-axis a,b and c. Using $\delta = x/a = y/b = z/c$. λ is defined by Webster (1897) as

$$x^2/(a^2+\lambda) + y^2/(b^2+\lambda) + z^2/(c^2+\lambda) = \delta^2 \qquad \ldots (1.32)$$

When $\delta = 0, \lambda = \infty$ and when $\delta = 1$, λ has a value which we will call σ defined by

$$x^2/(a^2+\sigma) + y^2/(b^2+\sigma) + z^2/(c^2+\sigma) = 1 \qquad \ldots (1.33)$$

By using the notation Ω for potential and R_λ as

$$R_\lambda = (a^2+\lambda)(b^2+\lambda)(c^2+\lambda)^{\frac{1}{2}} \qquad \ldots (1.34)$$

we can use the results given by Webster (1897) in the form

$$d\Omega/dx = -2\pi abcx \int_\sigma^\infty d\lambda/(a^2+\lambda) \cdot R_\lambda \qquad \ldots (1.35)$$

and for internal point

$$\partial\Omega/\partial x = -2\pi abcx \int_0^\infty d\lambda/(a^2+\lambda) \cdot R_\lambda \qquad \ldots (1.36)$$

put

$$A_n(\sigma) = \frac{abc}{2} \int_\sigma^\infty d\lambda/(\lambda+q^2) \cdot R_\lambda \qquad \ldots (1.37)$$

Notice that A_1, A_2 and A_3 are obtained by putting a,b,c respectively for q.

Suppose that the major axis (a) of the ellipsoid is parallel to the x-axis and the uniform magnetic field lies in the same direction. The potential on the axis is then $\Omega = -B_{ox}.x$. The following expressions are for the potential inside (Ω_{in}) and outside (Ω_o) when a homogeneous ellipsoid of permeability ε_2 is introduced in the field (Durand 1966 and 1968).

$$\Omega_0 = \Omega\left[1 - \frac{\frac{\varepsilon_2-\varepsilon_1}{\varepsilon_1}A_1(\sigma)}{1 + \frac{\varepsilon_2-\varepsilon_1}{\varepsilon_1}A(0)}\right] \qquad \ldots (1.38)$$

$$\Omega_{in} = \Omega\left[1 + \frac{1}{1 + \frac{\varepsilon_2-\varepsilon_1}{\varepsilon_1}A_1(0)}\right] \qquad \ldots (1.39)$$

The self-demagnetizing factors L, M and N can be denoted by $4\pi A_n(0)$, where n = 1,2,3 respectively. SO (N) can be written for an ellipsoid with a ≠ b = c when the ellipsoid is ellongated.

$$N = 4\pi(1/e^2-1)[(1/2e)\log_e(1+e/1-e) - 1] \qquad \ldots (1.40)$$

and the eccentricity (e) is given by

$$e = [1-c^2/a^2]^{1/2} \qquad \ldots (1.41)$$

When the ellipsoid is oblate

$$N = 4\pi[1/e^2-(1-e^2)^{1/2} \cdot \sin^{-1}e/e^3\ ] \qquad \ldots (1.42)$$

with

$$e = [1-a^2/c^2]^{1/2} \qquad \ldots (1.43)$$

The magnetic force (H) inside a magnetised ellipsoid induced by an external original force (H') is given by the equation (Ewing, 1891)

$$H/H' = 1/(N\kappa+1) \qquad \ldots (1.44)$$

Where κ is magnetic succeptibility and N takes the values in equations (1.40) and (1.42). The last parameter is called the magnetization factor by Professor H. duBois (Ewing, 1891).

The uniformly magnetized iron sphere

The iron sphere is a special case of the uniformly magnetized ellipsoid, and it seemed useful to investigate its electron-optical properties, since the analytical solution for the magnetic potential due to such a sphere has already been calculated (Kelvin, 1872).

If a sphere is placed inside a uniform magnetic field, it will take up a uniform field too (Kelvin 1872), fig.(1.12). If the external field is $B_o/2$ and the sphere has a radius (a), then the potential inside the sphere (Ω_i) follows the relation

$$\Omega_i = -[1.5(\mu+2)]B_o r\cos\theta \qquad \ldots (1.45)$$

while the potential outside the sphere (Ω_o) is

$$\Omega_o = \left[\left(\frac{\mu-1}{\mu+1}\right) \frac{a^3}{r^3} \right] \frac{B_o r}{2}\cos\theta \qquad .. (1.46)$$

where μ = the permeability, r = the radius vector and θ is the angle between r and the direction of magnetization (z-axis). Both r and θ are shown in fig.(1.12)

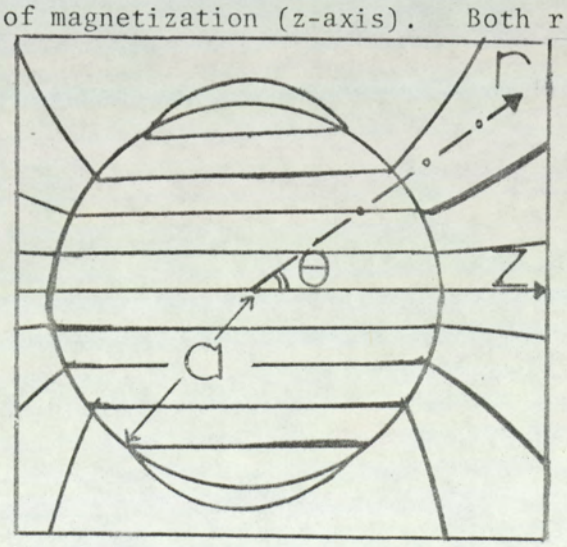

Fig. 1.12 The uniformly magnetized sphere (Kelvin, 1872) and the geometrical parameters θ, a and r.

The field due to different solid shapes need more experimental investigation and analysis. This thesis deals with one important and useful case, that is the sphere as will be shown later in Chapter 3 and uniformly magnetized sphere model (Alshwaik and Mulvey, 1977) called in this work spherical field.

This field is considered in more detail in Chapter 3. It may also be worth mentioning that all the work in this thesis dealing with single pole lenses is based on this class of field. Chapter 3 shows also some experimental results for various fields due to different solid shapes.

1.3 The image defects of magentic lenses

The quality of magnetic lens depends not only upon the paraxial electron optical characteristics but also upon the aberrations. The importance of a particular aberration depends on the function of the magnetic lenses. For intermediate and projector magnetic lenses, the radial and spiral distortions are the most important. For an objective lens, only the spherical and the chromatic aberrations are important. The chromatic changes in magntification and in rotation are serious for all lenses. The first three cause a shift of the image point, while the fifth aberration rotates the image, the chromatic aberrations being responsible for image blurring.

1.3.1 Image distortion

Image distortion takes place if the lens does not bend the incoming rays in strict proportion to their radial distance from the axis.

If the angle of rotation is not independent of the radial distance of the incoming rays from the axis, spiral distortion will occur in the

image. In radial distortion the image of each object point is shifted radially from the Gaussian image point either outwards, (pin-cushion distortion) or inwards (barrel distortion). The deviation $\Delta\rho$ of the Gaussian image at the image plane is given by

$$(\Delta\rho)_{rad} = D_{rad}\, M.r_o^{\,3} \qquad \ldots (1.47)$$

where r_o is the distance of the incoming ray from the axis and M is the magnification. The deviation $\Delta\rho$ in spiral distortion is given by

$$(\Delta\rho)_{sp} = D_{sp}\, M.r_o^{\,3} \qquad \ldots (1.48)$$

where D_{rad} and D_{sp} are the radial and spiral distortion coefficients in the standard notation which are most widely used. In spiral distortion the deviation $\Delta\rho$ is at right angles to the image radius ρ.

By using the relation $\rho = M.r_o$, these image distortion then become

$$(\Delta\rho/\rho)_{rad} = D_{rad} \cdot r_o^{\,2} \qquad \ldots (1.49)$$

$$(\Delta\rho/\rho)_{sp} = D_{sp} \cdot r_o^{\,2} \qquad \ldots (1.50)$$

The kind of distortion (pin-cushion or barrel) given by (1.49) depends upon the sign of D_{rad}. The appearance of some of these image distortions for a square mesh object, taken from Nasr (1978), are shown in fig. 1.13.

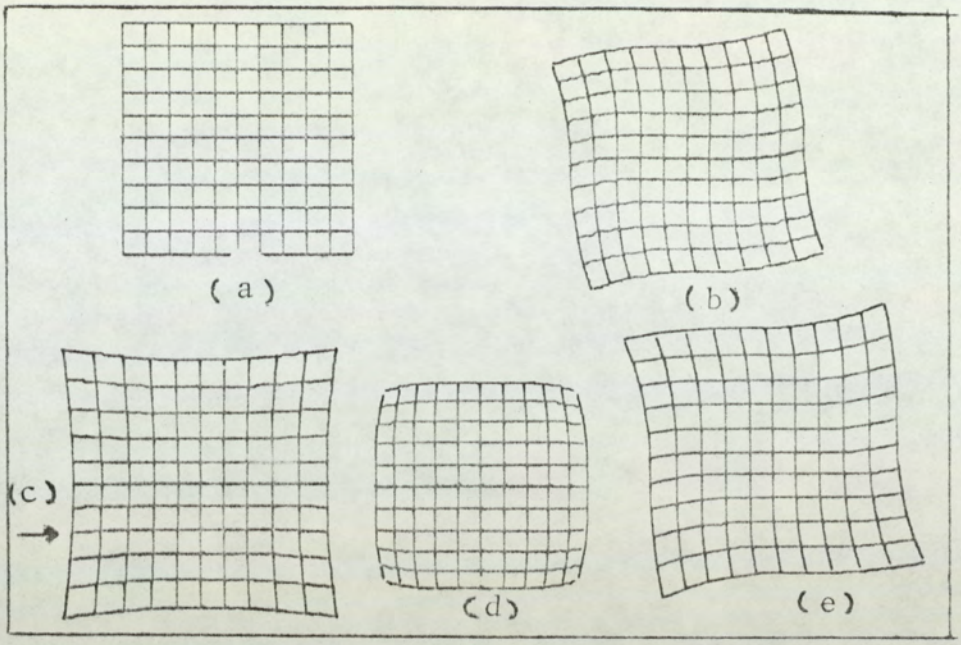

Fig.1.13 Typical image distortion patterns for a square mesh object, (a) perfect image; (b) spiral distortion; (c) pin-cushion radial distortion; (d) barrel radial distortion; (e) distorted image with mixed defects

By using the standard notation (Hawkes, 1972) and the rays X,Y described in Chapter 2 the coefficient D_{rad} for purely magnetic field are given as follows

$$D_{rad} = (3/8f^2\rho) + (e/96mV_r) \int_{-\infty}^{\infty} [2e/mV_r)B^4(z) + 5B'(z) - B'(z)B''(z)] Y^3X \, dz \qquad \ldots (1.51)$$

Here dashes denote differentiation with respect to z. For projector lenses in particular the integration is carried out from object plane to image plane which are assumed to be at infinity.

The numerical analysis was carried out by using the following expressions using Scherzer's expression (1937) for D_{rad}.

$$D_{rad} = (3/8f^2p) + (e/16mV_r) \int_{-\infty}^{\infty} [B'^2 + (3e/8mV_r)B^4(z) B^2(z) (Y'/Y)^2]Y^3 X dz \quad \ldots (1.52)$$

$$D_{sp} = (1/16V_r)(2e/mV_r)^{\frac{1}{2}} \int_{-\infty}^{\infty} B(z)[(3e/8m)B^2(z) + V_r(Y'/Y)^2]Y^2 dz \quad \ldots (1.53)$$

Both radial and spiral distortion coefficients depend on the geometry of the lens and its excitation. For double pole lenses, the radial and spiral distortion for different S/D ratios have been calculated by Liebmann (1952). The correction of radial distortion was examined by Haine and Page (1956), and Kynaston and Mulvey (1963).

One of the ideas of how to set about this correction was suggested by Hillier (1945), where the correction lens is placed at the focal point of the main projector lens. Both lenses were excited by the same number of ampereturns.

For both single and double pole lenses, radial distortion can be zero at the excitation parameter $(NI/V_r^{\frac{1}{2}})$ which is just above the excitation parameter at which the maximum magnification will occur.

A section of the research on the aberrations of single pole lenses has been carried out by Marai and Mulvey (1975), and by Alshwaikh and Mulvey (1977). A further extensive study of radial distortion in single pole lenses is given in Chapter 4, which includes a universal curve for the spiral distortion of all double pole magnetic lenses.

1.3.2 The lens aberrations

Two aberrations are specifically harmful for an objective lens; the first is spherical aberration which is the most important geometrical defect. This occurs when the outer regions of the lens have a stronger focusing effect than the region close to the axis. The result is that a point in the object plane will not be imaged as a point in the image plane but as a disc of radius Δr, where

$$\Delta r_s = C_s \alpha_i^3 \qquad \ldots (1.57)$$

Here α_i is the semi-aperture of the electron beam in image space and C_s is the spherical aberration coefficient, which varies with lens geometry and excitation as well as with the relative positions of the object and image planes.

The second aberration produces a blurring of the image known as chromatic aberration. Fluctuation in the lens focal length, due to a spread in electron energy and variations in lens excitation result in the superposition on the final screen of images of different sizes. There is then a consequent loss of image definition, and hence the aberration.

If the accelerating potential (V) and/or the lens excitation (NI) fluctuate, chromatic aberration will arise in the image, and the image point will appear blurred. This gives the contribution of the aberration disc of radius (r_{chr}) around the image

$$r_{chr} = C_c \alpha_o (\Delta V/V) \qquad \ldots (1.58)$$

in which $\Delta V/V$ is due either to a fluctuation of the applied voltage or to a loss in energy of electrons passing through specimen. The coefficient C_c is for chromatic aberration, and α_o is the angular aperture of the beam in object space.

The calculation of the coefficient C_s and C_c were discussed by Glaser (1933) originally using the point eiconal function and Scherzer (1937) using the electron path method. Later on (1952) Glaser carried out an intensive study on these coefficients and extensive research has been made into them by recent authors.

The spherical aberration coefficient can be written as

$$C_s = (e/96mV_r) \int_{z_o}^{z_i} [(2e/mV_r)B^4(z) + 5B'^2(z) - B(z)B''(z)]h^4 dz \quad \ldots (1.54)$$

here dashes denote differentiation with respect to z. The integration is carried out from object plane (z_o) to image plane (z_i).

To avoid the difficulty of calculating the second derivative B'' in C_s the numerical analysis was carried out by using the following expressions for the coefficient C_s and C_c (Hawkes, 1972 and Grivet, 1972).

$$C_s = (e/128mV_r) \int_{z_o}^{z_i} [(3e/mV_r)B^4(z) + 8B'^2(z) - 8B^2(z)(h'/h)^2]h^4 dz \quad \ldots (1.55)$$

$$C_c = (-e/8mV_r) \int_{z_o}^{z_i} B(z)h^2 dz \quad \ldots (1.56)$$

Numerous publications have appeared concerning these aberrations, such as those of Der Schwartz and Makarova (1968) for iron free coils, as well as Basset and Mulvey (1959). Mulvey and Wallington (1973) present a very useful review and critical comparison for a wide range of double pole lenses.

Both spherical and chromatic aberrations have been calculated for single pole piece lenses by Juma (1975), Marai and Mulvey (1975), Alshwaikh and Mulvey (1977), Juma and Alshwaikh (1979). A detailed account is given in Chapter 4.

1.3.3 The problem of the slope of the magnetic field distribution B(z) becoming infinite

Some of the aberration coefficients such as the spherical aberration coefficient C_s and the radial distortion coefficient D_{rad} depend directly on the slope B'(z) of the magnetic field distribution. However, when calculating such fields, a mathematical difficulty can arise if such a field distribution has an infinite slope at one or more points.

Some field models contain two distinct mathematical functions and their intersection point has two derivatives, one of them equal to infinity. There is also another problem when the slope is not known at a certain point.

This problem arises especially when calcualting C_s and D_{rad} for the square top field, and for single pole lens models when the rays are incident from the negative direction fig. 1.14, (i.e. they enter the steep edge of the field).

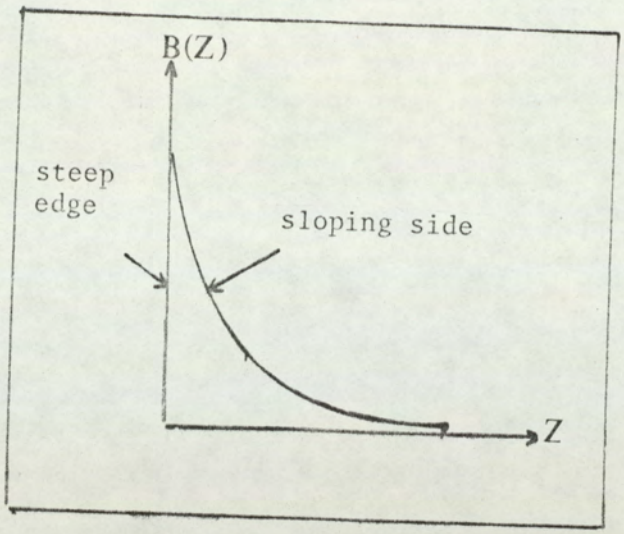

Fig. 1.14 Axial field distribution of a single-pole lens showing the two characteristics

Some authors committed conceptual errors in their calculations of C_s and D_{rad}. Marai (1976) shows the values of D_{rad} (dotted lines in Fig. 1.15) for the exponential field and Kanaya et al (1976) in their calculation for C_s for the square top field. Both authors calculated the coefficients by ignoring the presence of the vertical function.

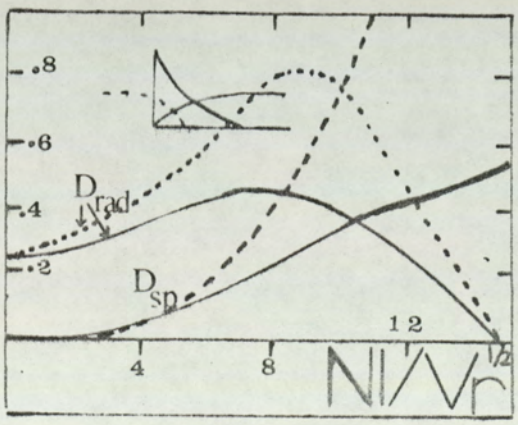

Fig. 1.15 Radial and spiral distortion coefficients of exponential field model according to Marai (1976).

There is a major difficulty when trying to find these coeffiecients in the square top field, that is the problem of the infinite value of the magnetic flux derivative (B'). However, Kanaya et al (1976) formulated expressions for C_s for square top field. They appear in standard notations as

$$C_s/S = [1/6\sin^4(KS)]\,[3+(2/\theta)\sin 2\theta-(1/4\theta)\sin 4\theta] \quad \text{for} \quad \theta \leqslant \pi/2 \qquad \ldots (1.59a)$$

and $$C_s/S = \pi/4\theta \quad \text{for} \quad \pi/2 < \theta < \pi \qquad \ldots (1.59b)$$

Since $\theta = 0.1863\ NI/V_r^{\frac{1}{2}}$.

Equation 1.59a is not correct for the square-top field, because these values hold only by ignoring the effect of the boundaries at which the axial field B_z has an infinite slope and so the correct value of C_s should approach infinity.

However, the above expression of C_s can be used to give an idea about the values of spherical abberation when the function has a very steep slope. More discussion about this problem are to be found in Chapter 4.

1.3.4 Quality factors of projector lenses

The quality of the image formed by a projector lens depends not only on the distortion coefficient (D) but also the projector focal length (fp). A relevant dimensionless factor (Q) can be found from the relation governing distortion.

$$\Delta\rho/\rho = D.r^2 \qquad \ldots (1.60)$$

where D is the distortion coefficient. It is easy to deduce from (1.60) with reference to fig.1.16 that

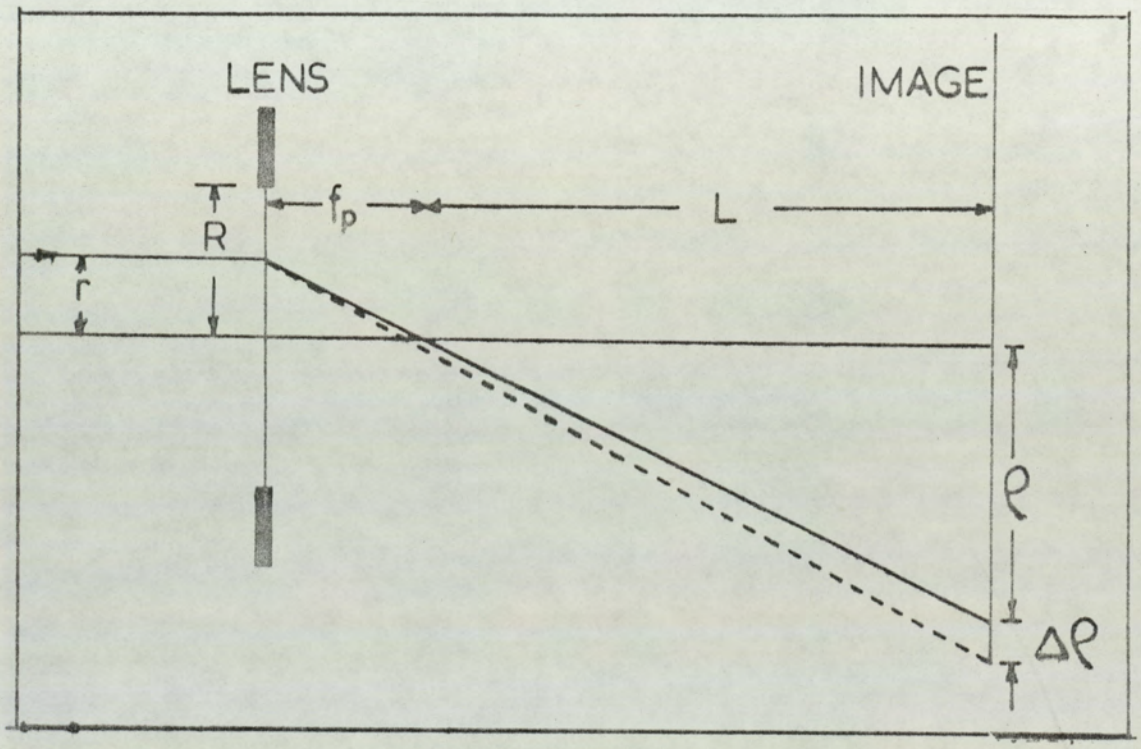

Fig.1.16 Schematic electron trajectory in the final connector stage of an electron microscopy

$$\Delta\rho/\rho = D(\rho/L)^2 . f_p^2$$

with $$\Delta\rho/\rho = Q^2(\rho/L)^2$$

the result being $$Q = D^{\frac{1}{2}} . fp \qquad \ldots (1.61)$$

The quality factor (Q) has been used to compare different projector lenses (Marai and Mulvey, 1977). This factor is used for both spiral and radial distortion corresponding to that of D.

It is important to remember that this definition of Q applies to one lens only and is not relevant when used as the distortion parameter for a complete lens system designed to remove distortion. The factor Q is independent on the kind of image distortion. For this purpose new definition of this quality factor is introduced in Chapter 4. However, this factor is very suitable for investigating the possibility of reducing the length of viewing chamber of an electron microscope as this involves only the final projector lens, since the other lenses do not significantly contribute to the image distortion

1.3.5 Comparison of objective lens

In order to compare the performance of different objective lenses an absolute standard is needed. This should inolve not only aberration coefficient but also technological factors such as the maximum flux density. This factor may refer either to the maximum permissable flux density in the polepieces, or the maximum current density in the windings of superconducting lenses.

Mulvey and Wallington (1973) made use of these relevant parameters which take the form $C_s B_o V_r^{-\frac{1}{2}}$ for spherical aberration and $C_c B_o V_r^{-\frac{1}{2}}$ for chromatic aberration.

It was also possible to use the corresponding absolute parameters $f_p B_o V_r^{-\frac{1}{2}}$, $z_o B_o V_r^{-\frac{1}{2}}$ and $f_{obj} B_o V_r^{-\frac{1}{2}}$ to compare values of the projector focal length, focal distance and objective focal length respectively for different lenses.

These parameters are used throughout this thesis for comparison purposes. The mathematical procedures for finding these parameters are discussed in Chapter 4.

1.3.6 Aberration coefficients for double pole lenses

Analytical expressions for the coefficients of double pole lenses are useful in the design of such lenses or to select optimum designs with minimum defects. Two models are commonly used for these purposes.

One of them is the well-known Glaser bell-shaped field and the other is the square top field, which is frequently used as the basis for universal curves of focal properties.

The distribution coefficient D_{rad}, the chromatic and spherical coefficients C_c and C_s are listed for the bell-shaped field by many authors, see for example, Kanaya (1958) and Hawkes (1972) as

$$C_c/d = \pi k^2 \operatorname{cosec}(\pi/\omega)/2\omega \qquad \ldots (1.62)$$

$$D_{rad}d^2 = 3\sin^2\omega\pi/2(4k^2+3)+\pi k^2\omega+\omega\pi/4\omega-(2k^2+3)/4\omega^2(4k^2+3) \qquad \ldots (1.63)$$

$$C_{s/d} = k^2/4\omega^2-(4k^2-3)\sin(2\pi/\omega)/8(4k^2+3)\operatorname{cosec}^4(\pi/\omega) \qquad \ldots (1.64)$$

Fig. 1.17 shows how these coefficients vary with lens excitation.

An extensive investigation has been carried out by Kamminga et al, (1968) on the C_c and C_s aberrations.

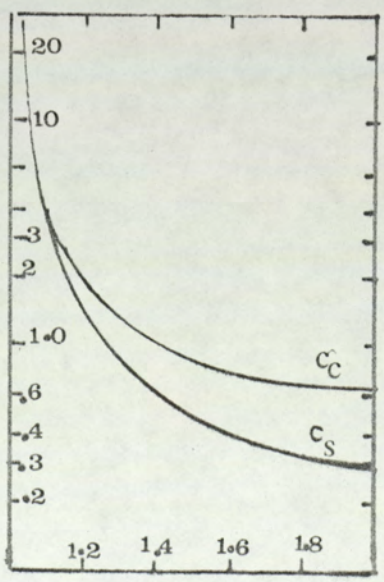

Fig.1.17 Chromatic C_c and spherical C_s aberration coefficients of Glaser bell-shaped field model

He gave a general expression for the Glaser field and discussed several particular cases. On the other hand C_s can be also written in a form depending on object position z_o and magnification (Hawkes, 1968). This takes the form:

$$\sum_{i=0}^{4} a_i (z_o/d)^i \qquad \text{and} \qquad \sum_{i=0}^{4} b_i (1/M)^i \qquad \ldots (1.65)$$

where a_i and b_i are tabulated as a function of K^2 in the above mentioned paper. The dependence of C_c on z_o is even simpler according to Hawkes (1968).

$$C_c = -4K^2 d(1+z_o)/2(1+K^2)^{3/2} \qquad \ldots (1.66)$$

The parameters D_{sp} (distortion) and C_c (chromatic aberration) appear in standard notations for square top field (Marai (1977), Kanaya et al (1976)) as

$$D_{sp}.S^2 = \theta^3/8 + (\theta^2/2)\sin(2\theta) \qquad \ldots (1.67)$$

$$C_c/S = [1/2\sin^2(KS)][1+(1/2\theta)\sin(2\theta)] \quad \text{for} \quad \theta < \pi/2 \qquad \ldots (1.68a)$$

$$= \pi/4 \qquad \text{for} \quad \pi/2 < \theta < \pi \qquad \ldots (1.68b)$$

The chromatic coefficient C_c is plotted as a function of lens excitation KS in fig.1.18

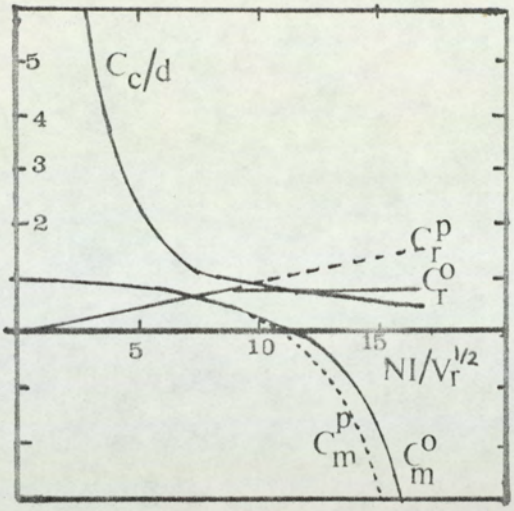

Fig.1.18 Chromatic aberration coefficient of the square-top field model

1.3.7 Optimization of magnetic lenses

Many papers have been published on the optimum design of magnetic lenses, (Kanaya et al (1976))(Szilagyi (1976), (1977)). A review of the literature of double pole lenses shows that spherical and chromatic aberrations are the aberrations that affect objective lenses most. These aberrations cannot be completely corrected as shown mathematically by Scherzer, (1936).

The smallest known spherical aberration coefficient can be achieved by the use of very thin coils (Bassett and Mulvey, 1969) but there are practical difficulties in realising such a lens. Marai (1977) found that there is an optimum geometry for iron-free lenses namely when the coil thickness is one-tenth of the mean diameter. Marai (1977) also found that $S/D_m = 0.1$, the spherical aberration parameter decreases as D_2/D_1 increases till the change in spherical indicator is very small and reaches a constant equal to $2.8 \times 10^{-6} m.T.V^{-\frac{1}{2}}$ at $D_2/D_1 = 999$.

Fig.1.19 shows the case mentioned above with the case $D_2/D_1 = 19$ which is plotted by Mulvey and Wallington (1973) with the parameter $C_s B_o V^{-\frac{1}{2}}$ at around 3. The figure also shows the theoretical limits calculated by Moses (1972) and Tretner (1959) .

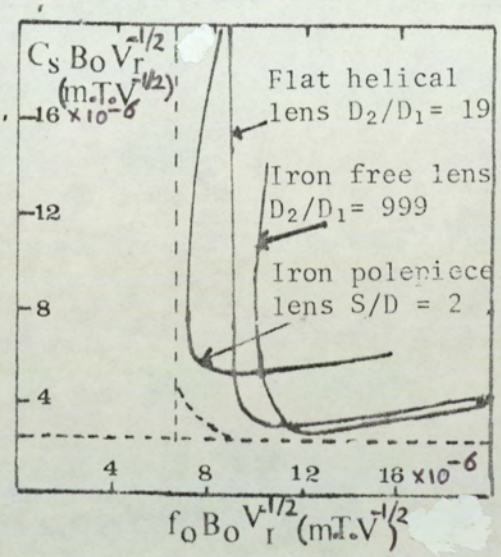

Fig. 1.19 Absolute spherical aberration parameter $C_s B_o V^{-\frac{1}{2}}$ as a function of absolute focal length parameter $f_p B_o V^{-\frac{1}{2}}$.

While iron-free coils have been proposed as objective lenses they are not suitable as projectors. This is due to the fact that the spiral distortion parameter Q_{sp} is slightly worse (by 10%) than that of conventional lenses.

It seems that iron pole piece lenses are more effective as projectors than iron-free lenses.

Marai (1977) for example, showed that, at minimum focal length (i.e. $NI/NI_o = 1$) where radial distortion is nearly zero, the spiral distortion quality factor Q_{sp} is the region of unity for all symmetrical double pole piece lenses.

It appears, however, that a better projector lens factor can be devised by using a single pole lens as described in Chapter 4.

Furthermore, the single pole lenses based on the uniformly magnetized sphere model (Alshwaikh and Mulvey 1977) have an encouragingly low spherical aberration coefficient value. This point is discussed further in Chapter 4.

1.3.8 Chromatic change in magnification and rotation

The aberrations known as chromatic change in magnification and chromatic change in rotation are important in high resolution electron microscopes. Their effect on the image is that an image point departs from its Gaussian position as the energy of the electron is varied. Chromatic change in magnification results in loss of image definition in the marginal zone of the images because a number of images of different sizes is superimposed resulting in blurring; the effect gets worse towards the outer regions as the field of view is increased.

This image blurring is caused by the electron energy spread in the beam arising from fluctuations in lens excitation and accelerating voltage, or by energy losses in the specimen.

The resulting image distortion $\Delta r_m/r$ may be written

$$\Delta r_m/r = C_m[(\Delta V/V) - (2\Delta I/I)] \qquad \ldots (1.70)$$

Fig. 1.20a shows the chromatic defects for the special case when the incident illumination is parallel to the axis and of very narrow aperture. The sketch (a) on the right shows the chromatic aberration and chromatic change in magnification by ignoring, in this instance, the chromatic

change in rotation. The radius of a circle of confusion is Δr_c and the displacement of its centre from the unaberrated image point is Δr_m.

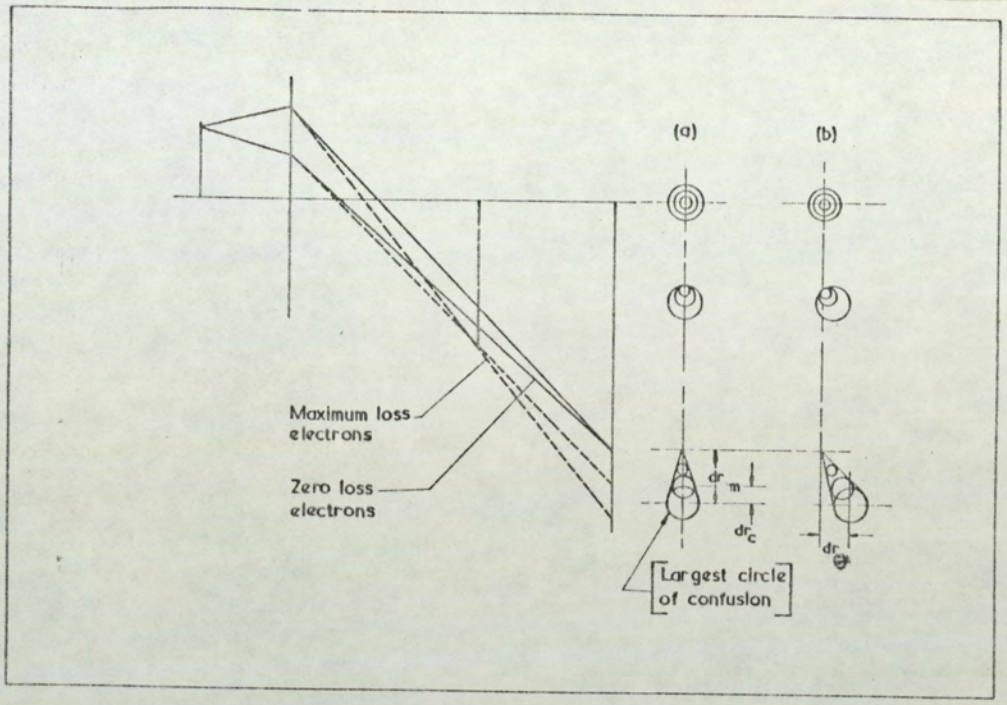

Fig. 1.20 Image appearance with chromatic defects

If Δr_θ is the tangential component of the image displacement. The chromatic change in the rotation angle ($d\theta$) produces a circumferential blurring Δr_θ in the image at height r from the axis. Thus we have

$$\frac{d\theta}{\theta} = \frac{dI}{I} - \frac{dV}{2V} \qquad \ldots (1.71)$$

Since $\Delta r_\theta = r d\theta$, equation (1.71) may be rewritten as

$$\frac{\Delta r_\theta}{r} = \theta \left[\frac{dI}{I} - \frac{1}{2}\frac{dV}{V}\right] \qquad \ldots (1.72)$$

C_r then takes the form

$$C_r = \left(\frac{dr_\theta}{r}\right) / \left(\frac{dV}{V} - 2\frac{dI}{I}\right) \qquad \ldots (1.73)$$

The effect of chromatic change in rotation is shown in fig.1.20b in addition with other chromatic defects. The radial displacement is Δr_m and the circumferential displacement is Δr_θ.

For convenience the terms C_m and C_r are used for coefficients of chromatic change in magnification and in rotation respectively, while the subscripts O, i and p will represent quantities concerned with the objective, intermediate and projector lens respectively.

By using the electron path method, Scherzer (1936) derived formulae for both C_m and C_r. Many authors, (e.g. Morito (1954) and Kanaya, (1955)) used these formulas to calculate the corresponding coefficients for objective lenses. The formulae are as follows

$$C_m^o = -e/8mV_r \int_{z_o}^{z_i} B(z)\, ghdZ \qquad \ldots (1.74)$$

$$C_r^o = -\tfrac{1}{2}(e/8mV_r)^{\frac{1}{2}} \int_{z_o}^{z_i} B(z)dz \qquad \ldots (1.75)$$

where g and h are particular solutions of the paraxial ray equation defined in Chapter 2. Most publications have been concerned mainly with the coefficients of the objective lens; only a few papers deal with the projector lens. One of the original investigations into projector lens coefficients was that of Morito (1957). Hawkes (1972) tabulated similar expressions using one of the most convenient forms of the chromatic change coefficients as shown below

$$C_m^p = -(e/8mV_r) \int_{\infty}^{\infty} B^2(z)xYdz \qquad \ldots (1.76)$$

$$C_r = (e/16mV_r)^{\frac{1}{2}} \int_{\infty}^{\infty} (B(z)dz \qquad \ldots (1.77)$$

Here X and Y stand for two independent particular solutions of the paraxial ray equation. These analytical solutions are given in Chapter 3 and the numerical solutions in Chapter 2.

1.4 Characteristic of the pre-field

The pre-field is that part of the magnetic field in front of the specimen. The pre-field can be as strong as the main imaging field and therefore can exert a considerable influence on the illuminating system. The theory of the pre-field was originally developed by Marton and Hutter (1944) for the bell-shaped field. Riecke (1962) has carried a comprehensive analysis of the pre-field of a mangetic objective with a Glaser bell-shaped field. He extended the idea pointed out by Glaser (1941) to obtain a very short focal length and low aberration coefficients by situating the object at the centre of the lens. In the lens which has this kind of field called 'condenser-objective' the spherical aberration was appreciably lower than that where the specimen were placed outside the magnetic field.

The practical realization of a symmetrical condenser-objective lens was due to Riecke and Ruska (1966). The first half of the field acts as a short focal length condenser lens while the second half acts as a short focal length objective.

Double pole lens pre-field

Consider first the general case of a condenser-objective with variable specimen position.

A good model for a doublepole lens is the rectangular field distribution fig.1.2 consisting of a uniform field of strength B_o, confined between two planes A and B separated by a distance S. The object is placed at O at an arbitrary distance from the lens centre. The pre-field is bounded between A and O, and converges the electron beam from r_o to r_i.

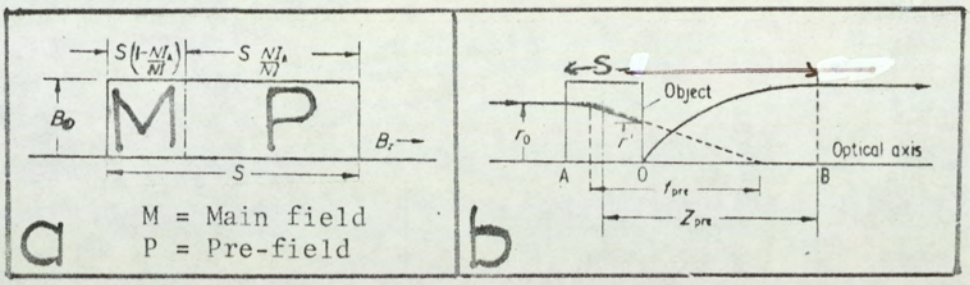

Fig. 1.21 (a) Axial distribution of the pre-field in a magnetic lens of large space compared with the bore (S > D). (b) Focal properties f_{pre}, Z_{pre} of the pre-field of the above field distribution. Z_{pre} is measured from the centre of the pre-field.

Mulvey and Wallington (1973) found that the pre-field focal length (f_{pre}) and focal distance (Z_{pre}) follow the relations

$$f_{pre}/S = [\pi/2.(NI/NI_A)\sin\{\pi/2.(NI/NI_A-1)\}]^{-1} \quad \ldots (1.78)$$

$$Z_{pre}/S = 1/2(1-NI_A/NI) + [\pi/2(NI/NI_A)\tan\{\pi/2(NI/NI_A-I)\}]^{-1} \quad \ldots (1.79)$$

where Z_{pre} is measured from the centre of the pre-field and NI_A is the excitation over the length OB.

It is possible to express the lens gap (S) and the fractional reduction of the illumination radius (i.e. r_1/r_o) = M_{pre} of the beam, in terms of the excitation ratio (NI/NI_A) as

$$S = 8.44\ (V_r^{\frac{1}{2}}/B_o)\ \mu_o\ (NI/NI_A) \quad \ldots (1.80)$$

$$M_{pre} = \sin(\frac{\pi}{2}.NI/NI_A) \quad \ldots (1.81)$$

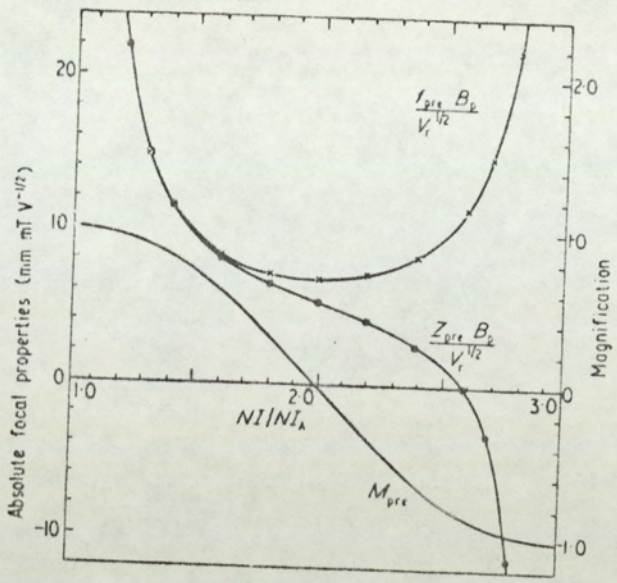

Fig.1.22 Absolute focal properties for a lens with $S \gg D$ (square-top field) in the excitation range $1 < NI/NI_A < 3$

Fig. 1.22 shows the absolute focal properties f_{pre}, z_{pre} and M_{pre} as functions of the relative excitation parameter NI/NI_o while the Universal Curve fig.1.23 shows the relative focal properties. This Universal Curve is valid in the range of NI/NI_o between 0.8 and 2.3

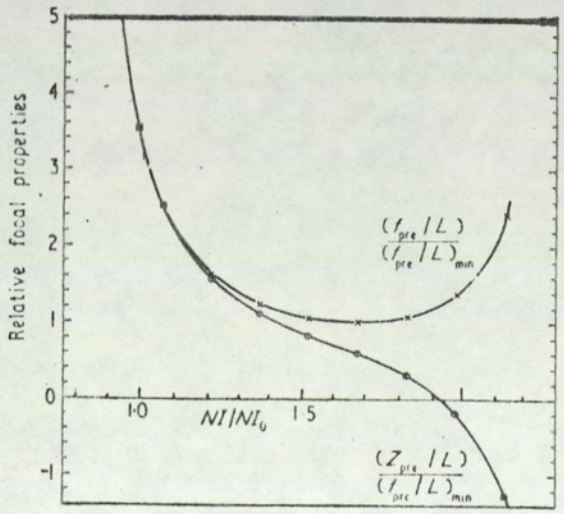

Fig. 1.23 Relative focal properties of the pre-field (Universal Curve) valid for all values of S/D in the excitation range $0.8 < NI/NI_o < 2.3$

The characteristics of the pre-field of single pole piece lens are discussed in Chapter 6.

1.5 Correction of Aberrations

1.5.1 Rotation-free projector system

Image rotation may be eliminated by using two or more magnetic lenses designed to have an overall rotation of zero, resulting in the so-called 'rotation-free' system. The first attempt to eliminate image rotation was that of Stabenow (1935), later followed by Becker and Wallraff (1940), all three of whom investigated the possibility of obtaining a rotation-free magnetic lens system by using two iron-free coils.

The first to report the use of two separate coils and lens gaps connected in a co-operative mode of operation was Ruska (1934). He did not, however, mention the possibility of employing this lens in a rotation-free mode. With a double projector, Prebus (1942) used such a double gap projector lens in an early experimental microscope. However, it was not possible to operate the lens gaps in a rotation-free mode.

Kanaya (1958) and Kanaya and Ishikawa (1958) discussed the theory of rotation-free imaging. They suggested the use of a rotation-free projector lens in order to avoid the astigmatism caused by the misalignment of electron lens elements. Juma and Mulvey (1974) described the successful performance of miniature rotation-free projector lenses in an electron microscope with the aid of double polepiece lenses and also with single poleiece lenses (Juma and Mulvey, 1975)

Each of these projector systems consisted of two identical magnetic lenses mounted back to back. The excitation of each lens gap was

equal and opposite, so that the net rotation was always zero. Further results concerning rotation free electron microscopes have been given by Juma and Mulvey (1975), also by Juma (1975).

The rotation-free projector system is the subject of investigation in this thesis as a possible system for correcting spiral distortion, (Chapter 7).

1.5.2 Correction of spiral distortion

Spiral distortion is probably the most important aberration affecting the projector system of the electron microscope. It is mainly produced by the final projector lens, and is extremely difficult to correct (Marai and Mulvey, 1977). Spiral distortion does not affect the resolving power of the microscope but makes quantitative analysis of the shape and size of object details difficult.

The spiral distortion $\Delta\rho/\rho$ at an image point of radius ρ is given by

$$\frac{\Delta\rho}{\rho} = (f_p{}^2 D_{sp})\ (\rho/L)^2 = Q^2_{sp}.\ \alpha^2_p \qquad \ldots (1.82)$$

Where L is the distance between the focal point of the projector and the flourescent screen (see fig.1.16), and α is the semi-angle subtended by the fluorescent screen at the focal point of the projector lens. The remaining parameters have already been defined.

Chapter 7 is concerned with a mathematical analysis of a two magnetic lens system devised for the correction of spiral distortion. The advantages of correcting spiral distortion lie not only in the fact

that the image is then a faithful copy of the object, but certain extra benefits can be derived, namely a substantial reduction in the length and volume of viewing chamber, and consequently a reduction in the sensitivity to the microscope to external alternating magnetic stray fields and mechanical vibrations. Both of these factors are important in obtaining very high resolution in the electron microscope.

A projector lens of low spiral distortion making use of permanent magnetic lenses has been described by Kubozoe et al, (1978). Unfortunately no photographs of the resulting images have yet been published and so it is not possible to evaluate the results.

A system with two single pole piece lenses were also used for correcting spiral distortion. Work in this direction was started by Marai (1977) and was continued by Lambrakis et al (1977) who used the miniature high voltage single pole lens described by Mulvey and Newman (1973) as a projector. They used as a correcting intermediate lens a single pole piece lens with 8mm bore designed by Juma (1975) for the 100Kv EM6 rotation-free projector system. A 30KV 'Intercol' electron optical bench was used in the above experiment. In one of their best photographs the spiral distortion was reduced by a factor of 4 (from 12% to 3%).

Finally, a full-scale experiment in the EM6 is now taking place to examine the effect of this correction system by Mulvey and his collaborators, and then to determine the optimum arrangement for correcting spiral distortion.

2. COMPUTATIONS

The use of a digital computer facilitates the calculation of focal properties and aberrations of magnetic electron lenses. Furthermore, it is used for numerical solution of problems when an analytical solution is not available.

2.1 Numerical integration for particular rays

The relations (1.55), (1.56), (1.52), (1.53), (1.74) and (1.76) for C_s, C_c, D_{rad}, D_{sp}, C_m^o and C_m^p respectively contain particular solutions for the paraxial ray equation. The following procedure shows the numerical solution for any magnetic field.

2.1.1. The fundamental rays Y and $\bar{Y}$

The solution denoted by Y (fig. 2.1) is specified by the condition

$$\lim_{z\to-\infty} Y(z) = 1, \qquad \lim_{z\to-\infty} Y'(z) = 0$$

In physical terms Y(z) is a ray incident from infinity at a hight equal to unity and travelling parallel to the z-axis

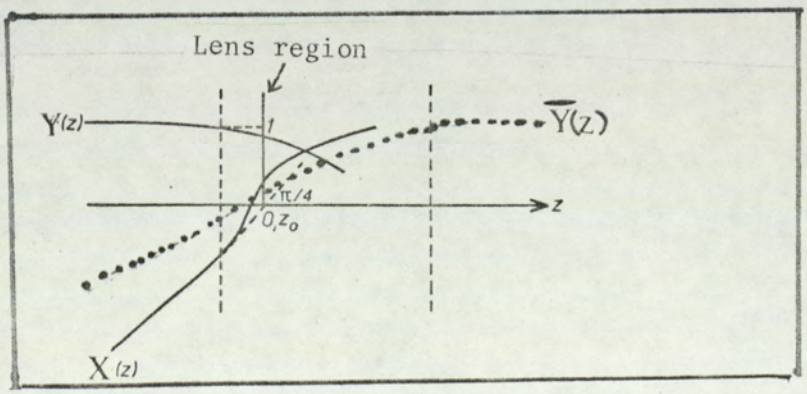

Fig. 2.1 The rays Y(z), X(z) and $\bar{Y}(z)$ used in the computation procedure

This Y(z) can be obtained analytically and then used to check the

numerical solution for its path. The calculation of this ray was performed by dividing the field into a number of successive intervals, each interval similar to a square top field (fig. 1.4), so the equations for this particular field are applicable.

Then a series of successive operations was performed through the field in which r and r' at the end of one interval are taken as the initial r_o and r_o' for the next.

The accuracy depends upon the number of intervals chosen; a hundred sections or more is adequate for an accuracy of one per cent. $\overline{Y}$ is a ray satisfying the conditions $\overline{Y}_i = 1$ and $\overline{Y}_i = 0$ at the image plane which is usually at infinity (fig.2.1).

The trajectory is calculated starting with the initial condition and then throughout the field up to the point at which ray Y intersects the z axis.

2.1.2 The particular solution X(z)

The ray X(z) (fig.2.1) is the solution following the boundary condition $\lim_{z\to-\infty} X(z) = z-z_o$. Physically this means that if the lens were removed a ray incident from field free space would intersect the axis at $z = z_o$ with unit slope.

This ray X(z) was computed by first calculating the ray $\overline{Y}$ and then normalising it by dividing $\overline{Y}$ by the value (-r') at the point r = 0 (i.e. y_i').

2.1.3 The particular solution h(z) and g(z)

h(z) is the ray satisfying the condition that at the object position $h(z_o) = 0$, the slope $h_o'(z) = 1$. This ray (fig.2.2) is usually used for objective lens aberrations

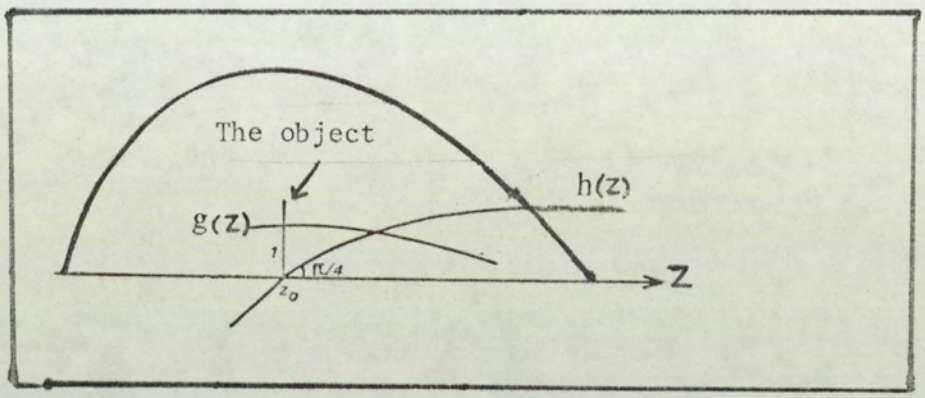

fig. 2.2 The rays h(z) and g(z) used in the computation procedure

By choosing the image plane z_i to be at infinity, the ray leaves the field parallel to the axis. The numerical integration is actually carried out in the reverse direction by starting with a ray which enters the field parallel to the z-axis; when this ray intersects the axis at the object plane the integration is stopped. The initial height of the ray is unity, so the computed trajectory was normalised so that the slope at the object point z_o was equal to unity. This was done by dividing the ray trajectory by the last r' value (i.e. r' (r=0)).

In similar way the ray g(z) can be selected to be the solution that is parallel to the axis at $z = z_o$ and unit distance from it $g(z_o) = 1$, $g'(z_o) = 0$.

2.2 The main programs

Five main programs have been written for various purposes and some

modifications were done to extend their usefulness. The first three programs which were originally written by Marai (1977) were used for electron optical focal properties, aberrations and distortions.

2.2.1 Program for calculating the electron optical properties

This program contains three main parts as follows:

(a) The first part computes the 'distance function' A(z) from the relation

$$A(z) = B(z)/NI \qquad \ldots (2.1)$$

where B(z) is the axial field distribution obtained from measured data or calculated from the known methods such as the finite element method (Munro, 1972) or finite integrated element method (Trowbridge et al 1972).

In the case of field models, equation (2.1) was rewritten as

$$A(z) = B(z)/d_f \mu_o \, NI \qquad \ldots (2.2)$$

for the convenience of the computations and to give the discretization of results, where d_f is a constant dependent upon the field deduced from Ampere's theorem

$$\int_{-\infty}^{+\infty} B(z) \, dz = \mu_o \, NI$$

The function A(z) is independent of the excitation NI and hence the program calculates it once and for all and then B(z) can easily be found by using one of the equations (2.1) and (2.2).

(b) The second part of the program calculates the trajectories at any values of NI as explained in (2.1) by using the relation

$$k = (e/8mV_r)^{\frac{1}{2}}.NI.A(z) \qquad \ldots (2.3)$$

It is necessary to remember that the unit of length in all parameters is the half-width when the program is run for a field model.

(c) The final part calculates the electron optical parameters f_{obj}, z_f and f_p as follows

$$f_{obj} = 1/r'_{(r=0)} \qquad \ldots (2.4)$$

$$z_f = z_{(r=0)} \qquad \ldots (2.5)$$

f_p is given by the reciprocal of the slope of the ray entering the field with the condition $r_o = 1$ and $r'_o = 0$ at the point where the ray leaves the lens field.

This program called 'DATA BZ' uses FORTRAN IV and is listed in APPENDIX (10.1).

2.2.2 Program for calculating chromatic and spherical aberration coefficients

The program called 'CABERRATION', whose particular application for the spherical field is listed in APPENDIX (10.2), is used to calculate chromatic and spherical aberration coefficients.

The first three parts are similar to those in the program 'DATA BZ' and the parameters B(z), B'(z), h(z) and h' are the same. There are two

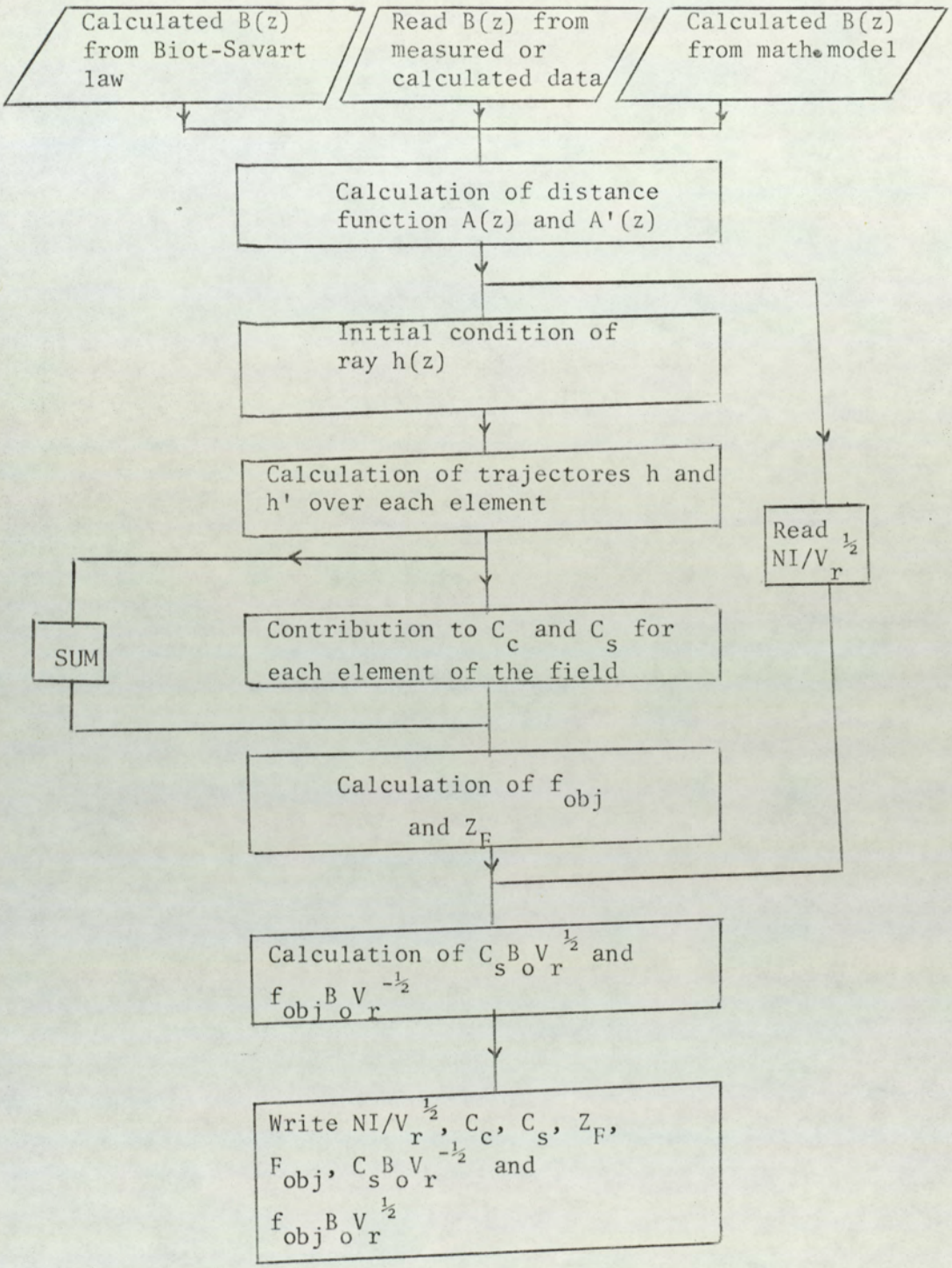

Fig. 2. 3 Flow diagram of the computer program 'CABERRATION'

more steps however,

(d) The cumulative summation of the contributions to C_s and C_c from each element from equations (1.55) and (1.56) is carried out over all the field.

(e) The print-out of the relevant electron-optical quantities C_c, C_s, $NI/V_r^{\frac{1}{2}}$, z_f and f_o with two sensitive indicators for high performance magnetic lenses (Mulvey and Wallington, 1973) namely

$$C_s(B_o/V_r^{\frac{1}{2}})10^6 \quad \text{and} \quad f_{obj}(B_o/V_r^{\frac{1}{2}})10^6$$

The flow diagram of this program is shown in fig.2.3.

2.2.3 Program for the calculation of radial and spiral distortion coefficients

This program follows the same procedure in the previous programs and the calculations of rays Y, $\bar{Y}$ and X are carried out.

The last two steps of the program are modified to calculate the radial and spiral distortion and to print out the coefficient D_r and D_{sp} with the relevant coefficients for the projector lens such as f_p, $NI/V_r^{\frac{1}{2}}$, Q_r and Q_s.

Numerical results of D_r and D_{sp} give the coefficients (Liebmann, 1952) as

$$C_d = D_r R^2 \text{ and } C_{sp} = D_{sp}.R^2$$

while the output in case of models is d^2D_{sp} and d^2D_r. Here R is the radius of the lens bore and d is the half-width of the model field.

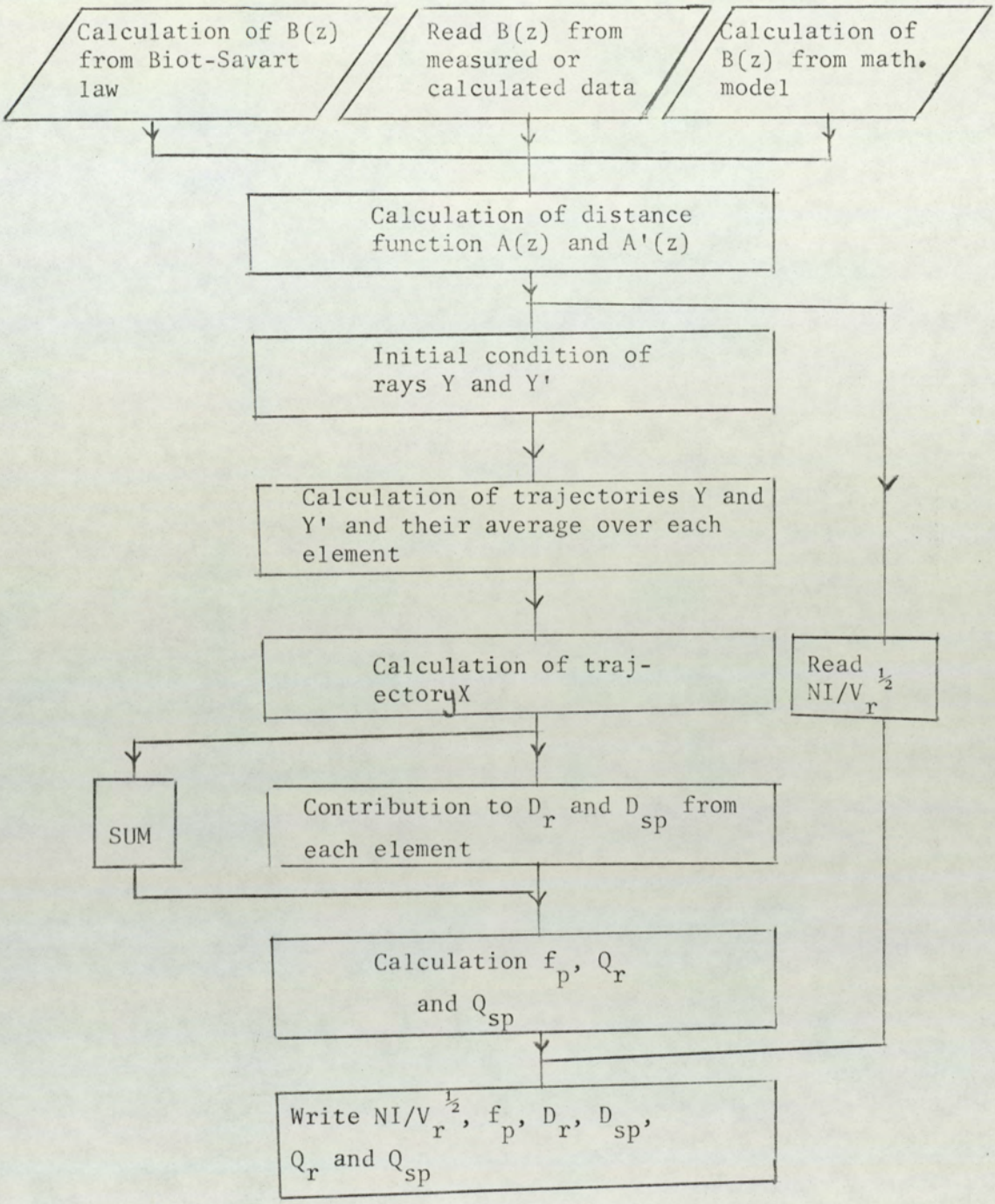

Fig. 2.4 Flow diagram for the program 'CDISTORTION'

The program 'CDISTORTION' which is used for the spherical pole piece model, is listed in APPENDIX (10.3), and its flow diagram in fig.2.4.

2.2.4 Program for the calculation of pre-field electron-optical parameters

The program 'PREFIELD' listed in APPENDIX (10.4) deals with the rest of the field used as objective field. So this program follows a similar procedure to that for calculating the aberration coefficients C_c and C_s, but the calculation of the rays and the summation of both C_c and C_s have been stopped at the point (Z_F).

The objective distance (Z_F) can be found for the original field from an analytical expression or from the output of 'CABERRATION' when it is run for the original field.

The output of this program gives the relevant electron-optical quantities of the pre-field such as Z_{pre}, F_{pre} and $NI/V_r^{\frac{1}{2}}$. Also Z_F and the corresponding value of r are printed for checking.

The aberration coefficients C_s and C_c for the pre-field are printed in the output as well. The flow diagram of 'PREFIELD' is shown in fig.2.5.

2.2.5 Program for the calculation of spiral distortion for two successive square top fields

This simple program is called 'SPIRALCOREC' APPENDIX (10.5). In this case, one of the most important parameters is D_{sp} for two successive square top fields separated by a distance (L_1/S), which is found

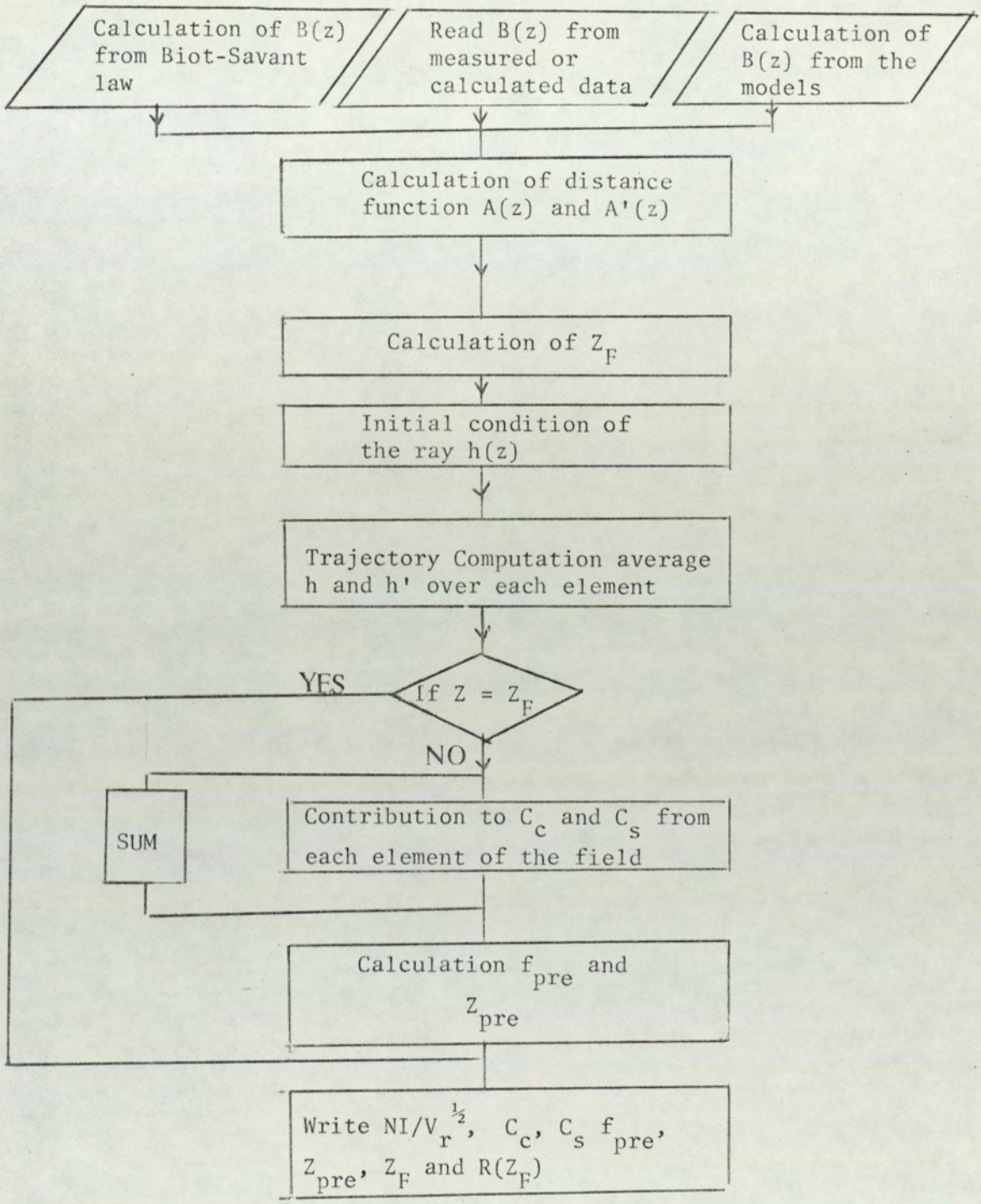

Fig. 2.5 Flow diagram of the program 'PREFIELD'

from the relation derived in Chapter 7.

Other useful quantities such as projector focal length (F_T) of two fields, magnification (M_1) of first lens and final magnification (M_F) are calculated in this program directly from the equations (A5.18), (A5.9) and (A5.17) respectively.

The results from this program are discussed in Chapter 4.

2.3 Modification of previous program

The programs discussed in this chapter can be used with analytical field distributions. They can also be used with measured or calculated field data. The changeover of each program from analytical to numerical or vice versa is done in the first part of each program. The second part of each program enables one to change the direction of the rays by changing one statement.

2.3.1 Program for calculating chromatic change in magnification and rotation

The computation of chromatic change of magnification and rotation for objective lenses can be carried out using the expressions (1.74) and (1.75) for C_m^o and C_r^o respectively.

The similar procedure of 'CABBERATION' was done and the calculation of rays h(z), X(z) and Y(z) was performed. When the same parameters are calculated for the projector lens, equations (1.76) and (1.77) for C_m^p and C_r^p are used, and the numerical integration is carried throughout the fields as in the 'CDISTORTION' program.

2.3.2 Programs for correcting systems

To investigate the possibility of correction of spiral distortion, chromatic change in magnification and chromatic change in rotation, a system of two lenses was used. The two lenses can consist of two single pole lenses, two double pole lenses or a combination of a single pole lens and a double pole lens.

All optical and aberration characteristics can be studied by using the same programs discussed before with the condition that the sum of the two fields of the lenses are considered as one field. This effects the calculation of the distance function only in part one of each program.

2.4 Program checking

2.4.1 Checking by comparison with analytical results

Many checks were carried out to examine the accuracy of the programs.

The Glaser bell-shaped field is a wellknown field distribution and its aberration coefficients such as C_s, C_c and D_r have been calculated analytically (Hawkes, 1972). The results were subsequently used by Marai (1977) to test the first three programs and there is excellent agreement between the calculated results and thos obtained analytically. In particular, the value of d^2D_{rad} for very weak lens (i.e. $NI/V_r^{\frac{1}{2}} = 0$) is 0.25 which is the same value obtained analytically.

A similar check for C_r and C_m of the bell-shaped field using a modified program (2.3.1) was performed by the present author; this showed full agreement between calculated results and those found analy-

tically by Morito (1953) and Kanaya(1955).

The calculted results for the focal properties f_p, f_{obj} and Z_F compared favourably with those calculated analytically for various models, such as those done by Marai (1974) for the exponential field in one axial direction, and by the present author for the same field in the other axial direction, and also for both directions in the spherical pole piece field.

Glaser (1952) showed that the minimum value of the chromatic aberration is (0.712d) for the exponential field; the same result was found by Marai numerically (1977); using the second program.

The distortion coefficients of double pole lens computed by Marai (1977), when contrasted with the results by Liebmann (1952), give satisfactory agreement except for spiral distortion which showed slight differences (Marai and Mulvey, 1977).

2.4.2 Checking by comparison with experimental results

The first experimental check consisted of comparing the computed results for the aberration coefficients of iron-free coils obtained by Marai (1977) with thos calculated experimentally (Bassett and Mulvey, 1969).

For the X-ray mini lens, whose axial field distribution follows spherical field model well (Christofides, 1978) there is good agreement between the experimental results for C_s and those found numerically for the spherical field model

The programs were run for many single pole lenses and the experimental results show an agreement within 10% which is reasonably within the experimental error.

Juma and Alshwaikh (1978) studied one of the important lenses APPENDIX (10.8). This study reflects the agreement between the experimental measurement and the computation for C_s and f_p performed by the program.

Juma (1975) studied the 30kV snorkel lens, 100kV snorkel lens, 4mm bore single pole lens and 8mm bore single pole lens. His results confirm the agreement of the computed results with the experimental results.

3. MATHEMATICAL MODELS AND THEIR ELECTRON OPTICAL PROPERTIES

In some of the double polepiece lens models that were described in Chapter 1, it was found (Mulvey and Newman, 1973) that it was very difficult to apply them to single polepiece lenses. Therefore, it is important to look at models that can give a representation of these single polepiece lenses and thus from these models, all the focal properties of magnetic lenses can be calculated.

3.1 Models for single polepiece lenses

In single polepiece lens (Mulvey, 1976) the axial magnetic field falls rapidly from a high value at the poleface. The main imaging field is therefore essentially outside the lens structure, whilst low aberration coefficients are preserved. Such lenses become a practical possibility when the lens excitation is concentrated into the region of the single polepiece by means of high current density windings. The focal properties of such lenses differ appreciably from those of conventional twin-polepiece lenses. For example, the objective focal length increases slowly with increasing lens excitation and the spherical aberration and image distortion can be appreciably lower than those of conventional lenses. This is a consequence of the differences in the axial field distributions (Marai and Mulvey 1974).

In the following, some fields were studied.

3.1.1 The exponential field model

The axial field distribution for single polepiece lens

can be represented as a first approximation by the exponential field model of Glaser (1952) which Marai (1977) did a study on the field for the ray incident at the sloping edge of the field. Some characteristics were found not too far to those of some experimental lenses. This field has analytical solution for the two cases at the incident rays. These two solutions can be found from equation (1.16) which has two linearly independent solutions $J_o(\xi)$ and $Y_o(\xi)$ (McLachlan, 1955), and namely, Bessel functions of zero order of the first and second kind respectively. In particular, $Y_o(\xi)$ is Neumann's Bessel function of the second kind and zero order. Hence

$$r/d = AJ_o(\xi) + BY_o(\xi) \quad \ldots\ldots \quad (3.1)$$

$$r'/d = AJ'_o(\xi) + BY'_o(\xi) \quad \ldots\ldots \quad (3.2)$$

where dashes indicate first derivatives of the corresponding Bessel functions.

The study of this field when the ray incident at the sloping edge is summarised in Chapter 1. The other solution which gives the analytical results can be used to check the numerical solution. This case is discussed in detail as follows:

<u>A particular solution for a ray incident on the steep edge of the field</u>

Suppose the initial conditions are $r_o = 1$ and $r'_o = 0$ at $z = 0$, figure (1.7), then both equations (3.1) and (3.2) can be written for A and B as follows:

$$A = -Y'_o/(Y_oJ'_o - Y'_oJ_o) \quad \ldots\ldots \quad (3.3)$$

$$B = J'_o/(Y_oJ'_o - Y'_oJ_o) \quad \ldots\ldots \quad (3.4)$$

Using Ampere's law $B(z)dZ = \mu_o NI$, one obtains

$$k = 0.1287\ NI/V_r^{\frac{1}{2}} \quad \ldots\ldots (3.5)$$

The objective focal distance (z_F) is found by putting $r = 0$,

i.e. $$J_o(\xi)/Y_o(\xi) = -B/A \quad \ldots\ldots (3.6)$$

The slope r'/d of the ray at a distance z from the origin is given by

$$r'/d = \ell n2.\,\xi\left[AJ_1(\xi) + BY_1(\xi)\right] \quad \ldots\ldots\ldots (3.7)$$

For an excitation parameter $NI/V_r^{\frac{1}{2}}$ less than 13, the objective and projector focal lengths for the exponential field are the same and equal to the reciprocal of the slope of the ray at $z = 0$. It is also clear that the objective focal length f_{obj}/d is constant for higher values of the excitation parameter, and takes the value

$$F_{obj}/ = 1/\ell n2 \cdot \xi_1\left[AJ_1(\xi_1) + BY_1(\xi_1)\right] \quad \ldots\ldots (3.8)$$

Figure (3.1) shows z_F/d and F_{obj}/d corresponding to different values of the excitation parameter $NI/V_r^{\frac{1}{2}}$.

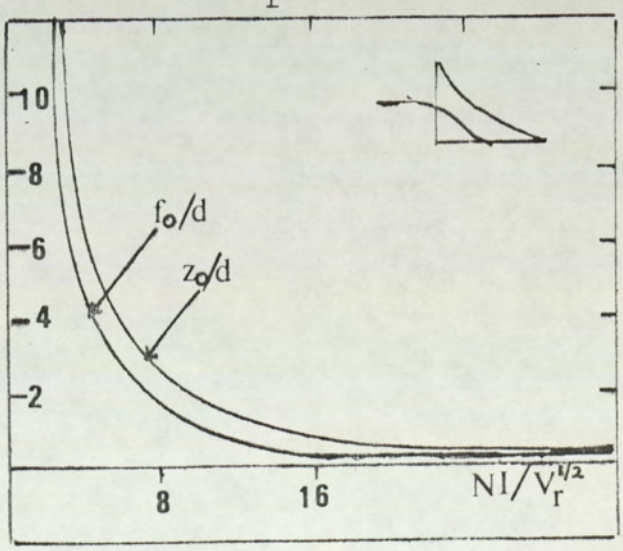

Fig.(3.1) The parameters f_{obj} and Z_o as a function of excitation parameter $NI/V_r^{\frac{1}{2}}$ for the exponential field model for the ray incident at the steep edge.

These results have good agreement with those found by numerical solution using the program 'CABERRATION'. This agreement confirms that the numerical method is accurate

for use with models that do not have an analytical solution.

The exponential field model exhibits certain properties that differ from those from experimentally measured field distributions. Some of these characteristics include chromatic aberration which is found experimentally to increase as the excitation parameter $NI/V_r^{\frac{1}{2}}$ is increased in the range $NI/V_r^{\frac{1}{2}} \gtrsim 13$. However, for the exponential field distribution, the chromatic and spherical aberration coefficients remain constant in this region.

A disadvantage of the exponential field is the difficulty of correlating this model with an actual polepiece structure, with the object of obtaining an optimum design. For this reason, therefore, it seemed desirable to search for a more realistic model and to investigate the effect of the pole-piece (snout) shape on the field distribution.

3.1.2 An iron cylinder in a uniform magnetic field

Some useful experiments were done in the electron-optics laboratory in this department with the co-operation of Ridha (1977) to find the field distribution produced by a magnetised iron cylinder in a uniform field. For the measurement of axial field distribution a Hall-probe gaussmeter was used.

To get meaningful results, three solenoids were used, plus a Helmholtz coil. The solenoids had different dimensions and numbers of turns. The Helmholtz coil consisted of two identical coils 22cm in diameter and of 29 turns each. The spacing of the coils was 11cm. and the

wire diameter 0.04cm. A Hall-probe gaussmeter was used to measure the axial field distribution. The fields produced by each of these coils were measured before placing the iron cylinders in them.

Three cylinders, with different dimensions, were used. All were made from the same material (soft iron). Each cylinder was placed in each of the fields produced by the four coils. Using the gaussmeter, the fields were measured with the presence of the cylinders. Later, the field due to the coils alone was subtracted from the latter readings in order to obtain the field due to the cylinders on their own. The results obtained approximately fitted the bell-shaped model shown in figure (3.2).

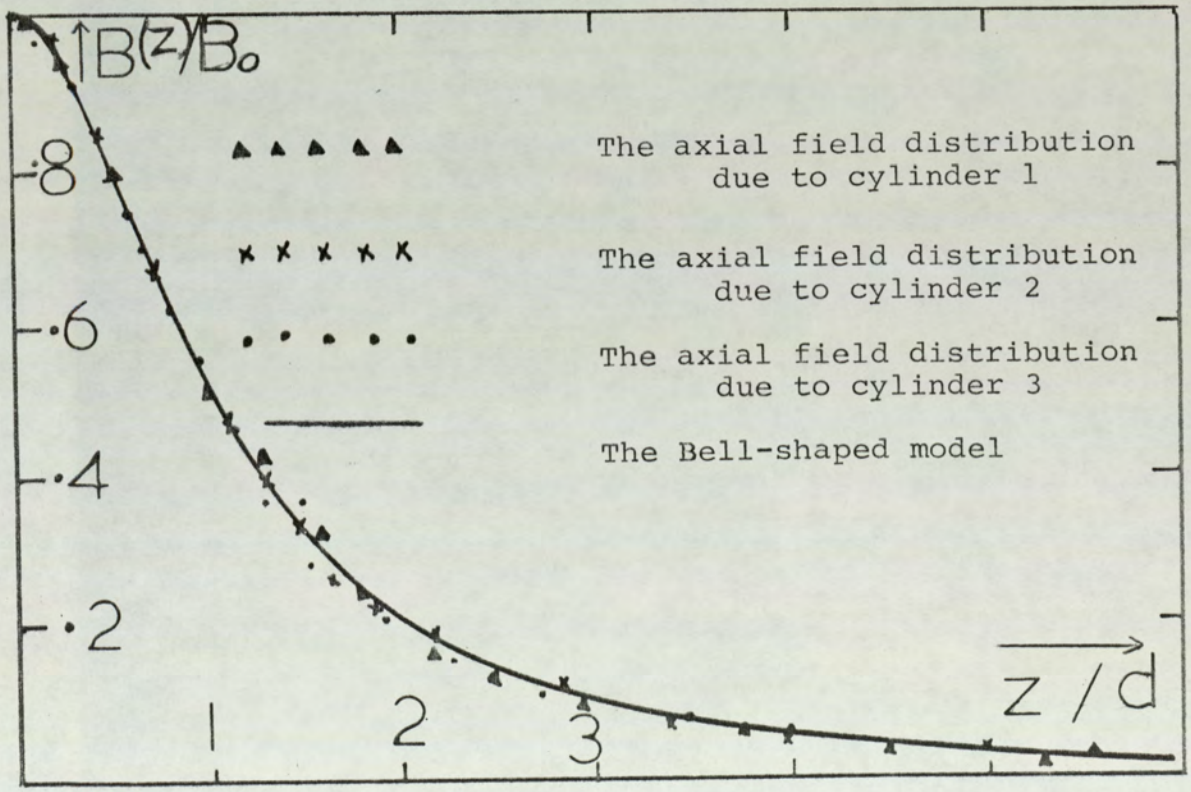

Fig. (3.2) The Bell-shaped model compared with experimental points due to magnetized cylinders in the uniform field.

Unfortunately, it is difficult to find an analytical solution for this case. So it seemed useful to examine the magnetic field due to uniformly magnetized solids which have analytical expression such as the ellipsoid.

3.1.3 An iron ellipsoid in a uniform magnetic field

If there is a uniform magnetic field ($B_{original}$) and an ellipsoid with semi-axis a, b and c is placed inside this, it is induced with a uniform field too (Webster, 1897). The magnetic field (B_o) inside the ellipsoid with c = b depends upon the factor N , where N which is called the magnetization factor by Professor H. duBois (Ewing, 1891) takes the values in (1.40) and (1.42).

The ellipsoid magnification (i.e. $B_o/B_{original}$) can be found from (1.44) as

$$B_o/B_{original} = 4\pi\mu/[(\mu-1)\ N+4\pi] \ldots\ldots \quad (3.9)$$

Figure (3.3) shows this relation for high permeability and it is clear that the value $B_o/B_{original}$ in the case of the sphere is three, since N takes the value $4\pi/3$. This is discussed later.

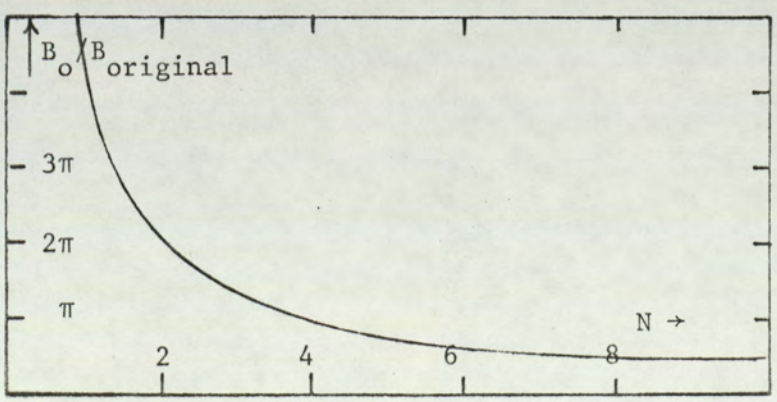

Figure (3.3) Magnetic field ratio ($B_o/B_{original}$) of a uniformly magnetized ellipsoid as a function of N

On the other hand, figure (3.4) shows the magnification parameter $B_o/B_{original}$ as a function of the ratio a/b where a in the direction of the original field. To test this fact experimentally, few ellipsoids with various values of a/b were used. The ellipsoid magnification of these ellipsoids are measured by using the same procedure described in (§ 3.1.2) and the experimental points are shown as crosses in figure (3.4)

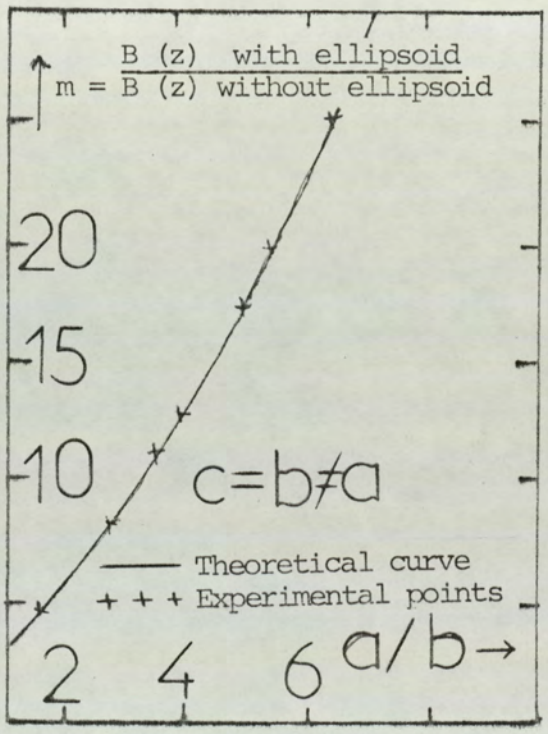

Fig.(3.4) The magnetic field ratio of a magnetized ellipsoid as a function of the axis-ratio (a/b)

Equations (1.38) and (1.39) are very useful to find analytically the magnetic field due to the uniformly magnetized ellipsoid.

By assuming μ is very large, the field B(Z) is in Z-direction and removing the original uniform field but leaving the magnetization in the iron, the external field along the Z-axis due to the ellipsoid itself follows approximately the relationship

$$B(Z) = B_o(ab^2/Z^3) \quad \ldots\ldots\ldots \quad 3.10a$$

This implies that $Z \geq a$. To make this equation applicable at $Z > 0$, it can be written as

$$B(Z) = B_o / \left[1 + Z/(ab^2)^{1/3} \right]^3 \quad \ldots\ldots\ldots \quad 3.10b$$

The half-width (d) of this field distribution is given by

$$d = 0.26 (ab^2)^{1/3} \quad \ldots\ldots\ldots\ldots \quad 3.11$$

For convenience, equation 3.10b is written as

$$B(Z) = B_o (3.847)^3 / \left[3.847 + Z/d \right]^3 \ldots\ldots \quad 3.12$$

Uniformly magnetized sphere is a special case of the ellipsoid with a=b=c, then the equation (3.11) takes the form

$$d = 0.26a \ldots\ldots\ldots\ldots\ldots\ldots \quad 3.13$$

and (3.12) is applicable for the sphere. This expression is called spherical field model. Moreover, it is important to remember that the maximum value of the field (B_o) is located at the end of magnetized body.

The experimental investigation

Experimental investigation of the shape of the axial field distribution due to a magnetized ellipsoid was carried out with the co-operation of Ridha (1977) in our laboratory. In these experiments the ellipsoids were used with dimensions b=c and a in the magnetization direction.

Two ellipsoids with ratios a/b = 3/1.25 and 1.25/3 were used. Both of them gave a magnification (i.e. the ratio of the field with iron in place of that with no iron in place)

of 5 and 2.2 respectively which is in agreement with the theoretical result in Figure (3.4). On the other hand the field distribution due to a magnetized ellipsoid agrees very well with the spherical single-pole field (3.12) as shown in Figure (3.5).

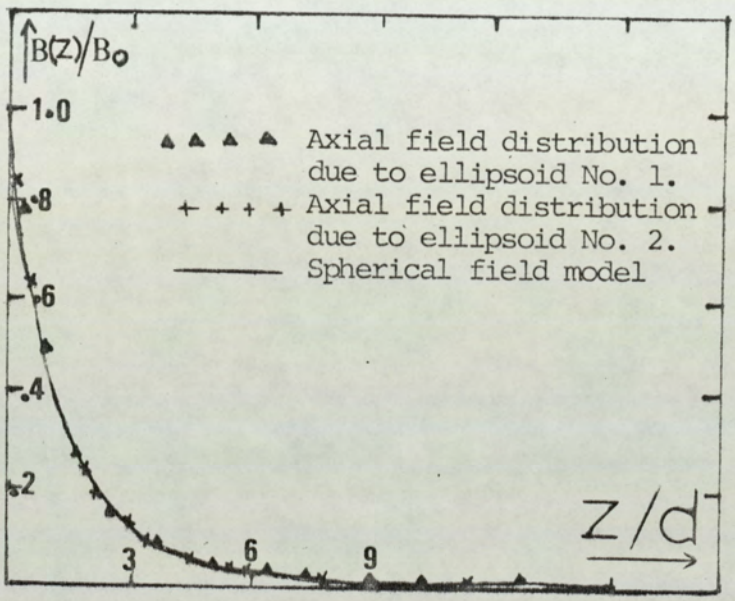

Fig. (3.5) The axial field distribution of the spherical model compared with the experimentally measured field due to a uniformly magnetized ellipsoid.

The sphere is, of course, a particular case of the ellipsoid; it is easier to study theoretically and easier to manufacture. It was therefore considered to be more profitable to study the uniformly magnetized iron sphere.

3.2 The Spherical pole-piece model

3.2.1 Uniformly magnetized iron sphere

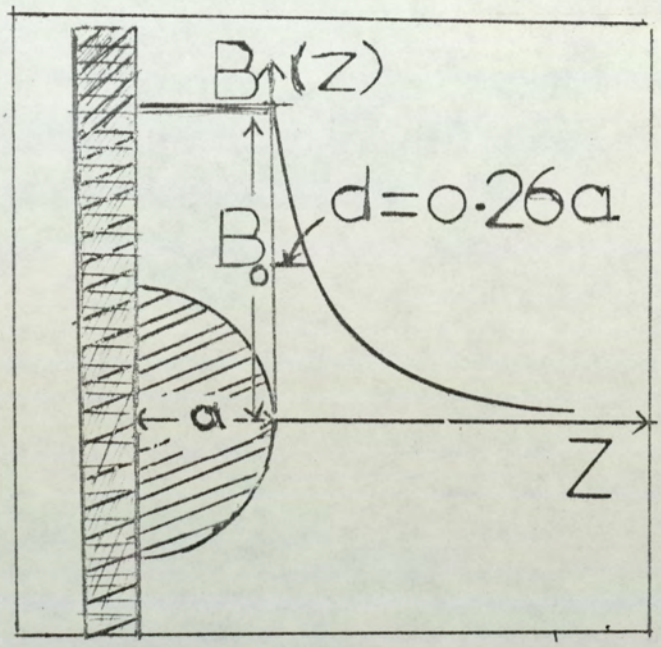

Fig.(3.6) The spherical field due to uniformly magnetized hemisphere

By assuming that μ is very large and that the field B(z) is in the z-direction (i.e. if $\theta = 0$, $r = z$), then the magnetic field inside the sphere (B_{in}) according to equation (1.45) is

$$B_{in} = -\partial\Omega/\partial z = 3/2B_o \quad \ldots\ldots\ldots\ldots \quad (3.14)$$

and the field outside the sphere (B_{out}) according to equation (1.46) is

$$B_{out} = B_o/2 + B_o(a^3/z^3) \quad \ldots\ldots\ldots \quad (3.15)$$

Subtracting the original uniform field ($B_o/2$) the magnetized iron sphere follows the relationship

$$B(z) = B_o(a/z)^3 \quad \ldots\ldots\ldots\ldots\ldots\ldots \quad (3.16)$$

Notice that z is measured from the centre of the sphere in the direction of magnetization and B_o is the uniform flux

density in the sphere in the same direction. The equation is a special case from the general form (3.10).

The spherical single-pole piece field figure (3.6) refers, of course, to the external flux density so that z/a is never less than unity. The axial flux density in the iron sphere itself is constant as shown in figure (3.6). For convenience the spherical pole piece model is sometimes simply called the 'spherical field' in this thesis. The equation 3.16 can be written as

$$B(z) = B_o/[1+z/a]^3 \text{ for } z \geqslant 0 \quad \ldots\ldots\ldots \quad 3.17$$

The half width (d) of this distribution is given by d=0.26a as in (3.13), then (3.17) rewritten as

$$B(z) = \frac{B_o(3.847)^3}{[3.847 + z/d]^3} \quad \ldots\ldots\ldots\ldots\ldots \quad 3.18$$

3.2.2 Investigation of the spherical pole-piece model

The investigation of the practical value of the spherical model was done experimentally and by using results available in the literature which were thought to be useful. A series of experiments was carried out to study the fields produced by iron spheres placed in uniform magnetic fields. The method used is described in (§3.1.2). The fields due to each of four coils previously described were used in turn to magnetize each of three iron spheres whose diameters were 1.3, 1.5 and 3.0cm respectively. After the usual subtraction of the fields of the coils, the results obtained show that the fields produced by uniformly magnetized spheres fit exactly the spherical model.

Although the results presented in this work show the significance of spherical snouts, a search of the literature did not reveal a lot of work on this important shape. The work of Munro and Wells (1976) by using Munro's method (1972), the only one that the author is aware of being of value using the results of the above two authors and taking into account the effects due to the coils and plates, the resulting field was in reasonable agreement with the spherical model described in equation (3.18). Figure (3.7) shows the spherical field distribution found by Munro and Wells (1976) compared with the spherical field model.

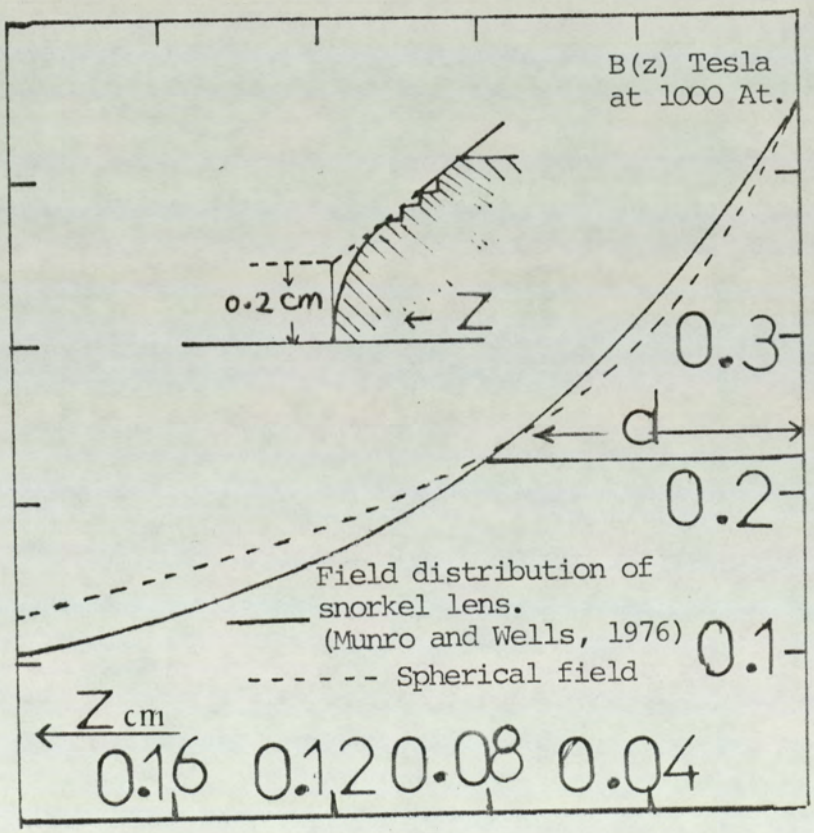

Fig. (3.7) The axial magnetic field distribution due to snorkel lens, Munro and Wells (1976) with spherical tip, compared with spherical field.

Fig. (3.8) Cylinder with spherical end cap

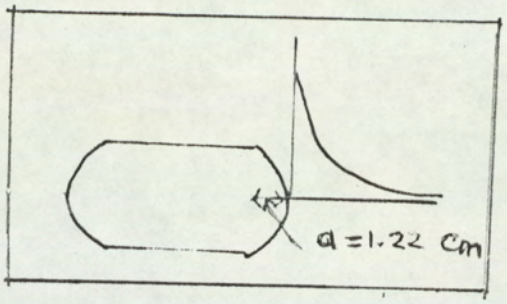

Another experimental investigation was done for a cylinder with spherical end cap (fig. 3.8).

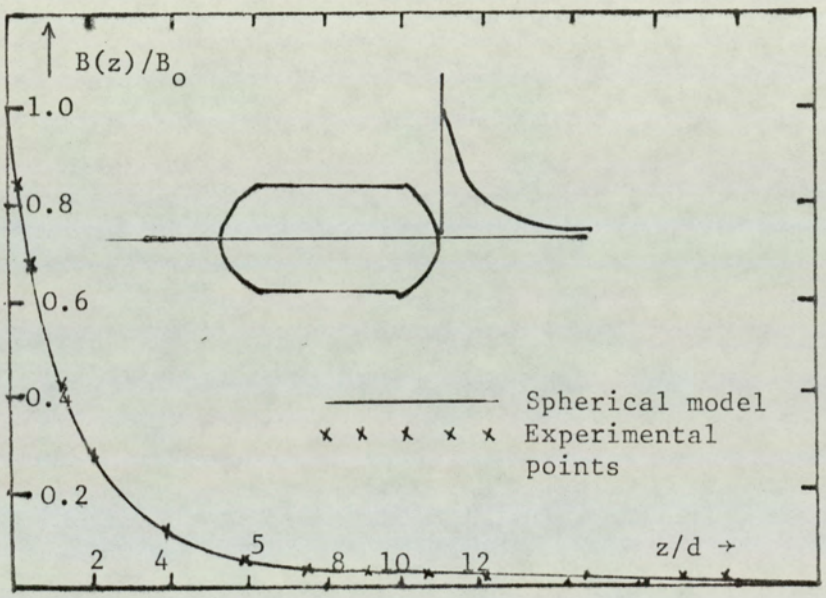

Fig. (3.9) The axial field distribution of a magnetized cylinder with a spherical end cap.

The axial field distribution due to this shape was measured and plotted in Figure (3.9). It is clear that this field follows the spherical single-pole field as does the field due to the ellipsoid.

3.2.3 The general solution of the spherical field model

The paraxial ray equation (1.1) for this field is given by

$$\frac{d^2r}{dz^2} + \frac{e}{8mVr}(B_o a^3/z^3)^2 . r = 0 \quad .... \quad (3.19)$$

The general solution of this equation (Appendix 10.6) is

$$r/a = (z/a)^{\frac{1}{2}}\left[AJ_{\frac{1}{4}}(u) + BJ_{-\frac{1}{4}}(u)\right] \quad ..... \quad (3.20)$$

where $J_{\frac{1}{4}}(u)$ and $J_{-\frac{1}{4}}(u)$ are Bessel functions of order one quarter and these solutions are linearly independent (or distinct) and constitute a fundamental system. A and B are arbitrary constants.

Putting $$u = ka^2/2z^2 \quad ..... \quad (3.21)$$

where $k = (e/8m)^{\frac{1}{2}} . (2\mu_o)(NI/V_r^{\frac{1}{2}}) = 0.3725\ (NI/V_r^{\frac{1}{2}})$

The slope r' may be written as

$$r' = \frac{a}{2(z/a)^{\frac{1}{2}}}\left[AJ_{\frac{1}{4}}(u)+BJ_{-\frac{1}{4}}(u)\right]+a(z/a)^{\frac{1}{2}}\left[-AJ'_{\frac{1}{4}}(u)\left(\frac{ka^3}{z^3}\right) + BJ'_{-\frac{1}{4}}(u)\left(-\frac{ka^3}{z^3}\right)\right] \quad .. \quad (3.22)$$

By using the rule $J'_\nu = \frac{1}{2}\left[J_{\nu-1}-J_{\nu+1}\right]$, where ν any real number, equation (3.22) reduces to

$$r' = \frac{a}{2(z/a)^{\frac{1}{2}}}\left[AJ_{\frac{1}{4}}(u)+BJ_{-\frac{1}{4}}(u)\right] - \frac{k}{(z/a)^{5/2}}\left[AJ_{-\frac{3}{4}}(u) - AJ_{\frac{5}{4}}(u)+BJ_{-\frac{5}{4}}(u)-BJ_{\frac{3}{4}}(u)\right] \quad .. \quad (3.23)$$

3.2.4 Particular rays in the spherical field

The electron optical characteristics of certain rays under different boundary conditions are determined below:

(a) Consider a ray starting at $z = \infty$ with unit height $r/a = 1$ and zero slope ($r'=0$). It may be remarked that as $z \to 0$, $J_{-\frac{1}{4}}(z) = \infty$, then the solution of the paraxial ray equation under these boundary conditions is given by Alshwaikh and Mulvey (1977) (Appendix 10.7) as

$$r/a = (z/a)^{\frac{1}{2}} A J_{\frac{1}{4}}(u) \quad \ldots\ldots\ldots \quad (3.24)$$

so that

$$A = 2^{\frac{1}{2}} K^{\frac{1}{4}} \Gamma 5/4 \quad \ldots\ldots\ldots\ldots \quad (3.25)$$

where Γ is a Gamma function. Hence

$$A = 0.164/(NI/V_r^{\frac{1}{2}})^{\frac{1}{4}} \quad \ldots\ldots\ldots \quad (3.26)$$

Substitution of (3.21) and (3.25) into (3.24) gives the following equations

$$r/a = (z/a)^{\frac{1}{2}} \left[\frac{1.6406}{(NI/V_r^{\frac{1}{2}})^{\frac{1}{4}}} \right] \cdot J_{\frac{1}{4}} \left[\frac{0.186}{z^2/a^2} (NI/V_r^{\frac{1}{2}}) \right] \quad (3.27)$$

It should again be noted that $z > 3.847d$. If we make $r/d = 1$ at $z = \infty$ we obtain

$$r/d = (z/d)^{\frac{1}{2}} \frac{0.836}{(NI/V_r^{\frac{1}{2}})^{\frac{1}{4}}} J_{\frac{1}{4}} \left[\frac{2.758}{z^2/d^2} (NI/V_r^{\frac{1}{2}}) \right] \quad \ldots (3.28)$$

The slope $r'(z)$ of the ray at a distance (z) is given by

$$r' = \frac{0.611}{(z/a)^{5/2}} \cdot (NI/V_r^{\frac{1}{2}})^{\frac{3}{4}} \cdot J_{5/4} \left[\frac{0.186}{z^2/a^2} (NI/V_r^{\frac{1}{2}}) \right] \quad \ldots (3.29)$$

and

$$r' = \frac{17.75}{(z/d)^{5/2}} \cdot (NI/V_r^{\frac{1}{2}})^{\frac{3}{4}} \cdot J_{5/4} \left[\frac{2.758}{z^2/d^2} (NI/V_r^{\frac{1}{2}}) \right] \quad (3.30)$$

Note that r' is dimensionless and $J_{5/4}$ is the Bessel function of order 5/4. In the particular case where z = a (measured from sphere centre), an important parameter in electron optics arises, namely

$$r'_{(z=a)} = 0.6114(NI/V_r^{\frac{1}{2}})^{\frac{3}{4}} \cdot J_{5/4}\left[0.186(NI/V_r^{\frac{1}{2}})\right] \quad (3.31)$$

(b) The ray for which $r/a_{(z=z_c)} = 1$ and $r'_{(z=z_c)} = 0$.

By substituting these conditions into equations (3.27) and (3.29) and using $U_c = K/[2(z_c/a)^2]$, we obtain

$$0 = A_o J_{\frac{1}{4}}(U_c) + B_o J_{-\frac{1}{4}}(U_c) \quad \ldots\ldots\ldots\ldots \quad (3.32)$$

$$-(z_{c/a})^{5/4}/K = A_o\left[J_{-\frac{3}{4}}(U_c) - J_{5/4}(U_c)\right] + B_o\left[J_{-5/4}(U_c) - J_{\frac{3}{4}}(U_c)\right] \quad \ldots\ldots\ldots\ldots \quad (3.33)$$

The solution is

$$r/a = (z_c/a)^{\frac{1}{2}}\left[A_o J_{\frac{1}{4}}(U_c) + B_o J_{-\frac{1}{4}}(U_c)\right] \quad \ldots\ldots\ldots\ldots \quad (3.34)$$

$$\text{and } r' = \left[a/2(z_c/a)^{\frac{1}{2}}\right]\left[A_o J_{\frac{1}{4}}(U_c) + B_o J_{-\frac{1}{4}}(U_c)\right] - K/(z_c/a)^{5/2}\left[A_o J_{-\frac{3}{4}}(U_c) - A_o J_{5/4}(U_c) + B_o J_{5/4}(U_c) - B_o J_{\frac{3}{4}}(U_c)\right] \quad \ldots\ldots\ldots \quad (3.35)$$

$$\text{where } A_o = (z_c/a)^{5/2}\, J_{-\frac{1}{4}}(U_c)/K\left[-J_{-\frac{1}{4}}(U_c)J_{-\frac{3}{4}}(U_c) + J_{5/4}(u_c)J_{-\frac{1}{4}}(u_c) + J_{\frac{1}{4}}(U_c)J_{-5/4}(U_c) - J_{\frac{1}{4}}(U_c)J_{\frac{3}{4}}(U_c)\right] \quad \ldots \quad (3.36)$$

$$B_o=-(z_c/a)^{5/2}\ J_{\frac{1}{4}}(U_c)/K\Big[-J_{\frac{1}{4}}(U_c)J_{-\frac{3}{4}}(U_c)+J_{-\frac{1}{4}}(U_c)J_{5/4}(U_c)$$

$$+\ J_{\frac{1}{4}}(u_c)J_{-5/4}(U_c)-J_{\frac{1}{4}}(U_c)J_{\frac{3}{4}}(U_c)\Big] \quad (3.37)$$

(c) Consider the special case in which the ray defined in (b) is brought to a focus at the tip of the sphere, i.e. $r/a_{(z/a=1)}=1$ and $r'_{(z/a=1)}=0$. The solution for r and r' as follows

$$r/a=A_1J_{\frac{1}{4}}(K/2)+B_1J_{-\frac{1}{4}}(K/2) \quad \ldots\ldots\ldots\ldots\ldots\ldots\ldots \quad (3.38)$$

$$r'=a/2\Big[A_1\ J_{\frac{1}{4}}(K/2)+B_1J_{-\frac{1}{4}}(K/2)\Big]-K\Big[A_1J_{-\frac{3}{4}}(K/2)-A_1J_{5/4}(k/2)$$

$$+B_1J_{-5/4}(K/2)-B_1J_{\frac{3}{4}}(K/2)\Big] \quad \ldots\ldots \quad (3.39)$$

$$\text{where } A_1 = \frac{J_{-5/4}(K/2)-J_{\frac{3}{4}}(K/2)-(1/2K)J_{-\frac{1}{4}}(K/2)}{J_{\frac{1}{4}}(K/2)J_{-5/4}(K/2)-J_{\frac{1}{4}}(K/2)J_{\frac{3}{4}}(K/2)-J_{-\frac{1}{4}}(K/2)J_{-\frac{3}{4}}\ldots\ldots\ldots\ldots\ldots\ldots\ldots(K/2)+J_{-\frac{1}{4}}(K/2)J_{5/4}(K/2)}$$

$$\ldots \quad (3.40)$$

$$B_1=\frac{J_{-\frac{3}{4}}(K/2)-J_{5/4}(K/2)-(1/2K)J_{\frac{1}{4}}(K/2)}{J_{-\frac{1}{4}}(K/2)J_{-\frac{3}{4}}(K/2)-J_{-\frac{1}{4}}(K/2)J_{5/4}(K/2)-J_{\frac{1}{4}}(K/2)J_{-5/4}(K/2)\ldots\ldots\ldots\ldots+J_{\frac{1}{4}}(K/2)J_{\frac{3}{4}}(K/2)} \quad \ldots\ldots \quad (3.41)$$

3.3 Focal Properties of the Spherical Pole-Piece Field

3.3.1 The properties when the ray incident on the sloping part of the spherical field

The rays described by the equation (3.28) intersect the axis at points distance (z_n) from the origin, (i.e. at the surface of magnetized sphere) where $Zn=2U_n/k$, where U_n

is the value at which $J_{\frac{1}{4}}(n) = 0$.

From tables (Jahnke et al, 1960) these values mean that there is only one focus at distance z_F from the origin given by

$$z_F/d = (NI/V_r^{\frac{1}{2}})^{\frac{1}{2}} - 3.847 \quad \ldots\ldots\ldots\ldots \quad (3.42)$$

or $$z_F/a = 0.26(NI/V_r^{\frac{1}{2}})^{\frac{1}{2}} - 1 \quad \ldots\ldots\ldots \quad (3.43)$$

Equations (3.42) and (3.43) are applicable only when $NI/V_r^{\frac{1}{2}} \geq 15$. The second term in both equations should be omitted when the origin is taken at the centre of the sphere.

The projector focal length (f_p) and objective length (f_{obj}) in the range of excitation parameters $NI/V_r^{\frac{1}{2}} \leq 14$ are the same and can be deduced from the relation $f_p = r/r' = 1/r'$. Then from the last equation it can be found that:

$$f_p/d = 6.29(NI/V_r^{\frac{1}{2}})^{-\frac{3}{4}}/J_{5/4}\left[0.186(NI/V_r^{\frac{1}{2}})\right] \ldots\ldots\ldots \quad (3.44)$$

or $$f_p/a = 1.63(NI/V_r^{\frac{1}{2}})^{-\frac{3}{4}}/J_{5/4}\left[0.186(NI/V_r^{\frac{1}{2}})\right] \ldots\ldots \quad (3.45)$$

The calculated values of f_p/d over a wide range of excitation parameter are therefore straightforward. In like manner we find that (Mclachlan, 1955)

$$J_{5/4}(u) = \frac{1}{2u} J_{\frac{1}{4}}(u) - J_{-\frac{3}{4}}(u) \quad \ldots\ldots\ldots \quad (3.46)$$

The corresponding values of $J_{5/4}(u)$ are calculated

and both $J_{\frac{1}{4}}(u)$ and $J_{-\frac{3}{4}}(u)$ are taken directly from tables of fractional order Bessel function (N.A.M.L., 1948). To find the values of r' at the point z(F), the equation (3.30) becomes

$$r' = 17.93(NI/V_r^{\frac{1}{2}})^{-\frac{1}{2}} J_{5/4}(u_1) \quad \ldots\ldots\ldots \quad (3.47)$$

assuming $z/a = (K/2U_1)^{\frac{1}{2}}$ $\ldots\ldots\ldots$ (3.48)

The objective focal length (f_{obj}) at the excitation parameter $NI/V_r^{\frac{1}{2}} \geq 14$ (i.e. positive z_f) is derived from the equation (3.47) by putting $f_{obj}=1/r'$ and $J_{5/4}(u_1) = 0.48$ then

$$f_{obj}/d = 0.447(NI/V_r^{\frac{1}{2}})^{\frac{1}{2}} \quad \ldots\ldots\ldots\ldots \quad (3.49)$$

$$f_{obj}/a = 0.116(NI/V_r^{\frac{1}{2}})^{\frac{1}{2}} \quad \ldots\ldots\ldots\ldots \quad (3.50)$$

It is useful to remember at this stage that the z_F for excitation parameter $NI/V_r^{\frac{1}{2}} < 15$ can be calculated by the relation

$$z_F = r/r' = r.f_p \quad \ldots\ldots\ldots\ldots\ldots \quad (3.51)$$

The variation of f_p/d, f_{obj}/d and z_p/d as a function of the excitation parameter $NI/V_r^{\frac{1}{2}}$ are shown in figure (3.10).

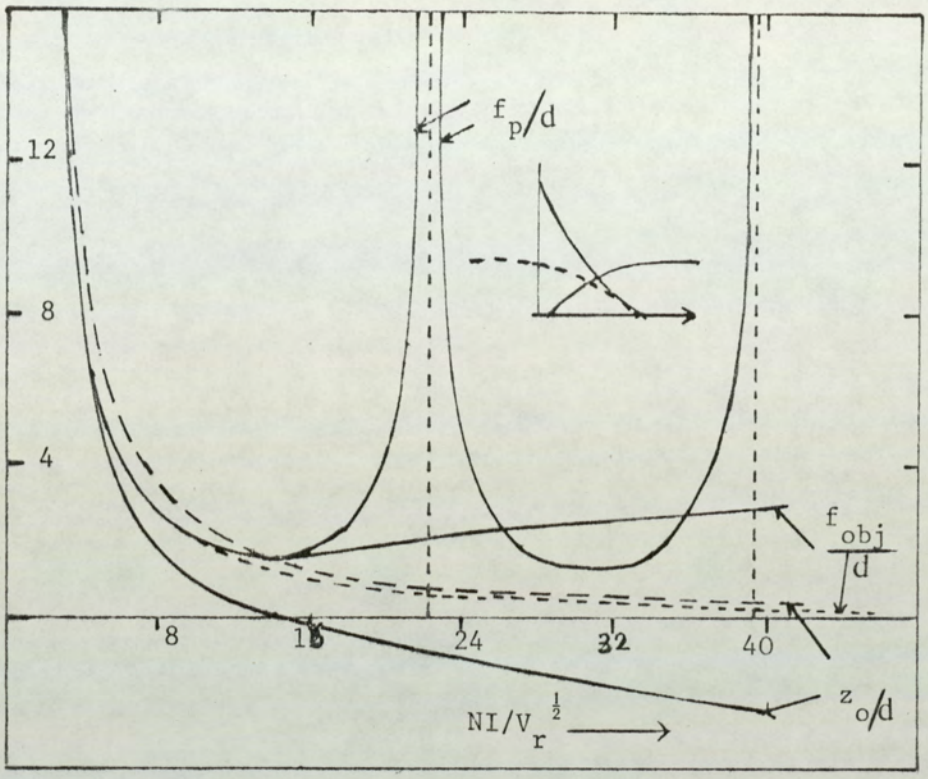

Fig. (3.10) The focal properties of the spherical field model

This curve covers the first two zones of operation and shows that f_p and f_{obj} are equal at the excitation parameters <14. In the first zone and the minimum focal length in this zone equals 1.693d (0.4a) and occurs at $NI/V_r^{\frac{1}{2}} = 14$.

At an excitation parameter greater than 14, the objective focal length (f_{obj}) is directly proportional to $(NI/V_r^{\frac{1}{2}})^{\frac{1}{2}}$. Figure (3.10) also shows that the second minimum projector focal length has the value 1.428d which occurs at $NI/V_r^{\frac{1}{2}} = 31$. From the analytical solution it is clear that the third minimum f_p occurs at excitation parameter 48 with avalue equal to 1.288d.

3.3.2 Focal properties of the spherical field for the ray incident on the steep slope of the field

The same electron-optical properties were studied for the case when the rays are incident on the steep edge of the single-pole field. The investigation was done by using a numerical method which is described in Chapter 2. A check for some points was made using the analytical solution described in (§3.2.3). The numerical method is more efficient than the analytical method since in the latter these are chains of mathematical operations containing higher functions, each of which can introduce an error in the calculations.

The numerical method for calculating f_p is listed in the first part of the program (CDISTØRTIØN) while f_{obj} and z_F calculations are listed in the first part of the program (CABERRATIØN). To check the accuracy of these two programs they were used for the positive direction, and the results show excellent agreement with the analytical solution, as shown in table (3.1).

Focal parameters	Analytical methods	Numerical methods
Minimum f_p at first two zones	1.69d, 1.43d	1.69d,1.46d
Minimum f_{obj}/d	1.69d	1.69d
f_p at $NI/V_r^{\frac{1}{2}} = 20$	3.78	3.68
f_{obj} at $NI/V_r^{\frac{1}{2}} = 20$	1.99	2.001
f_p at $NI/V_r^{\frac{1}{2}} = 10$	2.09	2.09
f_{obj} at $NI/V_r^{\frac{1}{2}} = 10$	2.09	2.09

Table 3.1

One of the important properties of the spherical field is that the lens becomes a focal (telescopic ray path) at an excitation parameter 22.36, 39.5 and 56.5 respectively.

3.4 Application of the Magnetized Sphere Model

The magnetized sphere model is closer than any other model to the field distribution in single pole piece lenses. However, in addition to the field due to the snout, there is another field produced by the coils themselves, and the total field of the lens is the summation of these two fields. The investigation of several lenses shows that there is hardly any effect from the coils, and some total fields follow the spherical model, but in this case the half-width is related to dimensions of the snout and coil. In particular the thin coils did not have an important effect on the field shape, since it also followed the spherical models. Figure (3.11) shows the spherical field compared with the field of iron-free coil coil at the case $D_o/D_i = 19$ calculated by Biot-Savart law.

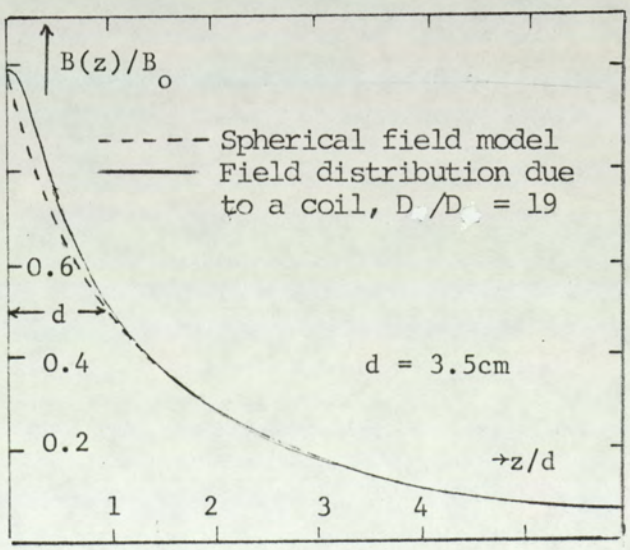

Fig.(3.11) The axial magnetic field distribution of an iron-free coil of outer to inner diameter $D_o/D_i = 19$ compared with that of the spherical field model.

3.4.1 Lenses with a conical-shaped snout

To investigate the field caused by a conical-shaped snout, two lenses constructed by Mulvey (figures (3.12) and (3.13))with 2cm snout and 1mm hole, their field distributions were calculated by the Rutherford Laboratory using the integral form of the finite element method (Trowbridge et al, 1972).

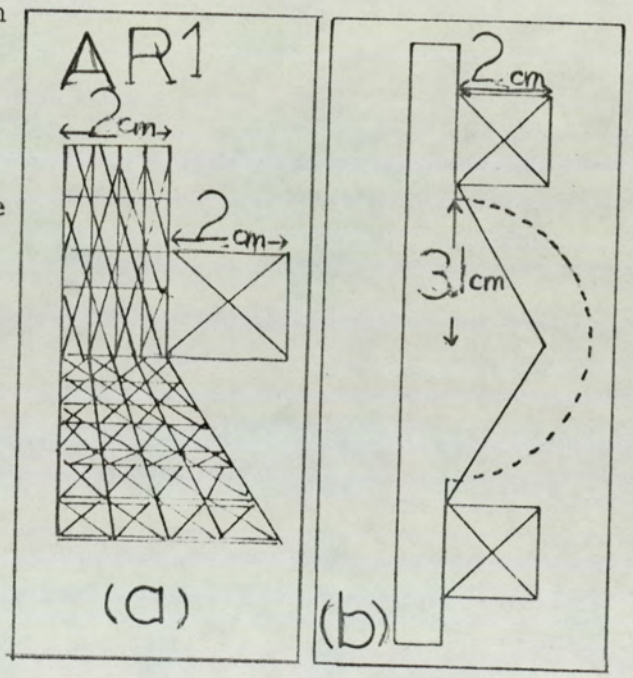

Fig.(3.12) Schematic diagram of a single pole lens with conical snout (AR1)
(a) Symmetrical half of the lens showing finite elements.
(b) Complete lens with equivalent spherical polepiece (dotted line) (equivalent radius a = 3.1cm)

This method divides the iron circuits of the lens and the exciting coil into small elements, the number and shape of which are chosen according to the accuracy required. The magnetic field from the coil is calculated by the Biot-Savart law. The magnetic flux in each element is calculated by an integral method taking into account the magnetic field of the coil and the magnetising effect of the other

iron elements. The total field at any point is the sum of the field produced by the coil and that produced by the iron circuit. For convenience these two lenses are denoted by AR1 and AR2.

Fig.(3.13) Schematic cross-section of lens AR2 with the equivalent spherical polepiece (dotted line) (equivalent radius a=1.9cm)

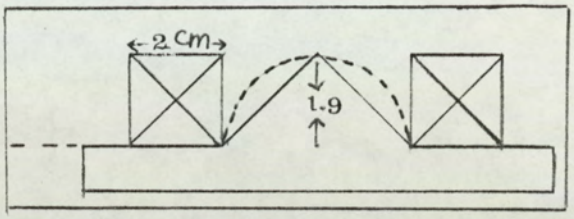

Figure (3.14) shows the field distributions for AR1 (crosses) and AR2 (squares) compared with spherical pole-piece field distribution which has a slope found to be a close on three on log-log paper. It can be seen that lenses AR1 and AR2 are a close fit to this distribution.

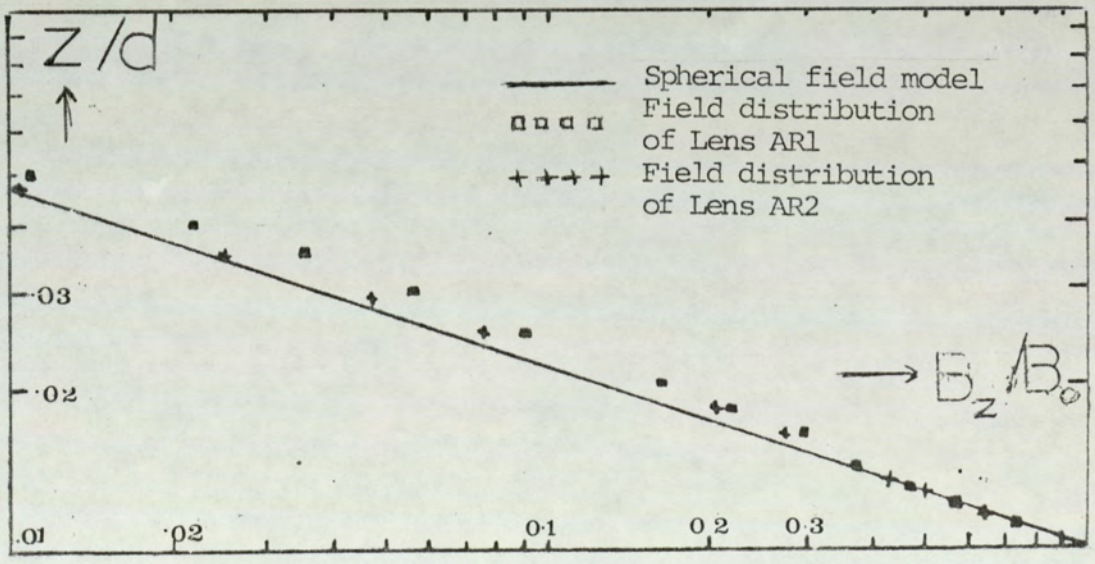

Fig. (3.14) The magnetic field distributions for lens AR1 (crosses) and lens AR2 (squares) compared with that of spherical field model on log-log paper.

Using the Biot-Savart law the program BZAXIAL (Chapter 2)was used to calculate the field for the two lenses and to subtract from it, the field due to the coils and back plate alone. This should give the magnetic field due to the magnetized snouts only.

These results are plotted in figures (3.15) and (3.16) and the important conclusion drawn is that the magnetic field due to conical iron snouts do not deviate too much from the spherical pole-piece model.

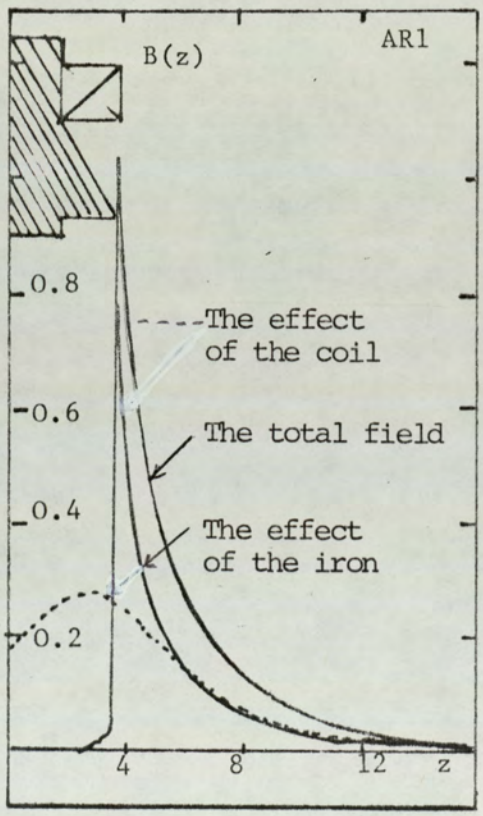

Fig. (3.15)

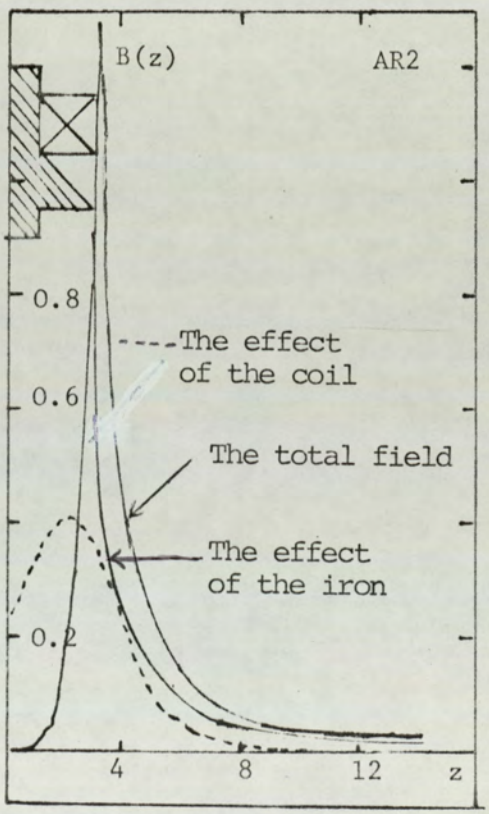

Fig. (3.16)

Fig. (3.15) The total axial magnetic field distribution of lens AR1 and the contribution of the exciting coil to the total field.

Fig. (3.16) The total axial magnetic field distribution of lens AR2 and the contribution of the exciting coil to the total field.

Both two spherical single pole models are plotted in figures (3.15) and (3.16) and can be produced by replacing the existing pole pieces by equivalent spheres. Dimensions of equivalent spheres are shown in figures (3.12) and (3.13).

The electron-optical characteristics and aberration coefficients for two possible directions of the ray are shown in figure (3.17) for AR1 while figure (3.18) shows similar characteristics for the other lens.

From figure (3.17) it is found that $f_{p(min)}$ is equal to 1.8mm and occurs at an excitation parameter $NI/V_r^{\frac{1}{2}}$ = 15, and from other figure $F_{p(min)}$ is equal to 1.2mm. Both F_{obj} and f_p are the same up to the minimum projector focal length position and than f_{obj} slowly decreases for excitations $NI/V_r^{\frac{1}{2}}$ higher than 15 in AR1 and 16 in AR2.

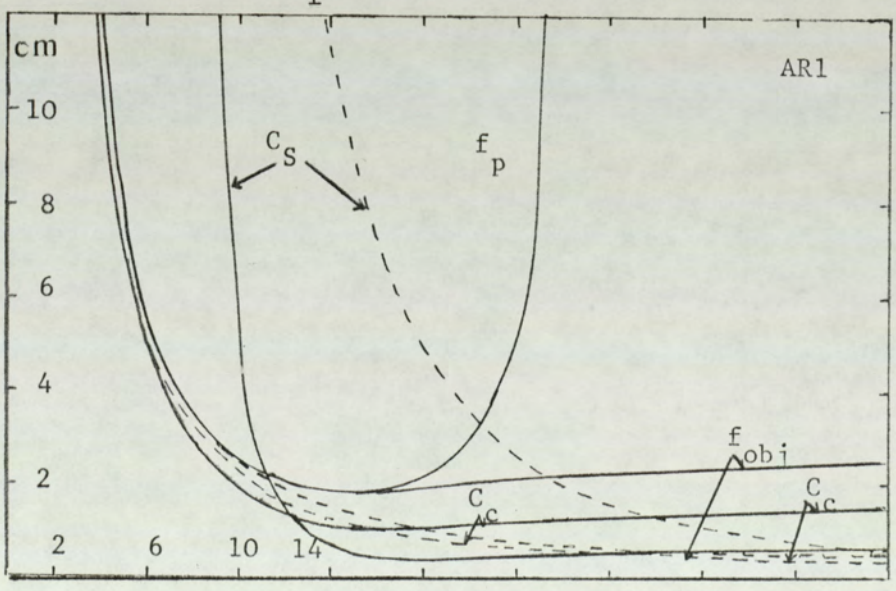

Fig. (3.17) Electron focal properties and aberration coefficients for lens AR1.

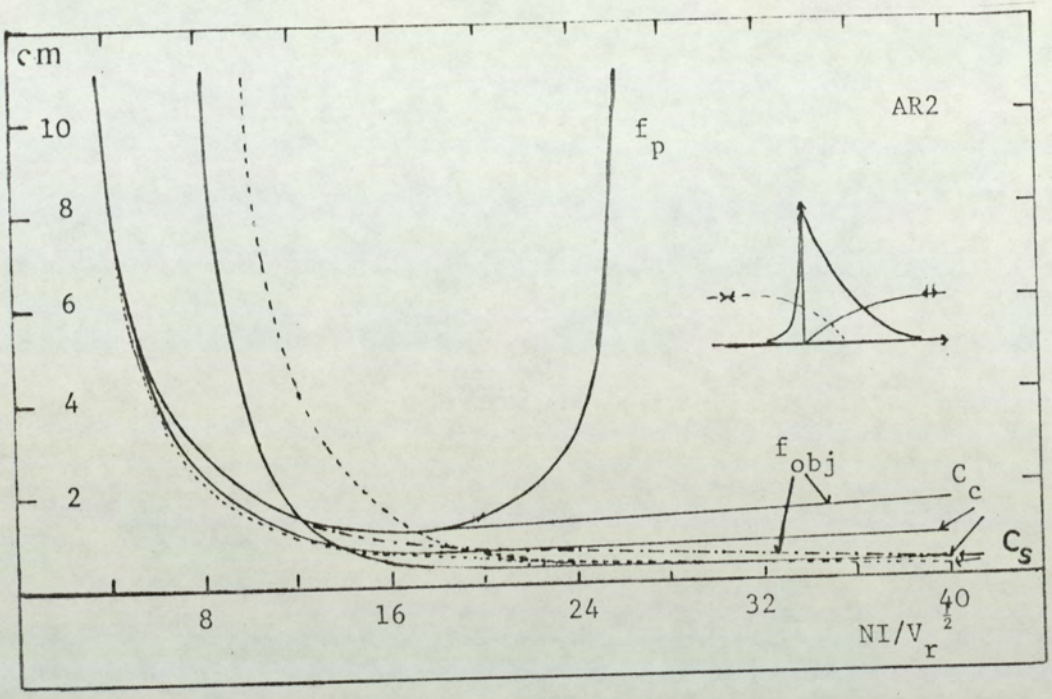

Fig. (3.18) Electron focal properties and aberration coefficients for lens AR2.

3.4.2 An experimental single pole-piece lens

Fig. (3.19A) shows the construction and the field distribution of an 8mm bore minilens used for the spiral distortion correction system in an EM6 electron microscope. The field was measured by Elkamali (1978) using a hall probe Gaussmeter, and is found to fit well into spherical pole-piece model.

The great advantage of this lens is that its wide bore makes it possible for a Hall probe Gaussmeter to be used to measure the field distribution. It was not possible to do this in other lenses because of the very narrow bore

of those lenses. Previous investigators do not seem to have been interested in the field in this part of the lens. The significance of this field is that it gives an idea of the shape and magnitude of the field on the negative part of the z-axis. There is no doubt that this result has its practical value and interpretation, the reason being that when a bore is drilled in a spherical snout this negative part of the field is bound to exist.

This lens is one of many examples which show that single-pole lenses even if used without exact spherical snouts can be important because of their approach to the spherical model.

3.4.3 Objective lenses for high resolution

A practical ultrahigh resolution lens (UHP) fig.(3.20a) was developed by K. Shirota et al (1977) with aberration constants (i.e. c_s and c_c) better than those of conventional lenses. The reduction of aberration was done by decreasing the half width value of the field distribution and increasing the peak value. The first effect was achieved by reducing pole-piece dimensions.

It is worth looking at the field distribution of this lens since its lower part seems to be conical. When the image rotation method was used for this purpose, it was found that the field produced by the lower half exactly fitted the spherical model figure (3.20b). We can thus suggest the use of spherical pole-pieces in electron microscopes fitted with double-pole lens (UHP) like JCM-100C and 100CX. Values of C_c = 1.05mm and C_s = 0.7mm

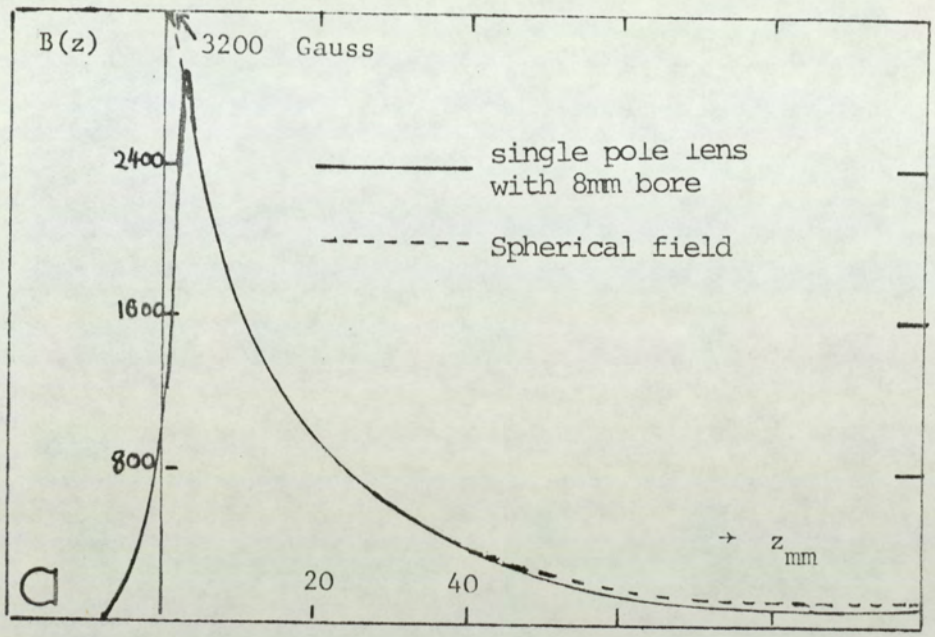

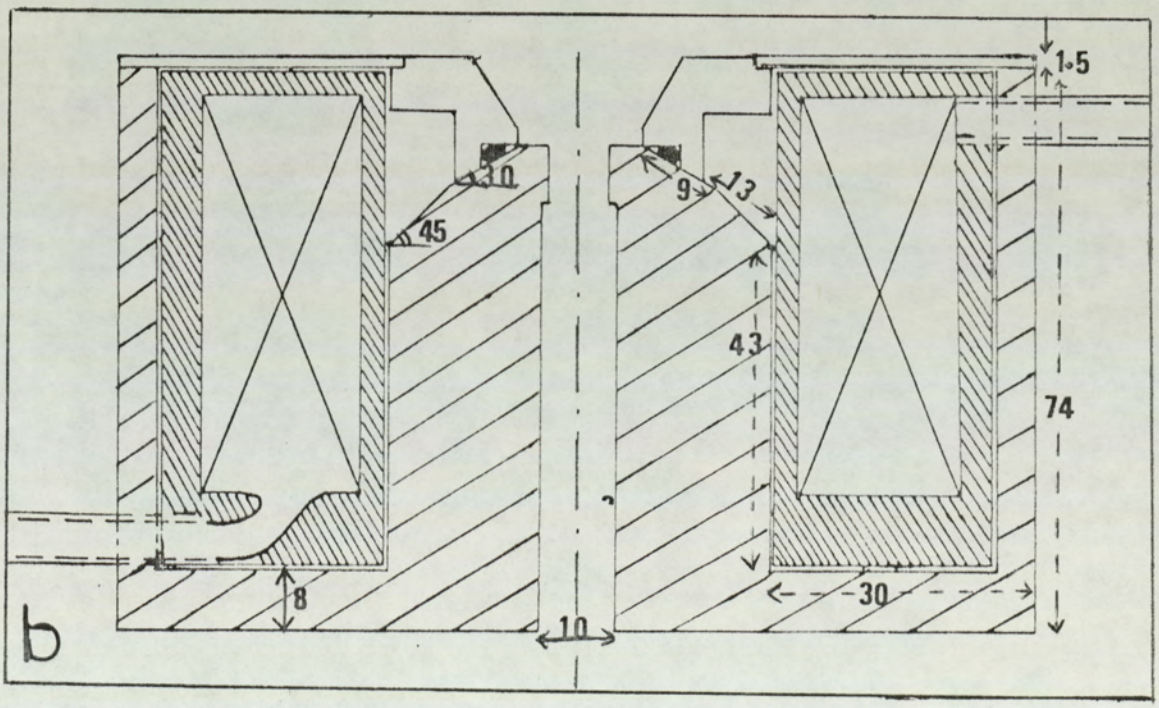

Fig. (3.19)(a) Field distribution and (b) Construction of an experimental corrector single pole-piece lens with an 8mm bore

which are found experimentally can be achieved by spherical pole piece lens with a radius of approximately 4mm.

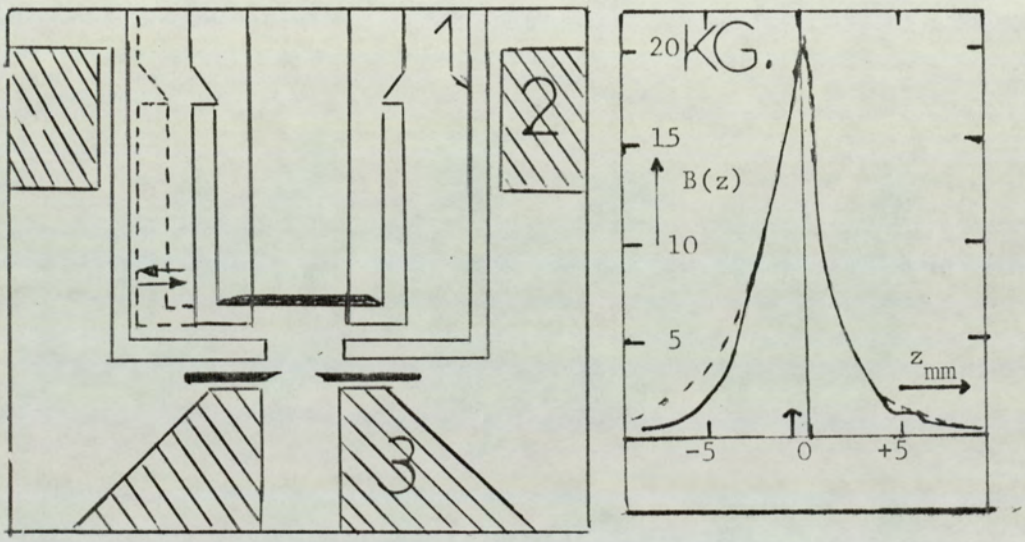

Fig. (3.20) (a) Schematic diagram of an asymmetrial objective lens (Shirota et al, 1977) showing (1) Anti-contamination trap (2) Upper pole-piece (3) Lower polepiece

(b) The axial field distribution measured by image rotation.(----Spherical field model)

3.4.4 Mini-X-ray single polepiece lens

An experimental lens that had been made in this department was slightly modified to meet the necessary requirements for using it for an X-ray source. The general cross-section is shown schematically in figure (3.22). This lens field distribution was the best check

for the validity of spherical model because the magnetic field distribution of this lens figure (3.23) was measured not only by Hall probe Gaussmeter and image rotation method (Christofides, 1978) but by the finite element method (Ferrier, 1978) as well.

Figure (3.24) shows some focal properties, and experimental points for object plane which are in good agreement with theoretical results of spherical model, noticing that this lens was operated with non-preferred direction.

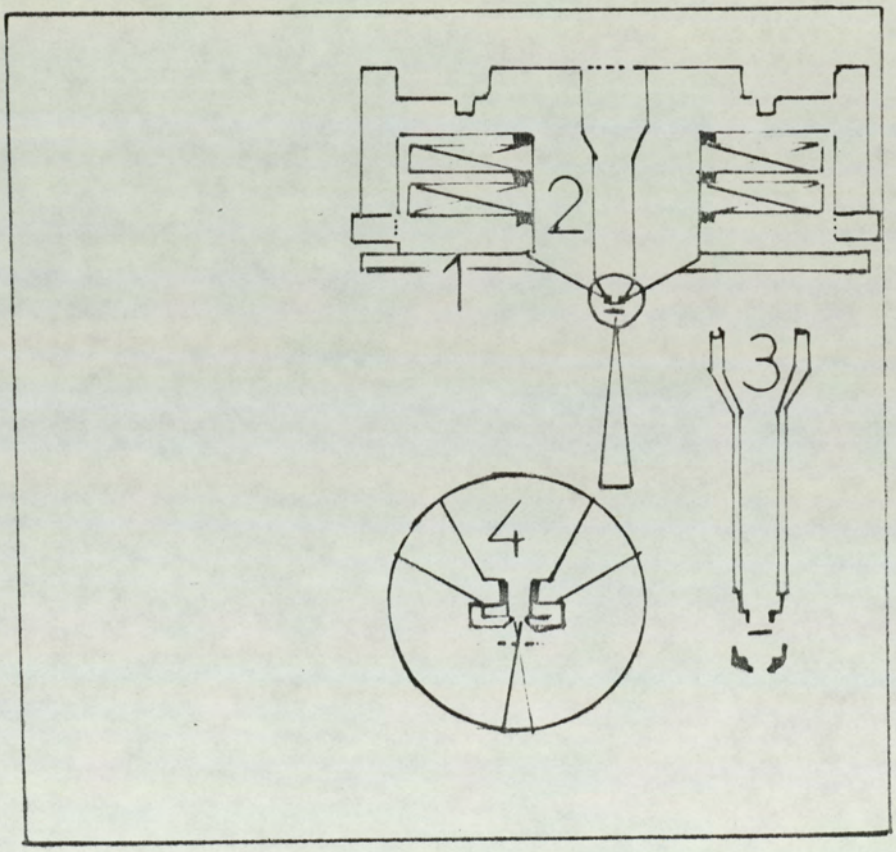

Fig. (3.22) Schematic cross-section of X-ray minilens. (Christofides, 1978) showing (1) Copper wire coil (119 turns) (2) Snout (3) Specimen holder (4) Aperture.

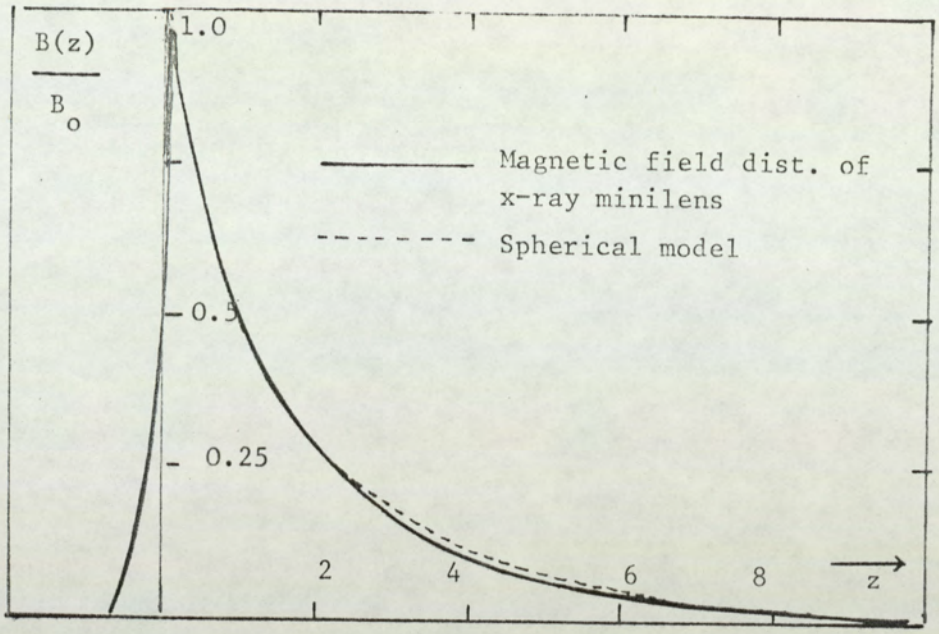

Fig. (3.23) The axial field distribution of mini X-ray lens compared with

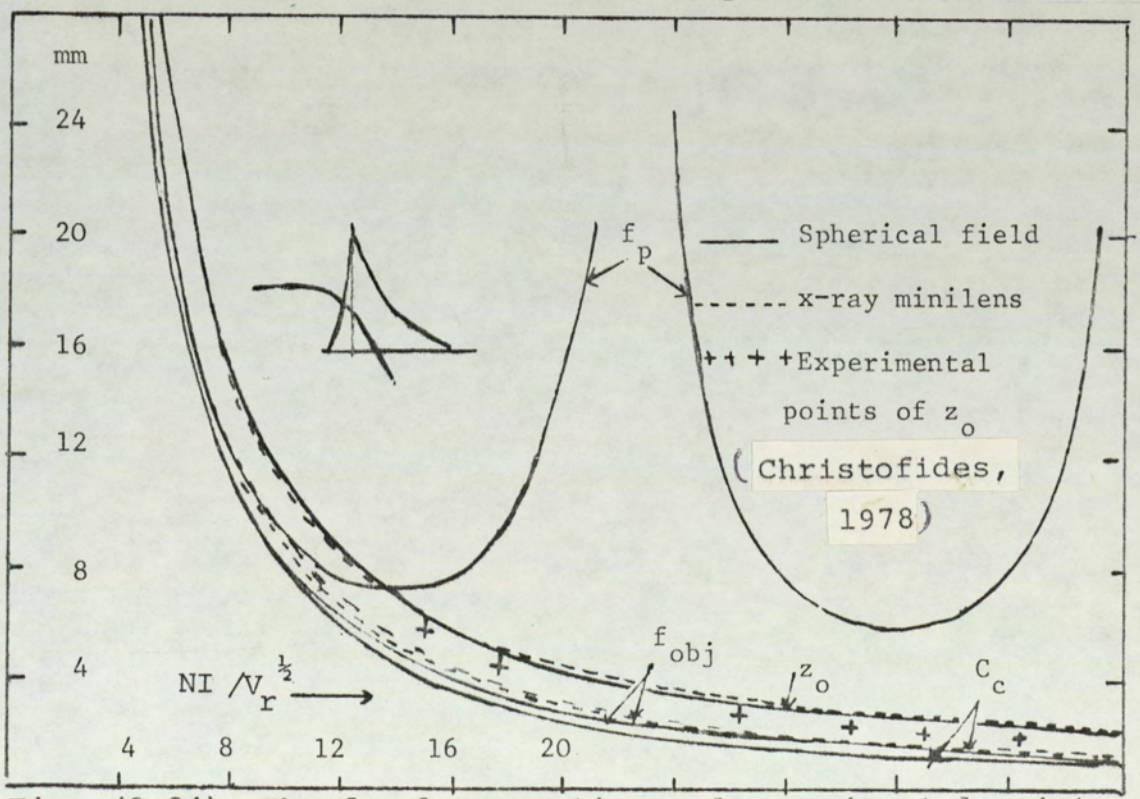

Fig. (3.24) The focal properties and experimental points of object plane for mini X-ray lens

3.4.5 Electron probe analysis superconducting lens

Another important example of asymmetric lens is the one designed by Dietrich et al (1977), in which the stray-field above the coil is responsible for the electron optical effect. A schematic diagram of the lens was shown in figure (3.25) while figure (3.26) shows its field distribution compared with the spherical field.

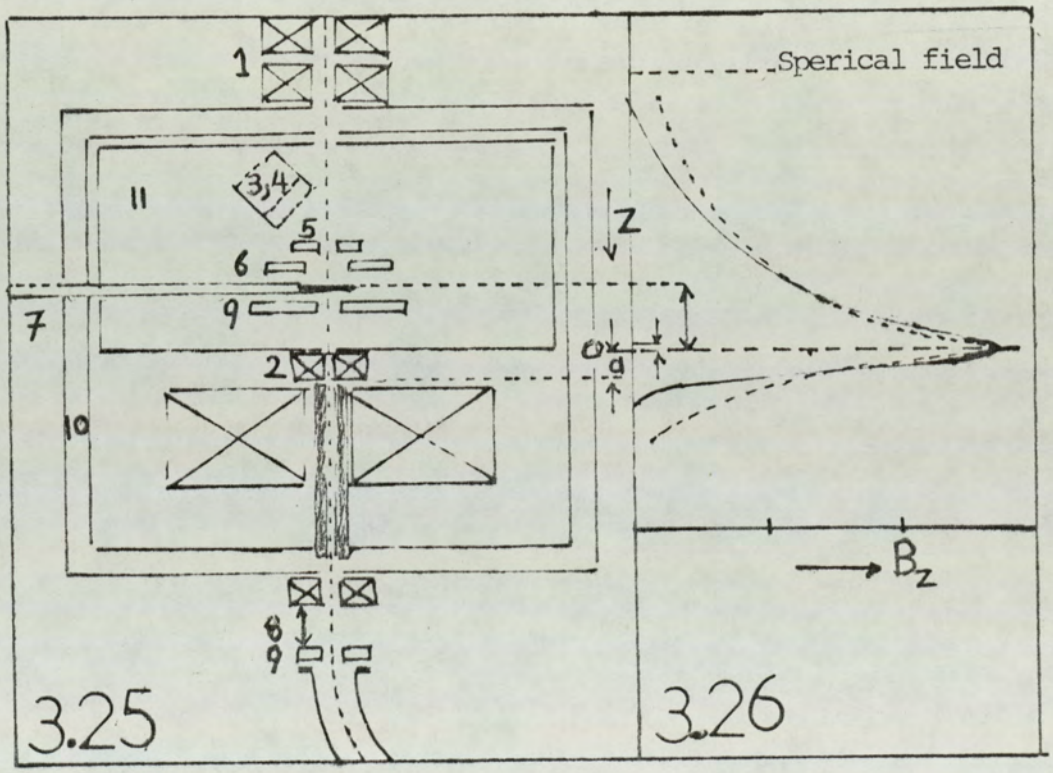

Fig. (3.25) Shielding lens for microprobe analysis 1 deflection systems for scanning mode; 2 stigmator; 3 detector for Auger electrons; 4 detector for secondary electrons; 5 detector for back scattered electrons; 6 SiLi-detector for energy dispersive X-ray analysis; 7 specimen holder (location for scanning mode); 8 further magnifying lenses; 9 detector for scattered electrons; 10 superconducting shielding; 11 vacuum chamber; 12 electron energy loss spectrometer; a distance between edge of shielding cylinder and zero position on z axis, defined by maximum induction B_0; z_1, z_2 abscissae for first and second crossover at 150 kV.

Fig. (3.26) Comparison of the axial field distribution of the superconducting lens of Dietrich et al (1977) and that of the spherical field.

It was noticed that the spherical field fits a part of this superconducting lens field, because the other part of the lens field is influenced by the presence of the shielding cylinder. The examination of this lens gives an idea of the wide range of applications of spherical lens; applications in probe analysis is certainly one of them. Finally, the results obtained from many lenses show that the spherical model appears to be the most appropriate model available for describing the focal properties for single pole lenses.

3.5 Peak Position in Single-Pole Lenses

One of the most important difficulties in theoretical studies for single pole lenses is that of determining the position of the peak axial field. This problem does not arise in symmetrical fields. It is, however, a serious one in asymmetric fields.

Liebmann (1955) found a relation between the position of maximum field with respect of lens bore (z_m/R_2) and the bore ratio (R_1/R_2). The present author examined the relation between the position of the peak with respect to the snout surface ($+z_m$) and the half width of the negative part of the asymmetric field distribution (d_2).

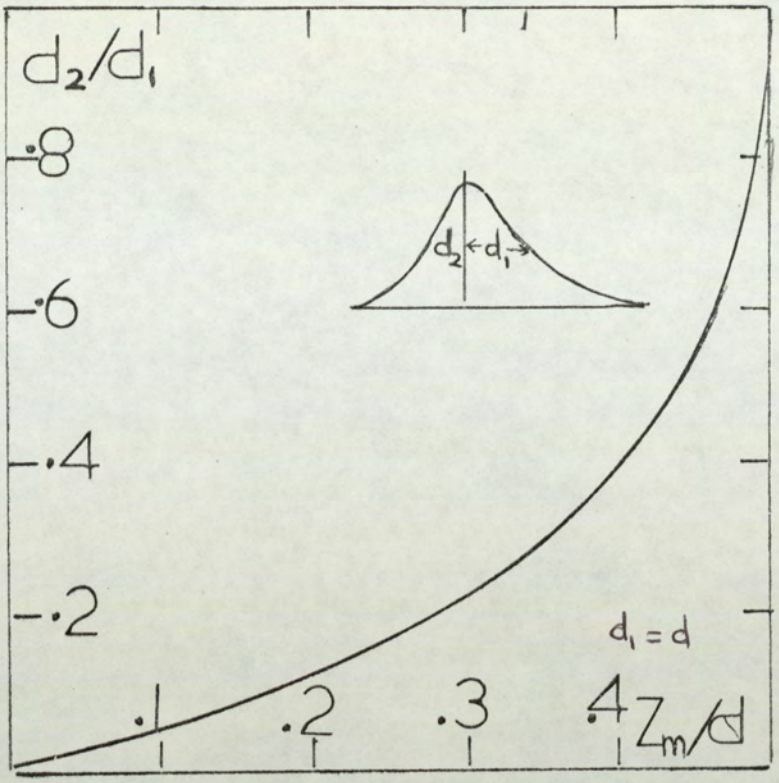

Fig. (3.27) The relationship between the relative peak position (z_m/d) and the field asymmetrical ratio d_2/d.

The result shows that a similar relation can be obtained using known field distributions for recently developed single pole lenses designed by various researchers in this laboratory. Those included various single pole lenses with different holes whose field distribution measured by Juma (1975).

Figure (3.27) was plotted for z_m/d versus d_2/d, where d is the original half-width. This curve can be used to determine the nagative part of the field distribution when experimental techniques are unavailable for that purpose. One of the useful applications of this method is that used by Juma and Alshwaikh (1979) for experimental single pole lenses.

4. MAGNETIC LENS ABERRATIONS

4.1 Methods of comparison between the magnetic lenses

The quality factor (Q) was introduced in Chapter 1. Equation (1.61) relates this factor to the distortion coefficient (D). However, on inspection, it becomes clear that this equation gives values for Q which do not have physical meanings. Thus when the distortion coefficient is negative, the quality factor should have a negative value. This does not always happen as the sign of f_{obj} may make the sign of Q opposite to that of (D). To get rid of this ambiguity, a further rearrangement of equation (1.61) was necessary. The new modified equation can be written as

$$Q = (\text{sign of } D) \left[f_p^2 . |D| \right]^{\frac{1}{2}} \quad \ldots\ldots \quad 4.1$$

This equation is efficient particularly in computation procedures.

In (4.1) f_p was introduced under the square root sign to become f_p^2 so as to make it always positive. Furthermore, the square root of the absolute value of D is taken for the same reason. To cater for the sign of D, we used (sign of D) outside the square root.

The equation 4.1 proposed to

$$Q = D \left[f_p^2 / |D| \right]^{\frac{1}{2}} \quad \ldots\ldots\ldots\ldots \quad 4.2$$

In 4.2 the same idea was used for f_p and D. The difference between (4.2) and (4.1) is that in the latter, modulus D was placed in the denominator and the square

root multiplied by D. This multiplication introduces D with its original sign. Thus in each case, Q takes the same sign as D.

One of the best examples is that for radial distortion, when the quality factor is positive the radial distortion is barrel while the negative means the pincushion distortion.

For most mathematical models, in actual fact, the parameters are calculated in the form, C_s/d, C_c/d, f_p/d, Z_o/d and f_{obj}/d. It is thus necessary to calculate $(B_o d/v_r^{\frac{1}{2}})$ in order to deduce the above sensitive indicators.

The parameter $(B_o d)$ can be found from the relation

$$B_o d = d_f \ \mu_o NI \quad \ldots\ldots\ldots \quad (4.3)$$

where d_f depends on the type of the field in question. If the Kanaya parameter (m_f) is used as an indicator of the type of field, then d_f is related to m_f as in fig.(3.11)

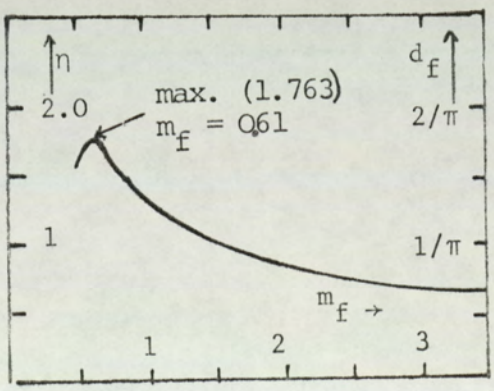

Fig.(4.1) The half-width function (d_f) as a function of the parameter (m_f)

It is worth noting that according to Kanaya's notation (Kanaya et al, 1976) d_f is (η/π). It takes the values 0.5 and 0.318 for square top field and Glaser Bell-shape.

4.2 Theoretical limits of performance of magnetic lenses

There are theoretical limits for focal properties and aberrations which actual lenses cannot reach.

The general expressions formulated by Kanaya et al (1976) were used in this work to find the theoretical limits. It may be helpful here to tabulate in table 4.1 some results which are used to calculate theoretical limits of some aberration coefficients.

Table 4.1

Character	Minimum value	$NI/V_r^{\frac{1}{2}}$	m_f	$d_f=B_o d/\mu_o NI$
fob_j/d	0.567	18.62	0.51	0.5612
f_p/d	0.956	18.62	0.62	0.56
C_c/d	0.414	18.62	0.62	0.56
C_s/d	0.291	33.5	∞	0.19
	0.394	18.62	0.61	0.5612

If the shape of the field distribution is fixed, essentially there will in reality be a minimum value of C_s and an optimum excitation assuming saturation lens is used to find the theoretical limit for C_s. The value of $[C_s f_p V^{-\frac{1}{2}} \times 10^{6} mTV^{-\frac{1}{2}}]$ according to table 4.1 is about 2.3375

while the same indicator was calculated by Moses (1972) as 2.338 and by Tretner (1959) as 2.225.

The chromatic sensitive indicator $C_c B_o V^{-\frac{1}{2}}$ in its theoretical limit takes the value 5.42×10^{-6} m.T.$V^{\frac{1}{2}}$ since the value d_f is 0.56 for the field with m_f = 0.62. This value of chromatic sensitive indicator is quite close to that reported by Mulvey and Wallington (1973) for the iron pole pieces lens in the case S/D = ∞. The corresponding value of spherical aberration C_s to this value is 0.394, lying at excitation 18.52 and giving the value of $(C_s B_o V^{-\frac{1}{2}})$ 5.173×10^{-6} m.T.$V^{-\frac{1}{2}}$. This value is just above 7% which is more than the value mentioned by Mulvey and Wallington (1973) for the lenses beyond the value of S/D = 2.

The theoretical limits of the focal length sensitive indicators $f_p B_o V^{-\frac{1}{2}}$ and $f_{obj} B_o V^{-\frac{1}{2}}$ are calculated in a similar way resulting in 12.52×10^{-6} m.T.$V^{-\frac{1}{2}}$ and 7.44×10^{-6} m.T.$V^{-\frac{1}{2}}$. The last parameter according to the paper mentioned above takes the value 6.75×10^{-6} m.T.$V^{-\frac{1}{2}}$ corresponding to the iron pole pieces lens with S/D=2. Kanaya et al (1976) reported that the best actual lens is the one which has a $(C_c B_o V^{-\frac{1}{2}})$ 5.4×10^{-6} m.T.$V^{-1/2}$ which is close to the value given by Mulvey and Wallington (1973) for the lens with S/D =∞. Kanaya's value is still 9% above the theoretical limit, while the same lens has a $C_s B_o V^{\frac{1}{2}}$ value of about 4.67×10^{-6} m.T.$V^{-1/2}$ which is not too far from the value of 4.8 for iron polepieces with S/D=2, a value which is well above the theoretical limit.

It is probable that one may reach a lower value of absolute spherical aberration parameter $C_s B_o V^{-\frac{1}{2}}$ than that mentioned above by using a thin coil having D_2/D_1=19 and a spherical single polepiece snout of small radius inside this

coil.

4.3 The problem of a magnetic field with infinite gradient $B'(z)$

The radial distortion (D_{rad}) and spherical aberration (C_s) coefficients are strongly dependent on the gradient of the magnetic field distribution when the ray incident at the steep edge as described in (§1.3.3). However, this problem arises especially for single polepiece lens models.

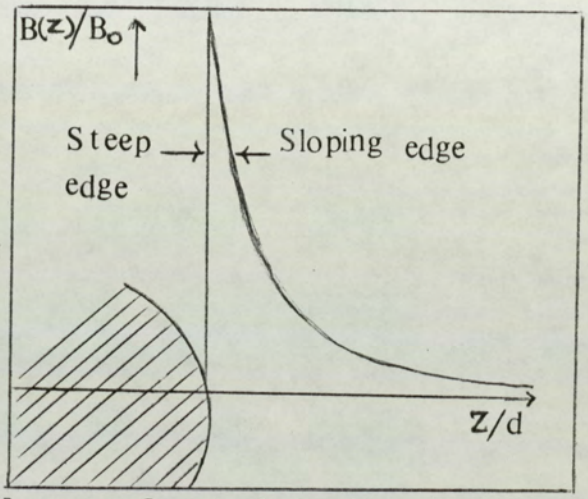

Fig. (4.2) The spherical field distribution showing two possible edges

An example of the problem confronted in this project is that of the spherical field Fig. (4.2). Fig. (4.3) shows that at the singular point z=0, there are two slopes, the first belonging to spherical field function and found analytically as

$$\left[\frac{dB(Z)}{dZ}\right]_{Z=0} = -0.78$$

as $[dB(Z)/dZ]$ at Z=0 equal to -0.78

While the other slope is infinite. This arises from the assumed vertical function f(x).

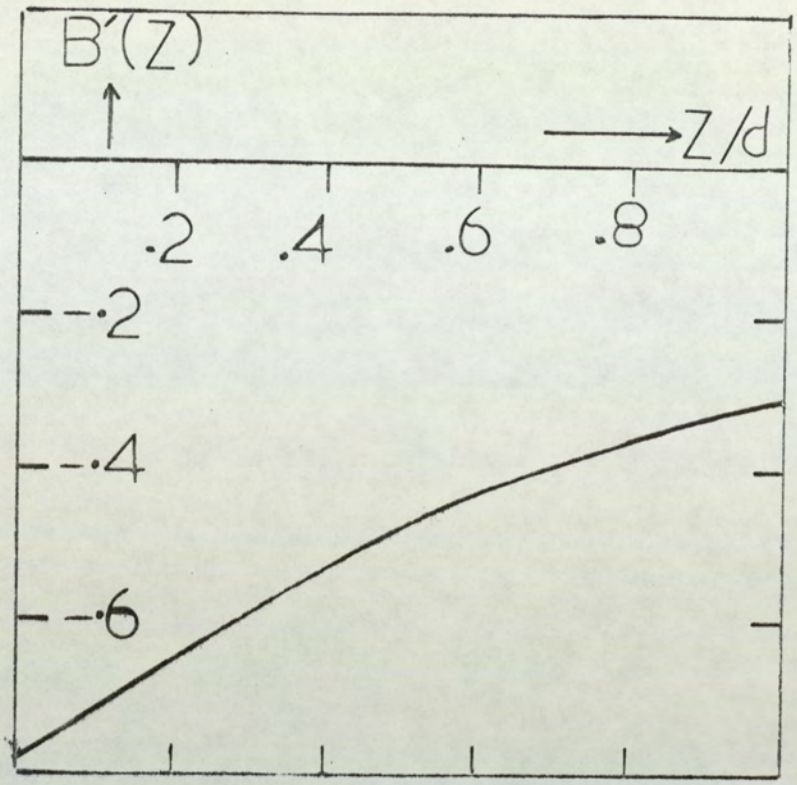

Fig. (4.3) Variation of axial field gradient B'(Z) as a function of Z for spherical field model.

To leave this point out of the numerical analysis would give a wrong result for C_s and D_{rad}. It is easy to check the results obtained by ignoring this point. One of the most significant methods of checking is to ensure that the sensitive aberration parameter $(C_s B_o V_r^{-\frac{1}{2}})$ obtained by ignoring the slope in the first step of the calculation for either the exponential or spherical field has passed the theoretical limit of the above indicator. There is also a great difference in the outcome of a calculation of C_s using this method as compared with that found from practical single pole lenses. (§4.5).

There are two possible methods of solving this problem. The first is used analytically, while the other is frequently used for numerical analysis.

The basis of first method is created by the generalization of the aberration coefficients, making the general formula dependent on a factor which is a function of the fields or B'(z). One example of this method is expressed in the discovery of Kanaya et al (1976). He found a general expression for the spherical aberration coefficient (C_s) in in terms of a parameter m_f, which can then be used to calculate (C_s) approximately for the square top field by making m_f approach 0.5. It is likely that (D_{rad}) for the same field can also be calculated using the same method. But it is a great conceptual error to calculate C_s for exact square top field as Kanaya et al did (1976) because they are in fact ignoring the field boundary.

The second method satisfactorily used by the author to solve the infinite slope problem is by replacing the infinite slope by a segment of a suitable function in the negative z-direction. This method is generally used in mathematics to solve problems in discontinuous functions.

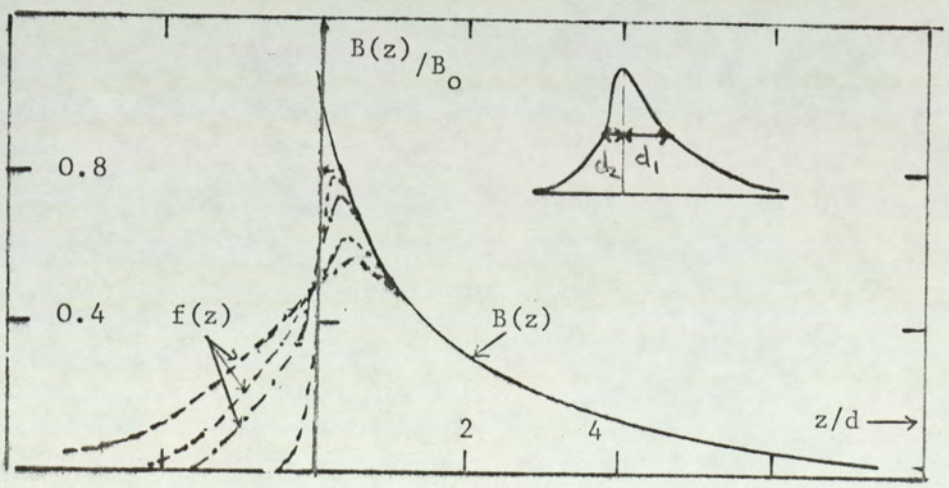

Fig. (4.4) A series of analytical functions representing the possible field distribution inside the lens snout

Certain conditions must be attached to the choice of function f(z) used in fig. (4.4); for example, the total area under the curve is constant, (constant excitation) and that the peak position is sited corresponding to the half-width (d_1) [§(3.7)] with both d_1 and d_2 as shown in Fig. (4.4).

At the position of maximum field, there are two slopes coming from two functions. To avoid this an auxiliary function with a slope equal to zero is used to connect the two functions. This also serves to make the final function closer to realistic asymmetric lenses. The great advantage in using this method for the spherical field is that it makes this field more realistic. This is because there are no real lens fields with sharp edges; in practice there is an axial field caused by the presence of the hole in the snout to the pole-piece.

The shape of the function f(x) strongly affects the values of C_s and D_{rad} when the ray incident from the steep edge of the field, so it is important to determine the function in the negative z-direction in any calculations for C_s and D_{rad} for single pole lenses.

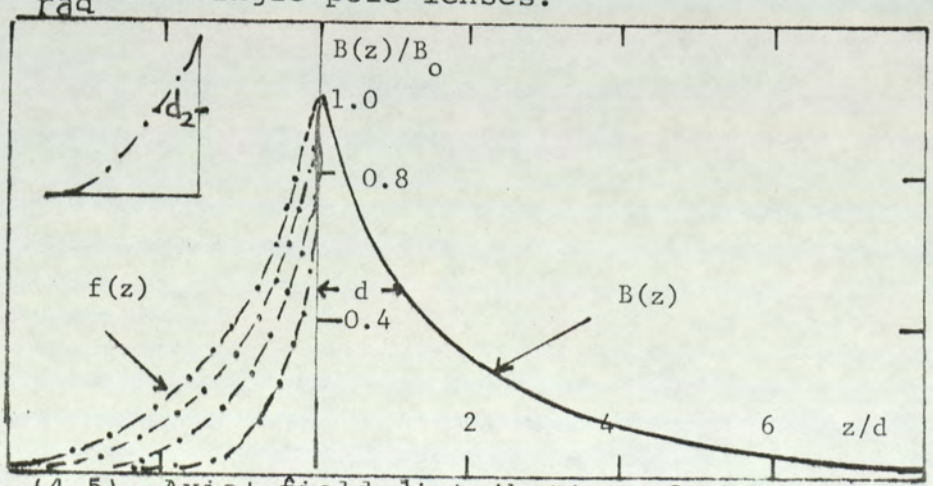

Fig. (4.5) Axial field distribution of the single polepiece incorporating analytical functions for negative Z-direction

In accordance with this, two auxillary functions are used to achieve the above aim. One of them is the Glaser Bell-shaped field with half width ($2d_2$); the spherical field with half-width (d_2) is also used.

Because this project is not primarily concerned with a study of the functions describing the field within the snout and its effect on aberrations, the present author modified the method mentioned above to solve this problem. The method used is to join the certain functions without changing the value or position of magnetic field peak as in fig. (4.5).

Fig. (4.6) shows D_{rad}/d for the spherical field in the positive z-direction using a series of Glaser Bell-shaped functions inside the snout with various values of the parameter q where q stands for the ratio d_1/d_2.
Fig. (4.7) also shows similar results which are

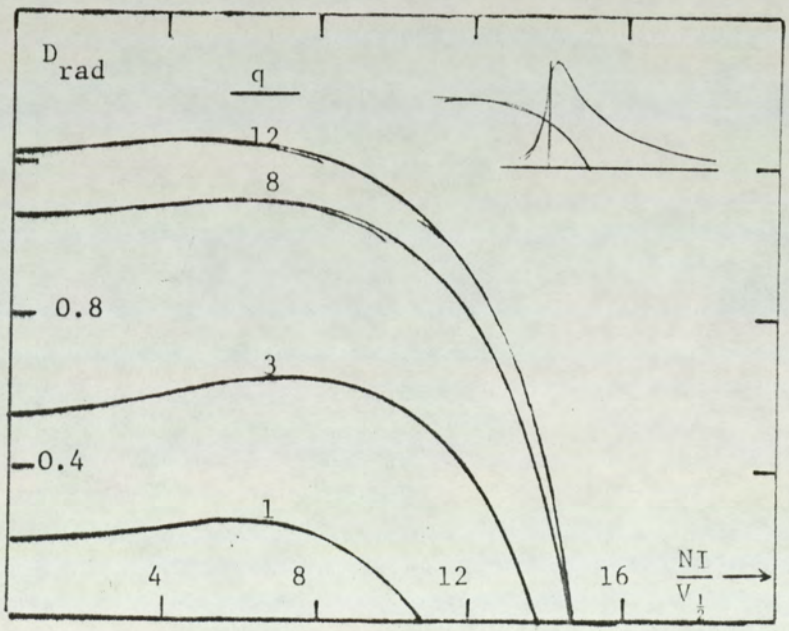

Fig. (4.6) Calculated radial distortion coefficient of the spherical field assuming a spherical field distribution inside the snout

obtained when using spherical function series for the function

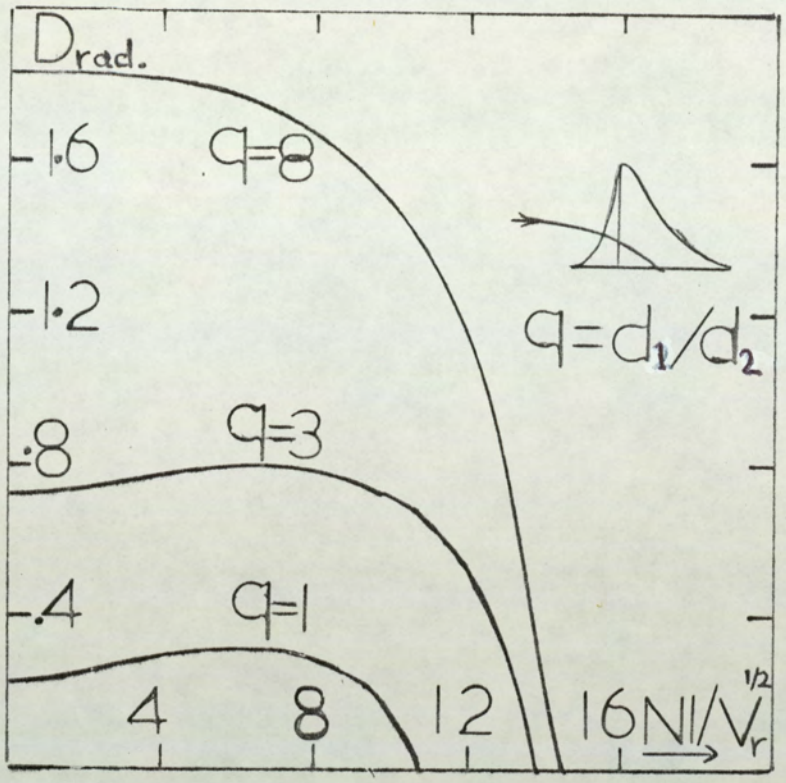

Fig. (4.7) Calculated radial distortion coefficient of the spherical field assuming a spherical field distribution inside the snout

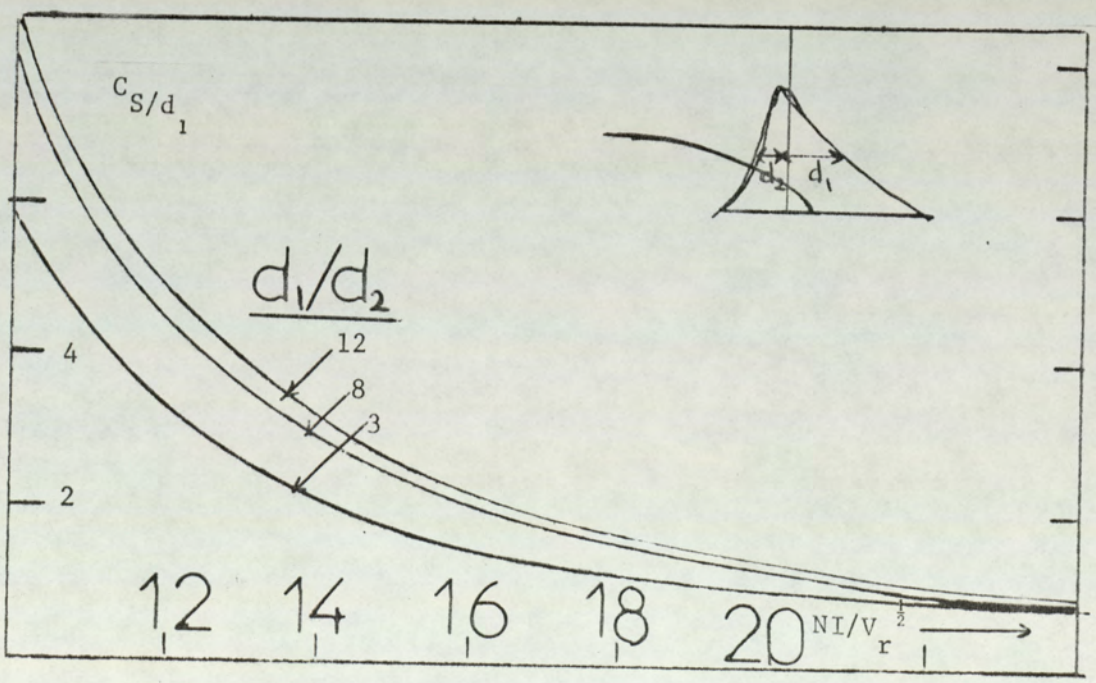

Fig. (4.8) Calculated spherical aberration coefficient C_s of the spherical field distribution assuming a spherical field distribution inside the snout

inside the snout. The general shape of D_{rad} confirms that the D_{rad} values depend upon the shape of the field distribution inside the single pole-piece snout.

The same method was used to find C_s for the spherical field model by adding a series of spherical fields of small half-width to represent the field inside the snout (fig.4.8).

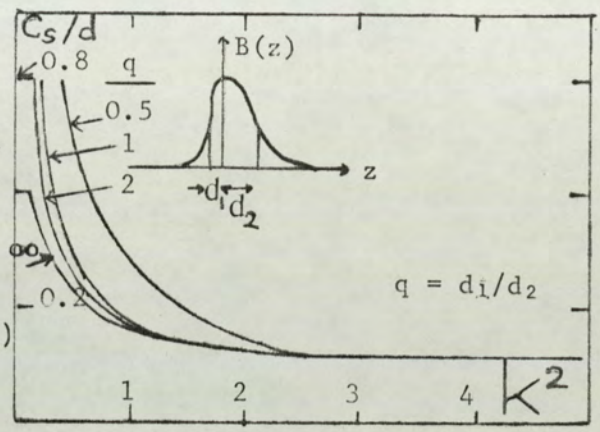

Fig.(4.9) Calculated spherical aberration coefficient C_s of a series of a symmetrical field distribution (Dosse,1941) $d = d_1 + d_2$

The general shape of the results for D_{rad} shows a close parallel with that found by Liebman (1952) for double pole lenses. A similar agreement for C_s was also obtained with that found by Dosse (1941) for asymmetrical lenses (fig.4.9).

Investigations of some experimental single-pole lenses show that they have an approximately spherical field inside the snout with q values between 1/4 and 1/7. So the numerical results for single-pole lenses aberrations using the addition of the above-mentioned functions is quite applicable.

4.4 Aberration of single pole lenses

It is impossible mathematically to correlate either a spherical or an exponential model with the general expression of Kanaya's model; it is therefore difficult to obtain the aberration coefficients for single pole lenses analytically. Consequently, most aberration coefficients are calculated numerically as described in Chapter 2.

4.4.1 Chromatic and Spherical aberrations of the spherical field

As the chromatic and spherical aberrations of a lens are closely related to the objective focal length (f_{obj}), of the spherical field will be directly proportional to the square root of the excitation parameter $NI/V_r^{\frac{1}{2}}$ (Alswaikh and Mulvey, 1977). This will occur when the ray is incident from the sloping side in the case of strong lenses (i.e. $NI/V_r^{\frac{1}{2}} \geq 15$).

When the ray is incident on the field in the other direction (i.e. onto the steep slope of the field), both C_c and C_s are approximately inversely proportional to the excitation parameter in the region $NI/NI_o < 1.0$. C_s strongly depends on the function inside the snout.

The coefficients C_c and C_s for the spherical field model were calculated numerically using Scherzer's formula (Scherzer, 1937) by means of a digital computer. The program used for this purpose was CABERATION which is described in chapter 2.

This showed that when the ray incident on the sloping part of the field, the minimum chromatic aberration coefficient (C_c) is equal to 0.96d (0.25a) and the minimum spherical aberration coefficient for the C_s is equal to 0.39d (0.1a) at an excitation parameter $NI/V_r^{\frac{1}{2}} = 15$. The C_s value of 0.1a is an especially low one for a magnetic lens.

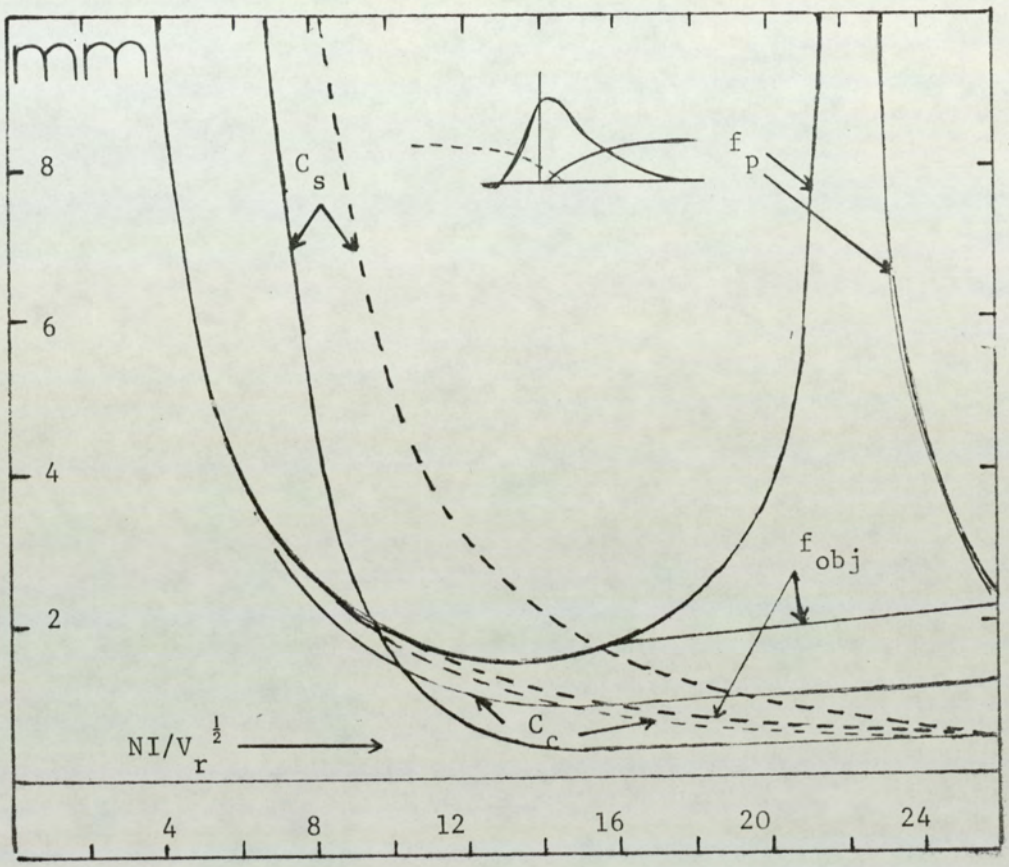

Fig. (4.10) Aberration coefficients of the spherical field as a function of the excitation parameter $NI/V_r^{\frac{1}{2}}$ for the two possible modes of operation

It is also clear that $C_{o/f_o} = 0.56$ and $C_s/f_o = 0.23$. These two coefficients corresponding to the excitation parameter are shown in fig. (4.10). Solid lines are used for the case when the ray is incident on the gradually sloping end of the field while the dotted lines are used in the same graph for other direction (i.e. the ray incident on negative z direction).

The chromatic and spherical parameters $C_s B_o V^{-\frac{1}{2}}$ and $C_c B_o V^{-\frac{1}{2}}$ take the values 9.47×10^{-6} m.T.V$^{-1/2}$ and 3.82×10^{-6} m.T.V$^{-1/2}$. The last indicator is 20% more than the best actual double

pole lenses. The parameter $\left[C_s B_o V^{-\frac{1}{2}} \ldots\right]$ for both spherical field and exponential may be shown for one direction of rays as in fig. (4.11).

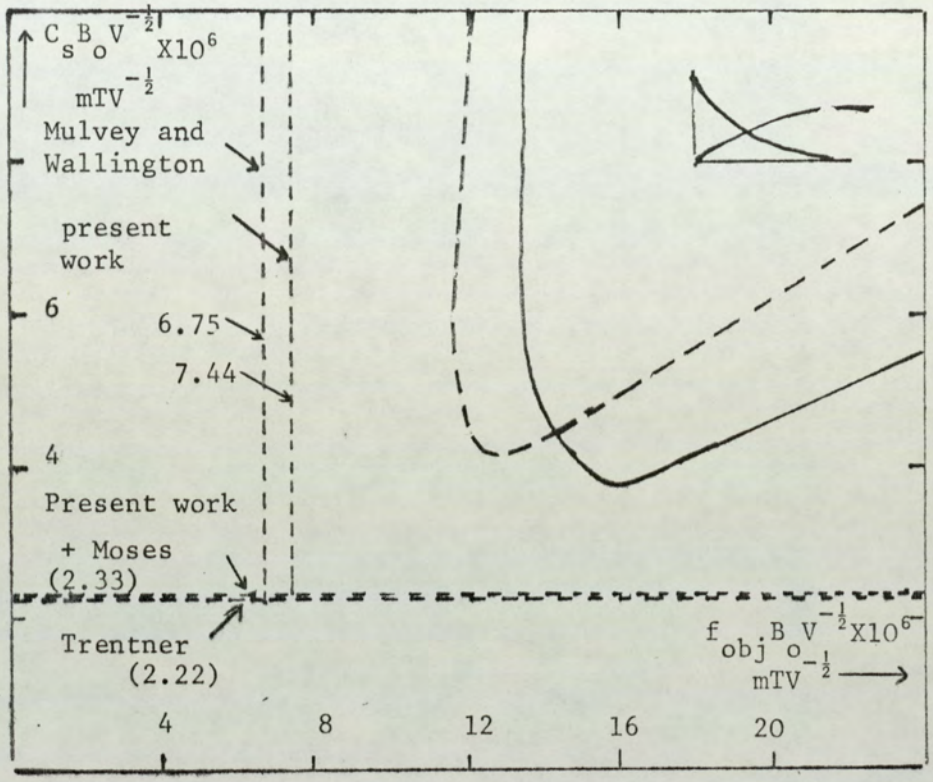

Fig. (4.11) Absolute spherical aberration parameter $C_s B_o V^{-\frac{1}{2}}$ for the spherical field (solid line) and the exponential field (dotted line).

It is noticeable from (4.10) that the coefficient C_c and C_s decrease as the excitation parameter increases for the field when the ray is incident on the steep edge. The preferred direction for C_c is when the rays' incident from the steep edge of the field. This direction gives a different value of C_s depending upon the shape of the function inside the snout.

The increase in C_c, C_s and f_{obj} in respect to $NI/V_r^{\frac{1}{2}}$ agrees with the characteristic properties observed in single pole lenses. It suggests that the spherical field

model is a remarkably realistic one.

Since both the exponential and spherical field models are relevant to single pole lenses, it may be useful to compare their properties from this point of view. A critical study shows that as well as there being no big difference in their general characteristics, they also yield a similar general asymmetric behaviour.

The spherical field model predicts that the objective focal length will be proportional to $(NI/V_r^{\frac{1}{2}})^{\frac{1}{2}}$ for an excitation parameter greater than that at minimum focal length (i.e. $NI/V_r^{\frac{1}{2}}=14$), while in the exponential field, the model predicts that it will be constant (Glaser, 1952 and Marai and Mulvey, 1974). The same trend occurs for those parameters such as C_s and C_c which are closely related to objective focal length. Figure (4.11) shows the properties in absolute terms for the exponential field and the spherical field. According to this, the spherical field has a lower spherical aberration, that is closer to the absolute minimum spherical aberration limit than is that of the exponential field.

4.4.2 Image distortion of single pole lenses

The determination of the distortion coefficients for the spherical field distribution has confirmed the general characteristics of the asymmetric field distributions previously referred to by Marai and Mulvey (1975).

The numerical method can also be used to calculate radial and spiral distortion coefficients by using program CDISTIORTION.

Fig. (4.12) shows the quantity $D_{sp}.d^2$ plotted with

respect to the excitation parameters NI/NI_o where NI_o is the excitation at minimum projector length. The figure shows the distortion coefficients when the beams entering either the steep edge of the field (dotted lines) or in the opposite direction (solid lines); note that the solid lines are always below the dotted ones. The curve of $D_{rad}d^2$ for the case when the ray is incident on the steep edge of the field (i.e. negative z-direction) was calculated by adding a spherical function with $q=d_2/d_1=4$ to represent the field inside the snout (cf§4.3).

At NI/NI_o in particular, D_{sp} for the first mentioned mode of operation is five times greater than the other mode.

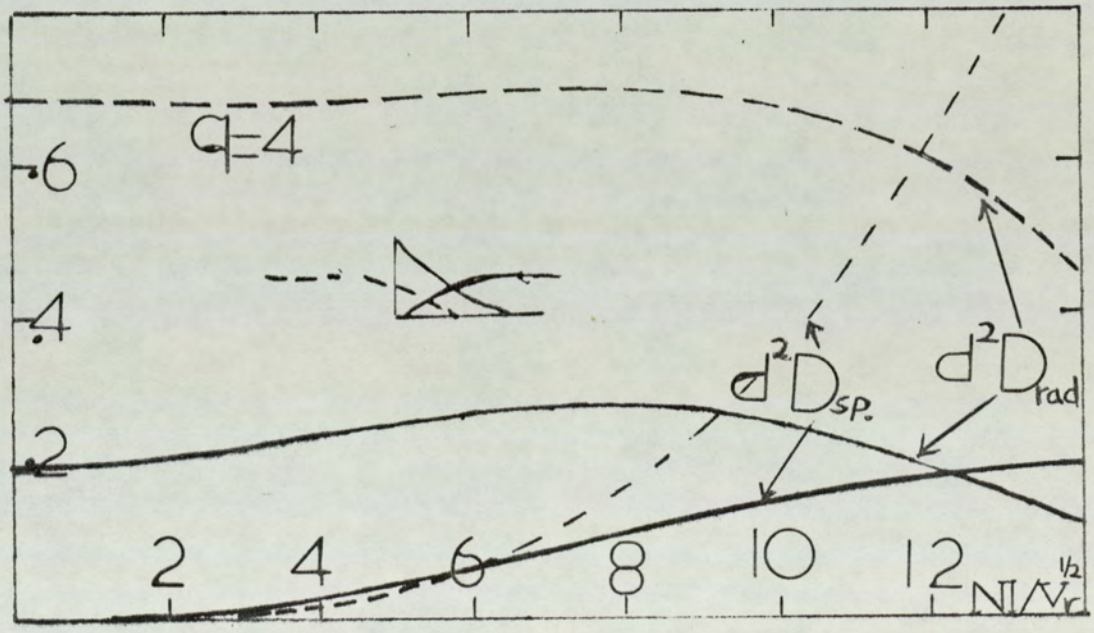

Fig. (4.12) The distortion coefficients D_{rad} and D_{sp} for the spherical field as a function of the excitation parameter $NI/V_r^{\frac{1}{2}}$ for the two possible modes of operation noticing that D_{rad} in both directions reach zero at $NI/V_r^{\frac{1}{2}} = 16$.

Fig. (4.12) also shows that the value of $D_{rad}d^2$ starts at 0.21 for an excitation parameter of $NI/V_r^{\frac{1}{2}} = 0$. For the positive direction of ray (i.e. the ray incident on the sloping side of the field). This starting value is similar to that of most double pole lenses.

In the case when the beam is incident at the steep edge the snout of the projector lens faces the fluorescent screen in TEM, while when the ray is incident on the sloping edge of the field (i.e. positive z-direction) the snout is facing the incoming parallel beam, in the projector lens of TEM.

The maximum value of $D_{rad}d^2$ when the beam comes from the positive side of z-direction is about 0.29 at $NI/V_r^{\frac{1}{2}} = 7$; it then falls steadily to zero at $NI/V_r^{\frac{1}{2}} = 16$. This coefficient also falls to zero at the same excitation parameter the beam travels in the opposite direction.

This shows that the radial distortion of this field when the snout faces the parallel incoming beam in TEM is always less than that for the beam entering the field in the opposite direction. This conclusion appears to be true for every asymmetric field so far encountered. It is clear that the lens is in its preferred mode of operation as projector when the ray incident on the sloping edge (i.e. the snout facing the incoming beam in the case of TEM).

Single pole lenses, however, whose axial field distribution can be described by the spherical field, should therefore have a lower distortion coefficient than those of the best double pole lenses. To represent this fact, fig. (4.13) has been plotted between Q_{sp} and Q_{rad} as a function of NI/NI_o.

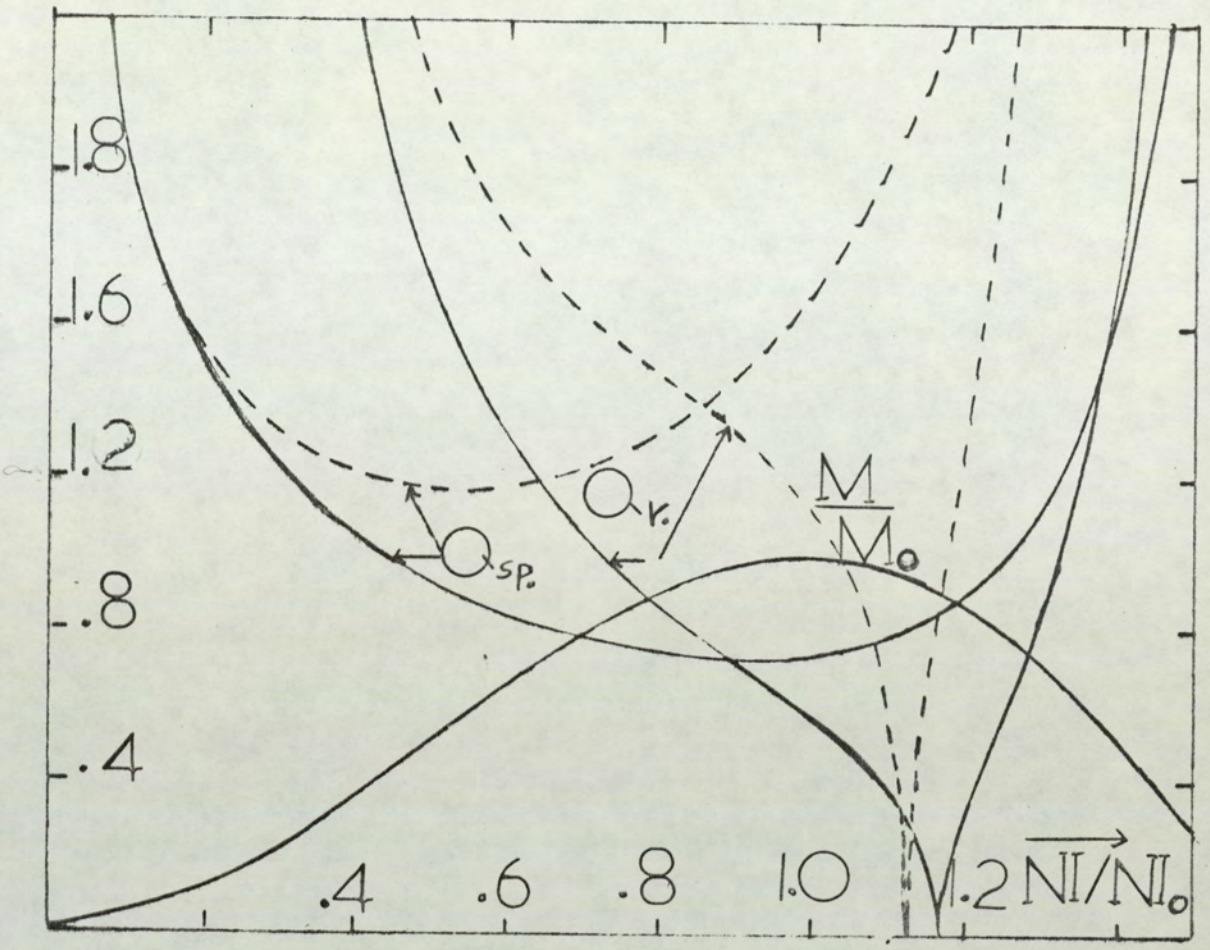

Fig. (4.13) Quality factor Q for image distortion in the spherical field model together with the relative image magnification M/M_o. Favourable orientation (full line), unfavourable (dotted line).

When the coefficient Q_{rad} passes through zero (i.e. $NI/NI_o \sim 1.0$) Q_{sp} is about 0.78, which is 30% less than that for conventional lenses. This shows strongly the advantage of using single pole lenses as projector lenses.

In addition to Q values in fig. (4.13) the relative magnification (M/M_o) is also plotted to give an overall view of the area of operation for the spherical field in its preferred direction.

It is important to remember that the main advantage of the spherical field is that it is a physically realisable magnetic field. All its characteristics can be related to the radius and flux density of a uniformly magnetized sphere of high permeability.

4.5 Aberrations of some experimental single pole lenses

The electron-optical properties of single pole lenses cannot be predicted from the data of the conventional lenses (Marai and Mulvey, 1974). From the previous statement one can conclude that if the effect of the coil on the axial field distribution of a single pole lens is small or takes a spherical function in shape, the total field of the lens will be approximately spherical in nature.

A single polepiece magnetic lens produces asymmetrical axial field distribution of distinctive shape. Thus there are two modes of operation according to the direction of the incident electron beam. The first (see Fig. 4.2) corresponds to a parallel beam entering the field from the sloping side of the field distribution (i.e. its snout facing the incoming parallel beam in the case of projector of TEM). The second corresponds to a parallel beam entering the steep slope of the field (i.e. with the snout facing the screen in the case of a projector of TEM).

The first mode of operation is the preferred direction for a projector lens because of its lower spiral distortion.

To investigate the aberrations of practical lenses several types of lenses were investigated as follows:

4.5.1 Single pole lenses with conical shape

The two lenses AR1 and AR2 have been described with their focal properties in §3.6.1 calculations of chromatic and spherical aberrations were carried out numerically. The results show that at the excitation for minimum focal length the ratio C_s/f_{obj} = 0.22 and C_c/f_{obj} = 0.55 for AR1 while that of AR2 for the same parameters are 0.237 and 0.567 respectively.

Comparison can then be made with the corresponding ratios for the spherical field distributions (i.e. C_s/f_{obj} = 0.235 and C_c/f_{obj} = 0.56). Fig. (3.17) shows the parameters of C_s and C_c with other focal properties corresponding to the excitation parameter $(NI/V_r^{\frac{1}{2}})$ in both modes of operation for AR 1 while fig. (3.18) shows the same phenomenon for AR 2.

The two figures demonstrate that the coefficients C_c and C_s increase slowly for excitation parameters greater than NI/NI_o = 1. These results confirm as in the case of spherical field model that minimum values of C_c and C_s and fp occurs at NI/NI_o=1.

A sensitive test for these lenses acting as objective lenses, figure (4.14) is plotted by using the parameters $C_s B_o V_r^{-\frac{1}{2}}$ and $f_{obj} B_o V_r^{\frac{1}{2}}$ as axis. From fig. (4.14) it will be seen that for AR1 the corresponding value is 3.6×10^{-6} m.T.$V^{-1/2}$ and for AR2 3.43×10^{-6} m.T.$V^{-1/2}$; these are lower values compared with that of double pole lenses (Mulvey and Wallington, 1973).

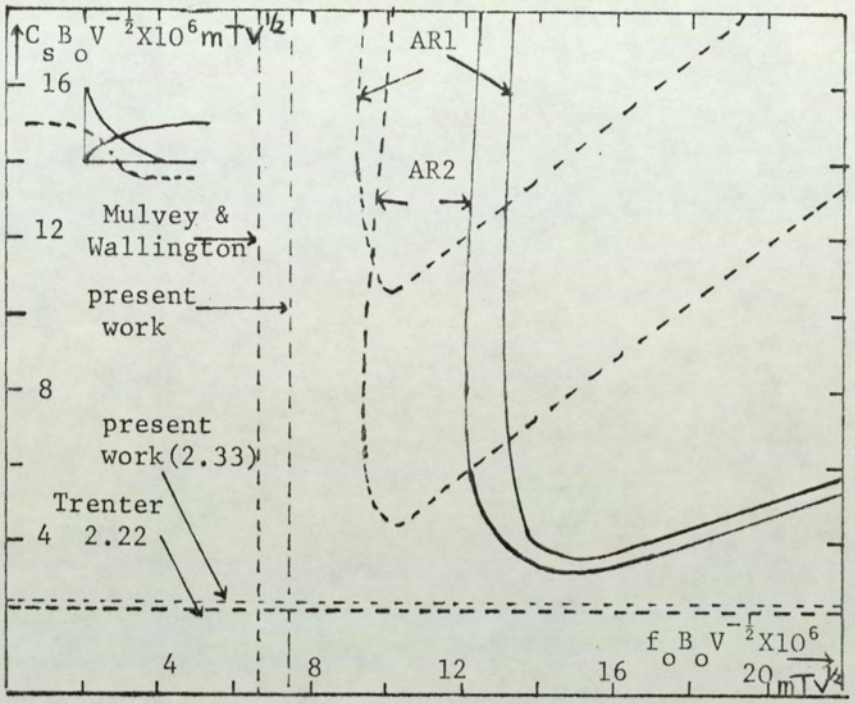

Fig. (4.14) The parameter $C_s B_o V^{-\frac{1}{2}}$ as a function of $f_o B_o V^{-\frac{1}{2}}$ for lenses AR1 and AR2

Numerical calculations were carried out to find the radial and spiral distortion coefficients for the two lenses. These two coefficients D_{rad} and D_{sp} can be related to Liebmann's (1952) coefficients D_d and C_{sp} of radial and spiral distortion respectively by the relations

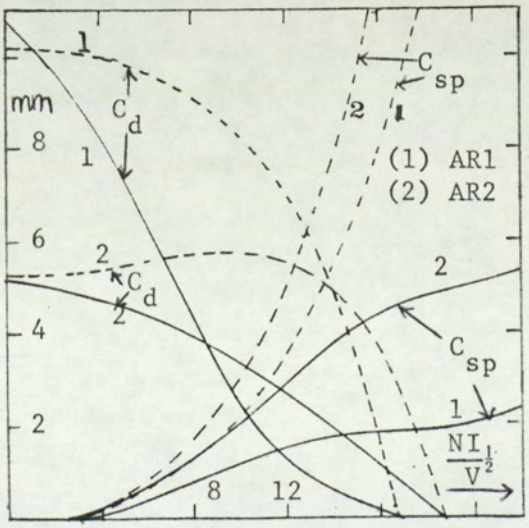

Fig.(4.15) The coefficients C_d and C_{sp} for lens AR1 and lens AR2 in the two possible beam directions

$C_d = D_{rad} \cdot R^2$ and $C_{sp} = D_{sp} \cdot R^2$ where R is the radius of the lens bore.

Fig. (4.15) shows the variations of the coefficients C_d and C_{sp} in both directions of the lens for the two lenses. From figure (4.15) it may be seen that C_d starts at a value, D_{do}=20.4 for AR1 and 10.4 for AR2. It decreases with increasing excitation and reaches zero at $NI/V_r^{-\frac{1}{2}}$ = 16.4 for AR1 and 18.6 for AR2. The same figure also shows the point of zero radial distortion, C_d= 0 occurs at an excitation NI/NI_o=1.1 (i.e. higher than that required for minimum focal length) The same figure shows that a considerable difference between the values of the radial and spiral distortion coefficients occurs in the two ways of operation.

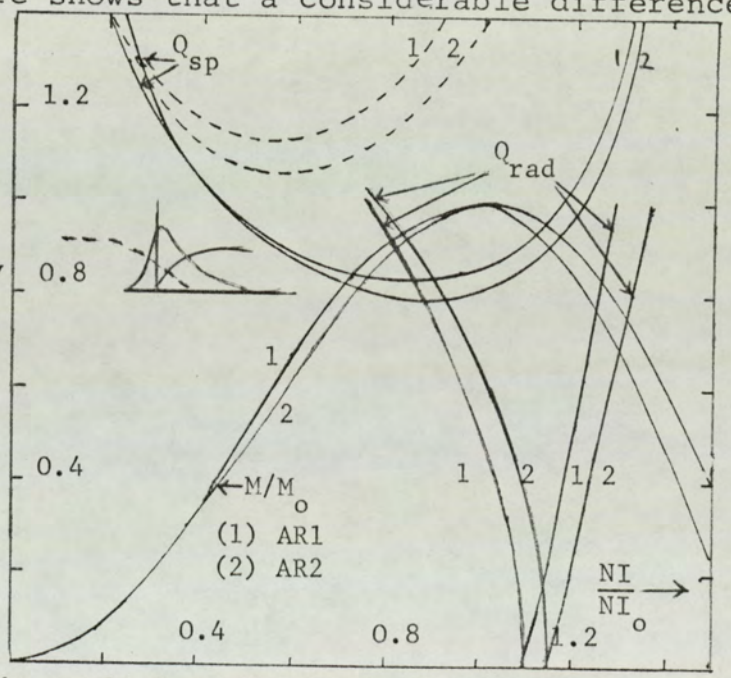

Fig.(4.16) The quality factors Q_{sp} and Q_{rad} for lens AR1 and lens AR2.

The distortion quality factors Q_{sp} and Q_{rad} for spiral distortion and radial distortion were also calculated for the two lenses in the two modes of operation as a function of the relative excitation parameter (M/M_o). The results are shown in fig. (4.16)

Typical results tabulated in table (4.2) enable one to make a comparison between the performance of experimental

single polepiece lenses and results calculated from various models.

Table 4.2

The lenses	C_s/f_o	C_c/f_o	$C_s B_o V_r^{-\frac{1}{2}} \times 10^5$	Q_{sp}(min)
Exponential field (Marai and Mulvey 1974)	0.315	0.632	4.2	0.78
Spherical field (Alshwaikh and Mulvey, 1977)	0.235	0.56	3.8	0.738
AR1 (§4.5.1)	0.22	0.55	3.6	0.8
AR2 (§4.5.1)	0.237	0.567	3.43	0.84
Experimental pole lens (Juma and Alshwaikh)	0.25	0.6	3.4	0.84
Double pole lenses (Mulvey and Wallington, 1973)			4.8	1.0

It is noticeable that from Table 4.2 the spherical field model gives C_s/f_o 25% and C_c/f_o 8% less than that for exponential field.

4.5.2 Experimental Single-pole lens

The experimental single pole 100 KV miniature lens designed by Juma (1975) is of importance here because some of the expected low aberrations have been proved experimentally as a projector lens in an AEI EM6 electron microscope. This lens was constructed by removing one pole from the 100KV miniature double polepiece projector lens (fig. 4.17).

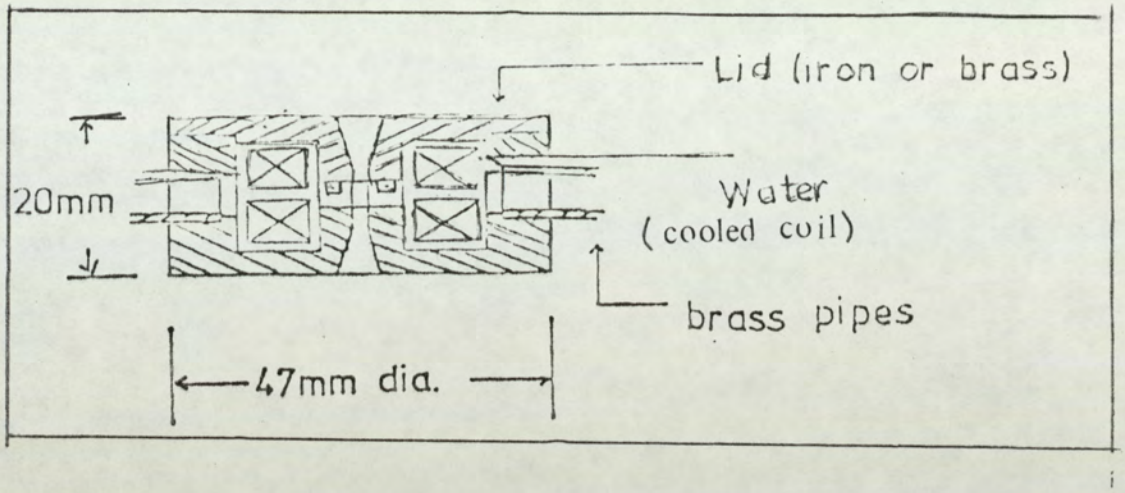

Fig. (4.17) Cross-section of the 100KV miniature double polepiece lens.

The cross-sectional diagram of the single polepiece lens, description of its materials, method of cooling and finding of the field distribution are described in more detail by Juma and Alshwaikh (1979) (Appendix 8).

This lens was tested under the microscope at 75KV for both directions to the electron beam. The imaging properties of the lens were recorded in both orientations at a constant projection distance (300mm) between the polepiece tip and the photographic plate. In both orientations the lens magnification is therefore the same since the projector focal length at a given excitation is the same.

The distortion in the final image is due chiefly to the distortion of this lens, since the contribution of the intermediate lens is negligible.

The projector focal length for the single and double pole lenses found experimentally are plotted in fig. (4.18) together with the computed results found by the program

DDISTORTION (Chapter 2) by using the measured field distribution.

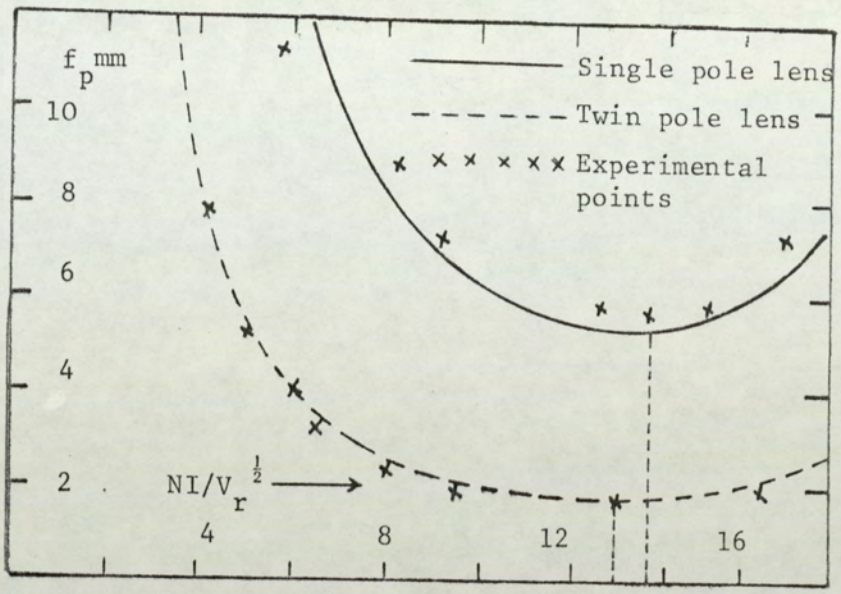

Fig. (4.18) Calculated and experimentally determined projector focal length for miniature single and double pole lenses described by Juma(1975)

Fig. (4.19) shows the variation of C_d and C_{sp} as a function of $NI/V_r^{\frac{1}{2}}$ for the two modes of operation.

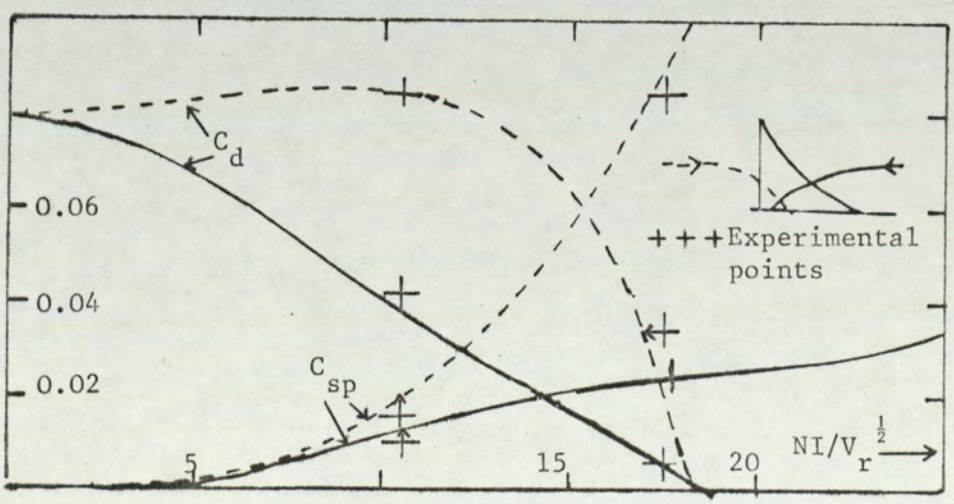

Fig. (4.19) Comparison of calculated and experimental values of D_d and C_{sp} as a function of the excitation parameter $NI/V_r^{\frac{1}{2}}$ for a single pole lens.

These coefficients are closely related to the corresponding coefficients for double pole lenses in the case of non-preferred direction (i.e. the snout facing the fluorescent screen in the case of TEM). For the preferred direction, the coefficient C_d decreases continuously with increase in excitation parameter. As for the C_{sp} coefficient it increases very slowly where at minimum projector focal length the value of C_{sp} is about twice that of C_d which is well accepted in microscopy. The computed results are plotted in the same curve and there is very good agreement between experimental and computed results.

Comparing the results in the two directions it is again confirmed that the most favourable arrangement for low distortion is that of the first direction (i.e. the pole-piece facing the incoming parallel electron beam (Marai and Mulvey, 1975).

At higher excitations, the C_{sp} coefficient of the lens operated by the second mode increases sharply, while in the opposite direction, this coefficient is slowly increased with noticeable fluctuation from $NI/V_r^{\frac{1}{2}}$= 12 to 18. The results in general are similar to that for the spherical field model.

The focal properties of the experimental lens as an objective lens were computed; the results showed that C_c=3mm at maximum magnification (i.e. $NI/V_r^{\frac{1}{2}}$=14).

The relative results corresponding to (f_o) are tabulated for comparison in table 4.2. The above-mentioned value of C_c is when the ray is incident in the steep edge of the field distribution (first mode of operation). The value of

C_s for this direction will be discussed by Juma and Alshwaikh (1979) (Appendix 8)

The performance figures of this experimental single pole-piece lens may be applied directly to the design of objective and projector lenses of high resolution microscopy. This can be done, by scaling the dimensions of this accordingly. It seems feasible to design electron-optical columns for 1MV with dimensions comparable to those of present conventional 100KV instruments.

4.5.3 Particular investigations for various single pole lenses

The previous discussion shows that many single-polepiece lenses have properties corresponding to that of spherical field model. However, to avoid repetition it may be sufficient to select a typical single pole lens from those that have been used successfully in practice by members of electron-optics group in the Physics department.

(a) The 100KV objective lens described by Marai and Mulvey (1974) has been studied in detail by Marai (1977). At the time it was considered that this lens was in very good agreement with the prediction of the exponential model but it now appears that the spherical field model gives an even closer approximation. One of the characteristics which illustrates this point is shown in the curve of Fig. (4.20) which shows the quality factor (Q) as a function of NI/NI_o.

(b) The chromatic and spherical aberrations of the x-ray minilens described in §2.5 were calculated by the present author and by Professor R.P. Ferrier who used Munro's method (Munro, 1972).

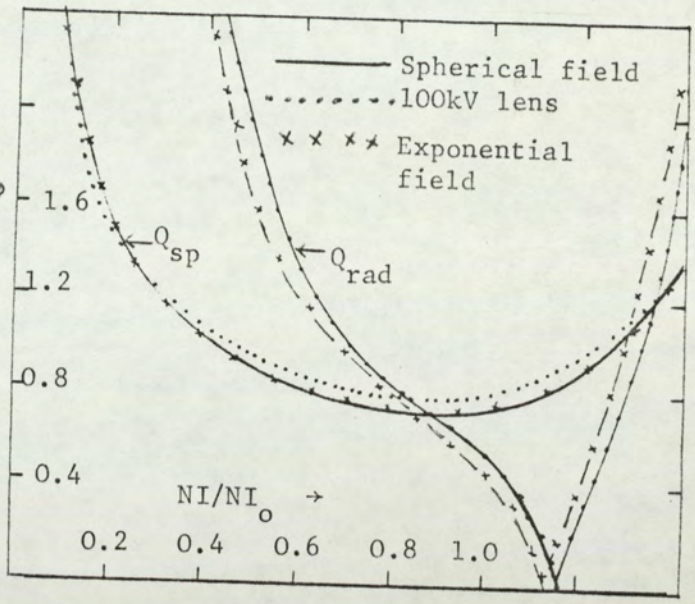

Fig. (4.20) The quality factor Q as a function of relative excitation NI/NI_o for a 100KV single-pole objective lens.

The results (fig. 4.21) show excellent agreement between two calculations for C_c, but there is about 10% difference in calculation of C_s. The reason is to be found in (a). Differences in the experimentally measured and calculated axial field distributions, and (b) some doubt in the Munro calculation about the exact number of ampere-turns enclosed by the field. These factors are discussed by Juma and Alshwaikh (1979). The figure also shows some experimental points of C_s measured by Christofides (1979) and these points are denoted as crosses. The parameter $C_s B_o V^{-\frac{1}{2}}$ for the preferred direction is shown in fig. (4.22). The minimum parameter ($C_s B_o V^{-\frac{1}{2}}$) of this lens is 3.7mmmT$V^{-\frac{1}{2}}$ which is an encouragingly small value. Fig. (4.23) shows C_c and C_s for the lens in both directions.

(c) Another practical lens successfully tested in the high voltage electron microscope is the 1MV lens described by Mulvey and Newman (1973).

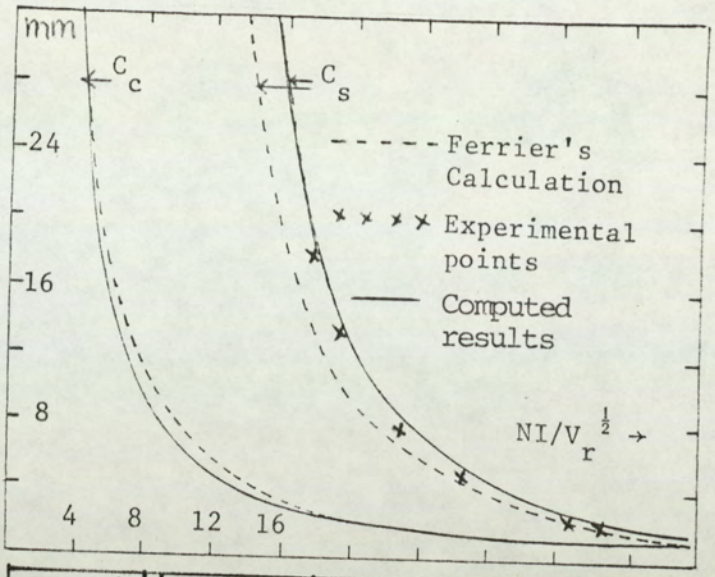

Fig. (4.21) Comparison of the chromatic (C_c) and spherical abberation of mini X-ray lens calculated by the finite element method and from experimentally measured field distribution

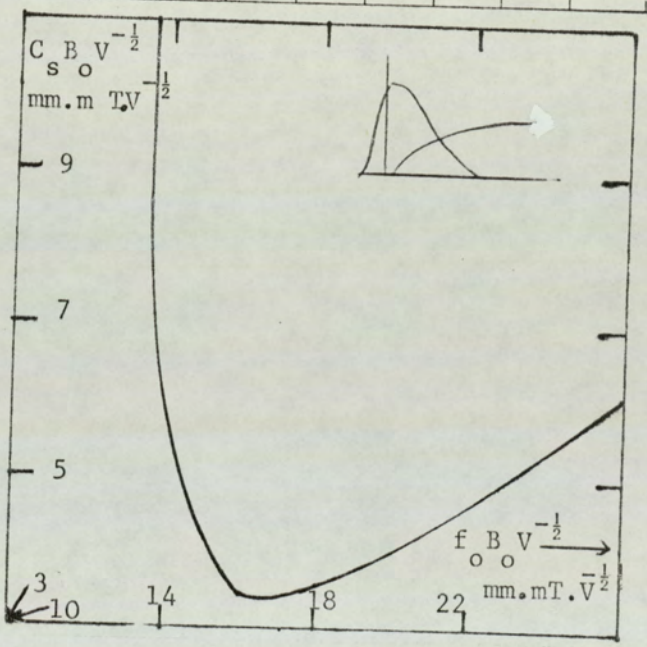

Fig.(4.22) The parameter $C_s B_o V^{-\frac{1}{2}}$ as a function of $f_o B_o V^{-\frac{1}{2}}$ for an experimental x-ray minilens

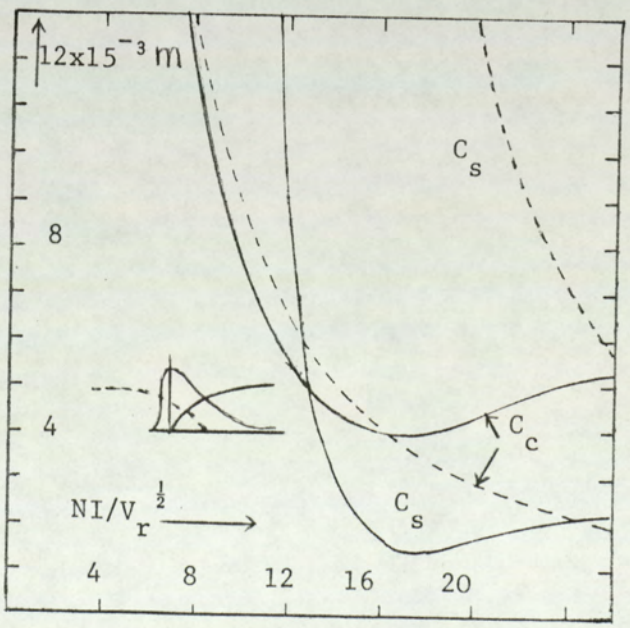

Fig. (4.23) The calculated values of the parameters C_c and C_s for experimental x-ray minilens in the two possible ray directions

The electron optical properties of this lens were found numerically by Marai (1977) by using measured and calculated field distributions, and it was studied before experimentally by Newman (1975). Some of the selected properties are that of C_c, C_s, f_p and f_{obj} which are used in fig. (4.24) to compare it with the similar parameters of the spherical field.

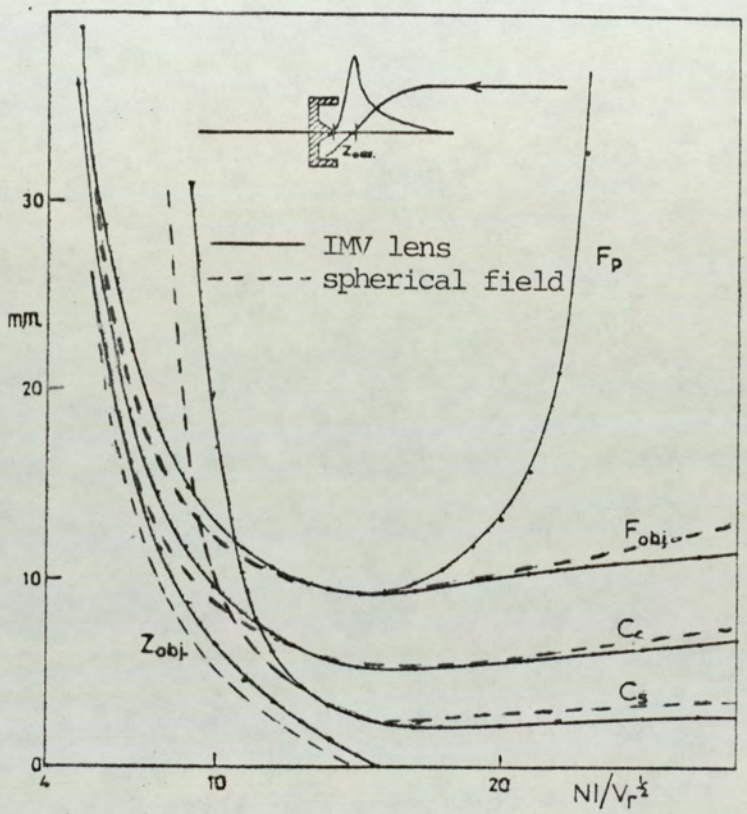

Fig. (4.24) Comparison of the focal properties of a 1MV single-pole calculated by an integral element method (Trowbridge et al, 1972) and those calculated from the spherical field model (dotted line). The equivalent sphere (a) = 2.16cm.

(d) There are two single pole lenses described by Juma (1975) and tested under EM6. One of them is a projector single pole lens with 8mm bore and the other is an objective lens. The present author chose the experimental points of the projector to compare its focal length with that of

spherical field in fig. (4.25). The parameters of C_c and C_s were selected from the objective lens characteristics (Juma 1975) to compare with those parameters of spherical field found numerically (fig. 4.26).

The results of all single pole lenses discussed in this chapter confirmed the conclusion found by spherical model.

In both cases C_d and C_{sp} are lower for the first mode of operation (i.e. the snout facing the parallel incoming beam). The lens performance is better than that of a conventional lens in the first mode but worse than that of a conventional lens in the second mode.

The C_d value for both modes of operation starts at the same point (i.e. $NI/V_r^{\frac{1}{2}} = 0$) when there is a smooth segment of field at negative z-direction.

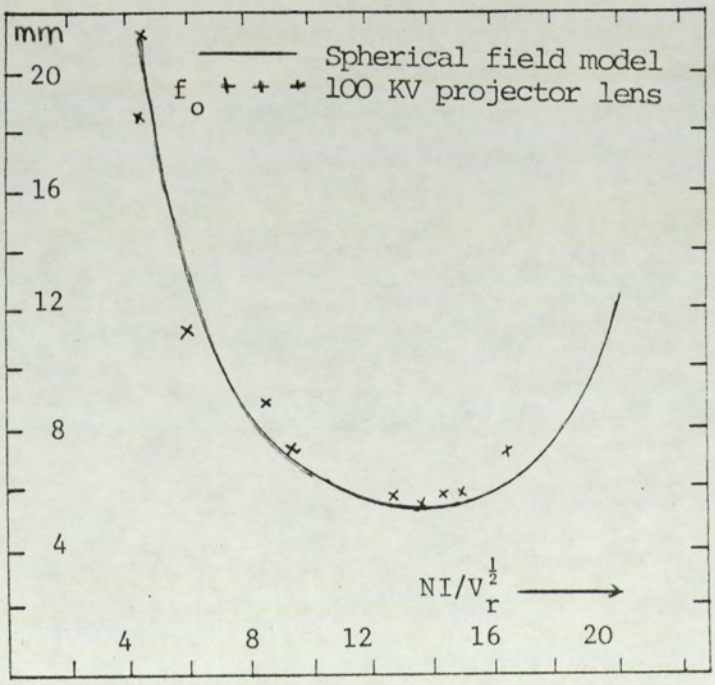

Fig. (4.25) Experimentally determined projector focal length of a single pole lens compared with that calculated from the spherical field model

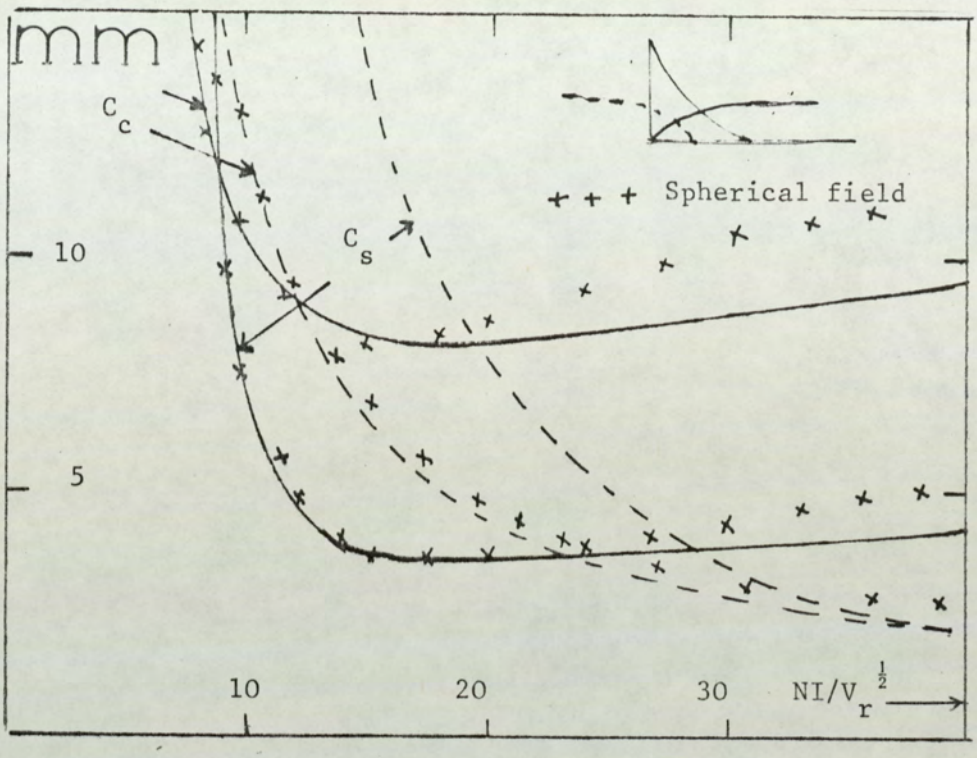

Fig. (4.26) Aberration coefficients C_c and C_s for a single pole lens with 8mm bore compared with those calculated from the spherical field model.

The general shape of spiral distortion was that there is a sinusoidal fluctuation thus proving the idea discussed later in Chapter 7.

The results obtained from single pole lenses have a quality factor smaller than that of double pole lenses.

The general results found from those experimental lenses provides a strong argument that single pole lenses in the first mode of operation are the preferred lenses as projector, while the other mode of operation is preferred as objective lens of low chromatic aberration.

Comparison between the lenses which have different geometry of the snouts shows there is a large difference in radial distortion. One can then conclude that the radial distortion and spherical aberration are strongly affected by the fields shape inside the snout.

Finally, the calculation of spherical aberration and radial distortion coefficients for practical lenses are very important since it depends on the slope B'(z) of the field distribution. The agreement between the results of both spherical aberrations and radial distortion calculated from such lenses and that of spherical field strongly supports the idea explained in section §4.3, that it is necessary to join a segment of realistic field in negative z-direction to represent the field inside the snout to obtain a correct result for the coefficients which depend on second derivative of axial field distribution.

Numerical analysis using the spherical field model and various real lenses has shown that single pole lenses based on the magnetized sphere should be used as objective with the ray incident on the sloping edge of the field for lower spherical aberration. This mode of operation has the advantage that both spherical and chromatic aberration coefficients, as well as the objective focal length, have their lowest values at the same excitation parameter ($NI/V_r^{\frac{1}{2}} = 14$).

For example, if a magnetized sphere of 10mm diameter is used, it would have C_c and C_s values of 1.3mm and 0.5mm respectively and occurs at $NI/V_r^{\frac{1}{2}}=15$. So the single pole lens with spherical snout is recommended as objective lens.

It has an appreciably lower spherical aberration parameter ($C_s B_m V_r^{-\frac{1}{2}}$) of 3.8 X 10^{-6} mTV$^{-\frac{1}{2}}$, while for the best double-pole objective lens is about 4.8 X 10^{-6} mTV$^{-\frac{1}{2}}$ (Mulvey and Wallington 1973). In addition, more space can be gained in the specimen region without an appreciable loss of resolving power (Mulvey, 1974) which is not the case in double polepiece lens.

When the ray is incident on the steep edge of the field, the single polepiece lens has a low chromatic aberration coefficient C_c, while the spherical parameter $C_s B_o V^{-\frac{1}{2}}$ is high depending on the magnitude of the slope of the field inside the snout. Since C_s depends on the magnetic field inside the snout, one experimental field distribution was investigated to see if lower values of C_s could be obtained together with acceptable low values of C_c. This lens was studied in detail by Juma and Alshwaikh (Appendix 8).

More investigations are required to study the possible use of the single polepiece lens, as an objective, with the ray incident on the steep edge of the axial magnetic field distribution, in order to give small values of both C_c and C_s.

5. CHROMATIC CHANGE IN MAGNIFICATION AND ROTATION

5.1 General expressions of chromatic change coefficients

The literature survey and fundamental equations are in Chapter 1. Some extended work done here to obtain the universal curve for chromatic changes in magnification and in rotation for double polepiece lens and then to study similar characteristics for single polepiece lens. Equation (1.70) is the general form of the chromatic change in magnification (C_m). Since lens current can usually be stabilized adequately it is permissible to neglect the term dI/I. The equation (1.70) reduces to the form

$$C_m = (\Delta r_m/r)/(\Delta V/V) \quad \ldots\ldots\ldots \quad (5.1)$$

In general for any lens is related to K as

$$K = \text{constant} \cdot V^{-\frac{1}{2}} \quad \ldots\ldots\ldots \quad (5.2)$$

where the constant holds the value $(e/8m)^{\frac{1}{2}}B_o d$ then it is easy to show that

$$dK/K = -\tfrac{1}{2}(dV/V) \quad \ldots\ldots\ldots \quad (5.3)$$

Putting last equation in (5.1), then it may be written as

$$C_m = (\Delta r_m/r)(K/-2dK) \quad \ldots\ldots\ldots \quad (5.4)$$

By using the same approximation, equation (1.73) reduces to

$$C_r = (dr_\theta/r)/(dV/V) \quad \ldots\ldots\ldots \quad (5.5)$$

It will be appreciated that since the fractional changes in electron energy are quite small (e.g. $\sim 10^{-4}$) the magnitude of the relative change in magnification is small. Thus the change in magnification can be expressed as

$$\frac{\Delta r}{r} = \frac{-\Delta f}{f}\left(1 + \frac{1}{m_1}\right) = \frac{-\Delta f}{f} \quad \ldots\ldots \quad (5.6)$$

where m_1 is the magnification due to the lens. By combining this equation with equation (5.4) gives

$$C_m = -(\frac{\Delta f}{f}) . (\frac{V}{\Delta V}) = -\frac{df}{dV} . \frac{V}{f} \quad \ldots \quad (5.7)$$

It is also useful to know that a variation in the exciting current Δi has a similar effect to that of a change in kinetic energy of the electron ($e\Delta V$), so

$$\Delta V/V = -2\Delta I/I \quad \ldots\ldots\ldots \quad (5.8)$$

5.2 Chromatic change coefficients of double pole lens

The chromatic change aberrations of double pole lens can be studied through double pole models. In this thesis two models have been chosen; the first is the Glaser-Bell shaped model because it is a model well studied analytically while the square top field model is used to give universal curves for double pole lens.

5.2.1 C_m and C_r for the Glaser-Bell shaped field

Morito (1954) gave the formulae for both coefficients for the projector lens according to the Glaser-Bell shaped field as follows:

$$C_m^p = \frac{\omega^2-1}{2\omega^2} (1-\omega\pi \cot \omega\pi) \quad \ldots\ldots \quad (5.9)$$

$$C_r^p = -\frac{\pi}{2}(\omega^2-1)^{\frac{1}{2}} \quad \ldots\ldots\ldots \quad (5.10)$$

Similar expressions were reported by Kanaya (1955), while Hawkes (1972) derived equation (5.9) with respect to magnification only. For the objective lens, Kanaya (1955) and Morito (1954) derived the equations

$$C_m^o = \frac{\pi(\omega^2-1)\cos(\pi/\omega)}{2\omega^3 \sin(\pi/\omega)} \quad \ldots\ldots\ldots \quad (5.11)$$

$$C_r^o = \frac{\pi(\omega^2-1)^{\frac{1}{2}}}{2\omega} \qquad \ldots\ldots\ldots \quad (5.12)$$

Both authors reported that Glaser (1941) gave different expressions which are as follows:

$$C_m^o = \frac{\pi(\omega^2-1)}{2\omega^3 \sin(\pi/\omega)} \qquad \ldots\ldots\ldots \quad (5.13)$$

$$C_r^o = \frac{\pi(\omega^2-1)^{\frac{1}{2}}}{2\omega^2} \qquad \ldots\ldots\ldots \quad (5.14)$$

The equations (5.13) and (5.14) gave lower values than those of the correct value.

Again, Kanaya et al (1976) gave the formulae for the coefficients as a function of the degree of flux concentration (m_f), and by assigning to m_f the value 1.5 for the case of the bell-shaped model then the results can be considered to be essentially the same.

The dependence of C_m^o on object distance (z_o) was derived by Hawkes (1968) and may be written as

$$C_m = \pi K^2 z_o / 2(1+K^2)^{3/2} \qquad \ldots\ldots \quad (5.15)$$

Kanaya (1955) formulated the coefficients corresponding to the three halves power field, and Morito (1954) calculated c_m for the intermediate lens. He proved that C_r is the same for both intermediate and projector lens.

The theoretical results obtained for the Bell-shaped field from the above equations together with the experimental data reported by Morito (1954) were used by present author to check the accuracy of the program used to calculate numerically the chromatic change in magnification and in rotation for both double and single polepiece lens. This numerical procedure is shown in Chapter 2.

Figure (5.1) shows very good agreement between analytical (solid lines) and numerical results (dotted lines) for the Glaser-Bell shaped model.

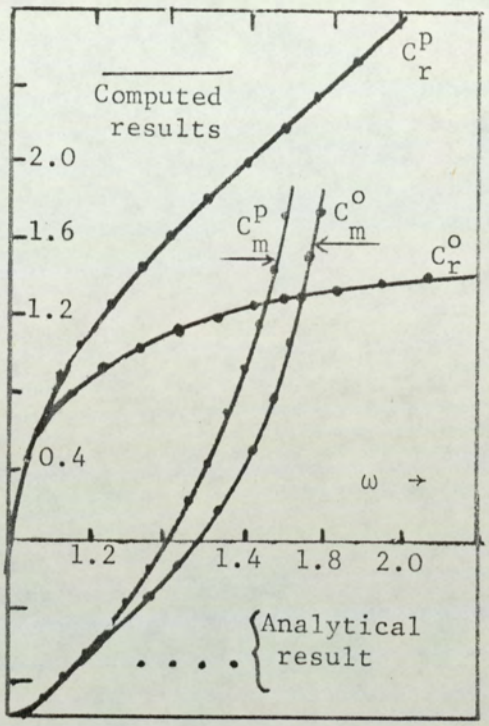

Fig. (5.1) Calculated coefficients of chromatic change of magnification and for chromatic change of rotation for the Glaser-Bell shaped field compared with the analytical solution (dotted lines)

5.2.2 Universal curves for C_m and C_r for double-pole lenses

An electron passing through the specimen loses energy and therefore has a trajectory different from that of an electron that has not lost energy. These trajectories are represented by the solid (no-loss) and broken (energy loss) lines in Fig. (5.2).

Referring to equation (1.2), the height of the trajectory at points z_o and $S/2$ is as follows:

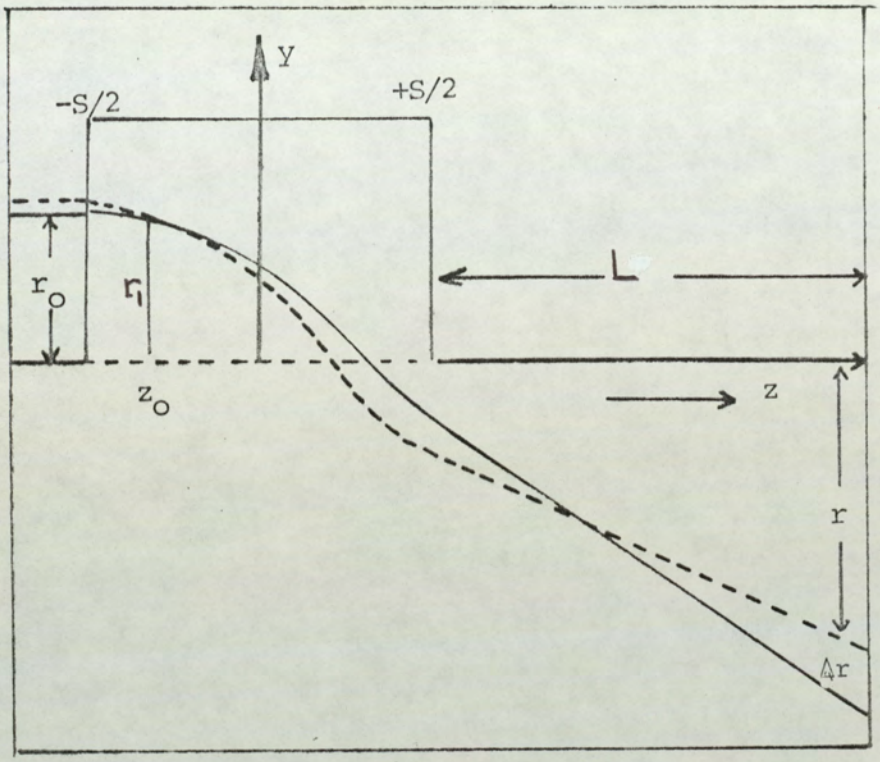

Fig. (5.2) Paraxial rays through a square top field. Solid line (no energy loss) Dotted line (with energy loss)

$$r_{1(z=z_o)} = r_o \cos K(z_o+S/2) \quad \ldots\ldots \quad (5.16)$$

$$r_{2(z=S/2)} = r_o \cos KS \quad \ldots\ldots\ldots \quad (5.17)$$

Hence

$$r_2' = -Kr_o \sin KS \quad \ldots\ldots\ldots \quad (5.18)$$

Substituting the value of r_o from equation (5.16) into equations (5.17) leads to

$$r_2 = \frac{r_1 \cos KS}{\cos K(z_o+S/2)} \quad \ldots\ldots\ldots \quad (5.19)$$

$$r_2' = \frac{-r_1 K \sin KS}{\cos K(z_o+S/2)} \quad \ldots\ldots\ldots \quad (5.20)$$

The image height r is given from figure (5.2) by

$$r = r_2 + L\, r_2' \triangleq L r_2' \quad \ldots\ldots\ldots \quad (5.21)$$

if the small contribution of r_2 is ignored.

Substituting equation (5.18) into (5.21) and differentiating r with respect to K, we obtain

$$\frac{1}{r}\,\frac{dr}{dK} = \left[\frac{1}{K} + S\cot KS + (z_o + \frac{S}{2})\tan K(z_o + \frac{S}{2})\right] . \quad (5.22)$$

(a) Chromatic change coefficients for objective lens

Substitution of equations (5.22) into (5.4), give

$$C_m = (\frac{dr}{r} / \frac{dV}{V}) = \tfrac{1}{2}\left[1 + KS\cot KS + K(z_o + \frac{S}{2})\tan K(z_o + S/2)\right] \quad (5.23)$$

putting $z_o = S/2 - \pi/2K$, then

$$C_m = -\tfrac{1}{2}(1 + \frac{\pi}{2}\cot KS) \quad \ldots\ldots\ldots\ldots\ldots \quad (5.24)$$

Equation (5.24) may be written as

$$C_m^o = -\tfrac{1}{2}\left[1 + \frac{\pi}{2}\cot\left\{(0.1863\,\frac{NI_o}{V_r^{\frac{1}{2}}})(\frac{NI}{NI_o})\right\}\right] \quad \ldots\ldots\ldots \quad (5.25)$$

and the universal curve is

$$C_m^o = -\tfrac{1}{2}\left[1 + \frac{\pi}{2}\cot\,(2.03\,\frac{NI}{NI_o})\right] \quad \ldots\ldots\ldots\ldots \quad (5.26)$$

Since $(0.1863\, NI_o/V_r^{\frac{1}{2}}) = 2.0306$ (Mulvey and Wallington, 1973) the latter equation shows that C_m takes the value zero at $NI/NI_o \simeq 1.062$.

Deviations in the electron path and speed can occur from two causes. One is due to the changes in accelerating voltage and the other to energy losses in the specimen.

When we consider energy losses in the specimen and the aberrated electron path will start to deviate from the

ordinary electron path at z_o and will start off with the same slope Figure (5.2).

If the co-ordinate and slope of the aberrated ray at the distance (x) from z_o are r_1 and r_1' it may easily be shown by applying equation (1.3) that

$$r_2' = r_1' \cos Kx - Kr_1 \sin Kx \quad \ldots\ldots\ldots\ldots \quad (5.27)$$

This expression gives the slope of the aberrated ray at the end of the field in terms of the beam energy represented by K.

Substituting the above value of r' in (5.21), takes the form

$$r = Lr_1' \cos Kx - KLr_1 \sin KX \quad \ldots\ldots\ldots \quad (5.28)$$

differentiation with respect to K gives

$$\frac{dr}{dK} = -Lxr_1' \sin KX - LKr_1 x \cos Kz - Lr_1 \sin Kx \quad \ldots\ldots\ldots \quad (5.29)$$

where $$x = S/2 - z_o \quad \ldots\ldots\ldots\ldots\ldots\ldots \quad (5.30)$$

Alternatively, substituting equations (5.28) and (5.29) in equation (5.4) the same expression as in (5.25) is obtained. Thus C_m for an objective lens is similar for fluctuations in accelerating voltage and for energy losses in the specimen, and so (5.25) can be used for universal curve for objective lens at the region $NI/V_r^{\frac{1}{2}} \geq 8.43$ (i.e. $ks \geq \pi/2$)

It must be remembered that the coefficient has been evaluated for the case of the incident electron beam on the lens parallel to the axis, which is a good approximation to the normal use of an electron microscope at lower magnification

where the illumination is spread out by the condenser.

The universal curve for C_m versus NI/NI_o is shown in figure (5.3) and it contains also C_m^o at the region $NI/NI_o < 0.773$ $(NI/V_r^{\frac{1}{2}} \leqslant 8.43)$ which is found by using the equation of the projector lens, because C_m^o and C_m^p follow the same relation for the weak lens (i.e. $\theta < \pi/2$).

Equation (1.74) is used to obtain C_r^o; this applies to two cases. The first is for a strong lens when $z_o = \pi/2K$. If the integration limits are taken between $\pi/2K$ and $-S/2$, we get

$$C_r^o = -\pi/4 \quad \text{for } [\theta \geqslant \pi/2] \quad \ldots\ldots\ldots \quad (5.31)$$

For a weak lens the chromatic change in rotation for the objective lens (C_r^o) takes the same value for the projector lens, and hence,

$$C_r^o = \tfrac{1}{2}kS = \theta/2 \text{ for } (\theta < 0.5\pi) \quad (5.32)$$

(b) C_m and C_r for projector lens

From equation (1.5), differentiation f_p with respect to K

$$\frac{df_p}{dK} = \frac{1}{\omega} \cdot \frac{S \cos KS}{\sin^2 KS} \cdot \frac{1}{\sin KS} \cdot \frac{1}{K^2} \quad \ldots\ldots \quad (5.33)$$

Hence $$\frac{df_p}{dK} \cdot \left(\frac{1}{f_p}\right) = S \cot KS - \frac{1}{K} \quad \ldots\ldots\ldots\ldots \quad (5.34)$$

Substituting equation (5.7) in (5.34)

$$C_m^p = \frac{df_p}{f_p} \cdot \frac{V}{dV} = \tfrac{1}{2}[1+KS \cot KS] \quad \ldots\ldots\ldots \quad (5.35)$$

This equation can also be obtained by using an analysis similar to that for objective lens. Equation (5.21) may be

written as

$$r = -LKr_1 \sin KS$$

which gives $\frac{1}{r}(\frac{dr}{dK}) = \frac{1}{K}(1-KS\cot KS)$ ..... (5.36)

and then leads easily to (5.35). To use equation (5.36) as a universal curve for C_m^p or C_m^o at the region $NI/V_r^{\frac{1}{2}} < 8.43$, it is convenient to put it in the form

$$C_m^p = -\tfrac{1}{2}\left[1+ 0.1863 \left(\frac{NI_o}{V_r^{\frac{1}{2}}}\right)\left(\frac{NI}{NI_o}\right) \cot\left(0.1863\frac{NI_o}{V_r^{\frac{1}{2}}} \cdot \frac{NI}{NI_o}\right)\right]$$

So $$C_m^p = -\tfrac{1}{2}\left[1+2.03\left(\frac{NI}{NI_o}\right) \cot \left(2.03\frac{NI}{NI_o}\right)\right] ..... \quad (5.37)$$

Figure (5.3) is the universal curve for double pole lenses chromatic change coefficients and is plotted for C_m^p C_r^o , C_r^p. The last coefficient C_r^p can be found by

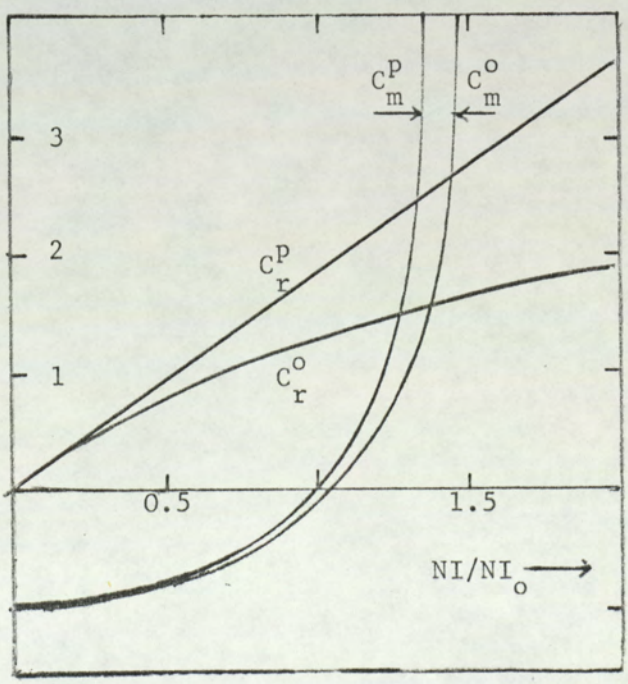

Fig.(5.3) Universal curve for the coefficient of chromatic change in magnification and in rotation for a double pole lens, based on the square top field model

substituting Amperes law (i.e. $\int_{\infty}^{\infty} B(z)dz = \mu_o NI$) in the equation (5.10) to obtain

$$C_r^p = -\tfrac{1}{2}(e/8mV_r^{\frac{1}{2}}) \mu_o NI = -\tfrac{1}{2}KS = \Theta/2 \quad \ldots\ldots \quad (5.38)$$

This result agrees with that which was found previously using the Glaser Bell shaped equation (5.9).

5.2.3 Application of C_m and C_r for double pole lenses

Many models such as the bell-shaped and Grivet-Lenz models are relevant to double pole lenses and can be used to confirm the universal curve (5.3) found analytically by using the square top field. They show as in Figure (5.4) excellent agreement with the universal curve with only very slight shift (less than 10%) of C_m^p found from the Grivet Lenz model at high excitation (i.e. $NI/NI_o > 1$).

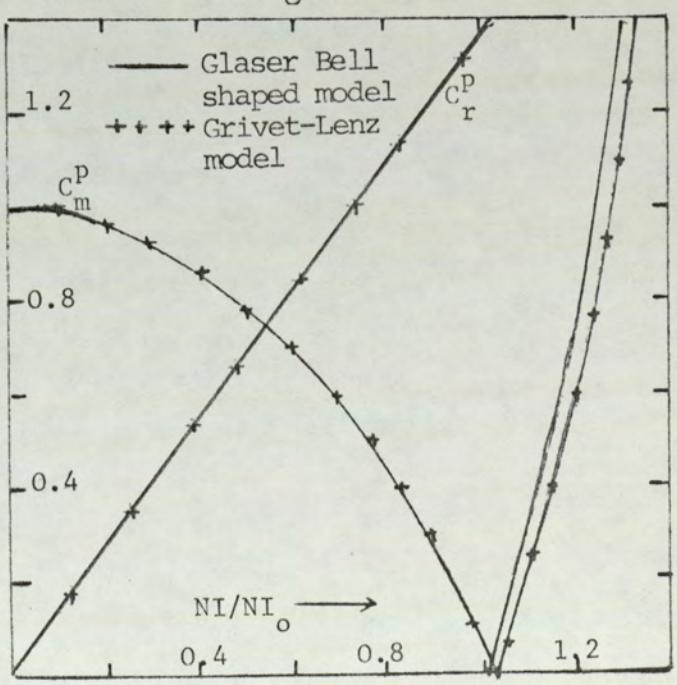

Fig.(5.4) Universal curve for the coefficient of chromatic change in magnification and in rotation based on the Glaser bell-shaped field and the Grivet-Lenz field.

To check the applicability of the universal curve for chromatic change coefficients of double pole lens, two double pole lenses were studied, one of them was used as projector and the other is objective and their field distributions were measured by Elkamali (1978). (Fig. 5.5).

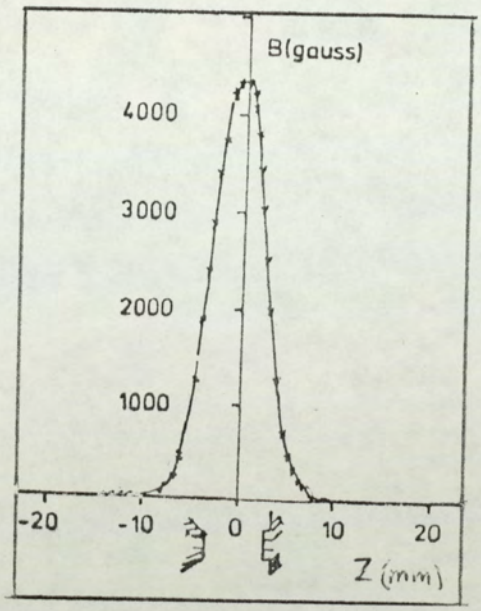

Fig.(5.5) The field distribution of the objective miniature double polepiece lens

These field distributions were used to calculate the chromatic coefficients for both lenses and the coefficients are shown on the universal curves as crosses (Figures 5.6 and 5.7).

It is clear that the coefficients found from real magnetic field distributions consistent with the results derived from the models from which the universal curves were derived.

5.3 Chromatic change coefficients of single-pole lens

The computation of C_m^o, C_m^p and C_r^o was carried out by using the special program described in Chapter 2 in the same way as the double-pole lens. The same was also done for C_r^p for which analytical solutions exist for any field distribution. This was used as a check for the numerical procedure.

5.3.1 The coefficient for projector lens

The analysis shows that both chromatic change in

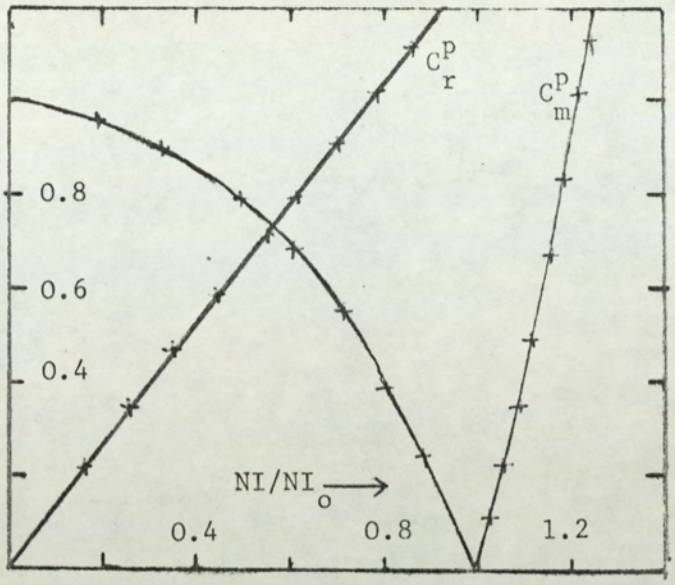

Fig.(5.6) The coefficients of chromatic change in magnification and rotation for conventional projector lenses (crosses) compared with the universal curve (solid line)

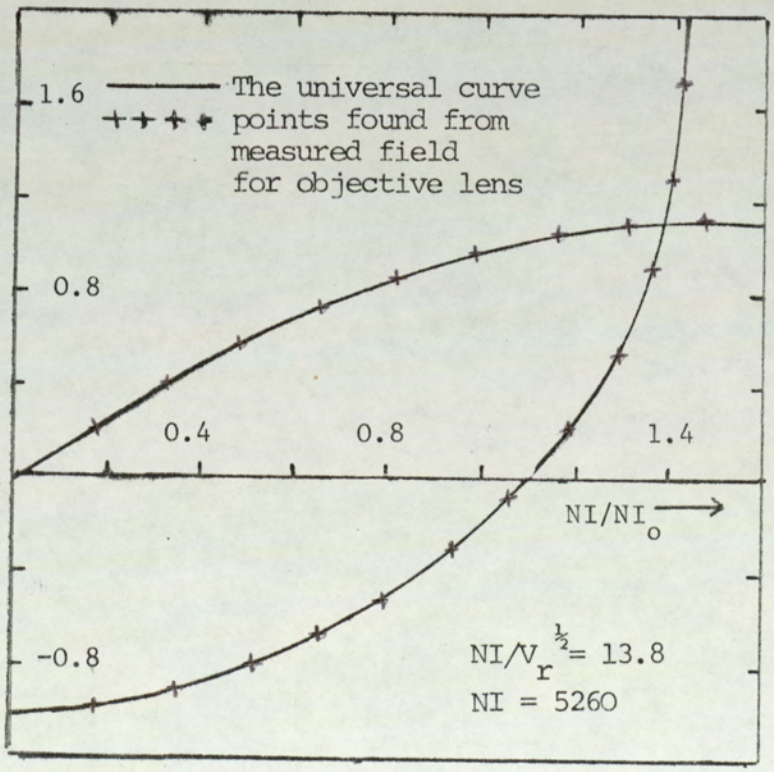

Fig.(5.7) Coefficients of chromatic change of magnification and of rotation for a conventional objective lens plotted on a universal curve.

magnification or in rotation for single pole lenses has a universal curve. This fact was proved by using experimental and spherical pole-piece model. This universal curve in the projector lens case applies for both modes of operation (i.e. independent of ray direction).

The solid line in Figure (5.8) shows the universal curve for projector single-pole lens found by using single pole models while crosses indicate same properties for 100KV single-pole lenses whose field distribution and focal properties were described in Chapter 3. The latter lens was used to confirm the applicability of the universal curve.

The conclusion to be drawn from the above results is that the chromatic change in magnification in the case of single-pole projector lenses is approximately the same as that of double pole lenses.

It is clear from Figure (5.8) that C_r^p is directly proportional to the excitation parameter and that $C_r(NI_o/NI)$ is approximately equal to 1.33.

5.3.2 The coefficients for the single pole objective lens

The characteristics of the chromatic change coefficients of objectives obtained by numerical calculation are different from those found for projectors. While the ray direction has no effect on C_m^p and C_r^p, both C_m^o and C_r^o are affected by the ray direction.

It is noticeable that when the ray enters from the steep end of the field, C_r always has a lower value than that obtained for a ray from the other direction. Thus when $NI/NI_o = 1$, the value of C_r for a ray from the steep end is half the

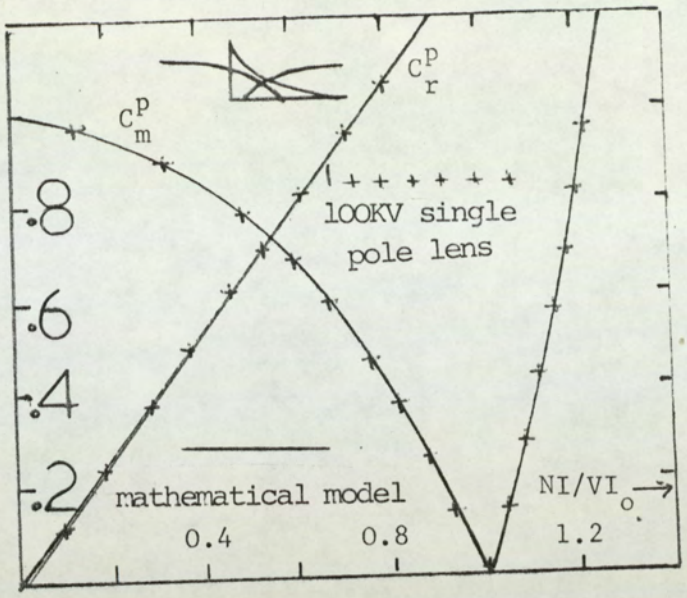

Fig.(5.8) Universal curve of the coefficients of chromatic change in magnification and rotation for a single polepiece projector lens for both modes of operation, using mathematical model (solid line) and experimental 100KV lens (crosses).

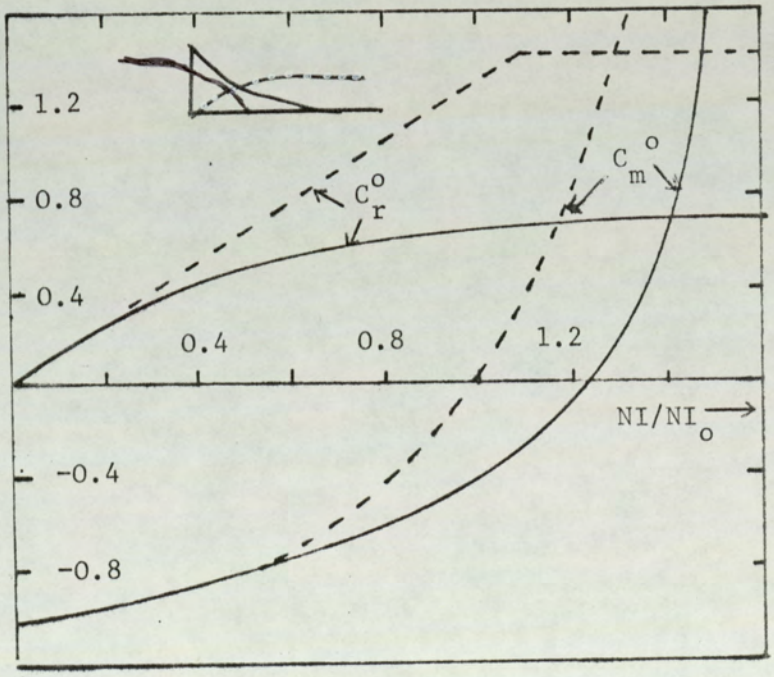

Fig.(5.9) The coefficients of chromatic change of magnification and of rotation for a single-polepiece objective lens in two modes of operation, using spherical field model, exponential field model and 100KV lens.

value for a ray from the other direction.

For a ray entering from the sloping end, C_r^o is proportional to NI/NI_o over the range $NI/NI_o \leq 1.0$ when $NI/NI_o > 1$, C_r takes approximately the constant value 1.21.

It seems that the C_r^o value for single pole lenses is lower than that for double pole lenses. When the ray comes from the steep edge of the field we also have values for C_r lower than from the other direction and it is 0.74.

This comparatively large value is less by an amount 6% than that found from double pole lens which is $\pi/4$.

It seems that the preferred direction is that when the ray enters from the steep edge of the single-pole lens field.

Figure (5.9) summarizes the above mentioned characteristics for C_r and also C_m^p for both modes of operation. The figure also shows that weak single pole lenses ($NI/NI_o < 0.3$) have the same values for the coefficients in either direction.

5.4 Two projector single pole lens systems

It is desirable in a projector system to eliminate image rotation which results from a change in the excitation of the intermediate and projector lenses. The chief objection to this defect is that it makes it inconvenient to interpret certain diffraction micrographs, namely those where the diffraction pattern of a crystalline structure and the corresponding image of the crystal is superimposed with different orientations.

The same numerical procedure was carried out to investigate the effect of two single pole lenses, the full distribution of the two lenses being considered as one combined field. The results show that the rotation vanishes as expected under the condition $(NI)_1 = -(NI)_2$.

These results confirm that it is possible to use miniature single pole piece lenses as a rotation-free system (Juma and Mulvey, 1975).

It was useful, however, to investigate C_m^p for a rotation free system by varying the distance between the two lenses (i.e. L/d).

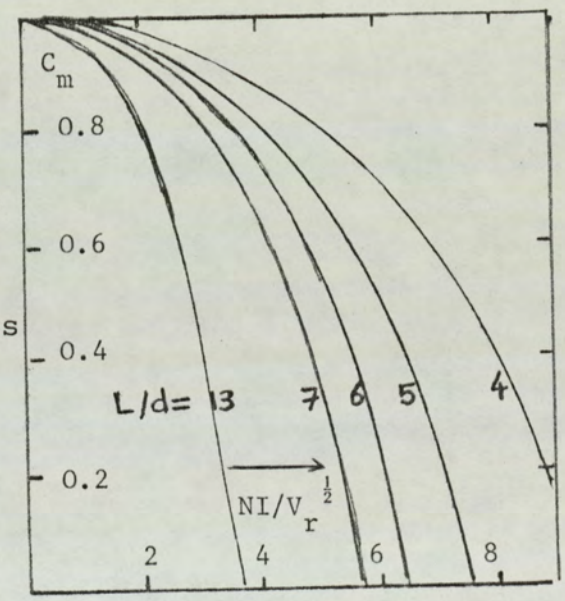

Fig.(5.10) C_m as a function of $NI/V_r^{\frac{1}{2}}$ for rotation-free system for various L/d values

Figure (5.10) shows C_m for a rotation-free system plotted against $NI/V_r^{\frac{1}{2}}$ for various L/d values. These results lead to the same universal curve for the single pole lens when C_m is plotted against NI/NI_o and confirm the fact that C_r^p is zero.

To gain more insight into the use of two projector lenses as a system the excitations of the two lenses were then adjusted so as to produce the same image rotation, (i.e. lens current in the same direction). The computed values of C_m and C_r so obtained are shown in Figure (5.11)

as a function of excitation the parameter $NI/V_r^{\frac{1}{2}}$ for various values of L/d.

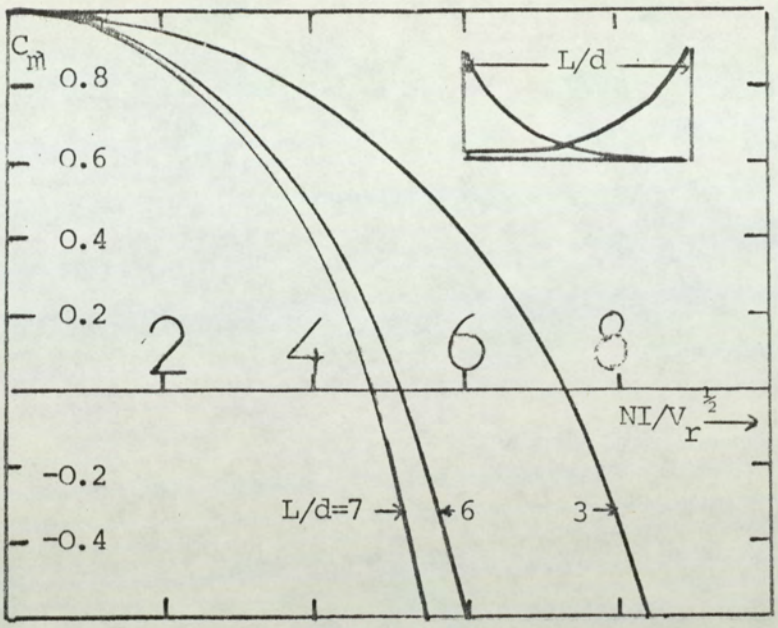

Fig.(5.11) Effective coefficient C_m for two lenses. $NI/V_r^{\frac{1}{2}}$ adjusted to produce the same image rotation.

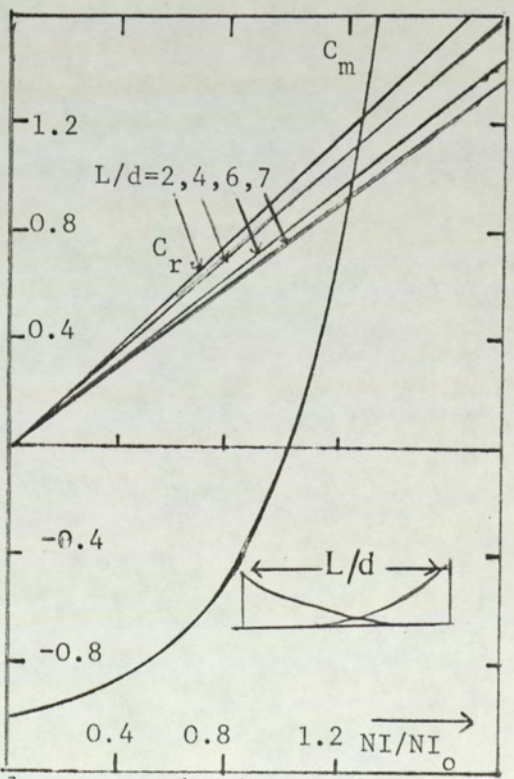

Fig.(5.12) The universal curve of C_m and relative excitation parameter NI/NI_o for two lenses each producing the same image rotation

If the quantity NI/NI_o is used as x-axis instead of $NI/V_r^{\frac{1}{2}}$, (it is shown in Figure (5.12) that C_m is again on the universal curve while C_r is not. This is because the field outside the area between the snouts of two lenses has

been ignored.

The calculations of chromatic change in magnification and in rotation for the square top field and spherical field model show that there is a universal curve for the projector lens and that the chromatic change coefficients (i.e. C_m and C_r) for single pole lens is slightly higher than those of double pole lens.

These results also show that when the snout is facing the incoming parallel beam in the case of TEM, both C_m and C_r have low values in the case of single-pole objective lens than those of the double pole objective one. This mode of operation is again the preferred one for obtaining low values of C_m.

A further conclusion drawn from these results is that it is easy to have a rotation-free system with minimum chromatic change in magnification; in such cases excitation parameters depend upon the distance between the two lenses. A system of two magnetic lenses separated by a certain distance is recommended to obtain the optimal minimization of chromatic changes in magnification and in rotation.

6. CHARACTERISTICS OF THE PRE-FIELD

The summary of the characteristics of the double polepiece lens is mentioned in (1.4). The following chapter deals only with the similar work for the single polepiece lens.

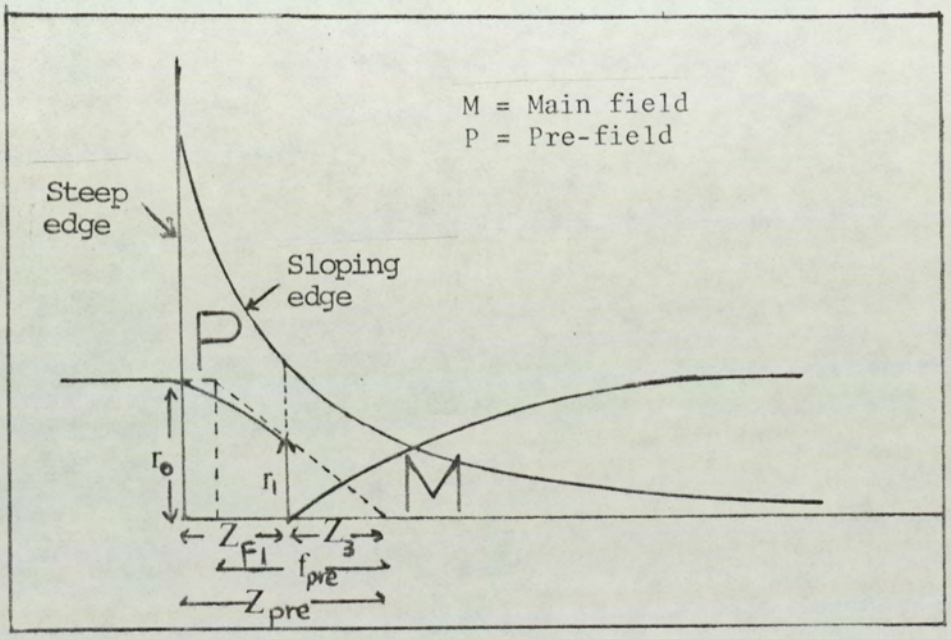

Fig.(6.1) Axial distribution of pre-field and main-field in the single-pole lens showing focal properties f_{pre}, z_{pre} of the pre-field.

6.1 Single-pole lens pre-field

There are two possible directions for beam entry in a single-pole field because of the asymmetry in the field (Marai and Mulvey, 1975). Accordingly, there are two possible arrangements for the prefield. The first consists of the field bounded by the sharp edge of the field and the

object (Fig. 6.1). In this case the ray enters the main field from the positive z-direction. (This case may be called high flux pre-field).

The pre-field focal length f_{pre} for this mode of operation is

$$f_{pre} = r_o/r' = 1/r' \quad \ldots\ldots\ldots \quad (6.1)$$

and from Fig. (6.1), the pre-field focal distance (z_{pre}) is

$$Z_{pre}/S = Z_{F1}/S + Z_3/S$$

then

$$Z_{pre} = Z_{F1} + r_1 \times f_{pre} \quad \ldots\ldots\ldots \quad (6.2)$$

Equation 6.2 is also valid for the second mode of operation when the pre-field and main field exchange places (Fig.6.2) i.e. low flux pre-field.

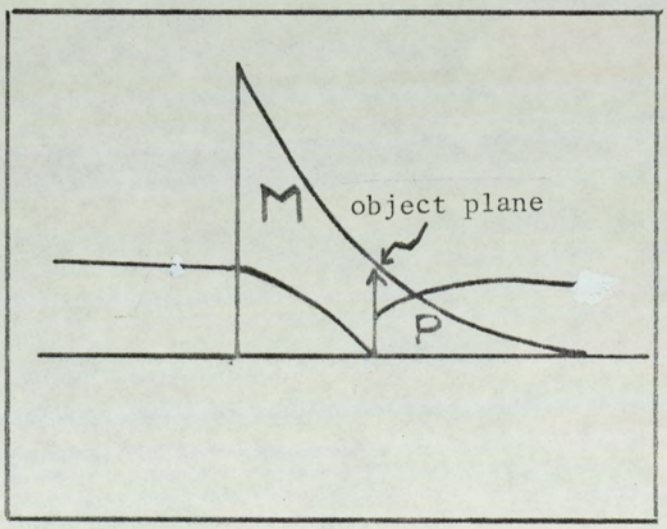

Fig.(6.2) Low-flux density pre-field of single polepiece lens.

For the spherical polepiece model which is a realistic model for single-pole lenses (Alshwaikh and Mulvey, 1977),

the telescopic ray path occurs at an excitation parameter $NI/V_r^{\frac{1}{2}} = 22.36$. A strong pre-field is created followed by an imaging field of low aberration when a specimen is placed at a distance $Z_o = 0.8d$ (0.2a). In this case the condenser-objective lens of Riecke and Ruska (1966) is achieved. Fig. (6.3) shows the above case with two possible directions of the illuminating beam.

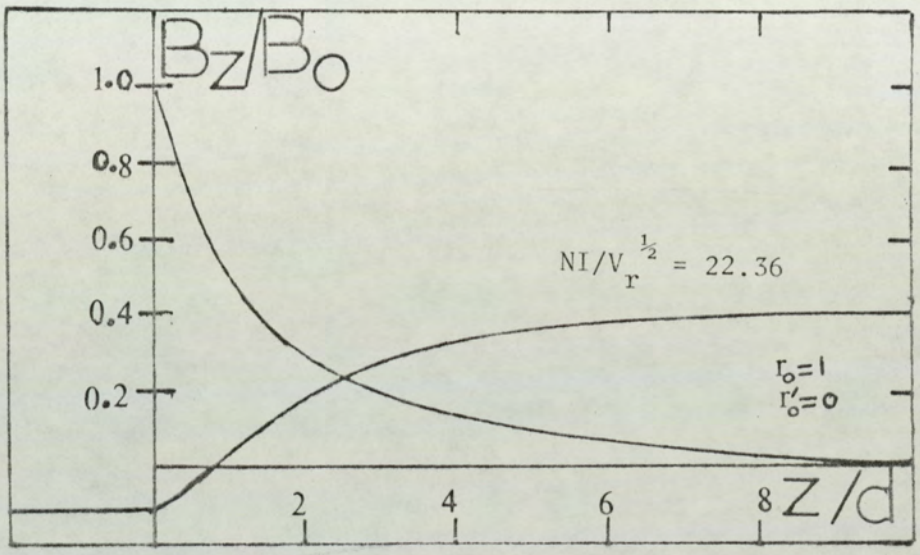

Fig.(6.3) Telescopic ray path in the spherical field model.

The electron optical properties of the pre-field for the first mode of operation is shown in solid line in (Fig. 6.4) while dotted line refers to the case where the main field is bounded between the sharp edge of the field and the object. The pre-field in this case has been constituted by the remaining field (i.e. high flux pre-field).

From the two figures it is noticeable that at an excitation parameter $NI/NI_o = 1.6$ one obtains a symmetrical 'condenser-objective'.

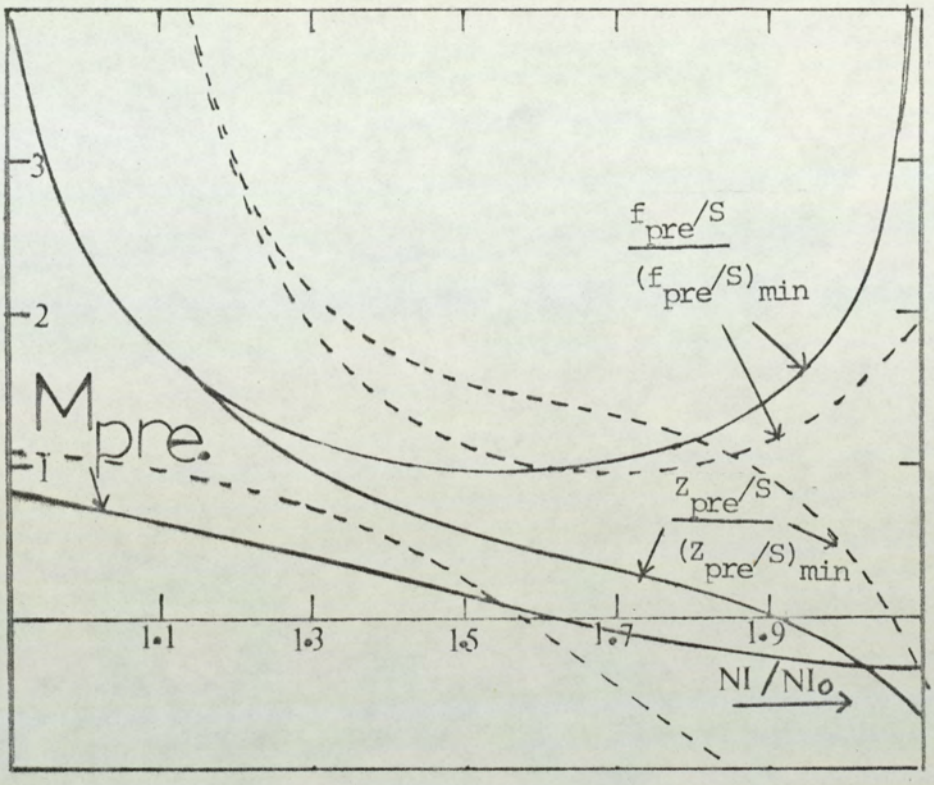

Fig.(6.4) The electron-optical properties of the pre-field of the single pole lens

6.2 Aberrations of the single-pole pre-field

Using the program 'PRE field' to calculate spherical and chromatic aberration coefficient of single-pole pre-field.

It is seen from Figure 6.5 that the coefficients C_c and C_s both decrease slowly to a minimum with increasing ampere-turns and then increase again. The same occurs for the other mode of operation. Solid and dotted lines in Fig. (6.5) are presented for both above cases respectively. From Fig. (6.5) one notices that the four curves have minima at $NI/NI_o = 1.6$ (i.e. $NI/V_r^{\frac{1}{2}} = 22.36$). The minimum values

for C_c/d and C_s/d for the first mode of operation are 0.5 and 0.8 respectively while for the second mode C_c/d is 1.15 and C_s depends upon the field distribution inside the snout as discussed in chapter 2.

The preferred mode of operation will depend on the optical characteristics that are required in a particular application. The preferred mode for chromatic aberration, as example, is the high-flux density pre-field.

Comparing these results with those in chapter 4, we notice that the minimum of both coefficients of the pre-field in the first mode differ

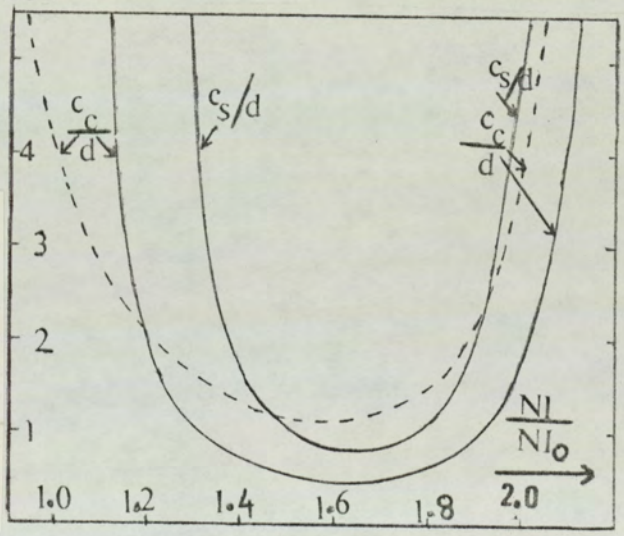

Fig. (6.5) C_c of the single pole lens pre-field in two possible modes of operation. C_s for the low flux density pre-field mode.

by only 2% from the corresponding coefficients for a single-pole objective, but they occur of course at different values of NI/NI_o. For the second mode of operation the pre-field, both C_c and C_s take the same values as in a single-pole objective case for the same excitation parameter which occurs usually at $NI/V_r^{\frac{1}{2}} = 22.36$.

7. THE CORRECTION OF SPIRAL DISTORTION

7.1 Spiral Distortion for one Lens

It follows from the discussion in Chapter 4 that for the square top field model, the spiral distortion coefficient can be represented by the relation (A9.5) as

$$D_{sp}S^2 = \frac{\theta^3}{2} + \frac{\theta^2}{8} \sin 2\theta \quad \ldots\ldots\ldots \quad (7.1)$$

where $\theta = KS = (e/8m)^{\frac{1}{2}}(BS/V_r^{\frac{1}{2}}) = 0.1863NI/V_r^{\frac{1}{2}}$ ..... (7.2)

The above relations are derived in (Appendix 9).

However, the spiral distortion of single pole lens or other model can be found numerically by the program 'CDISTORTION' (Chapter 2) using Scherzer's equation (Scherzer, 1937).

7.1.1 Universal curve for spiral distortion

The parameter θ_o has been defined in the relation

$$\theta_o = 0.1863\ NI_o/V_r^{\frac{1}{2}} = 2.03067 \quad \ldots\ldots\ldots \quad (7.3)$$

where $NI_o/V_r^{\frac{1}{2}} = 10.9$ for the square top field (Mulvey and Wallington, 1973). θ_o is assumed to be the corresponding value of θ at the minimum focal length of the lens.

Equation (7.1) can be written as

$$D_{sp.}S^2 = \frac{\theta_o^3}{2}\left(\frac{\theta}{\theta_o}\right)^3 + \frac{\theta_o^2}{8}\left(\frac{\theta}{\theta_o}\right)^2 \sin\left(2\theta_o\frac{\theta}{\theta o}\right)$$

$$D_{sp.}S^2 = 4.191\left(\frac{\theta}{\theta_o}\right)^3 + 0.51\left(\frac{\theta}{\theta_o}\right)^2 \sin 4.06\left(\frac{\theta}{\theta_o}\right) \quad .. \quad (7.4)$$

Let D_{spo} be the value of spiral distortion coefficient at the angle of rotation θ_o, then from equation (4.1)

$$D_{sp_o} = 4.22 \quad \ldots\ldots\ldots \quad (7.5)$$

From equations 7.4 and 7.5 it follows that

$$\frac{D_{sp}}{D_{sp_o}} = \left(\frac{\theta}{\theta}\right)^3_o + 0.12\left(\frac{\theta}{\theta}\right)_o \text{ Sin } 4.06\left(\frac{\theta}{\theta}\right)_o \quad \ldots \quad (7.6)$$

$$\frac{D_{sp}}{D_{sp_o}} = \left(\frac{NI}{NI_o}\right)^3 + 0.12\left(\frac{NI}{NI_o}\right)^2 \sin 4.06\left(\frac{NI}{NI_o}\right) . \quad (7.7)$$

The latter equation proves that the relative spiral distortion coefficient D_{sp}/D_{spo} differs from the cube of the relative excitation $(NI/NI_o)^3$ by a small additional oscillatory term which depends on the value of NI/NI_o. A similar relation with slight difference was obtained by Marai and Mulvey (1977)

The first term becomes remarkably accurate for conventional lenses and the general expression is approximately in agreement with the results found by Liebmann (1952) for various twin lenses. There is another relation found by Huang (1977) and takes the form $C_{sp} = 2.4\left(e^{-S/D}\right)\left(\frac{NI}{NI_o}\right)^{2.6}$

7.1.2 Finite conjugate effect

In a projector lens the object distance is not always at an infinite distance from the corresponding magnetic projector lens. So in the calculation of spiral distortion the finite conjugates of the final projector lens must be taken into consideration.

It is convenient to study the spiral distortion coefficient $\bar{D}_{sp.}$ of the constant field to assess the magnitude of this effect analytically (fig. 7.1).

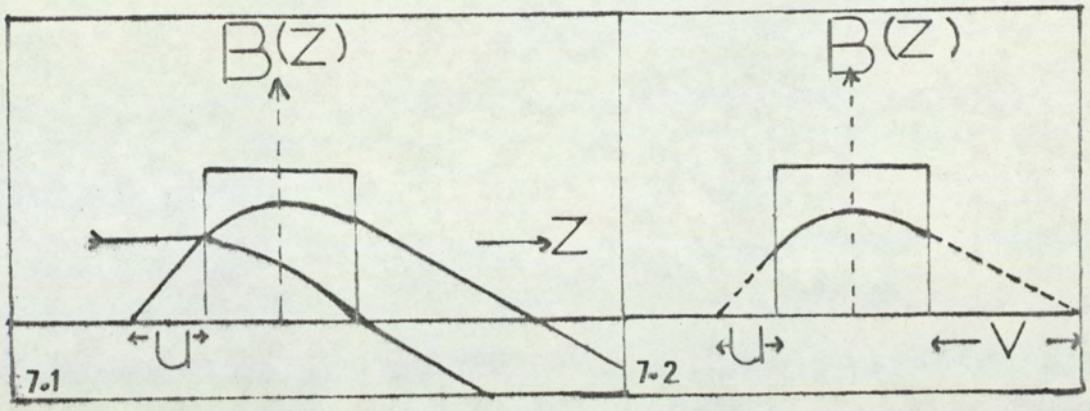

Fig.(7.1) Ray with finite conjugate in the square top field. Fig.(7.2) Relation between the object distance u, the field width s, and image distance v for the square top field

The equation (A.9.13) is re-arranged here as

$$\bar{D}_{sp} = \frac{K_2^3 r_2^2}{8}\left[4S + \frac{\sin(2K_2S)}{K_2}\right]\left[1 + \left(\frac{r_2'}{K_2 r_2}\right)^2\right]$$

$$- K_2^2 r_2^2 \left(\frac{r_2'}{K_2 r_2}\right)^2 \sin(2K_2S) - \frac{K_2 r_2 r_2'}{4}\cos 2K_2S$$

$$+ \frac{K_2 r r'^2}{4} \qquad \ldots\ldots\ldots (7.8)$$

noticing that $\bar{D}_{sp}$ is denoted spiral distortion coefficient in the case that the ray does not come from infinity.

From the fig. (7.2) it is found that

$$r_2/u = r_2' \qquad \ldots\ldots\ldots (7.9)$$

where u is the distance between the source and the lens

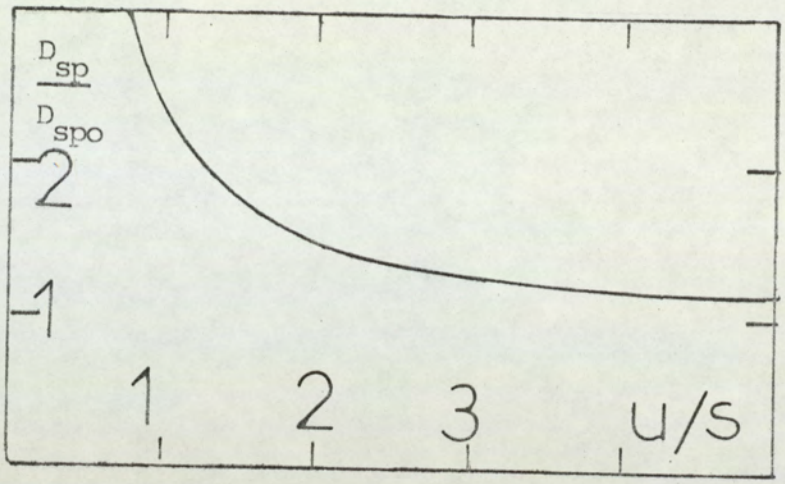

Fig.(7.3) The ratio $\bar{D}_{sp}/D_{spo}$ as a function of object distance u/S

Equation (7.8) is then written as

$$\bar{D}_{sp.} = \left[\frac{K_2^3}{8}\left(4S + \frac{\sin(2K_2S}{K_2}\right)\left(1+\frac{1}{K_2^2u^2}\right) - \frac{K_2}{4u}\cos 2K_2S\right.$$

$$\left. - \frac{1}{4u^2}\sin(2K_2S) + \frac{K_2}{4u}\right] r_2^2 \quad \ldots\ldots\ldots \quad (7.10)$$

where u is the distance between the source and the nearest boundary of the field (fig. 7.1)

Letting $K_2S = \theta_2$ and rearranging equation (7.10) leads to

$$\bar{D}_{sp.}S^2 = \left[\frac{\theta_2^3}{2} + \frac{\theta_2}{2(u/S)^2} + \frac{\theta_2^2\sin 2\theta}{8} + \frac{\sin 2\theta}{8(u/S)^2} - \frac{\theta_2\cos_2\theta_2}{4(u/S)}\right.$$

$$\left. - \frac{\sin 2\theta_2}{4(u/S)^2} + \frac{\theta_2}{4(u/S)}\right] r_2^2 \ldots\ldots\ldots \quad (7.11)$$

$$\bar{D}_{sp.}S^2 = \left[\frac{\theta_2^3}{2} + \frac{\theta^2\sin 2\theta_2}{8} + \frac{\theta_2}{2(u/S)^2} + \frac{\theta_2}{4(u/S)} - \frac{\sin 2\theta_2}{8(u/S)^2}\right.$$

$$\left. - \frac{\theta_2\cos 2\theta_2}{4(u/S)}\right] r_2^2 \quad \ldots\ldots\ldots \quad (7.12)$$

For a certain value of θ_2, equation 4.9 gives the variation of spiral distortion coefficient of the square

top field with u when $r_2^2 = 1$. And it is clear that the first two terms equal to D_{spo}.

An important case is that where $\theta_2 = \pi/2$ (i.e. when the magnification is near its maximum and the radial distortion is nearly zero). The spiral distortion $\bar{D}_{sp}S^2$ calculated from 7.12 under these circumstances is given by

$$\bar{D}_{sp.}S^2 = \frac{\pi^3}{16} + \frac{\pi}{4(u/S)^2} + \frac{\pi}{4(u/S)} \quad \ldots\ldots\ldots (7.13)$$

noting that $D_{spo}S^2 = \pi^3/16$ $\ldots\ldots\ldots\ldots\ldots$ (7.14)

then $$\bar{D}_{sp.}/D_{spo} = \left[1+\frac{4}{\pi^2}\left(\frac{S}{u}\right)^2 + \frac{4}{\pi^2}\left(\frac{S}{u}\right)\right] \quad \ldots\ldots\ldots (7.15)$$

Fig. 7.3 shows the relation between $\bar{D}_{sp}/D_{spo}$ as a function of u.

Let v be the distance from the far boundary of the field to the point at which $y_i = 0$ (fig. 7.1), then from equation (1.2) and (1.3)

$$y_i = y'_{io}/K \ , \ y'_i = -K \quad \ldots\ldots\ldots\ldots (7.16)$$

so $$v = \left|\frac{y_i}{y'_i}\right| = \frac{y'_{io}}{K^2} = \frac{1}{uK^2} \quad \ldots\ldots\ldots (7.17)$$

noticing that K as mentioned before

The magnification of the lens (m) defined as

$$m = \frac{v + 0.5S}{u + 0.5S} \ , \text{ and takes the value}$$

$$m = \frac{\frac{1}{uK^2} + 0.5S}{u + 0.5S}$$

for the case $\theta_2 = \pi/2$ as a particular case

$$m = \frac{4/\pi^2}{(u/S) + 0.5} \quad \ldots\ldots\ldots\ldots (7.18)$$

where the value of 0.5S represents the position of the principal plane of the lens which in this particular case (i.e. $\theta_2 = \pi/2$) is approximately at the middle of the lens.

Both $(\bar{D}_{sp}/D_{spo})$ and m can be found by substituting the value of u/S in the equations 7.15 and 7.18 respectively. To plot the graph in fig. (7.4) various values of $\bar{D}_{sp}/D_{spo}$ and m can be calculated for a range of u/S values.

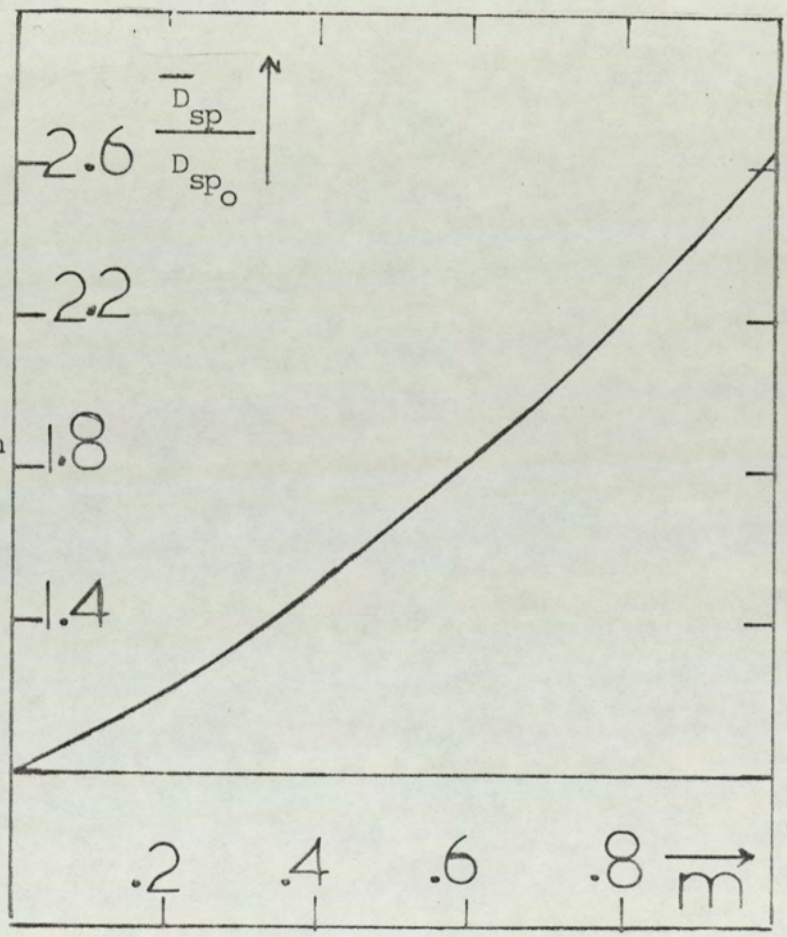

Fig.(7.4)a The ratio $\bar{D}_{sp}/D_{spo}$ as a function of the ratio of conjugates (m)

Fig. (7.4a) shows the relation between $\bar{D}_{sp}/D_{spo}$ and m which are taken for a wide range of values. The graph approximately obeys the relation

$$\bar{D}_{sp}/D_{spo} = 1 + 1.37m + 1.28m^2 \quad \ldots\ldots\ldots \quad (7.19)$$

But within the range $0 < m < 1$, the curve is better approximated by the relation

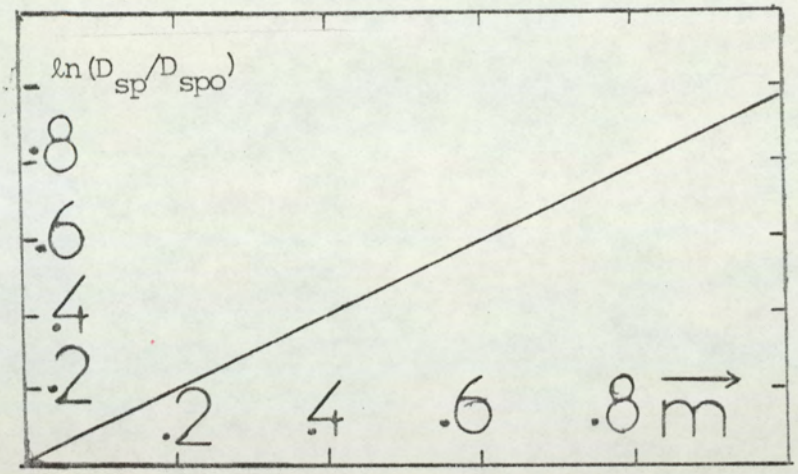

Fig.(4.4b) The ratio $\ln(\bar{D}_{sp}/D_{spo})$ as a function of ratio of conjugates(m)

$$\bar{D}_{sp}/D_{spo} = e^{m} \quad \ldots\ldots\ldots\ldots\ldots\ldots \quad (7.20)$$

and this fact is shown in fig.(7.4b)

7.2 Mathematical analysis for spiral distortion correction

The possibility of correcting spiral distortion can be examined mathematically in a rotation-free system (Fig.7.5). (i.e. the lenses with equal and opposite currents). The system contains two lenses; one is the corrector which has a spiral distortion coefficient $D_{sp}(1)$; this coefficient is reduced by a factor m^2 when the aberration is referred to the final image plane, where m is the magnification of the intermediate lens (i.e. magnification due to corrector lens at the projector lens). The second lens is the projector whose spiral distortion coefficient is $D_{sp}(2)$. The two lenses are separated by a distance L_1. (Fig. 7.5)

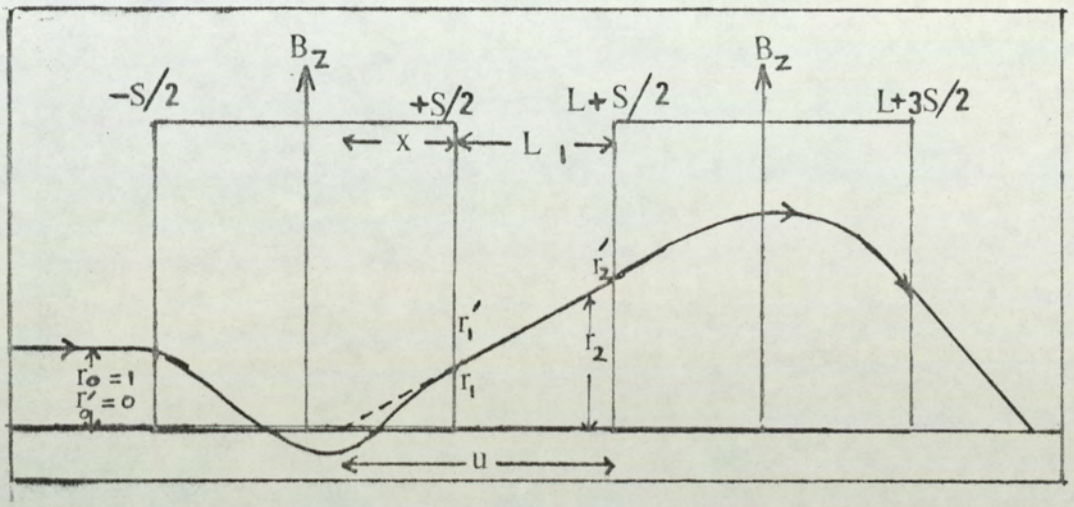

Fig. 7.5 System for correcting spiral distortion with two square top field distributions

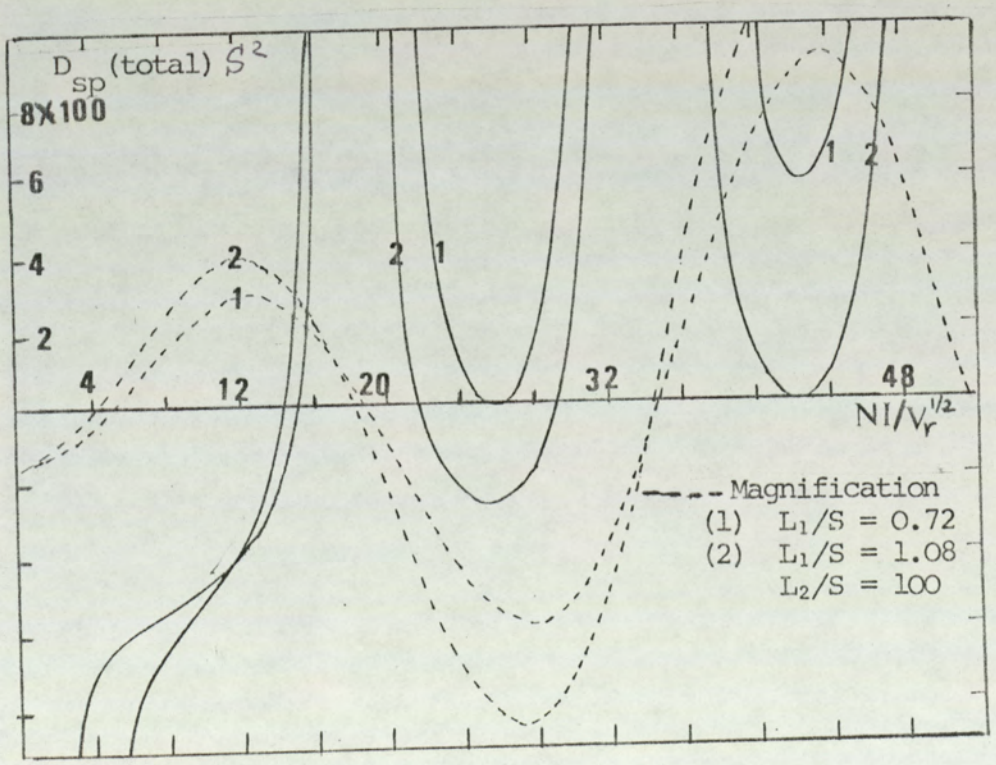

Fig. (7.6) The total spiral distortion coefficient and final magnification for various distances (L_1/S) between the two square top fields

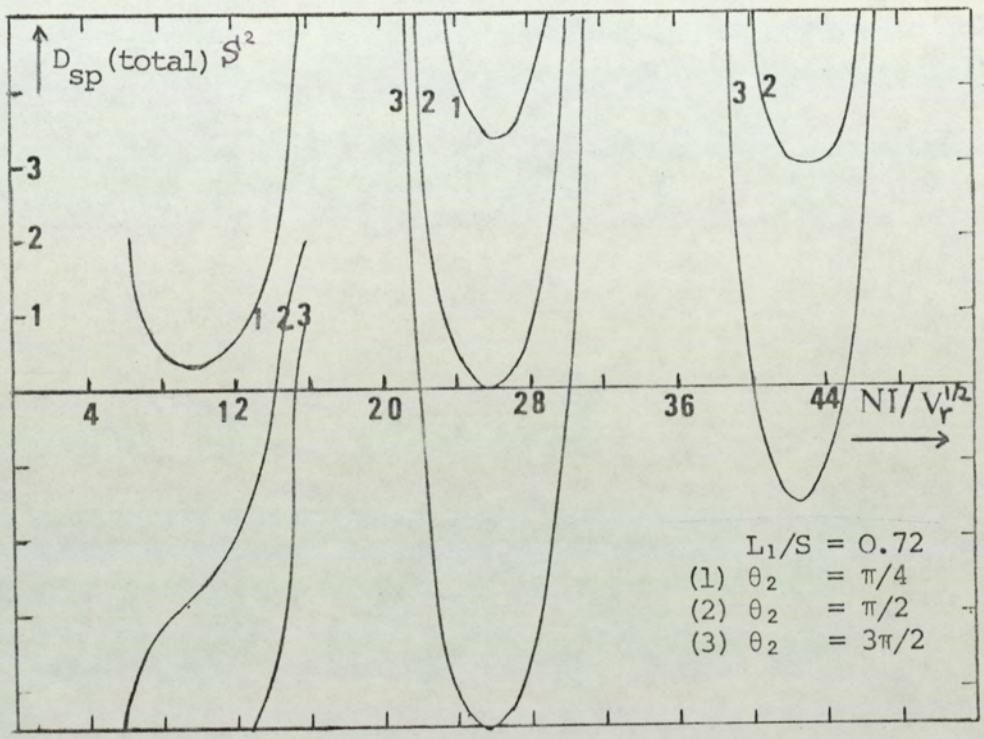

Fig. (7.7) The total spiral distortion coefficient (DT_{sp}) for two square top fields for various excitation parameters in the final field

Referring to fig. (7.5) it can be shown (Appendix 9) that

$$u/S = L_1/S - \text{Cos}\ \theta_1/\theta_1\ \sin\ \theta_1 \ldots\ldots\ldots\ldots \quad (7.21)$$

The magnification M_1 due to the first lens at the second lens is derived in Appendix (A10), and the equation A10.9 is

$$M_1 = r_2 = -(u/S)\theta_1 \sin\theta_1 = \cos\theta_1 - (L/S)\theta_1 \sin\theta_1 \quad \ldots\ldots \quad (7.22)$$

The total spiral distortion D_{Tsp} of the final image is

produced from the contribution from the final lens and that from the first lens i.e. an amount equal to $D_{sp}(1)/M_1^2$.

In the rotation free system the D_{Tsp} takes the value

$$DT_{sp} = D_{sp}(1)/M_1^2 - D_{sp}(2) \quad \text{----------} \quad (7.23a)$$

by substituting the values of parameters in equations (7.1) (7.11) and (7.22) the value of DT_{sp} may be written as

$$DT_{sp} = \frac{1}{8u^2}\left[\frac{4\theta_1 + \sin 2\theta_1}{\sin^2\theta_1} - 4u^2\theta_2^3 - u^2\theta_2^2\sin 2\theta_2 - 4\theta_2 - 2u\theta_2 + \sin 2\theta_2 + 2u\theta_2\cos 2\theta_2\right] \quad \text{---} \quad (7.23b)$$

Fig. (7.6) shows the curve of DT_{sp} versus $(\frac{NI}{V^{\frac{1}{2}}})$ (i.e. $\theta_1/0.186$) for various L/d

Also the final magnification of the system (M_F) found by the equation A10.20 is plotted in the same figure. By using a fixed distance DT_{sp} again is plotted as a function of $(NI/V^{\frac{1}{2}})$, for various values of θ_2 (fig. 7.7).

It is clear mathematically from 7.23 that there is no minimum value for $DT_{sp} \to -\infty$. But we can find a solution for any value of DT_{sp}. By rewriting 7.23 using the symbol D instead of DT_{sp} to avoid difficulties

$$8u^2D = \frac{4\theta_1 + \sin 2\theta_1}{\sin^2\theta_1} - 4u^2\theta_2^3 - u^2\theta_2^2\sin 2\theta_2 - 4\theta_2 - 2u\theta_2 + \sin 2\theta_2 + 2u\theta_2\cos 2\theta_2 \quad \text{.....} \quad (7.24)$$

then equation 7.24 takes the form

$$u^2(8D + 4\theta_2^3 + \theta_2^2\sin 2\theta_2) + u(2\theta_2 - 2\theta_2\cos 2\theta_2) + \left(\frac{-4\theta_2 - \sin 2\theta_1}{\sin^2\theta_1} + 4\theta_2 - \sin 2\theta_1\right) = 0 \quad \text{.....} \quad (7.25)$$

It is clear that this equation is a second order equation and can be solved by the relation

$$u = \frac{-B \pm [B^2+4AC]^{\frac{1}{2}}}{2A} \quad \ldots\ldots\ldots\ldots (7.26)$$

where $$A = 8D+4\theta_2^3+\theta_2^2 \sin 2\theta_2 \quad \ldots\ldots\ldots\ldots (7.26a)$$

$$B = 2\theta_2-2\theta_2 \cos 2\theta_2 \quad \ldots\ldots\ldots\ldots\ldots (7.26b)$$

and $$C = \frac{-4\theta_1-\sin 2\theta_1}{\sin^2\theta_1} + 4\theta_2-\sin 2\theta_2 \quad \ldots\ldots\ldots (7.26c)$$

We are concerned with the case where $DT_{sp} = 0$, so it is necessary to put D=0 in the equation 7.25 and 7.26a to obtain the suitable distance between the two lenses in a certain value at θ_1 and θ_2. It is useful to know that the general equation (7.26) is valid only for positive u.

Special cases :

By operating the projector lens at an excitation of $NI/V_r^{\frac{1}{2}} = 8.43$ [i.e. $\theta_2=\pi/2$] which is in the region of maximum magnification and low radial distortion, the parameters A, B and C take the values

$$A = \pi^3/2 \ . \quad B = 2\pi \ , \quad C = \frac{-4\theta_1-\sin 2\theta_1}{\sin^2\theta_1} + 2\pi$$

Equation 7.26 then becomes

$$u/S = -\frac{2}{\pi^2} \pm \frac{1}{\pi^3} \left[4\pi^2 - 2\pi^3 \left(\frac{-4\theta_1-\sin 2\theta_1}{\sin 2\theta_1} + 2\pi\right)\right]^{\frac{1}{2}} \quad \ldots\ldots (7.27)$$

Assuming that the corrector lens is operated at an excitation which is an odd multiple of $\pi/2$ (i.e. $\theta_1 = n\pi/2$) where n is odd number, it follows then that

$$u/S = L_1/S = \frac{-2 \pm \sqrt{1+\pi^2(n-1)}}{\pi^2} \quad \ldots\ldots\ldots (7.28)$$

For values of n=3, 5 and 7 a spiral distortion correction is obtained at the distances (L_1/S)=0.72, 1.08 and 1.37 respectively. That is mean spiral distortion can be corrected under special conditions of θ_1 and

θ_2 by choosing the suitable distance between the two lenses.

It may be useful to look at the results of some other special cases of θ_2 such as $\pi/4$, $3\pi/4$ and $3\pi/2$. To avoid unnecessary repetition of elaborate mathematical derivations, the final results obtained from equation 7.26. for $\theta_1 = n\pi/2$ are tabulated in table 7.1.

Table 7.1
The values of $u/S = L_1/S$ in which $DT_{sp} = 0$

$\theta_1 \rightarrow$ $\theta_2 \downarrow$	$\theta_1 = \pi/2$	$\theta_1 = 3\pi/2$	$\theta_1 = 5\pi/2$	$\theta_1 = 7\pi/2$
$\pi/4$	1.0029	2.2683	3.0916	3.7511
$\pi/2$	0.0	0.7202	1.0866	1.3698
$3\pi/4$	L_1/S is negative	0.3919	0.6273	0.8007
$3\pi/2$	L/S is negative	0.0	0.1522	0.2235

From the above analysis, it is clear that it is impossible to obtain spiral distortion correction with the condition $\theta_1 = \theta_2$.

This shows that spiral distortion can be corrected. For the excitation $NI/V_r^{\frac{1}{2}}$ of the correcting lens greater than the value at which the spiral correction occurs, the spiral distortion appears to be increased again without reverse of sign. However, the above results are sufficient to indicate

the feasibility of correcting spiral distortion by using two twin-pole lenses. Another advantage of this arrangement in the TEM is the reduction in the length of the viewing chamber.

The investigation of the system with two single pole lenses came as a result of the work done on the two square-top field system. When a system with two single pole lenses is used, it is found that no correction is achieved when the two lenses have the same excitation parameter. In this type of arrangement, the spiral distortion vanishes when the radial distortion approaches infinite values (i.e. the excitation parameter in which telescopic ray path takes place). When the radial distortion vanishes, the spiral distortion takes a value lower than that for one single-pole lens.

8. CONCLUSION

Theoretical and experimental investigations have been carried out for conical, cylindrical and ellipsoidal polepiece shapes in a single polepiece magnetic lens. The uniformly magnetized sphere model appears to account well for the measured focal properties of sirgle polepiece lenses. This model is also remarkably close to the field distribution of other kinds of single pole lenses with non-spherical polepieces. This mode therefore provides a firm basis for understanding single polepiece lenses and their application in electron microscopy and electron microanalysis. It has been shown experimentally that a uniformly magnetized ellipsoid gives essentially the same kind of field distribution as a magnetized sphere. However, further analysis of the field from a solid is required.

When a single-polepiece is used as a projector lens, there is a preferred direction of the asymmetrical field. Thus the incoming parallel electron beam from the objective lens should be incident on the sloping part of the field. This was proved theoretically using the spherical field model. This has also been confirmed using some real field distributions. To supplement these theoretical conclusions, experimental work was undertaken in collaboration with Juma (Appendix 8) using a 100kV lens. These experimental results fully confirm the above conclusions. As a practical example,in a TEM projector when the polepiece tip faces the incoming electron beam, the resulting distortion at maximum magnification, for a given projection distance, is about 44% less than that for the

corresponding value for conventional symmetrical projector lens. What is more significant, however, is that this spiral distortion can be corrected completely using two single polepiece lenses facing each other. This has been shown mathematically, and experiments by colleagues are now in progress to varify this result.

The question as to whether there is a "correct" orientation of the single polepiece lenses in an objective lens is still difficult to answer. This analysis of computed focal properties for an objective lens using the spherical field distribution as well as other real distributions indicates that at an excitation parameter $NI/V_r^{\frac{1}{2}} \simeq 14$ and with an arrangement in which the incoming illuminating beam is incident at the sloping edge of the field (the preferred direction for a projector) leads to essentially smaller spherical aberration coefficient than that obtained with an arrangement in which the poleface is turned through 180°. However, in this second arrangement, the spherical aberration is strongly dependent upon the field inside the snout. So, as the field distribution inside the snout becomes more steep, the spherical aberration becomes higher. It is generally true for this mode of operation that there is no optimum excitation for minimum spherical aberration. The C_s value falls steadily with excitation, levelling off at excitation parameters in the region of $NI/V_r^{\frac{1}{2}} \simeq 45$. It should be pointed out that since this excitation is much higher than in the first mode, it will usually be necessary to scale up the lens dimensions to avoid magnetic saturation of the polepiece. Each lens therefore should be

designed individually according to the special requirements of a particular instrument (TEM, STEM or SEM objective). In some cases it may be advantageous to use the single polepiece lens as a 'condenser-objective' at low aberration.

Finally, the relevant calculations show that chromatic change in magnification and in rotation for single polepiece projector lenses are similar to those for double pole lenses. However, for an objective lens, there is a preferred direction in which these aberrations are somewhat lower than those of conventional lenses.

We can therefore conclude that it is feasible to construct an entire electron microscope (TEM or STEM) using single polepiece lenses. They will produce a final image with significantly lower aberrations than those of conventional lenses.

In addition, the inherently compact form of these lenses will result in a significant reduction in the length of the electron optical column.

9. REFERENCES

Alshwaikh, A. and Mulvey, T. (1977) Development in Electron Microscopy and Analysis 1977, ed. D.L. Misell. Institute of Physics London. Conference Series No. 36, Chap.1. pp. 25-28.

Basset, R. and Mulvey, T. (1969) Zeitschrift für angewandte Physik, 27, 1969, 142-145.

Becker, H. and Wallraff, A. (1940) Arch. Elektrotech.34, 115-120.

Christofides, S. (1978) Final year project report, University of Aston in Birmingham

Chrsitofides, S. (1979) Private communication, Aston University.

Cosslett, V.E. (1946) Introduction to electron optics, Oxford University Press (1946)

Der-Schwartz, G.V. and Markarova, I.S. (1968), Radio Engineering and electronic physics, 13, No. 7, 1100-1103

Der-Schwartz, G.V. and Rachkov, V.P. (1965) R.E.E.P,10, 783-789.

Dietrich, I. ,Fox, F, Knapek, E. Lefrance,G.Nachtrieb,K.Weyl,P.and Zerbst,H.(1977) Ultramicroscopy,2,1977, pp.241-249.

Durand, E. (1966) Electrostatique pp. 241-305, Masson et cie, Paris

Durand, E. (1968) Magnetostatique pp. 350-351, Masson et cie, Paris

Durandeau, P. and Fert, C. (1957), Rev.Opt.Theor.Instrum. 36, 205-234

Elkamali, H. (1978) Private Communication, Aston University

Elkamali, H. and Mulvey, T. (1977) Developments in Electron Microscopy and Analysis 1977, ed. D.L. Misell. Institute of Physics London Conf.Ser.No.36, Chap.1 pp.33-34

Ewing, (1891) Magnetic induction in iron and other metals pp.24-26 3rd ed. (1900) Cambridge University Press

Ferrier, (1978) Private Communication, Glasgow University

Fert, C. and Durandeau, P. (1957) Focusing of charged particles Vol. 1, Ed. A. Septier, Academic Press

Glaser, W. (1933), Z. Physik 81, 647

Glaser, W. (1941), Z. Physik 117, 285

Glaser, W. (1941b), Z. Physik 118, 264

Glaser, W. (1952), Grundlagen der Elektronenoptik, pp.306-307, Springer

Grivet, P. (1972), Electron Optics, pp.164-170, Pergamon Press

Haine, M.E. and Page, R.S. (1956) Proc. 5th Eur.Conf. Elect.Micros. (Stockholm) pp.32-34

Hawkes, P.W.(1968) J. Physics Dr 1, 131, 1968

Hawkes, P.W. (1972) Electron Optics and Electron Microscopy, pp.70-71, Taylor and Francis Ltd.

Herrman, K.H. Ihmann, K. and Krahl, D. (1974), Eighth International Congress on Electron Microscopy, Canberra, Vol.1, pp.132-133

Hillier, J. (1946) J. App. Phys. 17, 411-419

Huang Lain-You (1977) Acta Physica Vol.26, No.3, May 1977 (In Chinese)

Jahnke, E., Emde, F., and Lösch, F. (1960) Tables of higher function 6th ed. McGraw-Hill Book Co. New York, pp. 195

Juma, S.M. and Alshwaikh, A. (1979) (To be published)

Juma, S.M. and Mulvey, T. (1974) Electron Microscopy 1974 eds. J.V. Sanders and N.J. Goodchild, Australian Academy of Science, Canberra, Vol. 1, pp.143-135

Juma, S.M. (1975) Ph.D. Thesis, The University of Aston in Birmingham

Juma, S.M. and Mulvey, T. (1975) Development in Electron Microscopy and Analysis (EMAG 75) Ed. J.A. Venables, pp.45-48, Academic Press (1976)

Kamminga, W., Verster, J.L. and Franken, J.C. (1968) Optik 28, 442-461

Kanaya, K. (1955) Researches of the electrotechnical lab No. 548 (1955) 1. pp.8-67

Kanaya, K. (1958) Bull, Electrotech. Lab. (Tokyo) 22, 615-622

Kanaya, K., Baba, N. and Ono, S. (1976) Optik 46, (1976) No.2, 125-148

Kanaya, K., Ishikawa, A. (1958) Bull, Electrotech. Lab. (Tokyo) 22, 641-646

Kelvin (Thomson W) (1872) in "Reprints of papers on electricity and magnetism" 2nd Ed. (London, Macmillan 1884) pp.489-491

Kūbozoe, M., Sato, H., Kasai, S. and Ozasa, S. (1978) J. Electron Micros. 27,No.2, 83-87

Klemperer, O. and Barnett, M.E. Electron optics 3rd Ed. Cambridge University Press (1971) pp. 213-

Kynaston, D. and Mulvey, T. (1963) Journal of Applied Physics, 14, 199-206

Lambrakis, E., Marai, F.Z. and Mulvey, T. (1977) Development in Electron Microscopy and Analysis 1977, ed. D.L. Misell, Institute of Physics, London, Conf.Ser.No.36, pp.35-38

Lenz, F. (1950) Optik, 7, 243-253

Lenz, F. (1951) Annalen der Physik, 9, 245-258

Liebmann, G. (1951) Proc. phys.Soc. B64, 972-977

Liebmann, G. (1952) Proc. Phys.Soc. B65, 94-108

Liebmann, G. (1955) Proc.Phys.Soc. B68, p.679

Liebmann, G. and Grad, E.M. (1951), Proc.Phys.Soc. B64, 956-971

Marai, F.Z. (1977), Ph.D. Thesis, The University of Aston in Birmingham

Marai, F.Z. and Mulvey, T. (1974) Electron Microscopy 1974, eds. J.V. Sanders and N.J. Goodchild, Australian Academy of Science, Canberra, Vol.1, 130-131

Marai, F.Z. and Mulvey, T. (1975) Developments in Electron Microscopy and Analysis, ed. J.A. Venables, pp.43-44, Academic Press (1976)

Marai, F.Z. and Mulvey, T. (1977) Ultramicroscopy, 2, 187-192

Marton, L. and Hutter, R.G. (1944) Proc. IRE 32, 3-12, 546-52

McLachlan, N.W. (1955) Bessel functions for engineers, 2nd ed., Oxford at the Clarendon Press, 1955

Morito, N. (1953) J.Appl.P.25, No.8 (August 1954)

Morito, N. (1957) J. Electronmicroscopy, 5, 1957

Morito, N. Tadana, B., and Katagiri, S. (1972) J. Electronmicroscopy,7, 1959

Moses, R.W. (1972) Electron Microscopy 1972, ed. W.C. Nixon, Inst. Phys.Conf.Series 14 (1972) (Proc.Fifth European Congress in Electron Microscopy, 1972)

Mulvey, T. (1967) in "Focusing of charged particles", Vol.1, Chapter 26, Academic Press Inc. New York

Mulvey, T. (1971) Electron Microscopy and Analysis, Proc. 25th Anniversary Meeting of EMAG Inst.Phys. 19

Mulvey, T. (1974) Proc.Seventh Annual Scanning Electron Microscopy Symposium, Chicago, Illinois, U.S.A. pp.43-49

Mulvey, T. (1976) Proc.6th Eur.Conf.Micros. ed. D.G. Brandon (Tel Aviv) 1, 59-64

Mulvey, T. and Newman, C. (1972), Fifth European Congress on Electron Microscopy, pp.116-117

Mulvey, T. and Newman, C.D. (1973a), Scanning electron microscopy: System and applications, pp.16-21, Institute of Physics

Mulvey, T. and Newman, C.D. (1973b) High voltage electron microscopy ed. P.R. Swann, C.J. Humphreys and M.J. Goringe, (Proc.3rd Int.Conf.H.V.Micros. Oxford 1973), Academic Press 1974

Mulvey, T. and Wallington, M. (1969) J. Sci. Inst. (J. of Physics E) pp.

Mulvey, T. and Wallington, M.J. (1973) Rep.Prog.Phys. 36, 347-421

Munro, E. (1972) Ph.D. Thesis, Cambridge University

Munro, E. and Wells, (1976) Scanning electron microscopy ed. O. Johari and I. Corvin

Nasr, H. (1978) M.Sc. Thesis, University of Aston in Birmingham

Newman, C.D. (1976) Ph.D. Thesis, The University of Aston in Birmingham

Prebus, A.F. (1942) Eng.Exp.Sta.News, 14 , 6-32, Ohio State University.

Ramsey, A.C. (1964) Electricity of magnetism, Cambridge University Press (1964)

Ridha, A . (1977) M.Sc. Thesis, University of Aston in Birmingham

Riecke, W.D. (1962) Optik, 19, 169-207

Riecke, W.D. and Ruska, E. (1966) Sixth Int.Cong. for Electron Microscopy, Kyoto, Vol. 1, 19-20

Ruska, E. (1934) Z.S. of phys. 87, 580-602

Scherzer, O. (1936) Z.Pys. 101, 593-603

Scherzer, O. (1937) in "Beiträge zur Elektronenoptik" ed. H. Busch and E. Brüche , J.A. Barth, Leipzig, pp.33-41

Shirota, K., Yonezawa, A. and Yanakas, T.JEOL News Vol.14e pp.9-10 (1977)

Stabenow, G. (1935) Zeits.phys. 96, 634-642

Szilagyi, M. (1976) Optik, 48, No.2, 215-224

Szilagyi, M. (1977) Optik, 49, No.2, 223-246

Tretner, W. (1959) Optik, 16, 155

Trowbridge, C.W. (1972) with Newman, M.J. Turner, L.R., Proc. 4th Int.Conf. on Magnet Technology, Brookhaven

Webster, A.G. (1897) The theory of Electricity and Magnetism pp.210-375 Macmillan and Co. 1897, New York

Yada, K. and Kawakatsu, H. (1976), J.Elec.Micros. 25, part 1, 1-9

Yanaka, T. and Watanabe, M. (1966) Proc. 6th Int. Cong.Elec.Micros., Kyoto, Japan, 141-142

Tables

(1) Tables of Bessel functions of fractional order prepared by the Computation Lab. of the National Applied Mathematics Lab. National (N.A.M.L.) Bureau Standards, New York, Columbia University Press 1948

(2) Tables of the Bessel functions of the first kind of orders zero and one by the staff of the Computation Laboratory, Harvard University Press 1947.

10. APPENDICES

10.1 Computer Program 'DATA-BZ'

```
      TRACE 1
      TRACE 2
      MASTER  ADIL
C     THIS PROGRAM USED TO CALCULATE THE FIELD DIS. OF THE COILS.
      REAL MUO
      DIMENSION A1(112),A2(112),A10(112),A11(112),A20(112),A22(112),
     1AS(112),AP(112),AZ(112),BZ(112),AZA(112),X(112)
      MUO=4.*3.14*(10.**(-7.))
      Z=0.0
  100 READ(1,3)D1,D2,S,P
    3 FORMAT(3F8.5,F8.1)
      WRITE(2,110)D1,D2,S,P
  110 FORMAT(1H1,3X,F7.3,7X,F7.3,6X,F7.3,6X,F8.1)
      ALPHA=D2/D1
      BETA=S/D1
      WRITE(2,999)ALPHA,BETA
  999 FORMAT(1H ,8X,F8.5,8X,F8.5)
      A0=MUO/(2.*D1*BETA*(ALPHA-1.))
   99 DO 5 K=1,112
      A1(K)=BETA-Z
      A2(K)=BETA+Z
      A10(K)=1.+SQRT(1.+A1(K)*A1(K))
      A11(K)=ALPHA+SQRT(ALPHA*ALPHA+A1(K)*A1(K))
      A20(K)=1.+SQRT(1.+A2(K)*A2(K))
      A22(K)=ALPHA+SQRT(ALPHA*ALPHA+A2(K)*A2(K))
      AS(K)=A1(K)*ALOG(A11(K)/A10(K))
      AP(K)=A2(K)*ALOG(A22(K)/A20(K))
      AZ(K)=(AS(K)+AP(K))*A0
      X(K)=Z
      BZ(K)=AZ(K)*P
      WRITE(2,20)Z,BZ(K),AZ(K)
   20 FORMAT(1H ,F5.1,8X,F14.8,8X,F17.11)
      IF(Z-4)6,8,8
    6 Z=Z+0.1
      GO TO 5
    8 Z=Z+0.5
    5 CONTINUE
      STOP
      END
```

10.2 Computer Program ' CABERRATION'

```
      TRACE 1
      MASTER  ADIL
      THIS PROGRAM IS USED TO EXAMINE THE CUBIC RELATION FIELD
      THE RESULTS ARE WITH RESPECT TO HALF WIDTH VALUE
      THIS PROGRAM TO EXAMINE THE CUBIC RELATION FIELD
      THE RESULTS RESPECT TO HALF WIDTH VALUE
      THE PROGRAM USES THE MEAN VALUE OF AZ BETWEEN THE TWO Z INTERVALS TO
      CONSTRUCT THE ELECTRON TRAJECTORY USING THE PARAXIAL RAY EQUATION.
      DIMENSION XH(182),GH(182),AZM(182),FM1(182),FM2(182),RMA(182),
     1RM1(182),RH(182),AZ(182),BZ(182),AZA(182),X(182)
      DIMENSION G1(181),F1(181),F2(181),R(181),R1(181)
      DIMENSION AZC(182),AZ1(182),AZ1C(182),RA(182),RAC(182),RAS(182),
     1R1AC(182),R1A(182),H(182) ,PAD(182),G(182),GA(182),AZD(182)
      S=SQRT(1.6*10.**(-19.)/(9.1*(10.**(-31.))*8.))*6.534*10.**(-7.)
      READ(1,44)N


 44   FORMAT(I4)
      Z=+54.00
 99   DO 5 K=1,N
      AZ(K)=56.895767/(3.346+Z)**3.
      X(K)=Z
      IF(K.EQ.1) GO TO 3
      AZA(K)=(AZ(K)+AZ(K-1))/2.0
      AZC(K)=AZA(K)**2.
      AZD(K)=AZC(K)*AZA(K)
      AZ1(K)=(AZ(K)-AZ(K-1))/(X(K)-X(K-1))
      AZ1C(K)=AZ1(K)*AZ1(K)
      IF(Z-4.000)6,6,8
  6   Z=Z-0.1
      GO TO 5
  3   R(K)=1.0
      R1(K)=0.0
  8   Z=Z-0.5
  5   CONTINUE
      DO 20 K=1,N
      AZM(K)=AZA(N+2-K)
      XH(K)=X(N+1-K)
 20   CONTINUE
      WRITE(2,999)
999   FORMAT(//,4X,' H1/SQRT(VR)',9X,' FPROJ(M)',18X,' DRADIAN(M(-2))',9
     1X,' DSPIRE(H(-2))',5X,'QR',10X,'QS')
```

```
    9 READ(1,11)R0,R01,P1
   11 FORMAT(2F4.1,F5.1)
      IF(P1)13,0,0
      AB1=0.0046943*P1**2.
      AB2=6.*AB1
      AB3=SQRT(2.0*AB1)**3./4.
      AB4=2.*AB1
      RH0=1.0
      RM01=0.0
      DO 7 K=2,N
      Z0=X(K)-X(K-1)
      G1(K)=S*AZA(K)*P1
      F1(K)=COS(G1(K)*Z0)
      F2(K)=SIN(G1(K)*Z0)
      R(K)=R0*F1(K)+R01*F2(K)/G1(K)
      RA(K)=(R(K)+R(K-1))/2.
      RAC(K)=RA(K)*RA(K)
      RAD(K)=RAC(K)*RA(K)
      R1(K)=R01*F1(K)-G1(K)*R0*F2(K)
      R1A(K)=(R(K)-R(K-1))/(X(K)-X(K-1))
      R1AC(K)=R1A(K)*R1A(K)
      H(K)=R1AC(K)/RAC(K)
      ZM=(XM(K)-XM(K-1))
      GM(K)=S*AZM(K)*P1
      FM1(K)=COS(GM(K)*ZM)
      FM2(K)=SIN(GM(K)*ZM)
      RM(K)=RM0*FM1(K)+RM01*FM2(K)/GM(K)
      RMA(K)=(RM(K)+RM(K-1))/2.
      RM1(K)=RM01*FM1(K)-GM(K)*RM0*FM2(K)
      RM0=RM(K)
      RM01=RM1(K)
   28 R0=R(K)
      R01=R1(K)
      IF(K.LT.N) GO TO 7
      FPROJ=1./R1(K)
    7 CONTINUE
      FS=FPROJ*FPROJ



      DO 40 K=2,N
      GA(K)=-RMA(N+2-K)*FPROJ
   40 CONTINUE
      FD=0.0
      FSD=0.0
      DO 10 K=2,N
      DX=X(K)-X(K-1)
      FD=FD+(AZ1C(K)+AB2*(AZC(K)**2.)-H(K)*AZC(K))*RAD(K)*GA(K)*DX
      FSD=FSD+(3.+H(K)/(AB4*AZC(K)))*AZD(K)*RAC(K)*DX
   10 CONTINUE
      AD=3.0/(8.0*FS)+AB1*FD
      SD=AB3*FSD
      QR=SQRT(ABS(AD))*FPROJ
      QS=SQRT(ABS(SD))*FPROJ
      WRITE(2,112)P1,FPROJ,AD,SD,QR,QS
  112 FORMAT(1H ,5X,F8.4,8X,F17.7,8X,F17.7,8X,F14.8,5X,F7.3,5X,F7.3)
      GO TO 9
   13 STOP
      END
```

10.3 Computer Program 'CDISTORTIØN

```
      TRACE 1
      TRACE 2
      MASTER  ADIL
C     THIS PROGRAM IS USED TO EXAMINE THE CUBIC RELATION FIELD
C     THE RESULTS ARE WITH RESPECT  HALFWIDTH VALUE
C     THE PROGRAM USES THE MEAN VALUE OF AZ BETWEEN THE TWO Z INTERVALS
C     CONSTRUCT THE ELECTRON TRAJECTORY USING THE PARAXIAL RAY EQUATION
      DIMENSION A1(175),A2(175),A10(175),A11(175),A20(175),A22(175),
     1AS(175),AP(175),AZ(175),BZ(175),AZA(175),X(175)
      DIMENSION G1(175),F1(175),F2(175),R(175),R1(175)
      DIMENSION AZC(175),AZ1(175),AZ1C(175),RA(175),RAC(175),RAS(175),
     1R1AC(175),R1A(175),H(175)
      AMUO=6.5345*10.**(-7.)
      G=SORT(0.2*10.**(12.)/9.1)*AMUO
      READ(1,77)N



   77 FORMAT(I4)
      Z=-54.00
   99 DO 5 K=1,N
      AZ(K)=56.895767/(3.8401538+Z)**3.
      X(K)=Z
      IF (X(K).GT. 0.000) GO TO 4
      AZH=AZ(K)
    4 IF(K.EQ.1)GO TO 3
      AZA(K)=(AZ(K)+AZ(K-1))/2.0
      AZC(K)=AZA(K)**2.
      AZ1(K)=(AZ(K)-AZ(K-1))/(X(K)-X(K-1))
      AZ1C(K)=AZ1(K)*AZ1(K)
      IF(Z-4.000)6,6,8
    6 Z=Z-0.1
      GO TO 17
    3 R(K)=1.0
      R1(K)=0.0
    8 Z=Z-0.5
   17 WRITE(2,25)K,X(K),AZ(K)
   25 FORMAT(I5,2F10.7)
    5 CONTINUE
      WRITE(2,300)AZH
  300 FORMAT(1HC,10X,5H AZM=,F14.11)
      WRITE(2,500)
  500 FORMAT(1H1,8X,3H ZF,5X,9H NI/V**1/2,8X,3H CC,14X,3H CS,13X,5H FOBJ,
     111X,4H CSM,10X,6H FOBJM)
```

```
  9 READ(1,11)R0,R01,P1
 11 FORMAT(2F4.1,F5.1)
    IF(P1)13,0,0
    AB1=(G*P1)**2.
    AB2=3.*AB1
    AB3=AB1/2.
    DO 7 K=2,N
    Z0=(X(K)-X(K-1))
    G1(K)=G*AZA(K)*P1
    F1(K)=COS(G1(K)*Z0)
    F2(K)=SIN(G1(K)*Z0)
    R(K)=R0*F1(K)+R01*F2(K)/G1(K)
    RA(K)=(R(K)+R(K-1))/2.
    RAC(K)=RA(K)*RA(K)
    RAS(K)=RAC(K)*RAC(K)
    R1(K)=R01*F1(K)-G1(K)*R0*F2(K)
    R1A(K)=(R(K)-R(K-1))/(X(K)-X(K-1))
    R1AC(K)=R1A(K)*R1A(K)
    H(K)=R1AC(K)/RAC(K)
    IF(R(K))31,31,28
 31 U1C=R1AC(K)
    FOBJ=1./R1A(K)
    ZF=X(K)
    GO TO 29
 28 R0=R(K)
    R01=R1(K)
    IF(K.LT.N) GO TO 7
    U1C=R1AC(K)
    FOBJ=1./R1A(K)
    ZF=FOBJ*R(K)
  7 CONTINUE
 29 U1S=U1C*U1C
    FC=0.0
    FS=0.0
    DO 10 K=2,N
    DX=(X(K)-X(K-1))

    FC=FC+AZC(K)*RAC(K)*DX
    FS=FS+(AZ1C(K)+AB2*(AZC(K)**2.)-H(K)*AZC(K))*RAS(K)*DX
    IF(R(K))27,27,10
 10 CONTINUE
 27 CC=(AB1*FC)/U1C
    CS=(AB3*FS)/U1S
    CSM=CS*AZM*(10.**6.0)*P1*AMUO
    FOBJM=FOBJ*AZM*(10.**6.0)*P1*AMUO
    WRITE(2,112)ZF,P1,CC,CS,FOBJ,CSM,FOBJM
112 FORMAT(1H ,5X,F8.4,5X,F5.1,5X,F12.7,5X,F12.7,5X,F12.7,5X,F10.5,5
   1F10.5)
    GO TO 9
 13 STOP
    END
```

10.4 Computer Program ' PREFIELD'

```
      TRACE 1
      MASTER  ADIL
C     THIS PROGRAM IS USED TO EXAMINE THE CUBIC RELATION FIELD
C     THE PROGRAM USES THE MEAN VALUE OF AZ BETWEEN THE TWO Z INTERVALS TO
C     CONSTRUCT THE ELECTRON TRAJECTORY USING THE PARAXIAL RAY EQUATION
      DIMENSION A1(222),A2(222),A10(222),A11(222),A20(222),A22(222),
     1AS(222),AP(222),AA(222),BZ(222),AZA(222),X(222)
      DIMENSION G1(222),F1(222),F2(222),R(222),R1(222)
      DIMENSION AZC(222),AZ1(222),AZ1C(222),RA(222),RAC(222),RAS(222),
     1R1AC(222),R1A(222),H(222)
      AMUO=6.5345*10.**(-7.)
      G=SQRT(0.2*10.**(12.)/9.1)*AMUO
      Z=-10.0
      N=201
   99 DO 5 K=1,N

      AZ(K)=56.895707/(5.846+Z)**3.
      X(K)=Z
      IF (X(K).EQ.0.00)AZM=AZ(K)
      IF(K.EQ.1)GO TO 3
      AZA(K)=(AZ(K)+AZ(K-1))/2.0
      AZC(K)=AZA(K)**2.
      AZ1(K)=(AZ(K)-AZ(K-1))/(X(K)-X(K-1))
      AZ1C(K)=AZ1(K)*AZ1(K)
      WRITE(2,18)K,X(K),AZ(K),AZ1(K)
   18 FORMAT(1H ,I4,5X,F10.6,5X,F9.6,5X,F12.6)
      Z=Z-0.05
      GO TO 5
    3 R(K)=1.0
      R1(K)=0.0
      Z=Z-0.05
    5 CONTINUE
      WRITE(2,300)AZM
  300 FORMAT(1H0,10X,5H AZM=,F14.11)
      WRITE(2,110)
  110 FORMAT(//,25X,'ELECTRON OPTICAL PROPERTIES OF MAGNETIC PREFIELDS')
      WRITE(2,111)
  111 FORMAT(//,9X,'ZOBJ',9X,'M',4X,'NI/SQRT(VR)',6X,'ZPRE/D',11X,'FPRE/
     1D',11X,'CC',11X,'CS',13X,'R(ZF1)')
```

```
  9 READ(1,11)P1,ZF1
 11 FORMAT(F5.1,F0.3)
    IF(P1)13,0,0
    FC=0.0
    FS=0.0
    R0=1.0
    R01=0.0
    AB1=(G*P1)**2.
    AB2=3.*AB1
    AB3=AB1/2.
    M=INT((10.0-ZF1)/0.05+0.5)+1
    DO 7 K=2,M
    Z0=(X(K)-X(K-1))
    G1(K)=G*AZA(K)*P1
    F1(K)=COS(G1(K)*Z0)
    F2(K)=SIN(G1(K)*Z0)
    R(K)=R0*F1(K)+R01*F2(K)/G1(K)
    RA(K)=(R(K)+R(K-1))/2.
    RAC(K)=RA(K)*RA(K)
    RAS(K)=RAC(K)*RAC(K)
    R1(K)=R01*F1(K)-G1(K)*R0*F2(K)
    R1A(K)=(R(K)-R(K-1))/(X(K)-X(K-1))
    R1AC(K)=R1A(K)*R1A(K)
    H(K)=R1AC(K)/RAC(K)
    R0=R(K)
    R01=R1(K)
    DX=(X(K)-X(K-1))
    FC=FC+AZC(K)*RAC(K)*DX
    FS=FS+(AZ1C(K)+AB2*(AZC(K)**2.)-H(K)*AZC(K))*RAS(K)*DX
    IF(K.LT.M) GO TO 7
    U1C=R1AC(K)
    FPRE=+1./R1(K)
    ZPRE=FPRE*R(K)+ZF1
    RZF=R(K)
    GO TO 29
  7 CONTINUE
 29 U1S=U1C*U1C
    CC=(AB1*FC)/U1C
    CS=(AB3*FS)/U1S



    WRITE(2,112)ZF1,M,P1,ZPRE,FPRE,CC,CS,RZF
112 FORMAT(/,1H ,5X,F8.4,5X,I5,5X,F6.2,5X,F12.7,5X,F12.7,5X,F10.5,5X,F
   110.5,5X,F8.4)
    GO TO 9
 13 STOP
    END
```

10.5 Computer Program 'SPIRALCOREC'

```
      TRACE 1
      MASTER STF1
      DIMENSION P(66),BS(66),AKS1(66),AD1(66),AD2(66),AD3(66),X(66)
      DIMENSION U(66),US(66),AM1(66),AM2(66),DSP1(66),DSP2(66),DSPT(66),
     1FPROJ(66),QS(66),AMF(66)
      THIS PROGRAMM TO INVESTIGATE THE POSSIPILITY TO CORRECT SPIRALDIS.
      BY USING TOW SUCCESSIVE SQUARE TOP FIELD BY SEBARATION 'L'
      REAL L
      PI=22.0/7.0
      PIS=PI*PI
      PIC=PIS*PI
      PF=8.43
      AL2=100.0
      BSF=4.*PI*10.**(-7.)*PF
      AKSF=SQRT(1.6*10.**(-19.)/(9.1*(10.**(-31.))*8.))*BSF


      ADF1=SIN(2.0*AKSF)
      ADF2=COS(2.0*AKSF)
      V=AKSF
    3 READ(1,4)L
    4 FORMAT(F7.4)
      IF(L)9,0,0
      WRITE(2,6)L
    6 FORMAT(F7.4)
      WRITE(2,7)
    7 FORMAT(1H ,3X,'NI/SQRT(VR)',4X,'FPROJ',8X,'DSPIRAL1',6X,'DSPIRAL2'
     1,5X,'DSP.TOTAL',9X,'QS',9X,'FIR.MAG.',5X,'F.MAG./L2')
      DO 5 K=1,66
      P(K)=FLOAT(K)
      BS(K)=4.*PI*10.**(-7.)*P(K)
      AKS1(K)=SQRT(1.6*10.**(-19.)/(9.1*(10.**(-31.))*8.0))*BS(K)
      AD1(K)=SIN(AKS1(K))
      AD2(K)=COS(AKS1(K))
      AD3(K)=AD1(K)*AD1(K)
      X(K)=-AD2(K)/AKS1(K)/AD1(K)
      U(K)=L+X(K)
      US(K)=U(K)*U(K)
      DSP1(K)=AKS1(K)**3.0/2.0+AKS1(K)*AKS1(K)*SIN(2.0*AKS1(K))/8.0
      IF(U(K)) 10,10,11
   10 DSP2(K)=0.0
      GO TO 12
   11 DSP2(K)=1.9378923*0.78539816/US(K)*0.78539816/U(K)
   12 AM1(K)=AD2(K)-L*AKS1(K)*AD1(K)
      DSPT(K)=DSP1(K)/AM1(K)/AM1(K)-DSP2(K)
      FPROJ(K)=-1.0/(AKS1(K)*AD1(K)*COS(AKSF)+AKSF*AD2(K)*SIN(AKSF)-AKS1
     1(K)*AKSF*L*AD1(K)*SIN(AKSF))
      AMF(K)=-2./PI*AKS1(K)*AD1(K)-PI/2.0*AL2*AM1(K)
      QS(K)=ABS(FPROJ(K))*DSPT(K)/SQRT(ABS(DSPT(K)))
      WRITE(2,8)P(K),FPROJ(K),DSP1(K),DSP2(K),DSPT(K),QS(K),AM1(K),AMF(K
     1)
    8 FORMAT(1H ,5X,F6.2,5X,F8.4,5X,F9.4,5X,F9.4,5X,F9.4,5X,F9.2,5X,F8.4
     1,5X,F10.2)
    5 CONTINUE
      GO TO 3
    9 STOP
      END
```

10.6 The general solution of the paraxial ray equation for the spherical single-pole field

The axial flux density distribution outside a uniformly magnetised sphere may be expressed as

$$B(z) = B_o \, a^3/Z^3 \quad \ldots\ldots\ldots\ldots\ldots\ldots \quad (A6.1)$$

where z is the distance from the centre of the sphere measured in the direction of magnetization and B_o is the uniform flux density in the sphere in the same direction.

Equation (A6.1) refers of course to the external flux density so that z/a is never less than unity.
The paraxial ray equation is given by

$$\frac{d^2r}{dz^2} + \frac{eB^2(z)}{8mV_r} \cdot r = 0 \quad \ldots\ldots\ldots\ldots \quad (A6.2)$$

where r is the radial height of the electron path, e/m is the ratio of charge to mass of the electron, and V_r is the relativistically corrected accelerating voltage

$$\text{i.e. } V_r = V(1 + 0.978) \times 10^{-6}V)$$

since $\int_{-\infty}^{\infty} B(z)\, dz = \mu_o \, NI$

$$\int_{-\infty}^{\infty} B_o(a^3/z^3)\, dz = \mu_o \, NI$$

$$B_o a = 2\mu_o \, NI \quad \ldots\ldots\ldots\ldots\ldots\ldots \quad (A6.3)$$

By substituting (A6.1) and (A6.3) in (A.6.2) the paraxial ray takes the form

$$\frac{d^2r}{dz^2} + \frac{4\mu_o^2 \, e(NI)^2 \, a^4}{8m \, V_r \, z^5} \cdot r = 0 \quad \ldots\ldots\ldots\ldots \quad (A6.4)$$

Putting $y = r/a$ and $x = z/a$, equation (A6.4) may be written

$$x^6 \frac{d^2y}{d^2x} + k^2 \quad y = 0 \quad \ldots\ldots\ldots\ldots\ldots \quad (A6.5)$$

where $k = \sqrt{\frac{e}{8m}} \cdot 2\mu_o \frac{NI}{V_r^{\frac{1}{2}}} = 0.3726 \frac{NI}{V_r^{\frac{1}{2}}}$ ..... (A6.6)

If $y = y_o$ at $x = 0$ then near this point we have approximately

$$y = - \frac{ky_o}{x^6}$$

then

$$y = \frac{A}{x^4} + B\,x + c$$

again let us try the transformation $y = t/x^4$ .... (A6.7)

then $y' = t'/x^4 - 4t/x^5$

and $y'' = \frac{t''}{x^4} - \frac{8t'}{x^5} + \frac{20t}{x^6}$ ..... (A6.8)

Substituting equations A6.7 and A6.8 in A6.5

$$x^2t'' - 8xt' + (20 + \frac{k^2}{x^4})\ t = 0 \ . \quad (A6.9)$$

This type of equation can be solved using Bessel functions.

The general equation

$$x^2t'' + x\ (1-2\alpha)\ t' + |(\beta\ \gamma x^{\gamma})^2 + \alpha^2 - n^2\gamma^2|\ t = 0 \quad (A6.10)$$

has the general solution (McLACHLAN, 1955)

$$t = x^{\alpha}\ [A\ J_n\ (\beta x^{\gamma}) + B\ J_{-n}\ (\beta x^{\gamma})] \quad \ldots\ldots\ldots \quad (A6.11)$$

Comparing equations (A6.9) and (A6.10)

$$-8 = 1 - 2\alpha, \text{ hence } \alpha = 4.5$$

$$\text{also} \quad 20 = \alpha^2 - n^2\gamma^2 \quad \ldots\ldots\ldots\ldots\ldots\ldots\ldots \quad (A6.12)$$

$$\text{and } k^2\ x^{-4} = \beta^2\gamma^2\ x^{(2\gamma)}$$

hence by comparison again

$$-4 = 2\gamma \text{ then } \gamma = -2 \text{ and } k^2 = \beta^2\gamma^2$$

The above relations lead to $\beta = k/2$

By substitution of the values α and γ in equation (A6.12) $n = \frac{1}{4}$. Clearly the nature of solution depends on whether k^2 is positive or negative, physically k^2 is positive whether the field B(z) is negative or positive.

Thus the solution described by equation (A6.11) reduces to

$$t = x^{4.5}\left|A\, J_{1/4}(k/2\, x^2) + B\, J_{1/4}(k/2\, x^2)\right|$$

and the general solution for equation (A6.5) is

$$y = \sqrt{x}\ \left|A\, J_{1/4}(k/2\, x^2) + B\, J_{-1/4}(k/2\, x^2)\right| \quad \text{(A6.13)}$$

or

$$r/a = (z/a)^{\frac{1}{2}}\left[A\, J_{1/4}(k\, a^2/2z^2) + B\, J_{-1/4}(ka^2/2z^2)\right]$$

* The author is grateful to Mr. N. Kerruish of the Department of Mathematics of this University for his help and advice in solving this equation.

Inst. Phys. Conf. Ser. No. 36 © 1977: Chapter 1

THE MAGNETISED IRON SPHERE, A REALISTIC THEORETICAL MODEL FOR SINGLE-POLEPIECE LENSES

A Alshwaikh and T Mulvey

Department of Physics, The University of Aston in Birmingham, B4 7ET, U.K.

1. Introduction

In a single-polepiece lens (Mulvey 1976) as shown, for example, in Figure 1a, the axial magnetic field falls rapidly from a high value at the poleface. The main imaging field is therefore essentially outside the lens structure, whilst low aberration coefficients are preserved. Such lenses become a practical possibility when the lens excitation is concentrated into the region of the single polepiece by means of high current density windings. The focal properties of such lenses differ appreciably from those of conventional twin-polepiece lenses. For example, the objective focal length increases slowly with increasing lens excitation and the spherical aberration and image distortion can be appreciably lower than those of conventional lenses. This is a consequence of the differences in the axial field distributions (Marai and Mulvey 1974). The axial field distribution can be represented to a first approximation by the exponential field model of Glaser (1952) but it is difficult to correlate this model with an actual polepiece structure, and so find an optimum design. For this reason, it seemed desirable to look for a more realistic model. A uniformly magnetized sphere seemed to be a good starting point.

2. The uniformly magnetized sphere

Consider the external magnetic field produced by a uniformly magnetized iron sphere (Fig.1b). Lord Kelvin (1872) has calculated the magnetic potential due to such a sphere; from his expression, we may deduce the axial flux density distribution in the direction of magnetization (Fig.1c) as follows:

$$B_z = B_o \, (a/z)^3 \quad \ldots\ldots\ldots\ldots\ldots\ldots\ldots\ldots \quad (1)$$

if the permeability of the iron is large. Here B_o is the uniform flux density in the iron sphere of radius a and z is the axial distance from the centre of the sphere, measured in the direction of magnetization. For the external field, z is, of course, never less than a. From Equation (1) the 'half-width' d of the distribution (Fig.1c) is equal to 0.26a. Thus, a magnetized sphere of 10mm diameter would produce two field distributions each with a 'half-width' of 1.3mm, which suggests that its focal length would be of the same order of size, a convenient value for electron microscopy. Consider one of these distributions as shown in Fig.1c which corresponds to a uniformly magnetized hemisphere bounded by an infinite plane of high permeability.

3. Focal properties

From Equation (1) the paraxial ray equation

$$r'' + (e \, B_z^2 / 8mV_r) \, r = o \quad \ldots\ldots\ldots\ldots\ldots\ldots \quad (2)$$

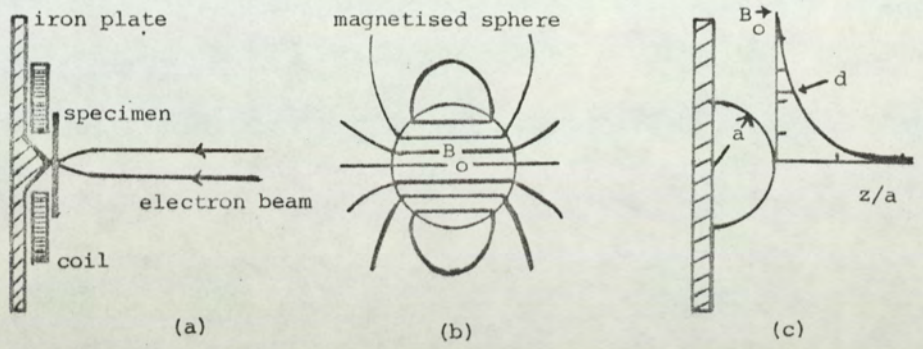

Fig.1. Development of the magnetized sphere model

becomes $$r'' + \left[e\,(B_o\,a^3/z^3)^2/8m\,V_r\right] r = o \quad \ldots\ldots\ldots\ldots\ldots\ldots \quad (3)$$

where dashes denote differentiation with respect to z; r is the radial height of the ray and e/m is the ratio of charge to mass of the electron. This equation has an analytical solution in terms of Bessel functions. Thus, for a ray of unit height starting at an infinite axial distance away, the trajectory is given by:

$$\frac{r}{a} = \left(\frac{z}{a}\right)^{1/2} \frac{1.6406}{\left(NI/V_r^{\frac{1}{2}}\right)^{\frac{1}{4}}} \; J_{\frac{1}{4}}\left[0.186 \; \frac{a^2}{z^2}\left(\frac{NI}{V_r^{\frac{1}{2}}}\right)\right] \quad \ldots\ldots\ldots\ldots \quad (4)$$

where $J_{\frac{1}{4}}$ is the Bessel function of order $\frac{1}{4}$, V_r is the relativistically corrected accelerating voltage and NI is the excitation required to maintain the axial field distribution from z = a to z = ∞

$$\text{i.e.} \quad \mu_o NI = \int_a^\infty B_z \, dz \quad \ldots\ldots\ldots\ldots\ldots\ldots\ldots \quad (5)$$

The corresponding slope r' of the ray is given by

$$r' = 0.611 \left(\frac{a}{z}\right)^{5/2} \left(\frac{NI}{V_r^{\frac{1}{2}}}\right)^{3/4} J_{5/4}\left[0.186 \; \frac{a^2}{z^2}\left(\frac{NI}{V_r^{\frac{1}{2}}}\right)\right] \quad \ldots\ldots\ldots \quad (6)$$

where $J_{5/4}$ is the Bessel function of order $\frac{5}{4}$.

Equations (4) and (6) allow the paraxial focal properties to be determined directly by reference to Tables of Bessel functions. In particular the minimum projector and objective focal lengths coincide at a value of f/a = 0.43 for an excitation parameter of $NI/V_r^{\frac{1}{2}} = 14$. Thus a sphere of 10mm diameter would produce a minimum focal length of about 2mm. At greater excitations the objective focal length is given by

$$f_{obj}/a = 0.116 \left(NI/V_r^{\frac{1}{2}}\right)^{\frac{1}{2}} \quad \ldots\ldots\ldots\ldots\ldots\ldots \quad (7)$$

The objective focal length thus increases slowly as the excitation is increased, a characteristic feature of single-polepiece lenses. The focal properties of the spherical field distribution calculated in this

way are shown in Figure 2. Here the projector and objective focal lengths, and the objective focal distance from the tip of the hemisphere are shown as a function of the excitation parameter $NI/V_r^{\frac{1}{2}}$. The focal properties are plotted in terms of the 'half-width' d rather than the radius a in order to facilitate comparison with other field distributions. The corresponding values relative to the radius a can be readily obtained from the relation a = 3.846d.

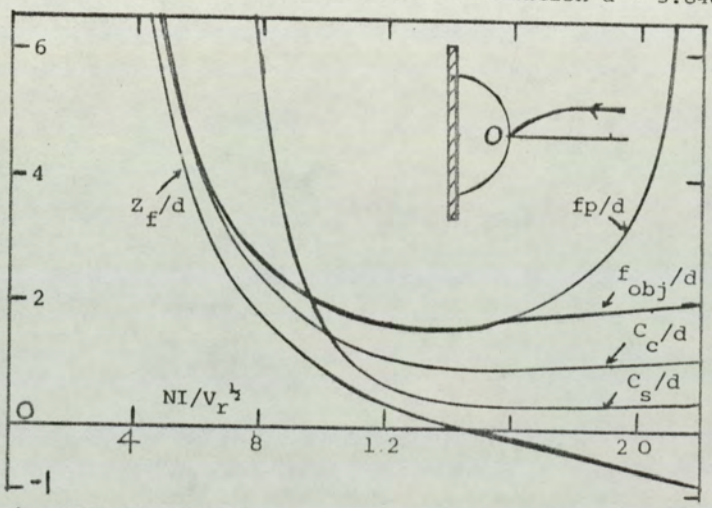

Fig.2. Focal properties of a uniformly magnetised sphere

4. Lens excitation

Nothing has yet been said about the method of magnetizing the hemisphere. The magnetizing coil will, in general, produce an additional field on the axis which must also be considered. However, if high current density coils are mployed, as indicated in Fig.1a, it seems likely that the stray field from the coil will play only a secondary role in the imaging process. It should also be pointed out that in order to employ such lenses in the TEM it is necessary to bore a hole along the axis of the sphere. This can be done without changing the essential features of the present calculations.

5. Aberrations

The corresponding spherical and chromatic aberration coefficients C_s/d and C_c/d respectively, of the spherical field distribution, calculated numerically by Scherzer's formula, are also plotted in Fig.2. For excitation parameters greater than that corresponding to minimum focal length, the curves are similar in shape to that of the objective focal length, i.e. the aberration coefficients increase only slowly with increasing excitation. In particular the minimum value of $C_s/d \simeq 0.4$ or $C_s/a \simeq 0.1$. Thus a sphere of 10mm in diameter would have a C_s value of 0.5mm, an encouragingly small value.

6. Image distortion

Low values of spherical aberration are often associated with low values of radial and spiral image distortion. The distortion in the image of an electron microscope does not depend directly on the corresponding radial or spiral distortion coefficient D but on a

dimensionless quantity Q (Marai and Mulvey 1977) where $Q = D^{\frac{1}{2}} f_p$, f_p being the projector focal length associated with D. Q_{sp} (spiral distortion) has a minimum value of about unity for all conventional double-polepiece lenses and does not depend significantly on lens geometry. Figure 3 shows the Q factors for the magnetized sphere model for both radial and spiral distortion as a function of the lens excitation parameter $NI/V_r^{\frac{1}{2}}$. The relative magnification M/M_o is also plotted as a function of excitation. In the region of maximum magnification, the radial distortion parameter Q_r is small, as in conventional lenses, but the spiral distortion parameter Q_{sp} is appreciably lower than that of conventional lenses.

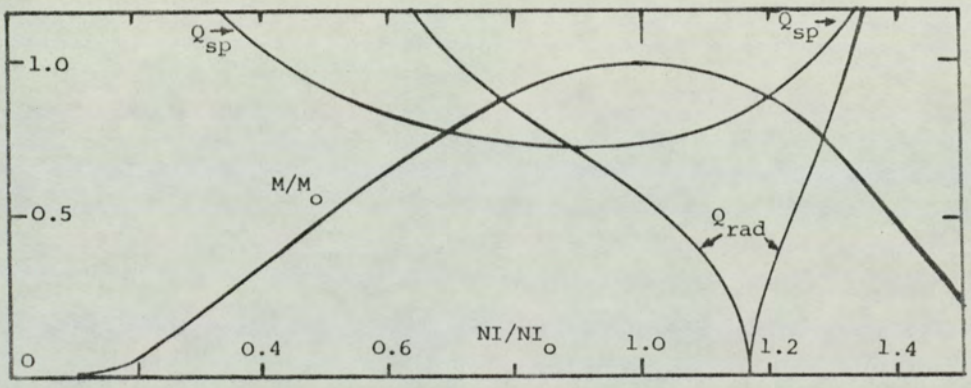

Fig.3. Quality factors Q_{sp} and Q_r for spiral and radial distortion of a uniformly magnetized sphere

7. Conclusion

It would appear that the uniformly magnetized sphere model provides a realistic basis for the understanding of single polepiece lenses and their application in electron microscopy.

8. Acknowledgments

The authors would like to thank Mr. F. Z. Marai of the Department of Physics for making available computer programs developed for the investigation of the exponential field distribution and Mr. N. Kerruish of the Department of Mathematics for his considerable help in solving the ray equation analytically.

9. References

Glaser W 1952 Grundlagen der Elektronenoptik 306-307. Springer

Kelvin (Thomson W) 1872 in "Reprints of papers on electricity and magnetism" 2nd. Ed. (London; Macmillan 1884)

Marai F Z and Mulvey T 1974 Proc.8th Int.Conf.Elec.Micros. eds J V Saunders and D J Goodchild (Canberra: Austral. Acad.Sci.) 1 pp.130-131

Marai F Z and Mulvey T 1977 Ultramicroscopy 2 187-192

Mulvey T 1976 Proc.6th Eur.Conf.Elec.Micros. ed D G Brandon (Tel Aviv: Tal) 1 59-64

10.8 Single-polepiece projector and objective magnetic lenses for the electron microscope

S.M. Juma* and A. Alshwaikh

(A paper to be presented at the Electron Microscopy and Analysis Group Conference in September (EMAG 79) in Sussex)

Department of Physics, The University of Aston in Birmingham, B4 7ET, England

ABSTRACT

There are two possible directions for the illuminating electron beam to enter the axial field of single-polepiece lenses. The preferred direction was determined for both projector and objective lenses using an experimental miniature 100 kV single-polepiece electron lens. The importance of this investigation is that it demonstrates the possibility of constructing a high resolving power objective lens for the TEM or STEM. In addition, such a lens can be used as a low-distortion projector lens. The lens described can be scaled up for employment in a million volt electron microscope.

---

* At present lecturer in the Department of Physics, College of Science, University of Baghdad, Iraq.

Introduction

The focal properties of single-polepiece lenses differ appreciably from those of conventional double-polepiece lenses. The axial magnetic field of a single-polepiece lens is strongly concentrated by the single polepiece rather than by two closely spaced polepieces;this field falls rapidly from a high value at the polepiece tip resulting in a small "half-width". Two models have been introduced to represent the axial field distribution of such a single-polepiece lens. The exponential field model (Marai and Mulvey 1974) gave a good first approximation but it was difficult to correlate this model with an actual polepiece structure, and so find an optimum design. The uniformly magnetized iron sphere model (Alshwaikh and Mulvey 1977) seemed to be a more realistic theoretical model for single-polepiece magnetic electron lenses. Both models have shown that single-polepiece lenses can have lower aberrations than those of conventional lenses.

Single-polepiece lenses have been used both as objective and projector lenses in experimental scanning and scanning transmission electron microscopes (Mulvey and Newman 1975) and transmission electron microscope (Juma and Mulvey 1975). However, no evidence has yet been given for the best orientation of the polepiece tip with respect to the illuminating electron beam. The focal properties of an experimental single-polepiece lens described in this paper are investigated both as an objective and as a projector lens. Conclusions have been drawn for the best utilization of the single-polepiece lenses in the field of electron microscopy.

The experimental single-polepiece lens

Figure 1 shows a cross-sectional diagram of a 100 kV miniature lens of unusual design. The lens has interchangeable lids of different materials. If the lid is made of a non-ferromagnetic material the lens becomes a single polepiece lens of 2 mm bore. However, if an iron lid is used the lens becomes a conventional double-polepiece lens of 2 mm bore diameter (D) and 3 mm gap (S), i.e. S/D = 1.5, giving a minimum projector focal length $(fp)_{min}$ of 1.8 mm, as calculated from the equation $(f_p)_{min} = 0.55\ (S^2 + 0.45\ D^2)^{\frac{1}{2}}$. Other values for the gap width are also possible.

This substantial reduction in lens volume, and therefore weight, is brought about by the use of miniature coils, efficiently water-cooled. The lens is excited by two flat coil windings of 12 mm inner diameter and 38 mm outer diameter which provide sufficient ampere-turns for operation up to an accelerating voltage of 100 kV (V_r = 110 kV). Each coil is 5 mm wide and has 190 turns of 24 SWG (0.56 mm diameter) insulated copper wire arranged in eight layers. The two coils are connected in series. Thus the lens is excited by 380 turns capable of carrying a current of about 15 amperes, an excitation of more than 5500 ampere-turns. The miniature lens requires an input power of about 500 watts for such an excitation. The cooling water circulates directly around the coils, which are separated from each other and from the lens casing by a gap of about 1 mm. This direct cooling is very effective, since it enables the wire to carry a current of over fifteen times the normal maximum rating without overheating. Water-flow

rates are not critical but in the experiments a flow rate of about 1 litre/min was maintained. The mean temperature rise in the coil is about 100°C, comparable with that of conventional lenses. The heating-up time constant is quite short, less than one minute. However, the transfer of heat to the outer casing is negligible.

The focal properties of the experimental single-pole-piece lens were computed from the axial flux density distribution. This field distribution was measured by a Hall-effect probe. Because of the construction of the lens, it was not possible to place the Hall probe at a smaller distance than z = 10 mm from the polepiece tip. The field distribution in the important range $0<z<10$ mm was estimated by considering (a) the exponential behaviour of the main part of the field, (b) the position of the maximum axial peak with respect to the polepiece tip and the steep decrease of the field inside the lens structure as determined on large scale models (Juma 1975). The self-consistency of the estimated field distribution was checked by Ampere's Law $\int_{-\infty}^{+\infty} B_z \, dz = \mu_o NI$ where B_z is the axial flux density distribution along the axis z, NI is the number of ampere-turns producing the field distribution and $\mu_o = 4\pi \times 10^{-7}$ henry/m. Figure 2 shows the axial field distribution of the experimental single-polepiece lens at 2200 ampere-turns where the maximum flux density (B_m = 0.39T) is about 1 mm away from the polepiece tip. The flux density falls to a negligible value at a value of z = -10 inside the iron polepiece and at z_F 50 mm outside the polepiece. This shape of field distribution is typical of all single-polepiece lenses.

Single-polepiece projector lens

The experimental 100kV miniature lens was tested as a projector by placing it in the diffraction stage under the final projector lens of the AEI EM6 electron microscope. It was supported by two brass flanges and aligned about the axis of the water pipes. The lens was cooled by the same cooling system of the microscope. Figure 3 shows the change in projector focal length when the lens is converted from a double-polepiece (iron lid) to a single-polepiece (brass lid). The figure shows that in the region of maximum magnification the projector focal length of the single-polepiece lens is more sensitive to the change in excitation than that of the double-polepiece lens. The agreement between the computed and the experimental results for the single-polepiece lens is excellent (within 5%). The minimum projector focal length of the single-polepiece lens is higher than that of the double-polepiece lens and occurs at a higher excitation.

The miniature single-polepiece lens was then tested in the EM6 electron microscope as the final projector lens (the original second projector lens is switched off) at 75kV in two orientations (i) with the polepiece tip facing the incident beam and (ii) with the polepiece tip facing the fluorescent screen. The imaging properties of the lens were recorded in both orientations at a constant projection distance (300 mm) between the polepiece tip and the photographic plate. In both orientations the lens magnification is the same since the projector focal length at a specific excitation is the same. It should be mentioned, however, that the contribution of the EM6 electron microscope inter-

mediate lens to the distortion of the final image on the photographic plate is negligible whether the excitation of the intermediate and the final single-polepiece projector lenses are co-operative or opposing. Therefore, the distortion in the final image is due chiefly to the distortion of the final single-polepiece projector lens.

Figure 4 shows the variation of the radial distortion coefficient, C_d and the spiral distortion coefficient C_{sp} with the excitation parameter $NI/V_r^{\frac{1}{2}}$ for the two directions of entry into the lens of a parallel electron beam. For a projector lens, when the polepiece tip faces the fluorescent screen, the behaviour of the C_d and C_{sp} curves is similar to that of the double-polepiece lenses. However, when the polepiece tip faces the incoming electron beam, the C_d coefficient decreases continuously with increase of excitation while the C_{sp} coefficient increases only very slowly; at maximum magnification the value of C_{sp} considerably lower than that of a conventional lens. Thus the curves show that the most favourable arrangement for low distortion is for the polepiece tip facing the incoming parallel electron beam (Marai and Mulvey 1975).

Figure 5 shows two micrographs taken under the same conditions (magnification = 5500X at $NI/V_r^{\frac{1}{2}} = 14$) which are the first of their kind in electron micrsocopy. In the region of maximum magnification, the radial distortion coefficients are very small for both orientations as in double-polepiece lenses but it is smaller by a factor of three at a negligible value (0.008) when the polepiece

tip faces the incoming parallel electron beam. However, the spiral distortion coefficients which are appreciably lower than that of double-polepiece lenses are largely different from each other, as shown by the micrographs in Figure 6, by a factor of more than three. At higher excitations, the C_{sp} coefficient of the lens whose polepiece tip faces the fluorescent screen increases sharply, while in the opposite direction, this coefficient is nearly constant from $NI/V_r^{\frac{1}{2}}$ = 12 to 18. Hence single-polepiece projector lenses should be operated with their polepiece tip facing the incident electron beam in order to obtain full advantage of their superior optical properties. Correction of the spiral distortion of the final projector lens with its polepiece tip in the favourable direction can be done by another single-polepiece lens with its polepiece tip in the unfavourable direction (Marai and Mulvey 1977, Lambrakis et al 1977). These results are important to the design of single-polepiece projector lenses which can have appreciably lower distortion coefficients than those of the best double-polepiece lenses.

Single-polepiece objective lens

The need for new objective lenses is not so much to improve resolving power, which is already near the theoretical limit, but to improve operational performance by removing restrictions placed on specimen size and manipulation. These restrictions usually arise from the fact that a high resolution objective lens has two polepieces with small bores separated by a relatively small gap. By employing a single-polepiece lens as an objective more space can be gained in the specimen region without

essential loss of resolving power (Mulvey 1974). Thus single-polepiece objective lenses provide minimum obstruction of the X-rays and other emissions from the specimen, particularly when excited by miniaturised coil windings.

The focal properties of the experimental single-polepiece lens as an objective were computed for the two directions of entry of the electron beam. Considering the objective focal length, f_o, Figure 6 shows that when the beam is incident on the steep edge of the field (i.e. the polepiece tip faces the incoming electron beam) f_o decreases continuously below the curve of the opposite orientation as the excitation parameter $NI/V_r^{\frac{1}{2}}$ exceeds 10. The single-polepiece lens can have an objective focal length f_o of the same order as that of double-polepiece lenses ($\sim$ 1mm) at high excitation as shown by the dashed curve in Figure 6. When the spherical aberration coefficient C_s is taken into consideration, Figure 7 shows that it is best to have the ray incident on the sloping edge of the field (i.e. the polepiece tip facing the fluorescent screen) since C_s is small at low excitations (1.3mm at $NI/V_r^{\frac{1}{2}} = 14$). However, the variations of the quotient C_s/f_o with the excitation parameter $NI/V_r^{\frac{1}{2}}$ (Figure 8) shows that it is best for low C_s to have the polepiece tip facing the fluorescent screen. Figure 8 shows that $C_s/f_o = 0.25$ at $NI/V_r^{\frac{1}{2}} = 14$; a very low quotient and excitation. At higher excitations, C_s/f_o remains nearly constant when the polepiece tip faces the fluorescent screen. Thus single-polepiece lenses can be operated at low excitations giving very small values

of C_s although f_o is relatively large. However, small C_s value is more important than small f_o. Therefore, the first arrangement is the best since it has the smallest C_s value.

The variation of the chromatic aberration coefficient C_c with the excitation parameter $NI/V_r^{\frac{1}{2}}$, Figure 9, is the same (C_c = 3mm) for the two directions of the electron beam until $NI/V_r^{\frac{1}{2}}$ exceeds 14. At high excitations the C_c coefficient of the lens whose polepiece tip faces the incoming beam is smaller than that of the other direction. Considering the variation of C_o/f_o quotient with the excitation parameter $NI/V_r^{\frac{1}{2}}$, Figure 10 shows that the two curves for the two different orientations of the lens, meet at very high excitations. At the excitation of $NI/V_r^{\frac{1}{2}}$ = 14 where C_s/f_o and C_o/f_o both have minimum values when the polepiece tip faces the fluorescent screen, the specimen is positioned at the polepiece surface as shown in Figure 11; the axial magnetic field inside the lens structure acts as a pre-field for this lens orientation. When the polepiece tip faces the incoming electron beam, the curves of f_o, C_s and C_o show that the lens behaves like a conventional symmetrical lens since the tail of the field distribution curve is not used in imaging but a strong pre-field condenser.

The variation of the lens resolution parameter $C_s B_m/V_r^{\frac{1}{2}}$ with the excitation parameter $NI/V_r^{\frac{1}{2}}$ for the two possible orientations of the lens is shown in Figure 12. It can be seen that best resolution is obtained at $NI/V_r^{\frac{1}{2}}$ = 14 when the polepiece tip faces the fluorescent screen, where the parameter $C_s B_m/V_r^{\frac{1}{2}}$ reaches a minimum value of 3.4×10^{-6}

$mTV^{-\frac{1}{2}}$. When the polepiece tip of the lens faces the incoming electron beam the $C_s B_m/V_r^{\frac{1}{2}}$ curve falls steadily with increasing excitation it never attains the above value. Thus as far as the ultimate resolution is concerned for a given value of B_m it is better to have the polepiece tip of a single-polepiece objective lens facing the fluorescent screen. The minimum value of $C_s B_m/V_r^{\frac{1}{2}}$ ($3.4 \times 10^{-6} mTV^{-\frac{1}{2}}$) at the favourable orientation of the polepiece is lower than that for the best double-polepiece objective lens which is $4.8 \times 10^{-6} mTV^{-\frac{1}{2}}$, (Mulvey and Wallington 1973).

The best resolving power of this experimental single-polepiece lens obtained by substituting for C_s and V_r in the well known expression for resolving power as limited by spherical aberration and diffraction is given by

$$d = 0.43\, C_s^{\frac{1}{4}}\, \lambda^{\frac{3}{4}}$$

where $C_s = 3.4 \times 10^{-6} \dfrac{V_r^{\frac{1}{2}}}{B_m}$ m and $\lambda = \dfrac{12.25 \times 10^{-10}}{V_r^{\frac{1}{2}}}$ m

Hence $d_{min} = 38 \times 10^{-10} / (V_r B_m)^{\frac{1}{4}}$

For example, when this lens is operated at 100kV (V_r=110kV), the maximum axial flux density B_m produced at 4650 ampere-turns is 0.825 T. Therefore, the minimum resolving power of this experimental single-polepiece objective lens is 0.22nm (2.2A^o) or 1.76A^o for B_m = 2 Tesla. This value of d is excellent compared with the best double-polepiece objective lenses used in high voltage electron microscopes (Mulvey 1977). A purpose-built single-polepiece objective lens can, of course, have a better resolution.

The curves showing the focal properties of the experimental

single-polepiece objective lens for the two possible directions of entry of the electron beam are shown in Figure 13. It can be seen from Figure 13a that short objective focal lengths and small aberration coefficients can be obtained at high excitations when the polepiece tip faces the incoming electron beam. However, when the polepiece tip faces the fluorescent screen, Figure 13b acceptably small aberration coefficients can be obtained at comparatively low excitations ($NI/V_r^{\frac{1}{2}}$) with a high resolving power ($\delta=2.2A^{o}$).

A purpose-built single-polepiece objective lens can be designed with the polepiece protruded outside the lens structure without seriously affecting its focal properties in order to have more freedom for the specimen and other equipments. The presence of the iron polepiece ensures that asymmetrics in the lens winding do not significantly affect the symmetry of the axial field distribution. These properties are useful in the design of transmission electron microscopes and scanning transmission electron microscopes particularly high voltage microscopes.

Application to high voltage electron microscopy

The performance figures of this experimental single-polepiece lens may be applied directly to the design of objective and projector lenses for high voltage microscopy. If the dimensions of a magnetic lens and its number of ampere-turns are scaled by a factor m, the magnetic field produced at corresponding points in the original and scale model will be the same. Consider therefore an increase of accelerating voltage from 100kV (V_r=110kV) to 1000kV (V_r=2000kV). If, for example, the experimental lens is scaled-up m times where $m = (2000/110)^{\frac{1}{2}} = 4.26$, the projector focal length will be scaled-up by the same factor i.e. f_p = 24.3mm, and hence the magnification will be reduced m times. The distortion coefficients C_d and C_{sp} are dimensionless and are therefore unaffected by scaling operations. The lens diameter and height will be scaled-up by m to 200 mm and 85 mm respectively, i.e. the volume and hence weight will be scaled-up by m^3 (i.e. 77.3X). The dimensions of such a scaled-up model are less than half those of the normal IMV projector lenses and are comparable to those of conventional 100kV lenses. The power consumption will increase by a factor of m^2 (i.e. 18.2X). The bore size will increase by a factor of m to a value of 8.5mm. There are advantages in such a large bore since it enables a vacuum liner to be inserted in order to improve the vacuum (Juma and Mulvey, 1975). It therefore seems feasible to design electron-optical columns for IMV with dimensions comparable to those of present conventional 100kV instruments.

Conclusions

It has been proved experimentally that a single-polepiece projector lens should be positioned on the axis so that the polepiece tip faces the incoming parallel electron beam emerging from the preceding objective lens. In this mode of operation, small radial distortion coefficients are obtained as in double-polepiece lenses but the spiral distortion coefficient C_{sp} is appreciably lower.

The correct orientation of the single-polepiece in an objective lens is a more complicated matter. The analysis of computed focal properties for a single polepiece objective lens indicate that at excitation parameter $NI/V_r^{\frac{1}{2}}=14$ (as used in conventional objective lenses) the arrangement in which the polepiece is placed between specimen and image plane leads to a lower spherical aberration than the arrangement in which the polepiece is turned through 180°, and the specimen is placed between the polepiece and image plane. However, at high excitations ($NI/V_r^{\frac{1}{2}} \simeq 40$) the second arrangement can also produce comparable values of spherical aberration coefficient, and possibly better values for the chromate aberration coefficient.

In order to exploit the advantages of each arrangement, care must be taken to design the lens so that the poleface works at the highest permissible flux density.

The results on this experimental lens can be useful in the design of high resolution transmission and scanning transmission electron microscopes consisting of single-polepiece.

objective and projector lenses. Also this lens design can be scaled exactly and so simulate accurately the electron-optical conditions in a million volt electron microscope.

Acknowledgments

The authors are very grateful to Professor T. Mulvey of the Physics Department for reading the manuscript and for the helpful and stimulating discussions. They also would like to thank Mr. J. Lloyd for constructing the lens and Mr. R. Keen of the Physics Department for his considerable assistance with the experimental work.

References

Alshwaikh, A. and Mulvey, T. (1977) (Appendix 7)

Juma, S.M. (1975) "Rotation-free magnetic electron lenses" Ph.D. Thesis, University of Aston.

Juma, S.M. and Mulvey T. (1975) "A new experimental electron microscope with a rotation-free projector system in "Developments in electron microscopy and analysis" (Venables, ed.) Academic Press, pp.45-48.

Lambrakis, E., Marai R.Z. and Mulvey, T.(1977) "Correction of spiral distortion in the transmission electron microscope"

Marai, F.Z. and Mulvey, T (1974) "Electron optical characteristics of single-pole magnetic lenses" in "Electron Microscopy 1974" (Sanders and Goodchild) Vol. I, pp 130-131, Austr. Acad.Sci. Canberra.

Marai, F.Z. and Mulvey, T. (1975) "Electron-optical characteristics of single-pole magnetic lenses" in "Developments in electron microscopy and analysis" (Venables, ed.) Academic Press, pp 43-44.

Marai, F.Z. and Mulvey T.(1977) "Scherzer's formula and the correction of spiral distortion in the electron microscope" Ultramicroscopy, 2, 187-192.

Mulvey, T. (1977) "Electron microscopy, present and future" Laboratory Equipment Digest, November 1977, 53-65.

Mulvey, T. and Newman, C.D. (1973) "New electron-optical systems for SEM and STEM" in "Scanning electron microscopy: systems and applications 1973" (W.C. Nixon, ed.) pp 16-21, Inst. Phys.Conf. Series.

Mulvey, T. and Wallington, M.J. (1973) "Electron lenses", Rep.Prog.Phys. 36, 347-421.

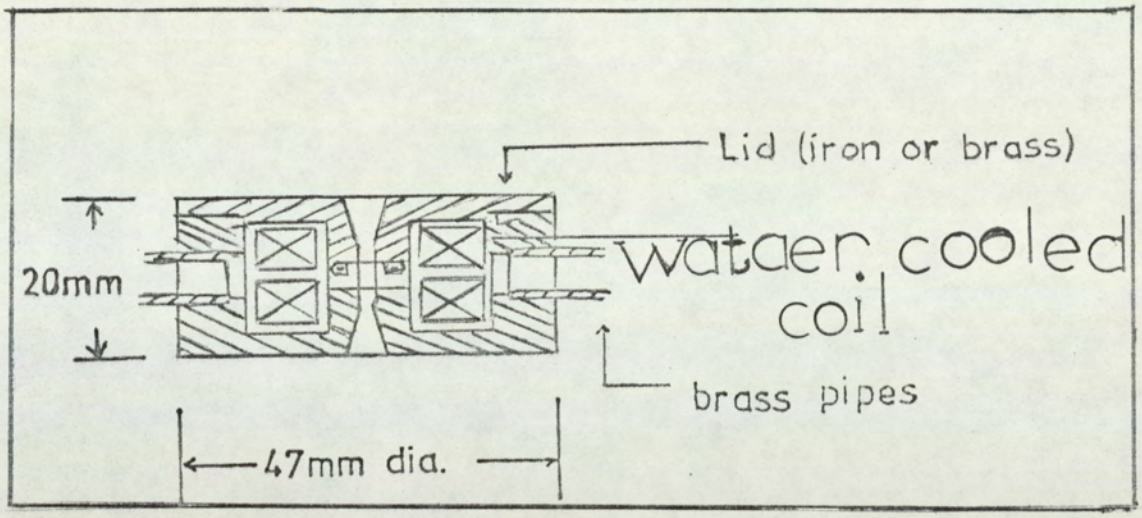

Figure 1 Cross-section of miniature electron lens for 100 kV electron microscope.

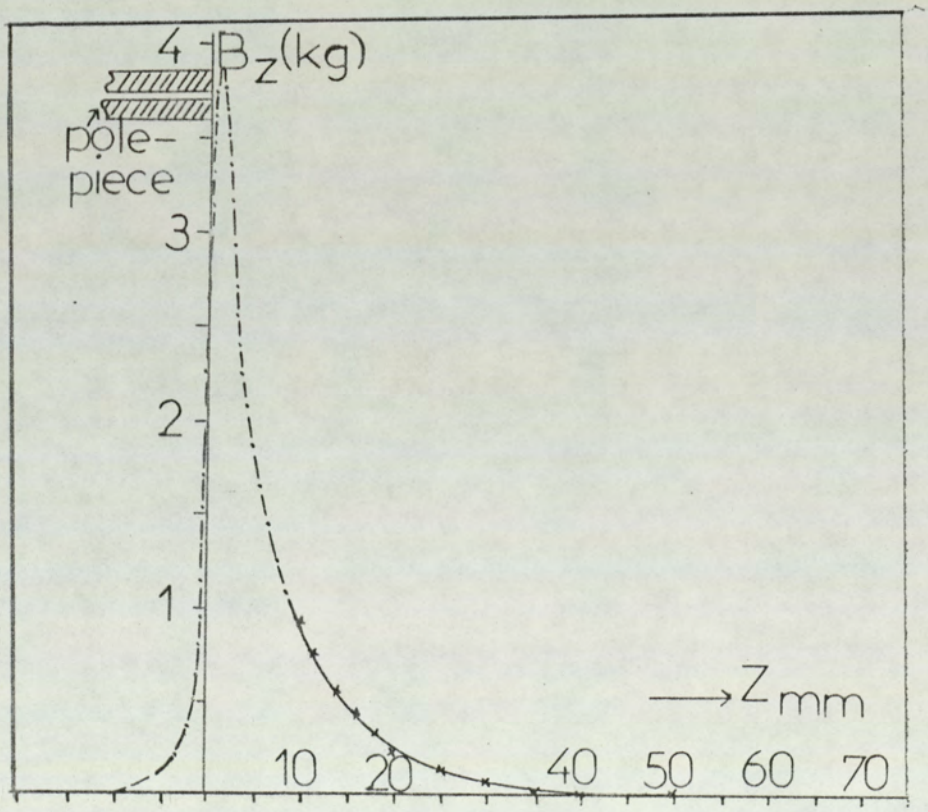

Figure 2 Axial flux density distribution of the experimental single-polepiece miniature lens at an excitation of 2200 ampere-turns.

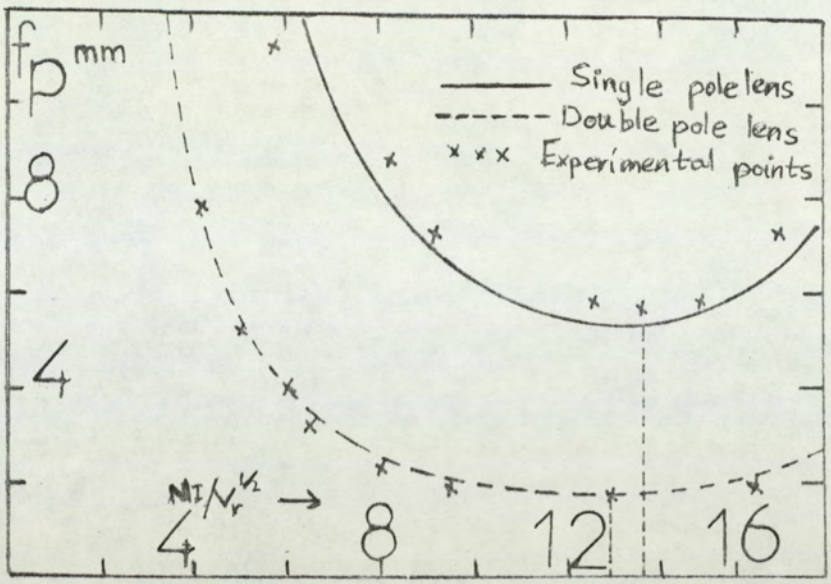

Figure 3 Projector focal length f_p as a function of lens excitation parameter $NI/V_r^{\frac{1}{2}}$. The solid curve is that computed for the single-pole-piece lens, computed $(f_p)_{mix}$ = 5.4mm at $NI/V_r^{\frac{1}{2}}$ = 13, experimental $(f_p)_{mix}$ = 5.7mm at $NI/V_r^{\frac{1}{2}}$ = 13.5. The dotted curve is that computed for the double-polepiece lens of gaps = 3mm, bore D = 2mm, $(f_p)_{mix}$ = 1.8mm at $NI/V_r^{\frac{1}{2}}$ = 12.9.

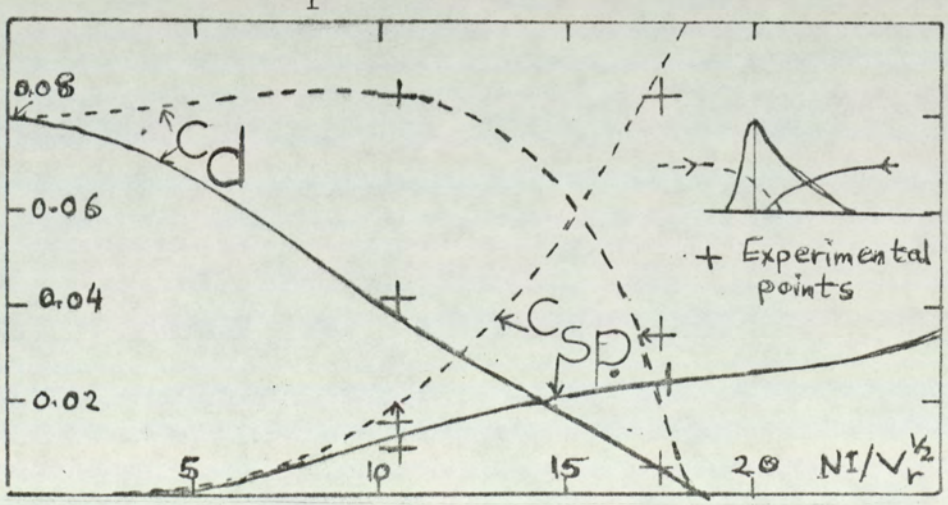

Figure 4 Radial, C_d and spiral, C_{sp} distortion coefficients of the single-polepiece lens as a function of the excitation parameter $NI/V_r^{\frac{1}{2}}$ for the two directions of entry of a parallel electron beam.

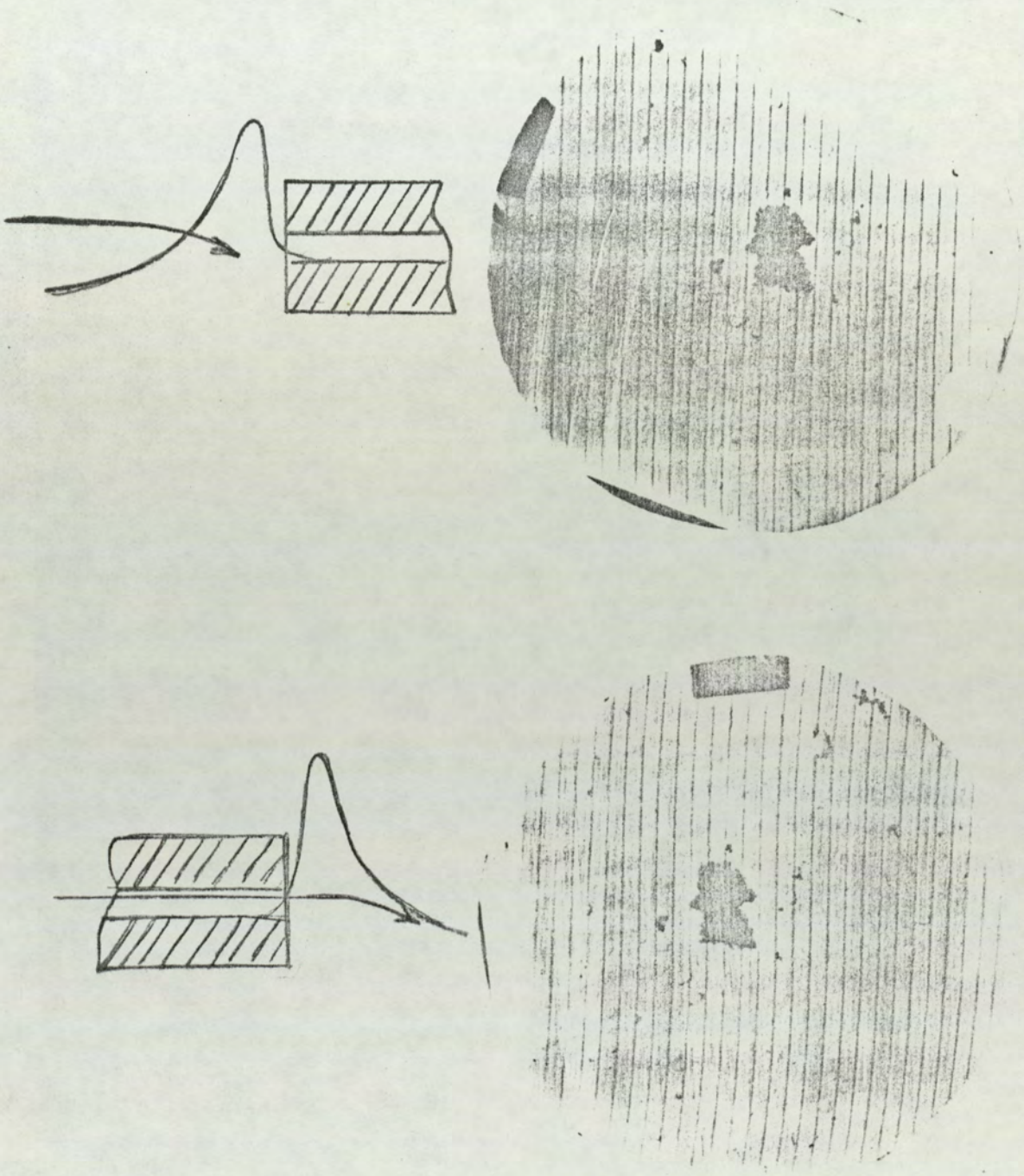

Figure 5 Micrographs of a line grating of the same field of view taken when the second projector lens in the EM6 electron microscope is the experimental miniature single-polepiece lens operated near its minimum projector focal length, showing different distortions for the two directions of entry of a parallel electron beam.

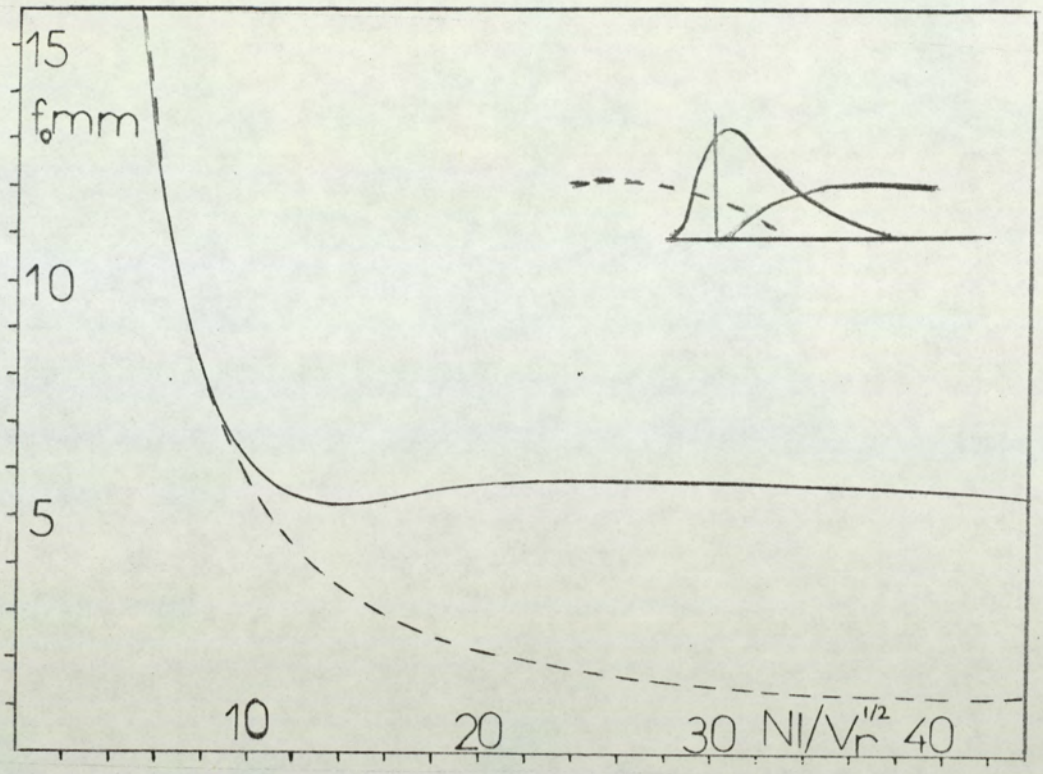

Figure 6 Objective focal length, f_o of the miniature single-polepiece lens as a function of excitation parameter $NI/V_r^{\frac{1}{2}}$ for the two directions of entry of the illuminating electron beam.

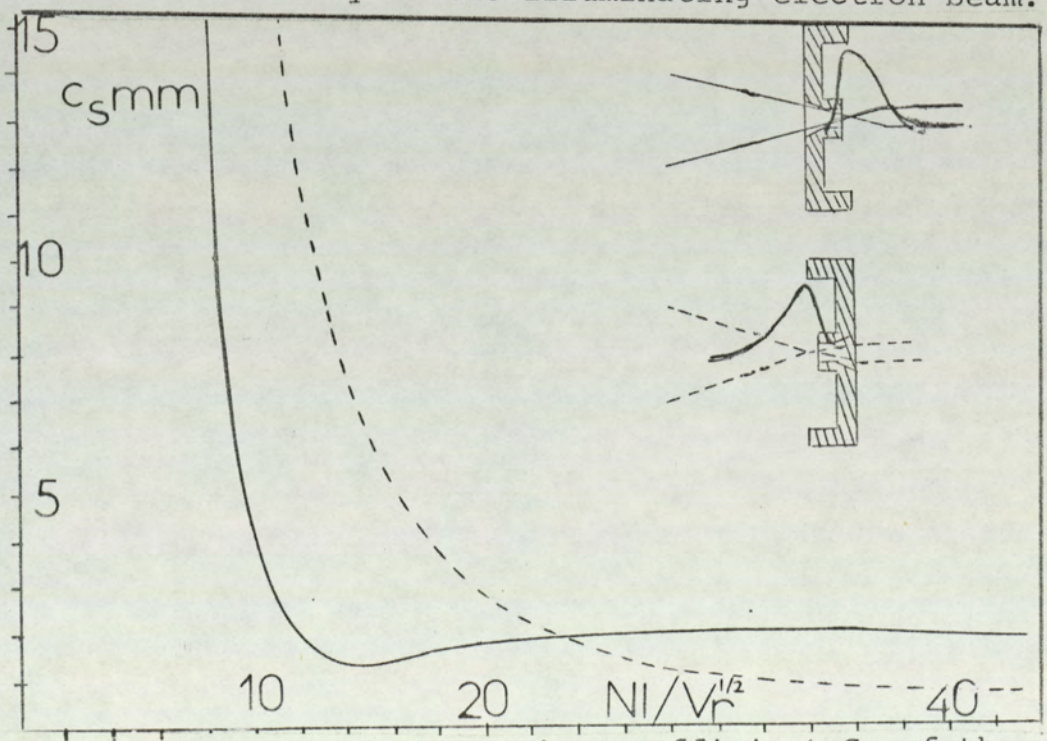

Figure 7 Spherical aberration coefficient C_s of the miniature objective single-polepiece lens as a function of excitation parameter $NI/V_r^{\frac{1}{2}}$ for the two directions of entry of the illuminating electron beam.

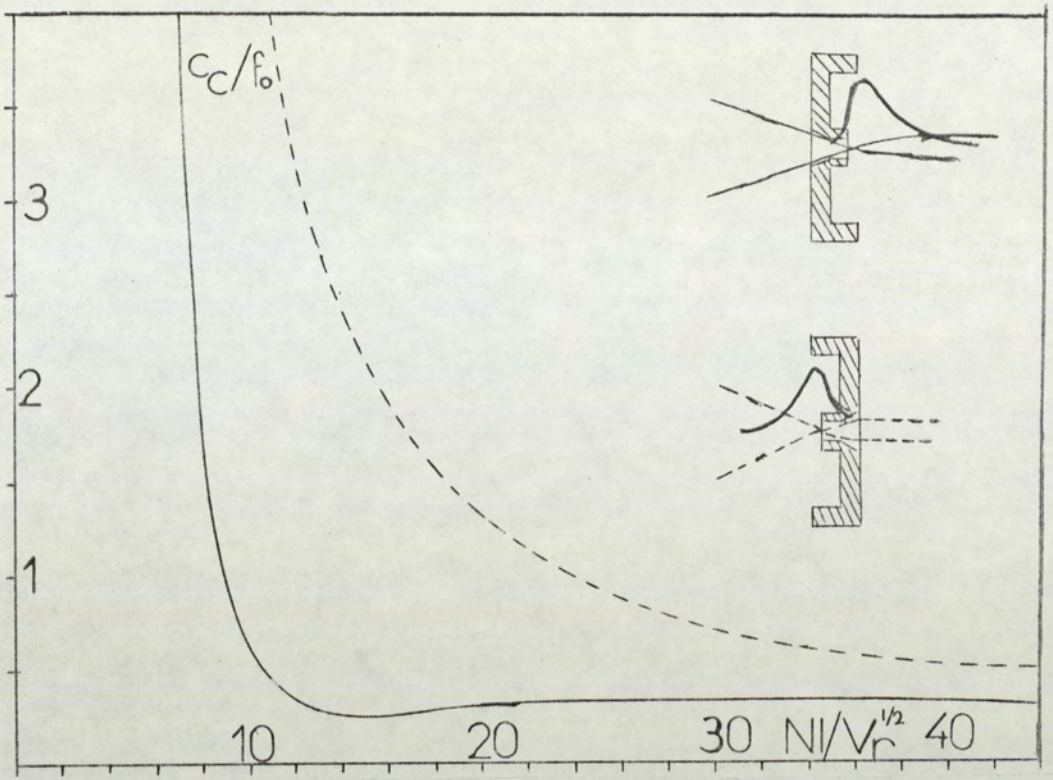

Figure 8 The C_s/f_o quotient of the miniature objective single-polepiece lens as a function of excitation parameter $NI/V_r^{\frac{1}{2}}$ for the two directions of entry of the illuminating electron beam.

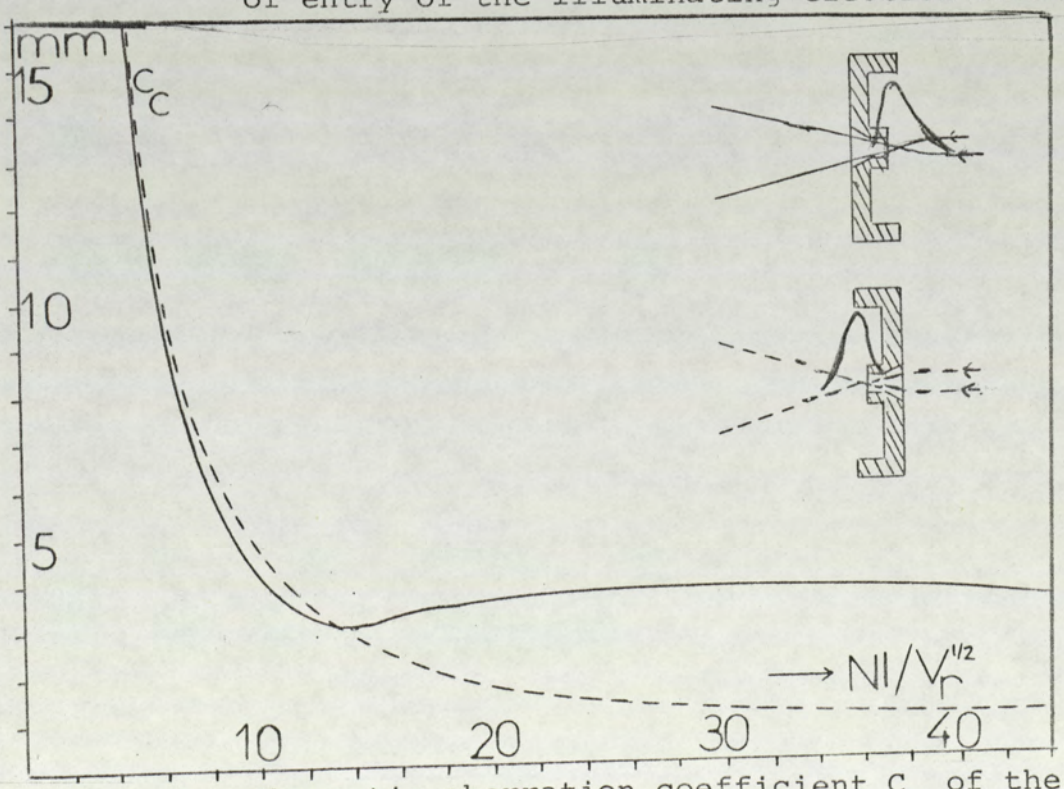

Figure 9 Chromatic aberration coefficient C_c of the miniature objective single-polepiece lens as a function of excitation parameter $NI/V_r^{\frac{1}{2}}$ for the two directions of entry of the illuminating electron beam.

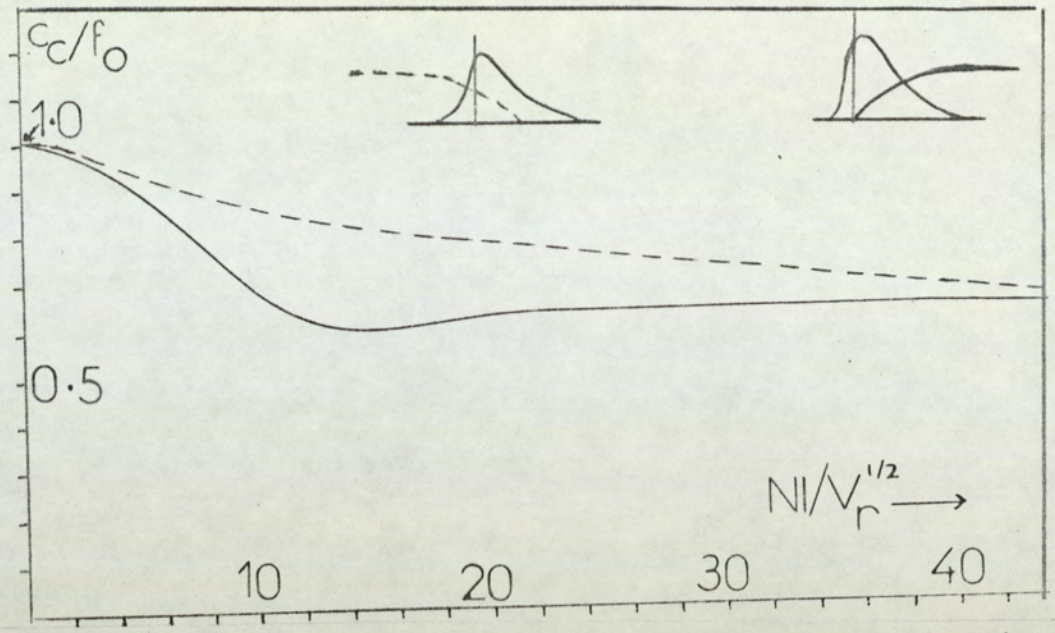

Figure 10 The C_o/f_o quotient of the miniature objective single-polepiece lens as a function of excitation parameter $NI/V_r^{\frac{1}{2}}$ for the two directions of entry of the illuminating electron beam.

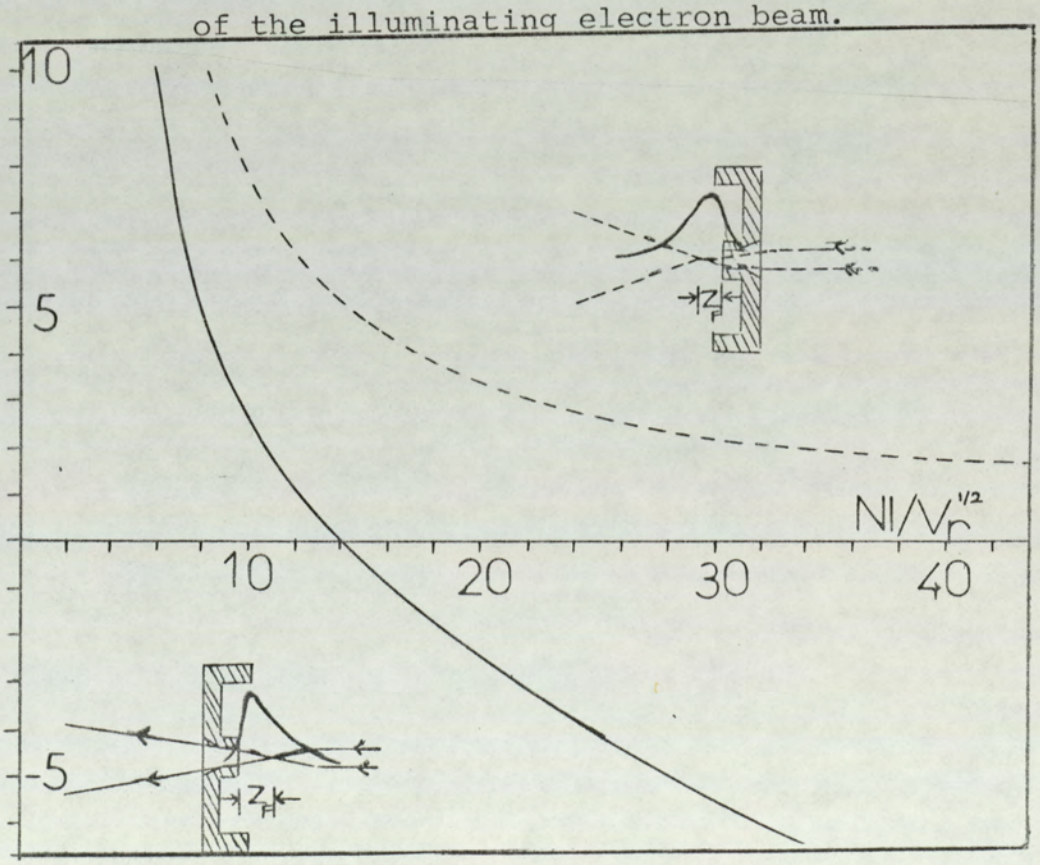

Figure 11 Focal distance Z_F of the miniature objective single-polepiece lens as a function of excitation parameter $NI/V_r^{\frac{1}{2}}$ for the two directions of entry of the illuminating electron beam.

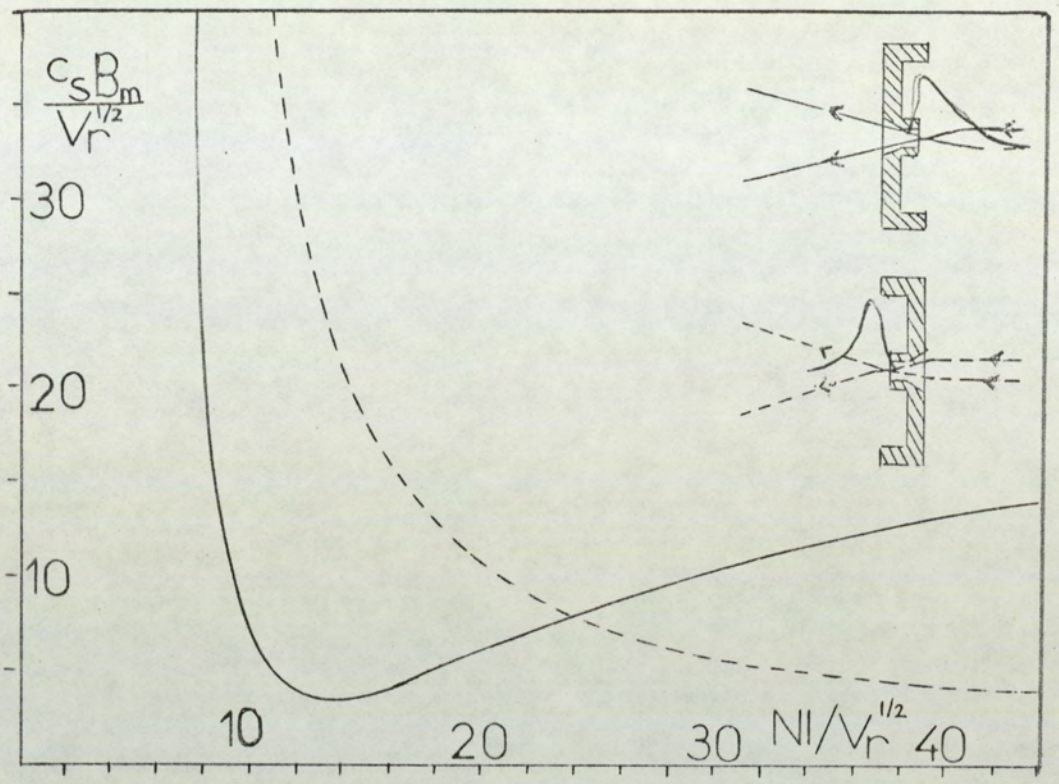

Figure 12 Spherical aberration parameter $C_sB_m/V_r^{\frac{1}{2}}$ of the miniature objective single-polepiece lens as a function of excitation parameter $NI/V_r^{\frac{1}{2}}$ for the two directions of entry of the illuminating electron beam.

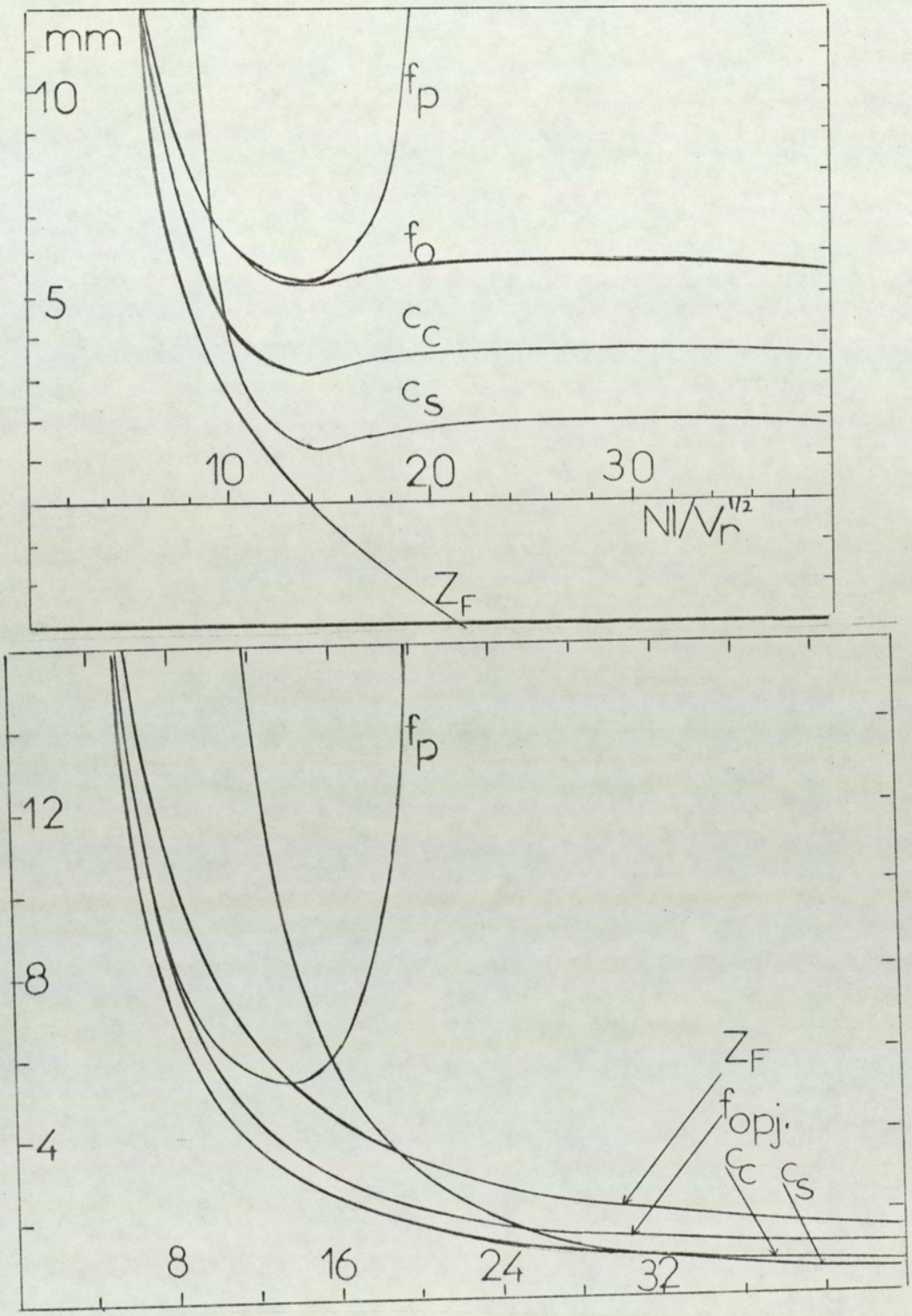

Figure 13 Focal properties of the miniature single-pole-piece lens (a) when the polepiece tip faces the incoming electron beam emerging from the preceding objective lens (b) when the pole face is turned through 180° and placed between specimen and image plane.

10.9 Analytical expression for the spiral distortion coefficient of a single square top field

Spiral distortion coefficient (D_{sp}) for purely magnetic field on object and image plane at infinity is given by

$$D_{sp} = \frac{1}{16V_r}\left(\frac{2e}{mV_r}\right)^{\frac{1}{2}} \int_{-\infty}^{\infty} B(z)\left[\frac{3}{8}\frac{e}{m}B^2(z)+V_r\frac{Y'}{Y}^{\frac{1}{2}}\right]Y^2 dz \quad \ldots\ldots\ldots (A9.1)$$

where Y is the particular solution with the boundary condition

$$\mathrm{Lim}Y_{(z=-\infty)} = 1,\ Y^1{}_{(z=-\infty)} = 0$$

Applying the above equation to a single-square top field, will take the form

$$D_{sp} = \frac{1}{16}\left(\frac{2e}{mV_r}\right)^{\frac{1}{2}}\cdot\frac{3}{8}\frac{e}{m}\frac{B^3(z)}{V_r}\int_{-\infty}^{\infty} Y^2\,dz + \frac{1}{16}\left(\frac{2e}{mV_r}\right)^{\frac{1}{2}} B(z) \int_{-\infty}^{\infty} Y'^2\,dz \quad \ldots\ldots\ldots (A9.2)$$

putting $K^2 = \frac{e}{8m}\frac{B^2(z)}{V_r}$, then

$$D_{sp} = \frac{3}{4}K^3\int_{-\infty}^{\infty} Y^2\,dz + \frac{1}{4}K\int_{-\infty}^{\infty} Y'^2\,dz \quad \ldots\ldots\ldots\ldots\ldots (A9.3)$$

From the solution of paraxial ray equation for a parallel beam of electrons

$$Y = r = r_o \mathrm{Cos}\left[K\left(\frac{s}{2}+z\right)\right]$$
$$Y' = r' = -K\,r_o \mathrm{Sin}\left[K\,(s/2+z)\right] \quad \ldots\ldots\ldots\ldots\ldots (A9.4)$$

Substituting A9.4 in A9.3 and changing limits of integration, then

$$D_{sp} = \frac{3}{4}K^3\int_{o}^{S} \mathrm{Cos}^2(KZ)\,dz + \frac{1}{4}K^3\int_{o}^{S} \mathrm{Sin}^2(KZ)\,dz$$

$$= \frac{K^3}{8} \left[3Z + \frac{3}{2K} \text{Sin } (2KZ) + Z - \frac{1}{2K} \text{Sin}(2KZ) \right]_0^S$$

$$= \frac{K^3}{8} \left[4S + \frac{\text{Sin}(2KS)}{K} \right]$$

putting $KS = \theta_1$, thus

$$D_{sp} \cdot S^2 = \frac{\theta^3}{2} + \frac{\theta^2}{8} \text{ Sin } 2\theta \qquad \text{(A9.5)}$$

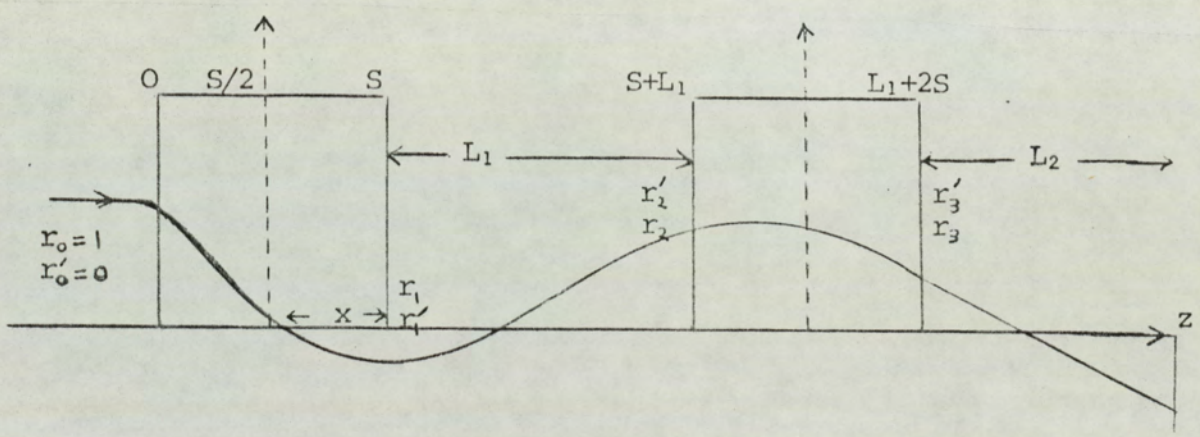

System for correcting spiral distortion with two square top field distribution.

To find the spiral distortion for the second magnetic lens in rotation free system (fig. A9.1), it is important that we should first go through the boundary conditions

From the figure

$$r_1' = r_1/x = r_2/(L+x)$$

$$x = r_1/r_1' = \text{Cos}k_1S/-k \text{ Sin}k_1S$$

$$r_2 = (L+x)r_1' = \left(L - \frac{\text{Cos}k_1S}{k_1 \text{Sin } k_1S}\right) (-k \text{ Sin } k_1S)$$

using $k_2S = \theta_2$, it is apparent that the boundary conditions for second magnetic lens are

$$r_2 = \text{Cos}\theta_1 - (L/S)\,\theta_1\ \text{Sin}\theta_1 \qquad \ldots\ldots\ (A9.6)$$

$$r_2' = r_1' = -k\ \text{Sin}\ \theta_1 \qquad \ldots\ldots\ (A9.7)$$

Applying the above boundary conditions to the equation 3.2 and 3.3 they become

$$Y = r_2\ \text{Cos}(kz) + \frac{r_2'}{k}\ \text{Sin}(kz) \qquad \ldots\ldots\ (A9.8)$$

$$Y' = r_2'\ \text{Cos}(kz) - kr_2\ \text{Sin}(kz) \qquad \ldots\ldots\ (A9.9)$$

These equations are substituted again in equation A9.3 to find the spiral distortion ($\bar{D}_{sp}$) in the second lens

$$\bar{D}_{sp} = \tfrac{3}{4}k^3 \int_0^S \left[r_2\ \text{Cos}(kz) + \frac{r_2'}{k}\ \text{Sin}(kz)\right]^2 dz$$

$$+ \tfrac{1}{4}k \int_0^S \left[r_2'\ \text{Cos}(kz) - r_2 k\ \text{Sin}\ (kz)\right]^2 dz \qquad (A9.10)$$

By using the mathematical formulas

$$\int \text{Cos}^2(kz) = \tfrac{1}{2}z + \frac{1}{4k}\ \text{Sin}\ (2kz)$$

$$\int \text{Sin}^2(kz)\,dz = \tfrac{1}{2}z - \frac{1}{4k}\ \text{Sin}(2kz) \qquad (A9.11)$$

$$\int \text{Cos}(kz)\ \text{Sin}(kz)\,dz = \frac{1}{2k}\ \text{Sin}^2(kz)$$

we get

$$\bar{D}_{sp} = \tfrac{3}{4}k^3 \left[\frac{r_2^2 z}{2} + \frac{r_2^2}{4k}\ \text{Sin}(2kz) + \frac{2r_2 r'^2}{2k^2}\ \text{Sin}^2(kz) + \frac{r_2^2{}'z}{2k^2} - \frac{r_2^2{}'\ \text{Sin}(2kz)}{4k^3}\right]_0^S + \tfrac{1}{4}k \left[\frac{r_2^2 z}{2} + \frac{r_2'^2}{4k}\ \text{Sin}(2kz) - \frac{2r_2 r_2'}{2}\ \text{Sin}^2(kz) + \frac{r_2^2 K^2 z}{2} - \frac{r_2^2 k^2}{4k}\ \text{Sin}(2kz)\right]_0^S \qquad \ldots\ldots\ (A9.12)$$

$$= \frac{K^3}{8}\left[(3r_2^2 + \frac{3r_2^{2\prime}}{k^2})\ S + (\frac{3r_2^2}{2k} - \frac{3r_2^{2\prime}}{2k^3})\mathrm{Sin2kS} + \frac{6r_2r_2'}{k^2}\mathrm{Sin}^2(kS)\right]$$

$$+ \frac{K^3}{8}\left[(\frac{r_2'^2}{k^2} + r_2^2)S + (\frac{r_2'^2}{2k^3} - \frac{r_2^2}{2k})\mathrm{Sin2kS} - \frac{2r_2r_2'}{k^2}\mathrm{Sin}^2(kS)\right]$$

$$= \frac{k^3}{8}\left[4S(\frac{r_2'^2}{k^2} + r_2^2) + \frac{\mathrm{Sin}(2kS)}{k}\ (r_2^2 - \frac{r_2^{2\prime}}{k^2}) + \frac{2r_2r_2'}{k^2} - \frac{2r_2r_2'}{k^2}\mathrm{Cos2kS}\right]$$

This equation could be written as

$$\bar{D}_{sp} = \frac{k^3r_2^2}{8}\left[4S + \frac{\mathrm{Sin}\,2kS}{k}\right] + \frac{k^3r_2^2}{8}\ (\frac{r_2'}{kr_2})\left[4S - \frac{2\ \mathrm{Sin}(2kS)}{k}\right.$$

$$\left. + \frac{\mathrm{Sin}\ (2kS)}{k}\right] - \frac{kr_2r_2'}{4}\mathrm{Cos2kS} + \frac{kr_2r_2'}{4}$$

$$\bar{D}_{sp} = \frac{k^3r^2}{8}\ (4S + \frac{\mathrm{Sin2kS}}{k})\left[1 + (\frac{r_2'}{kr_2})^2\right] - \frac{k^2r_2^2}{4}\ (\frac{r_2'}{kr_2})^2\mathrm{Sin}(2kS)$$

$$- \frac{kr_2r_2'}{4}\mathrm{Cos2kS} + \frac{krr_2'}{4} \quad \ldots\ldots \quad (A9.13)$$

10.10 Magnification and focal length of two rectangular field distributions of width S and separation L_1

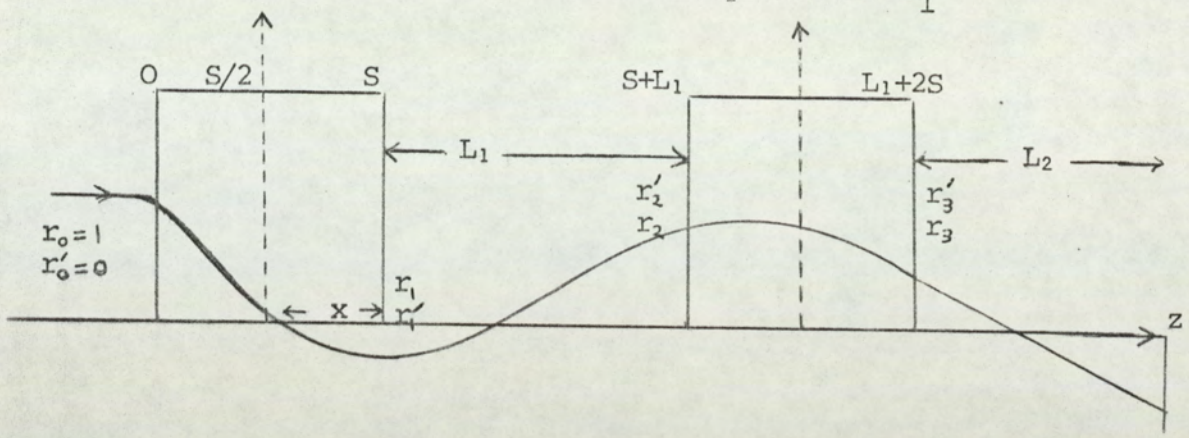

A trajectory through two successive square top field

The general solution of the paraxial ray equation $\frac{d^2r}{dz^2} + k^2r = 0$ for a square top field takes the form

$$r = A \text{ Cos } kz + \text{Sin } kz \quad \ldots\ldots\ldots\ldots \quad (A10.1)$$

where r is the displacement of the ray from the optical axis, A and B are constants and $k = \mu_o \text{ NI}(e/8Vm)^{\frac{1}{2}}$.

The refractive power $(\frac{1}{f})$ is given by the derivative r′ of equation (A10.1)

$$r' = -Ak \text{ Sin } kz + Bk \text{ Cos } kz \quad \ldots\ldots\ldots \quad (A10.2)$$

Using the boundary conditions

$$r = r_o, \; r' = r'_o \text{ at } z = 0$$

Equations A10.1 and A10.2 may be written as

$$r = r_o \text{ Cos } kz + \frac{r'_o}{k} \text{ Sin} kz \quad \ldots\ldots\ldots\ldots \quad (A10.3)$$

$$r' = -r_o \, k \text{ Sin } kz + r'_o \cos kz \quad \ldots\ldots\ldots \quad (A10.4)$$

To determine the ray trajectory through two similar successive magnetic fields, consider the two field distribution as in Figure A10.1.

For the first field, the boundary conditions are $r_o = 1$, $r'_o = 0$, then the equations 3 and 4 which describe the trajectory in field 1 become

$$r = \text{Cos } kz \text{ and} \quad \ldots\ldots\ldots\ldots\ldots\ldots \quad (A10.5)$$

$$r' = -k_1 \text{ Sin } k_1 z \quad \ldots\ldots\ldots\ldots\ldots\ldots \quad (A10.6)$$

The ray emerges at $z = S$ where

$$r_1 = \text{Cos} k_1 S \quad \ldots\ldots\ldots\ldots\ldots\ldots \quad (A10.7)$$

$$r'_1 = -k_1 \text{ Sin } k_1 S \quad \ldots\ldots\ldots\ldots\ldots\ldots \quad (A10.8)$$

After emerging from the first field, the ray traverses a distance L_1 along the optical axis and then enters the second field. The boundary conditions in field II at $z = L + S$ are

$r = r_2$ and $r' = r'_2$ thus

$$r_2 = r_1 - (L_1/S) \text{ Sin } k_1 S \quad \ldots\ldots\ldots \quad (A10.9)$$

$$r'_2 = r'_1 = -k \text{ Sin } k_1 S \quad \ldots\ldots\ldots\ldots\ldots \quad (A10.10)$$

The ray trajectory in field II is

$$r = r_2 \text{ Cos } k_2 \left[z - (L_1+S)\right] + \frac{r'_2}{k_2} \text{ Sin } k_2 \left[z - (L_1+S)\right] \quad (A10.11)$$

$$r' = r'_2 \text{ Cos } k_2 \left[z-(L_1+S)\right] + r_2 k_2 \text{ Sin } k_2 \left[z-(L_1+S)\right] \quad (A10.12)$$

At the point where the ray leaves the second lens, namely

where $z = L_1 + 2S$ we obtain

$$r_3 = r_2 \ \text{Cos}\ k_2S + \frac{r_2'}{k_2} \text{Sin}\ k_2S \quad \ldots\ldots \quad (A10.13)$$

$$r_3' = r_2' \ \text{Cos}\ k_2S\ r_2 \text{Sin}\ k_2S \quad \ldots\ldots\ldots \quad (A10.14)$$

Substituting for r_2 and r_2' in equations A10.16 and A10.17

$$r_3 = \text{Cos}\ k_1 \ \text{Cos}\ k_2S - L_1k_1 \ \text{Sin}\ k_1S \ \text{Cos}\ k_2S - \frac{k_1}{k_2} \text{Sin}\ k_2S$$

$$r_3' = -\left[k_1 \ \text{Sin}\ k_1S \ \text{Cos}\ k_2S + k_2 \ \text{Cos}\ k_1S \ \text{Sin}\ k_2S - k_1k_2L_1 \right.$$

$$\left. \text{Sin}\ k_1S \ \text{Sin}\ k_2S\right]$$

putting $k_1S = \theta_1$ and $k_2S = \theta_2$

$$r_3 = \text{Cos}\ \theta_1 \ \text{Cos}\ \theta_2 - (L_1/S)\ \theta_1 \text{Sin}\theta_1 - \frac{\theta_1}{\theta_2} \text{Sin}\theta_1 \text{Sin}\theta_2 \quad (10.15)$$

$$r_3' = -\left[\theta_1 \text{Sin}\theta_1 \text{Cos}\theta_2 + \theta_2 \text{Cos}\ \theta_1 \text{Sin}\theta_2 - \theta_1\theta_2 (L_1/S) \text{Sin}\ \theta_1 \text{Sin}\theta_2\right]$$

$$\ldots\ldots\ldots \quad (A10.16)$$

If the image is projected onto a screen at a distance L_2 from the point $z = L_1 + 2S$ the beam will strike the screen at a radial displacement M_f from the optical axis

$$M_f = \text{Cos}\ \theta_1 \ \text{Cos}\ \theta_2 - \frac{L_1}{S} \theta_1 \ \text{Sin}\theta_1 \ \text{Cos}\ \theta_2$$

$$-\frac{\theta_1}{\theta_2} \ \text{Sin}\theta_1 \ \text{Sin}\theta_2 - \frac{L_2}{S} \left[\theta_1 \ \text{Sin}\theta_1 \ \text{Cos}\ \theta_2 + \theta_2 \ \text{Cos}\theta_1 \text{Sin}\theta_2 - \right.$$

$$\left. -\theta_1\theta_2 \ \frac{L_1}{S} \text{Sin}\theta_1 \ \text{Sin}\theta_2\right] \quad \ldots\ldots\ldots\ldots\ldots \quad (10.17)$$

The combined projector focal length of the double lens system F_p is given by $F_p = \frac{r_o}{r_3'}$ then from equation A10.16 A.10.16

$$F_p/S = -\left[\theta_1 \ \text{Sin}\theta_1 \ \text{Cos}\theta_2 + \theta_2 \ \text{Cos}\theta_1 \text{Sin}\ \theta_2 \right.$$

$$\left. -\theta_1\theta_2 \ (\frac{L_1}{S}) \text{Sin}\ \ \theta_1 \text{Sin}\ \theta_2\right]^{-1} \quad \ldots\ldots\ldots\ldots \quad (10.18)$$

The special case of $\theta_2 = \pi/2$

When the second lens is operated at a constant excitation $\{(NI/V_r^{\frac{1}{2}}) = 8.43\}$ i.e. $\Theta_2 = \pi/2$ then

$$r_3 = -\frac{\theta_1}{\theta_2} \sin\theta_1 \sin\theta_2 = -\frac{2}{\pi}\theta_1 \sin\theta_1)$$

$$r_3' = -\frac{\pi}{2}\left[\cos\theta_1 - \theta_1'(L_1/S)\sin\theta_1\right]$$

and

$$F_p/S = \frac{-2}{\pi}\left\{1/\left[\cos\theta_1 - \theta_1\left(\frac{L_1}{S}\right)\sin\theta_1\right]\right\} \qquad \text{(A10.19)}$$

The final magnification is given by:

$$M_f = -\frac{2}{\pi}\left[\theta_1\sin\theta_1\right] - \left(\frac{L_1}{S}\right)\frac{\pi}{2}\left[\cos\theta_1 - \theta_1\left(\frac{L_1}{S}\right)\sin\theta_1\right]$$

(A10.20)